U.S. Department of Transportation

Federal Railroad Administration

Crash Energy Management: One- and Two-Car Passenger Rail Impact Tests – Summary of Structural and Occupant Test Results

Office of Research,
Development,
and Technology
Washington, DC 20590

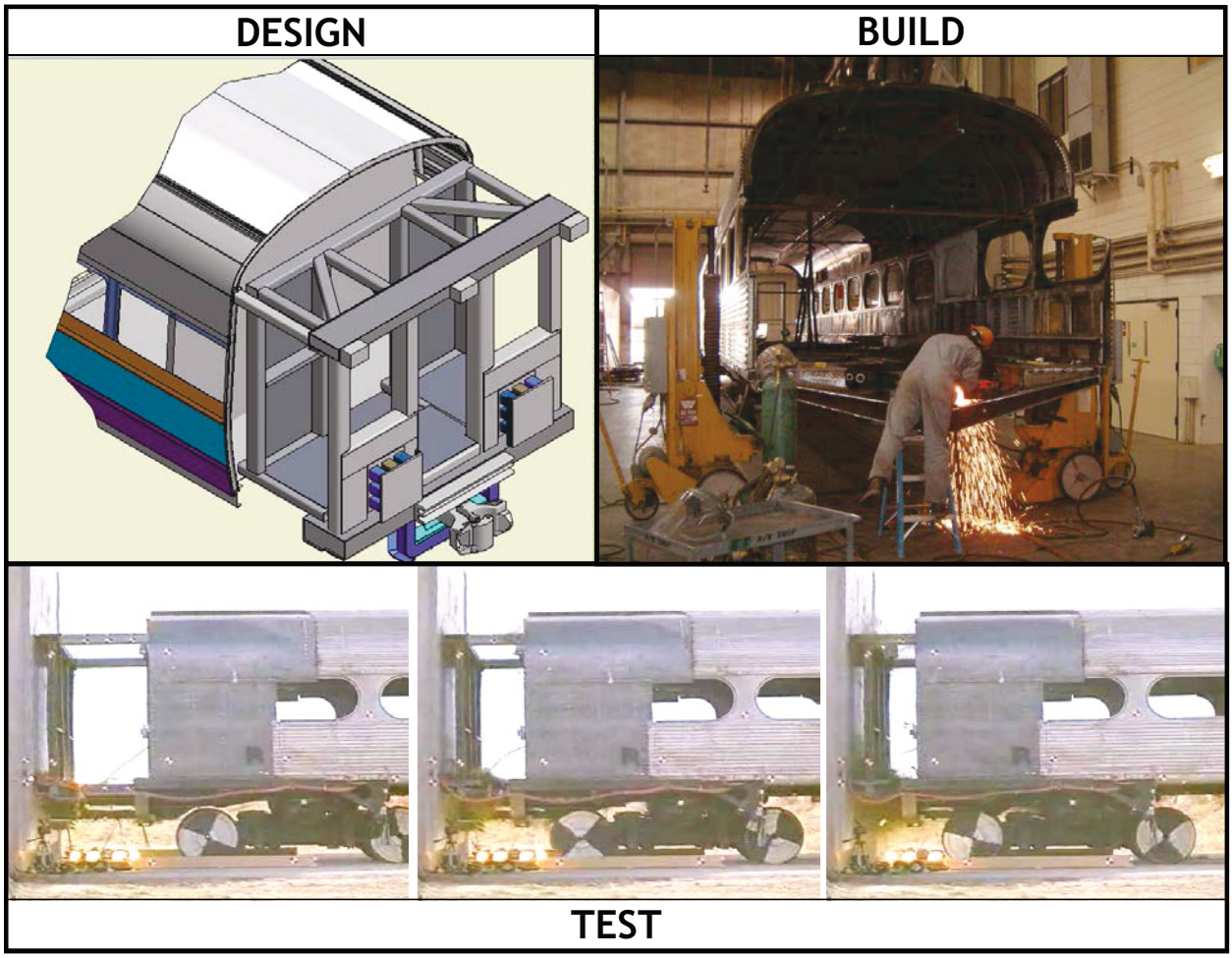

DOT/FRA/ORD-16/37

Final Report
December 2016

REPORT DOCUMENTATION PAGE

Form Approved
OMB No. 0704-0188

1. AGENCY USE ONLY (Leave blank)	2. REPORT DATE	3. REPORT TYPE AND DATES COVERED
	December 2016	Technical Report December 2003 – March 2004

4. TITLE AND SUBTITLE
Crash Energy Management: One- and Two-Car Passenger Rail Impact Tests
Summary of Structural and Occupant Test Results

5. FUNDING NUMBERS

6. AUTHOR(S)
Karina Jacobsen, David Tyrell, Kristine Severson, Dan Parent, Eloy Martinez

7. PERFORMING ORGANIZATION NAME(S) AND ADDRESS(ES)
U.S. Department of Transportation
John A. Volpe National Transportation Systems Center
55 Broadway
Cambridge, MA 02142-1093

8. PERFORMING ORGANIZATION REPORT NUMBER

9. SPONSORING/MONITORING AGENCY NAME(S) AND ADDRESS(ES)
U.S. Department of Transportation
Federal Railroad Administration
1200 New Jersey Avenue, SE
Washington, DC 20590

10. SPONSORING/MONITORING AGENCY REPORT NUMBER
DOT/FRA/ORD-16/37

11. SUPPLEMENTARY NOTES

12a. DISTRIBUTION/AVAILABILITY STATEMENT

12b. DISTRIBUTION CODE

13. ABSTRACT (Maximum 200 words)

Two full-scale impact tests were conducted to measure the crashworthiness performance of Crash Energy Management (CEM) equipped passenger rail cars. On December 3, 2003, a single car impacted a fixed barrier at approximately 35 mph and on February 26, 2004, two-coupled passenger cars impacted a fixed barrier at approximately 29 mph. Coach cars retrofitted with CEM end structures, designed to crush in a controlled manner, were used in the tests. These test vehicles were instrumented with accelerometers, string potentiometers, and strain gauges to measure the gross motions of each car body in three dimensions, the deformation of specific structural components, and the force-crush characteristic of the CEM end structure. Five occupant experiments were conducted onboard the test vehicles in the two-car test to measure the secondary impact conditions. Collision dynamics models were developed to predict the gross motions of the test vehicles. Crush estimates as a function of test speed were used to guide test conditions. Using the crash pulse derived from the collision dynamics model, computer models for the occupant tests were developed to determine the severity of the collision environment and predict the motions of the Anthropomorphic Test Devices (ATDs) used in two-car tests. This report describes the details of the CEM single-car and two-car tests, and reports the findings of the structural and occupant tests.

14. SUBJECT TERMS
transportation, safety, crash energy management, crashworthiness, passenger rail vehicles, cab car end structure, impact test

15. NUMBER OF PAGES
188

16. PRICE CODE

17. SECURITY CLASSIFICATION OF REPORT	18. SECURITY CLASSIFICATION OF THIS PAGE	19. SECURITY CLASSIFICATION OF ABSTRACT	20. LIMITATION OF ABSTRACT
Unclassified	Unclassified	Unclassified	

NSN 7540-01-280-5500

Standard Form 298 (Rev. 2-89)
Prescribed by ANSI Std. 239-18
298-102

METRIC/ENGLISH CONVERSION FACTORS

ENGLISH TO METRIC	METRIC TO ENGLISH
LENGTH (APPROXIMATE)	**LENGTH (APPROXIMATE)**
1 inch (in) = 2.5 centimeters (cm)	1 millimeter (mm) = 0.04 inch (in)
1 foot (ft) = 30 centimeters (cm)	1 centimeter (cm) = 0.4 inch (in)
1 yard (yd) = 0.9 meter (m)	1 meter (m) = 3.3 feet (ft)
1 mile (mi) = 1.6 kilometers (km)	1 meter (m) = 1.1 yards (yd)
	1 kilometer (km) = 0.6 mile (mi)
AREA (APPROXIMATE)	**AREA (APPROXIMATE)**
1 square inch (sq in, in^2) = 6.5 square centimeters (cm^2)	1 square centimeter (cm^2) = 0.16 square inch (sq in, in^2)
1 square foot (sq ft, ft^2) = 0.09 square meter (m^2)	1 square meter (m^2) = 1.2 square yards (sq yd, yd^2)
1 square yard (sq yd, yd^2) = 0.8 square meter (m^2)	1 square kilometer (km^2) = 0.4 square mile (sq mi, mi^2)
1 square mile (sq mi, mi^2) = 2.6 square kilometers (km^2)	10,000 square meters (m^2) = 1 hectare (ha) = 2.5 acres
1 acre = 0.4 hectare (he) = 4,000 square meters (m^2)	
MASS - WEIGHT (APPROXIMATE)	**MASS - WEIGHT (APPROXIMATE)**
1 ounce (oz) = 28 grams (gm)	1 gram (gm) = 0.036 ounce (oz)
1 pound (lb) = 0.45 kilogram (kg)	1 kilogram (kg) = 2.2 pounds (lb)
1 short ton = 2,000 pounds (lb) = 0.9 tonne (t)	1 tonne (t) = 1,000 kilograms (kg) = 1.1 short tons
VOLUME (APPROXIMATE)	**VOLUME (APPROXIMATE)**
1 teaspoon (tsp) = 5 milliliters (ml)	1 milliliter (ml) = 0.03 fluid ounce (fl oz)
1 tablespoon (tbsp) = 15 milliliters (ml)	1 liter (l) = 2.1 pints (pt)
1 fluid ounce (fl oz) = 30 milliliters (ml)	1 liter (l) = 1.06 quarts (qt)
1 cup (c) = 0.24 liter (l)	1 liter (l) = 0.26 gallon (gal)
1 pint (pt) = 0.47 liter (l)	
1 quart (qt) = 0.96 liter (l)	
1 gallon (gal) = 3.8 liters (l)	
1 cubic foot (cu ft, ft^3) = 0.03 cubic meter (m^3)	1 cubic meter (m^3) = 36 cubic feet (cu ft, ft^3)
1 cubic yard (cu yd, yd^3) = 0.76 cubic meter (m^3)	1 cubic meter (m^3) = 1.3 cubic yards (cu yd, yd^3)
TEMPERATURE (EXACT)	**TEMPERATURE (EXACT)**
[(x-32)(5/9)] °F = y °C	[(9/5) y + 32] °C = x °F

QUICK INCH - CENTIMETER LENGTH CONVERSION

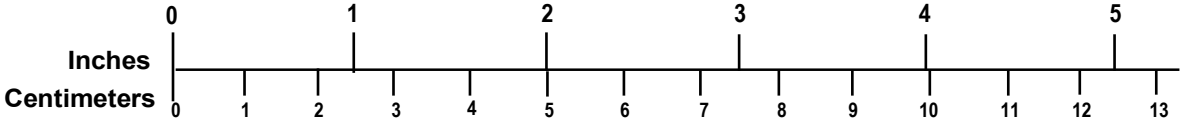

QUICK FAHRENHEIT - CELSIUS TEMPERATURE CONVERSIO

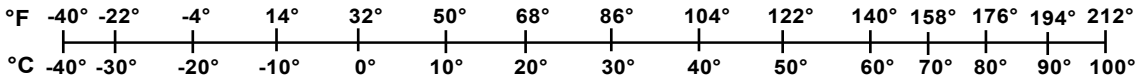

For more exact and or other conversion factors, see NIST Miscellaneous Publication 286, Units of Weights and Measures. Price $2.50 SD Catalog No. C13 10286

Updated 6/17/98

Preface

The impact tests of the Crash Energy Management (CEM) design mark the second stage of studying in-line train-to-train collisions involving passenger equipment. CEM equipment demonstrates improved crashworthiness performance over conventional equipment; CEM equipment collision behavior is characterized by controlled crush of car ends and distribution of crush among multiple car ends.

The authors would like to thank Dr. Tom Tsai, Program Manager, retired, and Claire Orth, Division Chief, retired, of the Equipment and Operating Practices Research Division, Office of Research and Development, Federal Railroad Administration (FRA), for their support. The authors would also like to thank Gunars Spons, FRA Resident Manager, retired, at the Transportation Technology Center, for managing the full-scale test effort.

The authors would also like to acknowledge the work of others in designing, building, analyzing, and testing the CEM cars: Kent Johnson of Premiere Engineering, who was the principal designer of the coach car crush zone; Gabriel Amar of TRA Associates, who changed the design of the coach car crush zone during the retrofit process for both the single-car and two-car tests; Dr. Richard Stringfellow and Patricia Llana of TIAX, LLC, who developed the finite element model of the CEM crush zones; Dr. Ronald Mayville of R.A. Mayville and Associates (formerly with Arthur D. Little, Inc.), who led the overall effort to develop the coach car crush zone design; Ken Laine and Russ Walker, of the Transportation Technology Center Inc. (TTCI), led the effort to implement the tests; and Tom Roderick, who was also from TTCI, led the effort to integrate the crush zones onto the Pioneer and M1 cars.

The authors would also like to acknowledge those who contributed to the occupant experiments: Simula Technologies, Inc., who implemented the occupant experiments; Mark Haffner, THOR Program Manager at the NHTSA National Transportation Biomechanics Research Center, who provided the THOR ATD; and the United Kingdom's Rail Safety and Standards Board, who provided the Hybrid 3 Rail Safety ATD.

Contents

Executive Summary **1**

1. Introduction **2**

2. Crash Energy Management Design **6**

3. Structural Test Description **9**

4. Modeling Approach **11**

5. Analysis of Structural Test Results **14**

5.1 Post-Test Results of Crush Zone Performance 14
5.2 Post-Test Results of Vehicle Gross Motions 15

6. Discussion of Structural Test Results **19**

7. Description of Occupant Tests **20**

7.1 Experiment 1-1: Forward-Facing Intercity Seats, Two 95th Percentile Male ATDs, Leading Car 20
7.2 Experiment 2-1: Rear-Facing Commuter Seat, One 50th Percentile Male ATD, Trailing Car 21
7.3 Experiment 2-2: Forward-Facing Commuter Seat, Three 50th Percentile Male ATDs, Trailing Car 22
7.4 Experiments 1-2 and 1-3: Facing Commuter Seats with Workstation Table 23

8. Analysis of Occupant Test Results **25**

8.1 Experiment 1-1: Forward-Facing Intercity Seats, Two 50th-Percentile Male ATDs, Leading Car 26
8.2 Experiment 2-1: Rear-Facing Commuter Seat, One 50th-Percentile Male ATD, Trailing Car 28
8.3 Experiment 2-2: Forward-Facing Commuter Seats, Three 50th-Percentile Male ATDs, Trailing Car 29
8.4 Experiment 1-2: Forward-Facing Intercity Seats with Table, One Hybrid 3RS ATD, Leading Car 30
8.5 Experiment 1-3: Forward-Facing Intercity Seat with Table, One THOR ATD, Leading Car 31

9. Discussion of Occupant Tests **33**

10. Summary and Conclusions **34**

References **36**

Abbreviations and Acronyms **39**

Appendix A. Retrofit of Existing Budd Pioneer Cars with CEM Crush Zones 40
Integration Sequence 42
Lessons Learned 46

Appendix B. Structural Instrumentation 48
Accelerometers 48
Strain Gauges 55
String Potentiometers 60
High-Speed Cameras and Video 64
Data Acquisition 68

Appendix C. Collision Dynamics Modeling 69
Single-Car Model Description 69
Two-Car Model Description 70
Selected Results 71

Appendix D. Data Reduction 72
Single-Car Test 72
Two-Car Test 74

Appendix E. The Crash Zone Force/Crush Characteristic 78
Introduction 78
Crush Zone Force/Crush Characteristic 78
One-Dimensional Single Degree-of-Freedom Model 82
One-Dimensional Three Degree-of-Freedom Model 84

Appendix F. Occupant Test Requirements 88
Background Information 88
Test Objectives 89
Test Requirements 89
Required Test Measurements 91
Required Test Measurements, Table Experiments 93
Test Documentation 95

Appendix G. Occupant Model Descriptions 97
Experiment 1-1. Forward-Facing Intercity Seats 97
Experiment 1-2: Facing Commuter Seats with Intervening Workstation Table, Hybrid III Railway Safety ATD 104
Experiment 1-3: Facing Commuter Seats with Intervening Workstation Table, THOR ATD 109
Experiments 2-1 and 2-2: Rear- and Forward-Facing Commuter Seats 115

Appendix H. Occupant Modeling and Test Results 119
Experiment 1-1. Forward-Facing Intercity Seats 119
Experiment 1-2. Facing Seats with Workstation Table 135
Experiment 1-3: Facing Seats with Workstation Table 150
Experiment 2-1: Rear-Facing Commuter Seat 170
Experiment 2-2: Forward-Facing Commuter Seat 174

Figures

1. Location of Occupant Experiments in Leading Cab Car 4
2. Location of Occupant Experiments in Trailing Coach Car 5
3. Idealized Force-Crush Curve for Conventional Design 6
4. Idealized Force-Crush Curve for CEM Design 7
5. Cross Section of Crash Energy Management (CEM) Design 8
6. Test Vehicles Prior to Two-Car Test 9
7. Modeling Process Flow Diagram 11
8. CEM Force-Crush Curve from Finite Element Model 12
9. Schematic of Collision Dynamics Model 12
10. Crush Estimation Versus Impact Speed 13
11. Post-Test Photographs of Conventional (left) and CEM (right) Vehicles 14
12. Post-test Photographs of Conventional (top) and CEM (bottom) Coupled Connections 15
13. Still Photographs of Coupled Interface for Conventional (top) and CEM (bottom) at Time of Impact (left) and Maximum Crush (right) 16
14. Single-Car Velocity-Time History Plot 17
15. Two-Car Velocity Plots 18
16. Pre-test Photo of Experiment 1-1 21
17. Pre-test Photo of Experiment 2-1 22
18. Pre-test Photo of Experiment 2-2 22
19. Pre-test Photo of Experiment 1-2 24
20. Pre-test Photo of Experiment 1-3 24
21. Longitudinal Car Acceleration 25
22. Relative Velocity versus Relative Displacement 26
23. Photo Series for Experiment 1-1: Forward-Facing Intercity Seats, Leading Car 27
24. Photo Series for Experiment 2-1: Rear-Facing Commuter Seat, Trailing Car 28
25. Time-Sequence for Experiment 2-2, Forward-Facing Commuter Seat, Trailing Car 29
26. Photo Series for Experiment 1-2: Hybrid 3RS with Table, Leading Car 30
27. Photo Series for Experiment 1-3, THOR with Table, Leading Car 31

Appendix A

A1. Flow Chart, Retrofit of Crush Zones onto Existing Conventional Cars 40
A2. Example Assemblies Fabricated at Rail Car Shop 41
A3. Pre-integration Photograph of a Budd Pioneer Car 41
A4. Reinforcing the Existing Body Bolster 42
A5. Reinforcing the Existing Side Sills and Extending the Cant/Roof Rails 43
A6. Fixed Sill and Cross-Bearers Installed 43
A7. Integration of the Sliding Sill into the Fixed Sill 44
A8. Placement of End Frame onto Sliding Sill 45
A9. Placement of the Primary Energy Absorbers and Floor Plates 45
A10. Final Assembly Stage: Placement of Partition Wall and Roof 46
A11. Retrofitted Design Against Rigid Barrier Test Wall 47

Appendix B

B1. Schematic of CEM Two Car Impact into a Rigid Barrier Test Layout 48
B2. Typical Placement of Push-Back Coupler Accelerometers 49
B3. Typical Placement of Accelerometers on the Sliding Sill 49
B4. Typical Placement of Accelerometers on End/Buffer Beam and Anti-Telescoping Plate 50
B5. Typical Placement of Accelerometers mounted on the Body Bolster and Truck 50
B6. Typical Placement of Accelerometers Mounted at Longitudinal CG of Coach Car 50
B7. Vertical View of Car 248 (Leading) Accelerometer Pre-Test Measurement Layout 52
B8. Lateral View of Car 248 (Leading) Accelerometer Pre-Test Measurement Layout 52
B9. Longitudinal View of Car 248 (Leading) Accelerometer Pre-Test Measurement Layout 53
B10. Vertical View of Car 244 (Trailing) Accelerometer Pre-Test Measurement Layout 53
B11. Lateral View of Car 244 (Trailing) Accelerometer Pre-Test Measurement Layout 54
B12. Longitudinal View of Car 244 (Trailing) Accelerometer Pre-Test Measurement Layout 54
B13. Strain Gauge Layout on Car 248 (Leading) End Fixed/Sliding Sill 56
B14. Strain Gauge Layout on Car 248 (Trailing) End Fixed/Sliding Sill 57
B15. Strain Gauge Layout on Car 244 (Leading) End Fixed/Sliding Sill 57
B16. Strain Gauge Layout on Car 248 (Leading) Center and Side Sills 58
B17. Strain Gauge Layout on Car 248 (Trailing) Center and Side Sills 58
B18. Strain Gauge Layout on Car 244 (Leading) Center and Side Sills 59
B19. Strain Gauge Layout on Cars 248 and 244 Cant Rails 59
B20. Vertical Location of String Potentiometers on Leading Car 248 61
B21. Lateral Location of String Potentiometers on Leading Car 248 61
B22. Longitudinal Location of String Potentiometers on Leading Car 248 62
B23. Vertical Location of String Potentiometers on Leading Car 244 62
B24. Lateral Location of String Potentiometers on Leading Car 244 63
B25. Longitudinal Location of String Potentiometers on Leading Car 244 63
B26. Inter-Car Location of String Potentiometers 64
B27. Schematic of Exterior Camera Locations 65
B28. Top View of Target Locations on Lead Car 248 65
B29. Side View of Target Locations on Test Lead Car 248: Lead End 66
B30. Side View of Target Locations on Test Lead Car 248: Trailing End 66
B31. Top View of Target Locations on Car 244 67
B32. Side View of Target Locations on Car 244 67

Appendix C

C1. Single Car Lumped Mass Model Schematic 69
C2. Component Force-Crush Characteristics 70
C3. Schematic of Two-Car Three-Dimensional Model and Close-up of Coupled Ends 71

Appendix D

D1. Right Side View of Impacting End 72
D2. Influence of Filter Bandwidth on Accelerometer Results for Coupler Longitudinal Displacement 73
D3. Coupler Longitudinal Displacement Time History 73
D4. End Frame Longitudinal Displacement Time History 73
D5. Car Body Longitudinal Displacement Time History 74
D6. Schematic of Test, Elevation View of Left Side 74

D7. Position of the First Car Body with Respect to Time 75
D8. Position of the End Frame, at Car 1 and End 1, with Respect to Time 76
D9. Relative Displacement Between the First End Frame and the First Car Body 76
D10. Relative Displacements of the Two Car Bodies with Respect to Time 77

Appendix E
E1. Idealized CEM Force/Crush Characteristic 79
E2. Strains in Sliding Sill Near Shear-back Coupler Fuse Bolts 79
E3. Strains in Fixed Sill Near Sliding-Sill Fuse Bolts 80
E4. Measured and Idealized Force from Crush of Pushback Coupler Energy Absorber 81
E5. Measured and Idealized Force from Crush of Primary and Roof Energy Absorbers 81
E6. One-Dimensional Single Degree-of-Freedom Model 82
E7. Car Acceleration Time History, Test and Model Results 82
E8. Car Velocity Time History, Test and Model Results 83
E9. Car Displacement Time History, Test and Model Results 83
E10. Force/Displacement Characteristic, Calculated from Test Measurements and Model Results 84
E11. One-Dimensional Three-Degree-of-Freedom Model 84
E12. Component Force/Crush Characteristics for Three-Degree-of-Freedom Model 85
E13. Model and Test Results for Accelerations of the Coupler, Sliding Sill and End Frame, and Carbody and Truck Masses 85
E14. Model and Test Results for the Velocities of the Coupler, Sliding Sill and End Frame, and Carbody and Truck Masses 86
E15. Model and Test Results for the Displacements of the Coupler, Sliding Sill and End Frame, and Carbody and Truck Masses 87
E16. Model and Test Results for CEM Force/Crush Characteristic, Calculated from Component Accelerations 87

Appendix F
F1. Location of Leading Car Occupant Experiments 89
F2. Location of Trailing Car Occupant Experiments 90
F3. Placement of High-Speed Video Cameras and Photo Targets in the Experiments Without Workstation Tables 91
F4. Placement of Photo Targets Visible to the Side-View Camera in the Experiments Without Workstation Tables 92
F5. Placement of High-Speed Video Cameras and Photo Targets in the Experiments with Workstation Tables 93
F6. Placement of Photo Targets Visible to the Top- and Side-View Cameras in the Experiments with Workstation Tables 93
F7. Load Cell Installation Positions for Experiments 1-2 and 1-3 94

Appendix G
G1. Test Photograph and Model Depiction of Forward-Facing Intercity Seat Experiment 97
G2. Measured Acceleration, Relative Velocity, and Relative Displacement of the Lead Car Body 99
G3. Contact Characteristics A, B, and C for MADYMO Model of Experiment 1-1 100
G4. Load Characteristics A, B, and C for MADYMO Model of Experiment 1-1 101
G5. Struck Seat Model 102

G6. Seatback Deformation 103
G7. Struck Seat System 103
G8. Test Photograph with H3RS ATD and Model Depiction with HIII ATD of Facing Seat Experiment with Workstation Table 104
G9. Measured Acceleration, Relative Velocity, and Relative Displacement of the Lead Car Body 106
G10. Contact Characteristics for MADYMO Model of Experiment 1-2 107
G11. Load Characteristics for MADYMO Model of Experiment 1-2 108
G12. MADYMO Model of Experiment 1-2 108
G13. Test photograph and Model Depiction of Facing Seat Experiment with Workstation Table with THOR ATD 109
G14. Measured Acceleration, Relative Velocity, and Relative Displacement of the Lead Car Body 112
G15. Contact Characteristics for MADYMO Model of Experiment 1-3 113
G16. Load Characteristics for MADYMO Model of Experiment 1-3 114
G17. MADYMO Model of Experiment 1-3 114
G18. Hybrid III 50th-Percentile ATD in the Middle Seat Position 115
G-19. Uninstrumented Hybrid II 50th-Percentile Male ATD in the Middle Seat Position 116
G20. Cylinder Identification 117
G21. Force vs. Crush of Contact Surfaces 117
G22. Moment vs. Rotation of Seat Back 118

Appendix H

H1. Head CG Acceleration, Local X 119
H2. Head CG Acceleration, Local Y 120
H3. Head CG Acceleration, Local Z 120
H4. Head CG Acceleration, Resultant 121
H5. Head CG Acceleration, Resultant 121
H6. Chest Acceleration, Local X 122
H7. Chest Acceleration, Local Y 122
H8. Chest Acceleration, Local Z 123
H9. Chest Acceleration, Resultant 123
H10. Left Femur Force, Local X 124
H11. Right Femur Force, Local X 124
H12. Upper Neck Shear Force, Fx 125
H13. Upper Neck Axial Force, Fz 125
H14. Upper Neck Occipital Condyle Bending Moment, M_y 126
H15. Head CG Acceleration, Local X 127
H16. Head CG Acceleration, Local Y 127
H17. Head CG Acceleration, Local Z 128
H18. Head CG Acceleration, Resultant 128
H19. Head CG Acceleration, Resultant 129
H20. Chest Acceleration, Local X 129
H21. Chest Acceleration, Local Y 130
H22. Chest Acceleration, Local Z 130
H23. Chest Acceleration, Resultant 131
H24. Left Femur Force, Local X 131

H25. Right Femur Force, Local X 132
H26. Upper Neck Shear Force, Fx 132
H27. Upper Neck Axial Force, Fz 133
H28. Upper Neck Occipital Condyle Bending Moment, M_y 133
H29. Test Dummy Kinematics in Forward-Facing Rows of Seats, Simulation Results and Test Observations 134
H30. Head CG Acceleration, Local X 135
H31. Head CG Acceleration, Local Y 136
H32. Head CG Acceleration, Local Z 136
H33. Head CG Acceleration, Resultant 137
H34. Chest Acceleration, Local X 137
H35. Chest Acceleration, Local Z 138
H36. Chest Acceleration, Resultant 138
H37. Upper CRUX/Sternum Displacement, Resultant 139
H38. Lower CRUX/Upper Abdomen Displacement, Resultant 139
H39. Left Femur Force, Local X 140
H40. Right Femur Force, Local X 140
H41. Upper Neck Shear Force, Fx 141
H42. Upper Neck Axial Force, Fz 141
H43. Upper Neck Occipital Condyle Bending Moment, M_y 142
H44. H3RS Test Dummy Kinematics in Table Test, Simulation Results and Test Observations 143
H45. Table Displacement, Window Side, Global X 144
H46. Table Displacement, Middle, Global X 144
H47. Table Displacement, Aisle Side, Global X 145
H48. Table Attachment Load, Near Wall, Global X 145
H49. Table Attachment Load, Near Wall, Global Y 146
H50. Table Attachment Load, Far Wall, Global X 146
H51. Table Attachment Load, Far Wall, Global Y 147
H52. Table Attachment Load, Leg to Floor, Global X 147
H53. Table Attachment Load, Leg to Floor, Global Z 148
H54. Table Attachment Load, Table to Leg, Global X 148
H55. Table Attachment Load, Table to Leg, Global Z 149
H56. Head CG Acceleration, Local X 150
H57. Head CG Acceleration, Local Y 151
H58. Head CG Acceleration, Local Z 151
H59. Head CG Acceleration, Resultant 152
H60. Chest Acceleration, Local X 152
H61. Chest Acceleration, Local Y 153
H62. Chest Acceleration, Local Z 153
H63. Chest Acceleration, Resultant 154
H64. T12 Spine Acceleration, Local X 154
H65. T12 Spine Acceleration, Local Y 155
H66. T12 Spine Acceleration, Local Z 155
H67. Upper Abdomen Acceleration, Local X 156
H68. Upper Abdomen Displacement 156

H69. Lower CRUX, Local X 157
H70. Lower CRUX, Local Y 157
H71. Lower CRUX, Local Z 158
H72. Lower CRUX, Resultant 158
H73. Head Rotation Angle, RY, at OC 159
H74. Left Femur Force, Local X 159
H75. Right Femur Force, Local X 160
H76. Upper Neck Shear Force, Fx 160
H77. Upper Neck Axial Force, Fz 161
H78. Neck Cable, Front 161
H79. Neck Cable, Rear 162
H80. Upper Neck Occipital Condyle Bending Moment, My 162
H81. THOR Test Dummy Kinematics in Table Test, Simulation Results and Test Observations 163
H82. Table Displacement, Window Side, Global X 164
H83. Table Displacement, Middle, Global X 164
H84. Table Displacement, Aisle Side, Global X 165
H85. Table Attachment Load, Near Wall, Global X 165
H86. Table Attachment Load, Near Wall, Global Y 166
H87. Table Attachment Load, Far Wall, Global X 166
H88. Table Attachment Load, Far Wall, Global Y 167
H89. Table Attachment Load, Leg to Floor, Global X 167
H90. Table Attachment Load, Leg to Floor, Global Z 168
H91. Table Attachment Load, Table to Leg, Global X 168
H92. Table Attachment Load, Table to Leg, Global Z 169
H93. Head Resultant Acceleration 170
H94. Chest Resultant Acceleration 171
H95. Upper Neck Shear Force, Fx 171
H96. Upper Neck Axial Force, Fz 172
H97. Upper Neck Occipital Condyle Bending Moment, My 172
H98. Time Sequence of ATD Kinematics 173
H99. Head Resultant Acceleration 174
H100. Chest Resultant Acceleration 175
H101. Left Femur Force 175
H102. Upper Neck Shear Force, Fx 176
H103. Upper Neck Axial Force, Fz 176
H104. Upper Neck Occipital Condyle Bending Moment, M_y 177
H105. Time-Sequence of ATD Kinematics 178

Tables

Table 1. Full-Scale Impact Tests 3
Table 2. Test Descriptions and Critical Measurements 4
Table 3. Experiment 1-1: Injury Results for 95th Percentile Male 27
Table 4. Experiment 2-1: Injury Results 28
Table 5. Experiment 1-2: Injury Results for Hybrid 3RS 30
Table 6. Experiment 1-3 Injury Results for THOR 32

Appendix B
Table B1. Summary of Accelerometer Channels on the Lead Vehicle 51
Table B2. Strain Gauge Placement on the Test Cars: Carbody 55
Table B3. Strain Gauge Placement on the Test Cars: Crush Zone 56
Table B4. Summary of String Potentiometers Used for Two-Car Test 60

Appendix C
Table C1. Vehicle Mass Properties 70
Table C2. Vehicle Mass Properties 71

Appendix F
Table F1. Previous and Planned Occupant Experiments Performed on Board Full-Scale Collision Tests of Conventional and CEM Equipment 88
Table F2. Summary of Data Channels for Experiments 1-1, 2-1, and 2-2 92
Table F3. Summary of Data Channels for Experiment 1-2 94
Table F4. Summary of Data Channels for Experiment 1-3 95
Table F5. Summary of Deliverables 96

Executive Summary

Two full-scale impact tests were conducted by the Federal Railroad Administration (FRA) to measure the crashworthiness performance of Crash Energy Management (CEM) equipped passenger rail cars. On December 3, 2003, a single car impacted a fixed barrier at approximately 35 mph and on February 26, 2004, two-coupled passenger cars impacted a fixed barrier at approximately 29 mph. Coach cars retrofitted with CEM end structures, which are designed to crush in a controlled manner, were used in the tests. These test vehicles were instrumented with accelerometers, string potentiometers, and strain gauges to measure the gross motions of each car body in three dimensions, the deformation of specific structural components, and the force-crush characteristic of the CEM end structure. Five occupant experiments were conducted onboard the test vehicles in the two-car test to measure the secondary impact conditions.

Collision dynamics models were developed to predict the gross motions of the test vehicles. Crush estimates as a function of test speed were used to guide test conditions. Using the crash pulse derived from the collision dynamics model, computer models for the occupant tests were developed to determine the severity of the collision environment and predict the motions of the Anthropomorphic Test Devices (ATDs) used in the two-car test. This report describes the details of the CEM single-car and two-car tests, and reports the findings of the structural and occupant tests.

The single-car test and two-car test demonstrated that the CEM design successfully prevented intrusion into the occupied volume, under conditions similar to those present for the conventional (non-CEM) tests performed in 1999 and 2000. During both CEM tests, the leading passenger car crushed approximately three feet, preserving the occupant compartment. In the two-car test, energy dissipation was transferred to the coupled interface, with crush totaling two feet between the two CEM end structures. The pushback of the couplers kept the cars in-line, limiting the vertical and lateral accelerations. In the corresponding conventional tests, intrusion into the occupant compartment occurred, and in the conventional two-car test, sawtooth lateral buckling occurred at the coupled connection.

Overall, the test results and model show close agreement for the gross vehicle motions. The measurements made during both tests demonstrated that the CEM design provides improved crashworthiness performance over the conventional design. Test results confirmed that the interior secondary impact environment for the CEM-equipped cars is more severe than in conventional equipment. The test of rear-facing seats showed that strategic modifications to the interior can mitigate the trade-off associated with a more severe CEM secondary impact environment.

1. Introduction

Cab car-led trains present a challenging situation in collisions. They present greater risks due to the presence of passengers and have a lighter weight and lower strength in comparison to locomotives. To address this exposure, the Federal Railroad Administration (FRA) has conducted research on various modifications intended to improve the crashworthiness of cab cars. As part of this research, FRA previously considered modifications that were focused on strengthening existing members of the cab car-end structure. Crash energy management (CEM) offers a 'clean-sheet' strategy for cab and coach car structural designs. This CEM approach includes structural crush zones at the ends of the car that require less longitudinal force to collapse than the occupied areas.

In designing for crashworthiness, the first objective is to preserve a sufficient volume for occupants to ride out the collision without being crushed. Excessive forces and decelerations also present a potential for injury to the occupants. Relatively large forces (secondary impacts) and decelerations can occur when an unrestrained occupant strikes the interior. Occupant impacts with the interior or collisions between occupants and loose objects thrown about during the collision are usually termed "secondary collisions." The second objective of crashworthiness is to limit these secondary collision forces and decelerations to tolerable levels.

Preserving occupant volume is accomplished by managing the strength of the structure. If the occupant compartment is sufficiently strong, there will be sufficient survival space for the occupants. Secondary impacts are limited through a combination of structural crashworthiness and occupant protection measures. Allowing portions of the vehicle to crush in a predetermined manner can control the decelerations of the cars. Occupant protection measures include the use of restraints, such as seatbelts, shoulder harnesses, and strategies such as compartmentalization. The severity with which the occupant strikes the interior depends upon the deceleration of the train itself during the collision and the degree of 'friendliness' of the interior.

A trade-off exists between increased occupant volume strength and secondary impact velocity. If a single car has uniform crush strength, increasing the crush strength increases the speed at which the occupants impact the interior. For a train of cars, the issue is more complex. The cushioning of the cars ahead and the pushing of the cars behind influence the deceleration of any particular car. In general, any crashworthiness strategy that better preserves the occupant volume will make the secondary impacts more severe for the occupants in the interior.

Conventional practice is oriented toward making the individual cars as strong as possible within weight and other design constraints. This approach attempts to control the behavior of the individual cars during the collision. The CEM approach is train oriented, apportioning the structural crushing to unoccupied areas throughout the train.

As part of the FRA's Equipment Safety Research Program, a series of full-scale impact tests were conducted. The purpose of this program was to propose strategies for improving occupant protection under common impact conditions. This was accomplished by comparing conventional passenger equipment to a modified design under similar collision conditions. The sequence of tests shown in Table 1 allowed the study of in-line collisions in increasing levels of complexity. The modified equipment was expected to show incremental crashworthiness improvement over the current equipment.

Table 1. Full-Scale Impact Tests

	Test Description	Conventional Design Equipment	Modified Design Equipment
In-line impact tests	Single coach car with fixed barrier [1], [5]	11/16/1999 35.1 mph	12/3/2003 34.1 mph
	Two coach cars with fixed barrier [2]	4/4/2000 26.3 mph	2/26/2004 29.3 mph
	Cab car-led train with locomotive-led train [3]	1/31/2002 30.0 mph	February 2006
Oblique impact tests	Single cab car with steel coil [4]	6/4/2002 14.4 mph	6/7/2002 14.0 mph

The completed conventional tests were intended to establish a performance baseline for the existing fleet. The first two in-line tests of the modified design were completed and the train-to-train test was tentatively planned for February 2006. The first half of this report will discuss the comparisons of the baseline crashworthiness performance of the conventional passenger equipment with modified equipment as well as the structural performance of the design through the test data. The second half will discuss the results of the occupant experiments.

The secondary objectives of the structural tests are related to the modeling development process. Computer models were used to predict collision outcomes and to determine the pre-test conditions. The models were modified based on the test results for future use in predicting outcomes for similar collision scenarios.

In the single-car test, the critical measurements were made to obtain a force-crush characteristic and to measure the gross motions of the test equipment. The two-car test added consideration of the interactions of the coupled connection, i.e., measuring the vertical and lateral motions of the cars respective to each other and observing the potential for sawtooth lateral buckling to occur. The train-to-train test focused on the interactions of the colliding equipment, i.e., how the equipment engages and the potential for override of the colliding vehicles. Additionally, the effects of the collision throughout the train were measured.

Table 2 lists the key measurements made during each test. The modified design for the in-line collisions consisted of a crush zone intended to provide controlled progressive collapse of an unoccupied region. The modified design enhanced the crashworthiness performance of the passenger car by limiting the vertical and lateral motions of the vehicle and allocating crush to the designated crush zones at each end of the passenger cars.

For the CEM tests, a single coach car retrofitted with CEM end structures impacted a fixed barrier at 34.1 mph, and two coupled coach cars retrofitted with CEM end structures impacted a fixed barrier at 29.3 mph. The following sections present a detailed description of the CEM features and functions, an analysis of the structural test results, model predictions, and a comparison with the corresponding conventional equipment.

In the two-car CEM test, anthropomorphic test devices (ATDs) were included on the rail cars to measure occupant response during the collision. These ATDs were instrumented with accelerometers and load cells to measure injury risk to the occupants. The results from the occupant experiments are included in Section 8 of the report.

Table 2. Test Descriptions and Critical Measurements (*The italicized text of this table identifies the benefits of the crush zone)*

Test Description	Key Observations
Single-car test	• Modes of deformation • Dynamic crush force • Gross motions of vehicles • Minimized vertical and lateral motions
Two-Car Test	• Interactions of coupled cars • *Cars remain in-line* • *Distribution of crush to the trailing car*
Train-to-Train Test	• Interactions of colliding equipment • Override of colliding cars • Lateral buckling of coupled cars • *Distribution of crush along consist* • *No override and no lateral buckling*

While the CEM design preserves more occupied area of the car during a train collision when compared to conventional equipment, it comes at the expense of a more severe secondary impact environment for occupants seated in the first two cars of the train (see Section 8 for a discussion of the occupant environment). To assess injury risks in different seating configurations, five occupant experiments were included in the two-car test. Three of the experiments were similar to those conducted on the two-car test of conventional equipment that were being held on April 4, 2000: forward-facing occupants in intercity seats, forward-facing occupants in commuter seats, and rear-facing occupants in commuter seats. Two of the experiments examine the interaction of an occupant with a workstation table in a facing-seat configuration. These two tests used experimental ATDs with an increased capacity for recording abdominal impact response. The occupant experiments and their placement in the cars are depicted in Figure 1 and Figure 2.

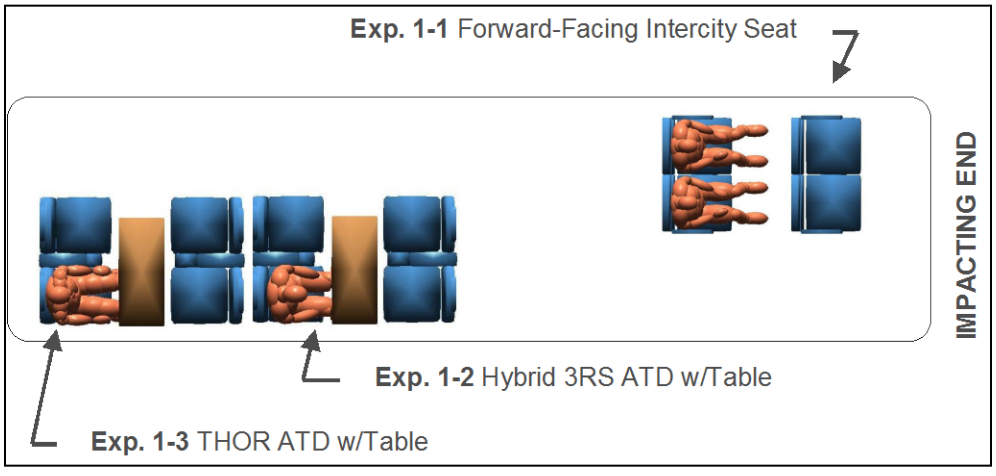

Figure 1. Location of Occupant Experiments in Leading Cab Car

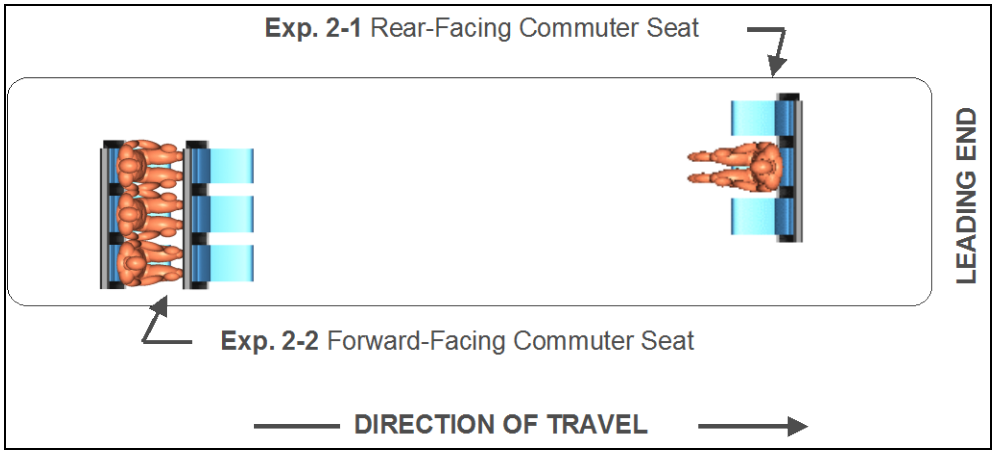

Figure 2. Trailing Coach Car Experiments: Location of Occupants

To aid the analysis of these experiments, computer models were developed in MADYMO for four of the five of the occupant experiments. The models were either modified from earlier simulations, in the case of the commuter seats, or newly developed, in the case of the commuter seats and table experiment with the Test Device for Human Occupant Restraint (THOR) anthropomorphic test device (ATD). The models were validated based on test and/or accident data. Predictions of the ATD response agreed closely with the overall kinematics of the ATDs, and with many of the measurements made with the ATDs in full-scale tests. See Appendix C for detailed modeling results.

Note: Future action items and dates referenced in this report may be subject to change following the publication of this report as such information was based upon the context of the testing taking place in 2003 and 2004.

2. Crash Energy Management Design

A goal of the full-scale testing program is to show how a modified design can improve crashworthiness performance by increasing occupant volume preservation. Testing of conventional equipment has established a baseline against which this second set of tests can be evaluated.

There are two important performance differences between conventional and CEM designs. CEM cars can more efficiently absorb collision energy and crush is transferred to the following cars in a train rather than being concentrated exclusively on the lead car(s). The CEM design developed for these tests is intended to absorb at least 2.5 million ft-lb in the first three feet of each end structure [6]. This dissipation is accomplished by the controlled crush of three primary components: the pushback coupler/draft gear assembly, primary energy absorbers, and the roof absorbers.

The distinctions between the conventional and CEM equipment can be illustrated in idealized force-crush characteristics. Collision performance of conventional equipment typically concentrates crush at the front end of the lead passenger car of the colliding vehicles. Figure 3 shows that there is little resistance to deformation once the peak load is exceeded. The tiered force-crush behavior that characterizes a CEM design is illustrated in Figure 4. The dashed line shows the concept used to prescribe the design and the solid line is a schematic representation of the test results.

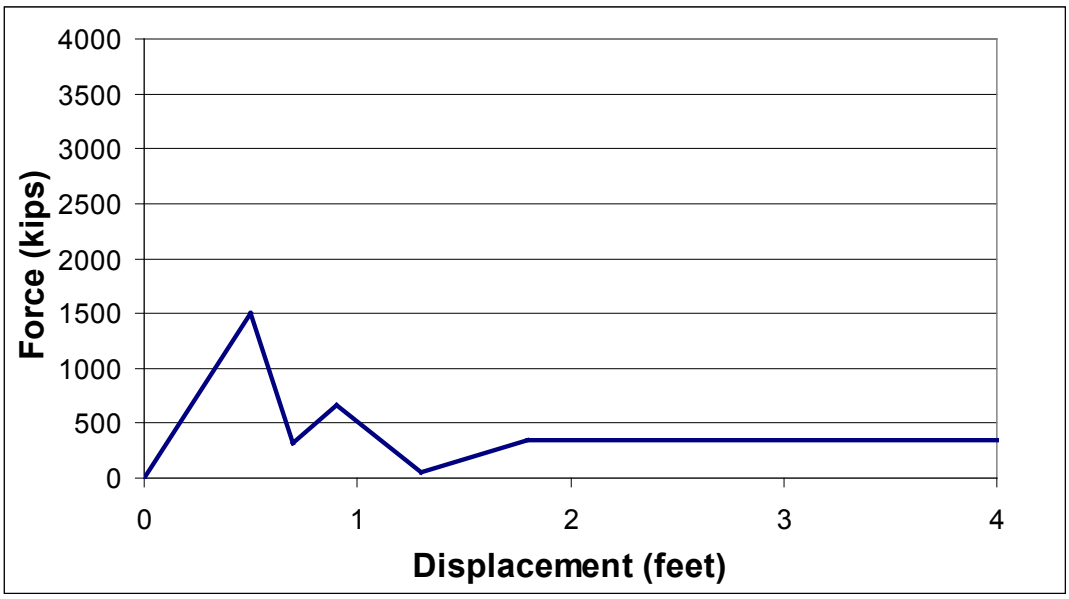

Figure 3. Idealized Force-Crush Curve for Conventional Design

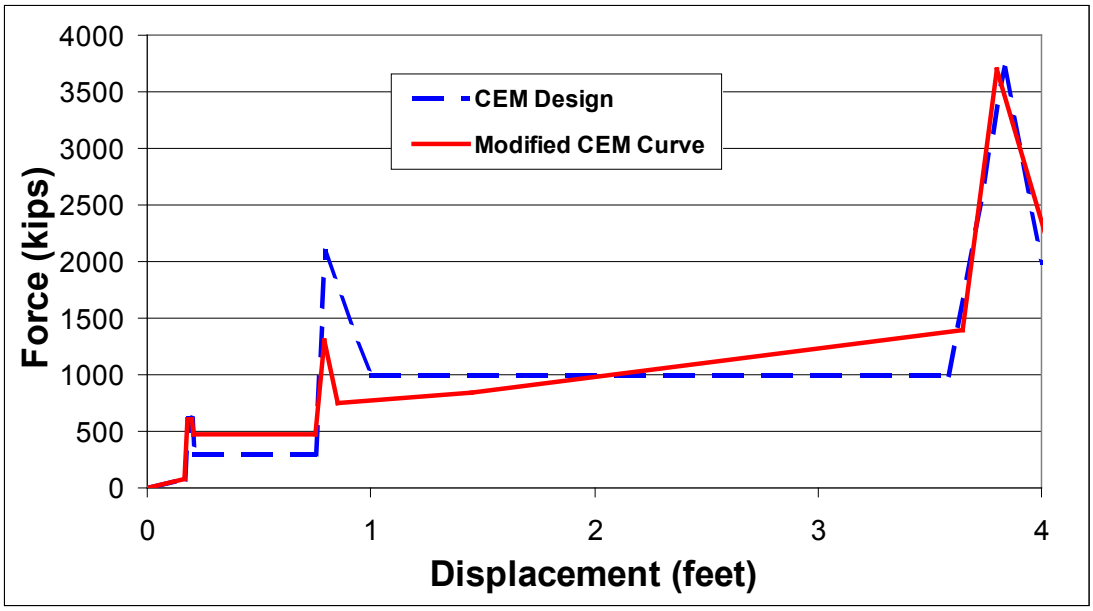

Figure 4. Idealized Force-Crush Curve for CEM Design

The initiation of failure at each stage involves a peak load followed by a slightly lower constant load that sustains the progressive collapse of each element. The third peak represents the loading of the draft sill. The occupant compartment begins to be challenged when the third peak of the CEM load characteristic is exceeded. Beyond this point, the passenger car crushes with a load characteristic similar to that of a conventional car. The series of elements that make up the CEM design create the double-tiered characteristic, which causes the load to be passed to successive crush zones before the leading one is exhausted. Note that both figures have the same load scale.

The scale of crush distance shows the unoccupied region of the car. Once the initial peak of the conventional characteristic is reached the passenger car crushes at a relatively constant load. The response of the CEM design must exceed the increasing double-tiered load characteristic before intrusion into the occupant compartment occurs. Comparison of the areas under the curves in Figure 3 and Figure 4 shows that the CEM design can absorb a larger amount of energy than the conventional design before compromising the passenger compartment.

The Crash Energy Management design developed for these tests is characterized by a collection of trigger mechanisms supported by crushable elements. Figure 5 [6] shows a cross-section taken from a finite element model developed for analysis of the CEM system during design. This schematic identifies the primary components and the layout of the system. The first set of bolts shear at a prescribed load, allowing the coupler/draft gear assembly to slide back and crush an aluminum honeycomb module. When the coupler has reached its full stroke, resting in a position in-line with the end frame, the load is then transferred to the anti-telescoping plate and the end beam via the anticlimber. A second series of shear bolts act as a fuse for the sill, which slides back into the underframe causing the end frame to crush the primary energy absorbers. Simultaneously, rivets fail in shear, triggering the collapse of the roof absorbers and the resultant crush of additional aluminum honeycomb modules.

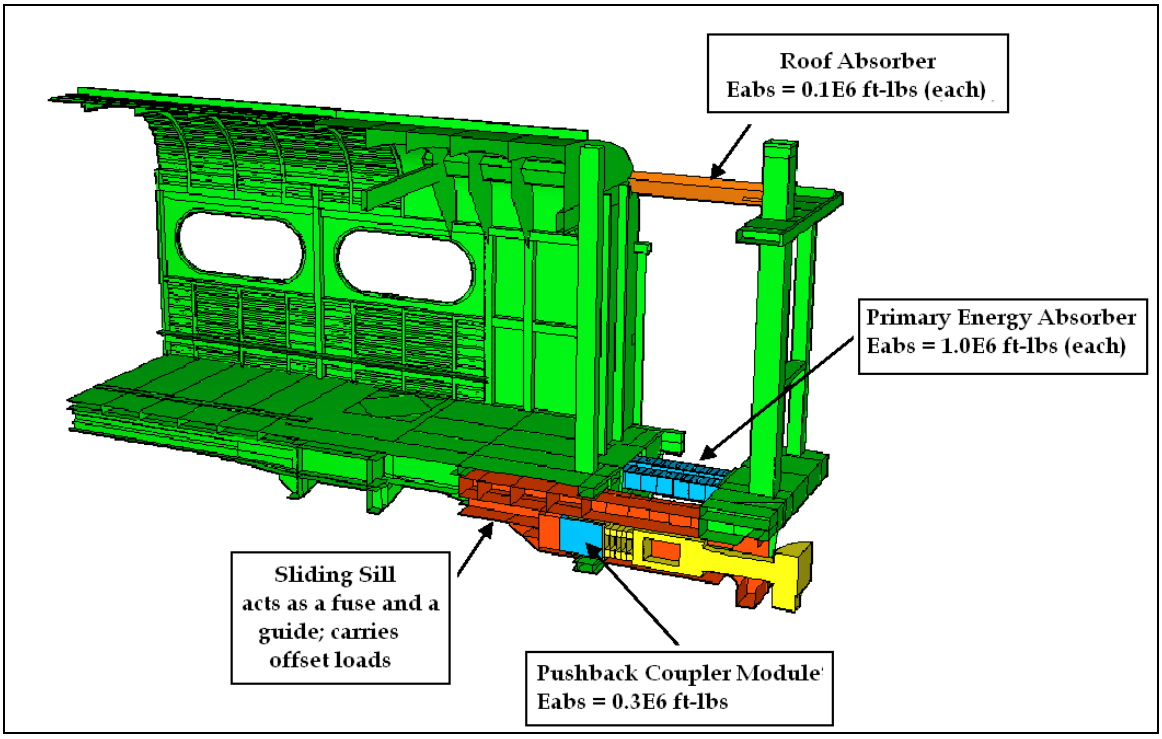

Figure 5. Cross Section of Crash Energy Management (CEM) Design

The end structure has a multi-tiered load path, allowing for service loads and collision loads to be accommodated separately. Low-level service loads are absorbed by the elastic deformation of the conventional draft gear and the coupler/draft gear assembly can absorb higher service loads. The primary energy absorbers are activated only when this system is exhausted, as in a collision condition. This feature ensures the integrity of the crush zone by preventing the primary energy absorbers from being inadvertently triggered during daily operation.

3. Structural Test Description

The single-car test of a passenger car retrofitted with a CEM end structure was conducted on December 3, 2003, at the Transportation Technology Center (TTC) in Pueblo, Colorado. At a closing speed of 35.1 mph, approximately 3 feet of crush occurred, measured from the end frame. The crush zone collapsed as intended in a progressive controlled manner, and was nearly exhausted. Details of the test set-up, test conditions, and instrumentation are described in Appendix B and Appendix C.

On February 26, 2004, the CEM design was tested in a two-car impact with a fixed barrier. The test vehicles were Budd Pioneer cab cars retrofitted with the same CEM end structure. The cars were pushed by a locomotive and released approximately 1,000 feet from the wall, colliding at a closing speed of 29.3 mph. A target test speed of 28 mph was chosen from pre-test models to load the crush zone just below its capability.

A typical passenger car in service weighs approximately 100,000 lb. The Budd cars used in the CEM test were stripped of all interior seating and fixtures, as well as some exterior operational equipment. The final weights of the two test vehicles were 74,875 lb (lead car) and 75,250 lb (trailing car). Each CEM end structure (two per car) accounts for about 5000 lb and each truck weighs about 7,700 lb.

The building of the test vehicles was a careful integration process performed at TTC by Transportation Technology Center Inc. (TTCI). Initial preparation of the Budd Pioneer passenger cars involved precise cuts of the car body skin and underframe just outboard of the bolster and removal of the existing end structure. The CEM end structure was then carefully integrated onto the current structure, with measures taken to meet all fabrication and construction practices. Note: because the CEM system was designed to be retrofitted onto an existing passenger car, it adds no extra length or weight to the replaced structure of the Budd Pioneer coach cars. Figure 6 shows a photograph of the test vehicles located near the fixed barrier just prior to the test.

Figure 6. Test Vehicles Prior to Two-Car Test

Instrumentation was located to provide the post-test data necessary to make the critical measurements described in Table 2. Each test car was instrumented with displacement transducers, accelerometers and strain gauges to collect on-board data of critical measurements for analysis and modeling comparisons. String potentiometers measured relative displacements in the critical areas of the crush zone, which are useful for evaluating the timing and sequence of events. Accelerometers were placed along the carbody and on the primary components of the crush zone to measure the gross motions in three dimensions. Strain gauges were used to gather strain rates to measure the timing and follow the path of structural deformation through the crush zone as well as the pulse of the collision force through the car body.

There were 123 data channels used for the 46 accelerometers, 39 strain gauges, and 38 string potentiometers. Thirteen high-speed cameras and four video cameras recorded numerous views of the test and were used to perform post-test photometric analysis to provide a secondary set of relative gross motions and displacement measures. The cars were also equipped with test dummies in various seating configurations and instrumented with an additional system of data channels. Additional details are provided in Appendix H.

4. Modeling Approach

Developing computer models prior to the test provides the benefit of conducting a test that is properly documented and understood. With the model results as a guide, the instrumentation can be located and ranged to most effectively specify critical measurements. Details of the test conditions, such as closing speed are determined from pre-test simulations so that the equipment can be tested to a predetermined critical failure point. These models can then be used to extrapolate results to other test conditions.

Figure 7 shows a flow diagram that maps out the strategy used when conducting a full-scale test. The diagram shows how the test has been broken down into various levels of necessary analysis. The finite element model evaluates the various modes of deformation that occur and identifies the load path. The force-crush behavior of the system is then used as model input that defines a non-linear spring of a lumped-parameter collision dynamics model. The model produces the gross motions of the car bodies and timing of events. The collision dynamics model supplies a three-dimensional crash pulse for the interior occupant models. These models generate the secondary motions experienced by the occupants in various seating arrangements. These three models are developed prior to the test and aid in determining the test conditions and required instrumentation. Once the test is completed the collision data are then compared to the models and refinements can be made to further the understanding of the collision scenario. These models can then be used to predict results for similar collision conditions.

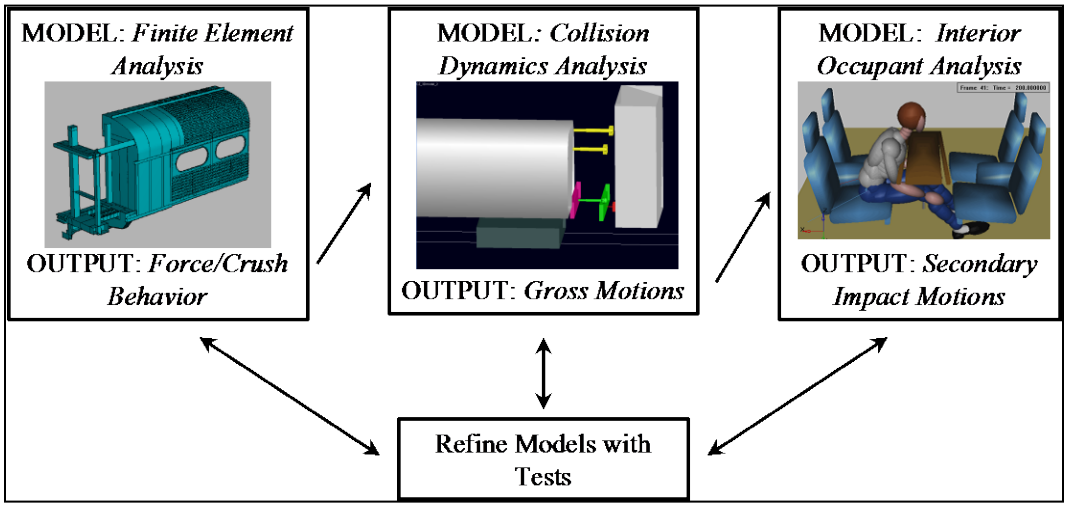

Figure 7. Modeling Process Flow Diagram

The finite element model was developed during the CEM design process [6]. Component testing relied on detailed simulations to verify that each component crushed as expected. The full-car model was built in accordance with the assembly drawings used for the integration of the CEM design onto the Budd coach car. The finite element model produced the initial representation of the composite force-crush characteristic of the CEM system, as shown in Figure 8.

Prior to the single-car test of the CEM design, the finite element model provided the estimate for the input parameters used in the collision dynamics model. The idealized form of this curve is the dotted trace shown in Figure 4. The solid line shows revisions made to this characteristic after the test data were processed and analyzed.

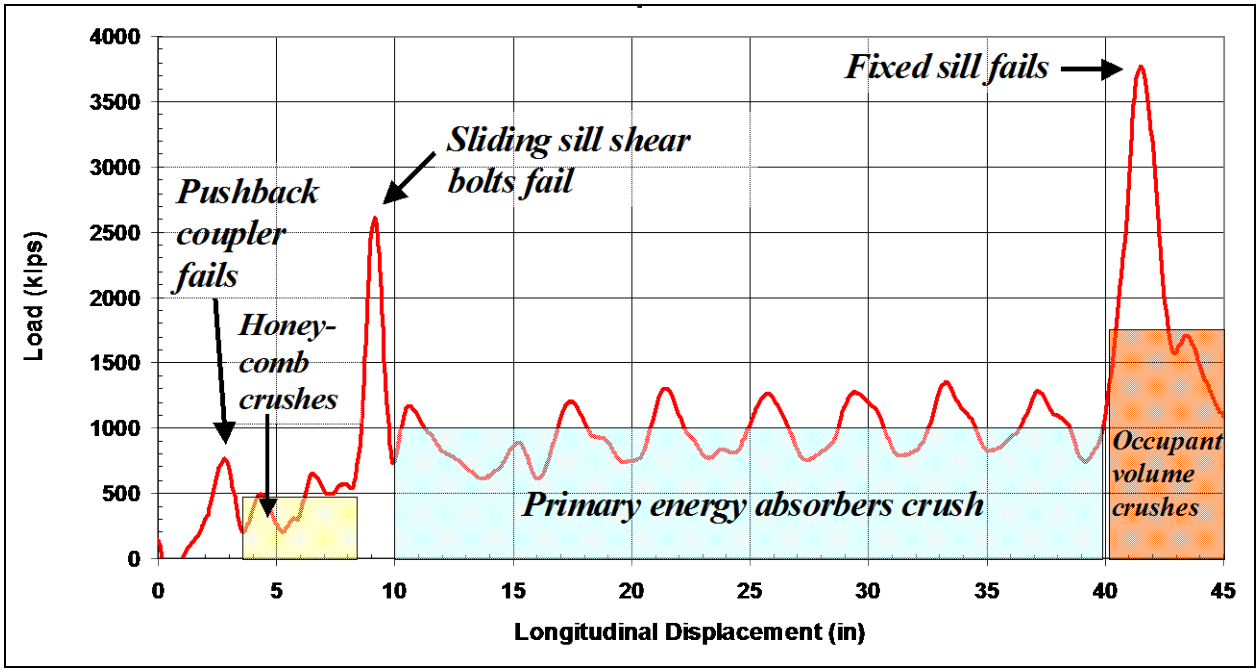

Figure 8. CEM Force-Crush Curve from Finite Element Model

The collision dynamics model is a lumped-parameter representation of the colliding bodies. The schematic shown in Figure 9 shows the CEM two-car mass-spring representation. The vehicles are separated into smaller sub-systems (i.e. main car body, individual components of the crush zone, trucks) connected by springs to represent their structural stiffness or suspension characteristics. Various connecting joints allow for the appropriate multi-dimensional movement between each rigid body. Constraints are applied to simulate structural limitations. Point-to-point impact forces are tuned to classify the interaction of colliding surfaces. From this three-dimensional model, the gross motions of each rigid body can be produced for any set of initial conditions. Additionally, the extent of crush of each crush zone can be simulated, as well as the sequence of activation of each component in each crush zone.

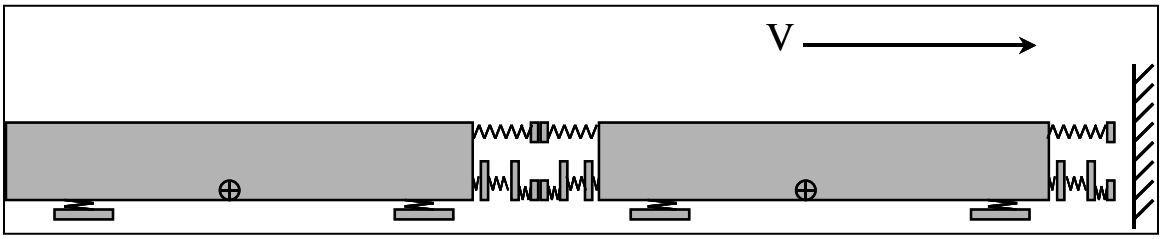

Figure 9. Schematic of Collision Dynamics Model

The amount of crush was estimated at varying test speeds to determine the impact speed at which the test should be conducted. Figure 10 shows the plot used to choose the speed for the two-car test. The pre-test force-crush characteristic was used to make these predictions. The dashed blue and solid green curves show the amount of crush at the colliding end of the lead car and coupled interface, respectively. The solid horizontal line shows the distance at which the crushed structure begins to intrude into the occupant compartment. The test speed, indicated by the dashed vertical line was chosen to challenge the lead crush zone to just below its capability for

preserving occupant volume. At the test speed, the lead car was expected to nearly exhaust the CEM system, crushing almost 40 inches. At the coupled interface, the couplers would pushback, crushing 8 inches each and the primary energy absorbers would just begin to crush. The solid green curve indicates the cumulative crush of the two crush zones at the coupled interface. The CEM design is intended to: (1) restrict damage to the unoccupied area at higher speeds than the conventional test and (2) transfer the crush to the successive crush zones.

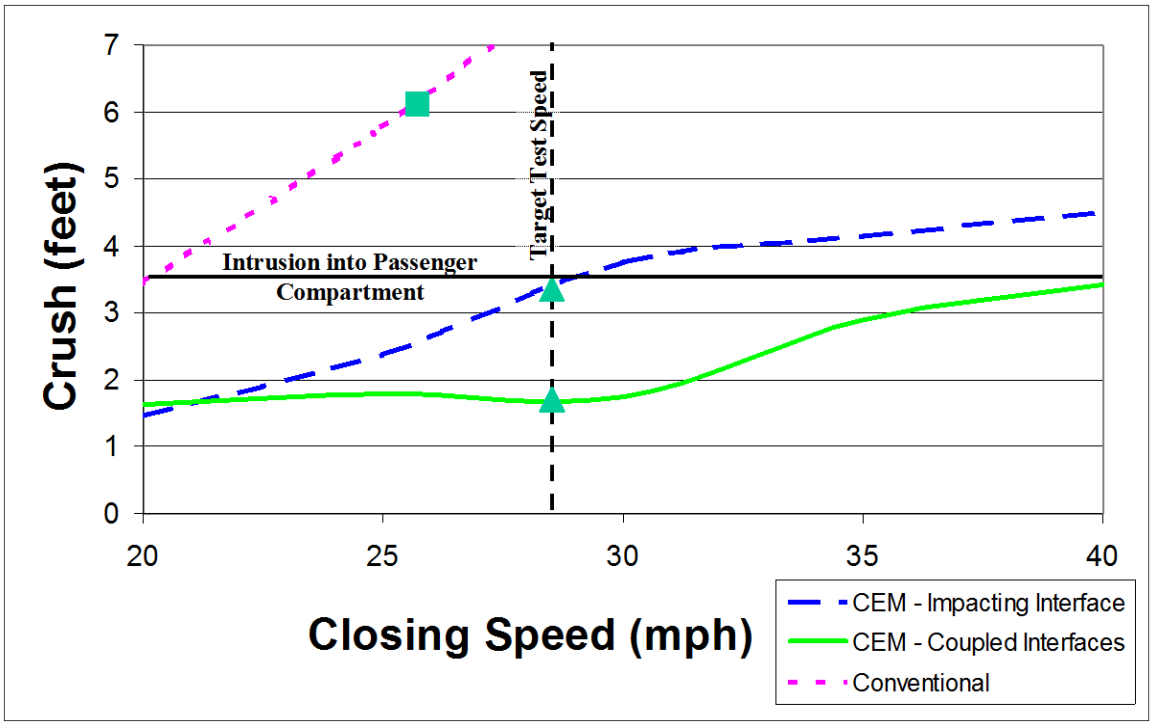

Figure 10. Crush Estimation Versus Impact Speed

The corresponding results from the conventional test are plotted on the graph by the dotted pink line. The conventional test was conducted at a speed of 26 mph. At this speed, about 6 feet of crush occurred. Comparing these results illustrates the incremental increase in crashworthiness protection. The line marking intrusion into the passenger compartment is a critical condition in determining the "safe speed" for the operation of each of these designs. This plot anticipates the CEM design to have an effective safe speed increase over the conventional design of almost 50 percent.

A detailed analysis of the secondary impact between the occupant and the interior seats or tables is conducted with lumped mass models. A separate model is developed for each occupant experiment. The models are used to estimate the test results for different initial conditions. These estimates are used in designing the occupant experiments.

The acceleration time history calculated from the collision dynamics analysis is used as input to these models, along with appropriate seat/table geometry and stiffness properties. The model is used to calculate the forces and accelerations experienced by the occupants during the secondary impact, and to calculate the associated injury criteria. These injury criteria can be compared to accepted threshold values, and the probability of fatal injuries can be calculated. More details on the occupant models are presented in Appendix G.

5. Analysis of Structural Test Results

During the CEM two-car test the lead car crush zone was nearly exhausted, crushing 3 feet in less than 120 milliseconds. At the coupled interface, both pushback couplers were triggered, allowing the anticlimbers to engage and both crush zones to activate; the coupled interface crushed a total of 2 feet. Intrusion into the occupant volume was prevented and the vertical and lateral motions were limited. The three crush zones absorbed approximately 3.5 million ft-lb of energy.

5.1 Post-Test Results of Crush Zone Performance

The photographs in Figure 11 compare the damage of the lead car in both the conventional and CEM tests. Using the trucks as a reference point in each photograph, the difference in the amount of structure crushed is readily discernible. The conventional car impacted with the wall and climbed the wall as the car body crushed a total of 6 feet. The sill is the most significant structural member of the underframe and tends to deform gracelessly into a contorted mass of metal, resulting in uncontrolled crushing of the end. The conventional tests established that the draft sill can have varying modes of deformation under similar impact conditions [8]. Consequently, the uncontrolled crush of the draft sill at the base of the structure causes the car to climb the wall as it crushes.

Figure 11. Post-Test Photographs of Conventional (left) and CEM (right) Vehicles

On the other hand, the lead car of the CEM test crushed a total of 3 feet, as intended. This measurement from the end of the car corresponds to the lower triangular marker in Figure 10, which includes the crush of the coupler in the total crush measurement. Each element of the crush zone is designed to crush in a controlled manner, which effectively limits the vertical and lateral motions of the carbody during the impact. The CEM end structure collapsed in the

prescribed series of events shown in Figure 8. The coupler initially impacted the wall, causing the bolts to shear at a load of approximately 600 kips and the honeycomb module to crush as the coupler slid back. The end frame was then loaded to approximately 1,300 kips, activating the trigger mechanisms in the sill and the roof absorbers. The primary energy absorbers and the roof absorbers subsequently crushed as the gap between the end frame and the vestibule wall/bolster diminished.

Crush was successfully passed to the coupled interface as the first crush zone collapsed. At approximately 60 milliseconds, both couplers triggered and began to recede into the underframe. The anticlimbers engaged as the end frames came together and load then passed into the crush zones of both ends. The load pulse through the two cars triggered the rear crush zone of the lead car slightly before the second car crush zone. The bolts of the sliding sills failed causing the primary energy absorbers to begin to crush as predicted. The primary energy absorbers of the trailing end of the lead car crushed a total of 10 inches. The second car's energy absorbers just began to crush, deforming approximately 1 inch.

5.2 Post-Test Results of Vehicle Gross Motions

Figure 12 shows the final positions of the two cars during the conventional and CEM tests. During the conventional two-car test, sawtooth lateral buckling occurred at the coupled connection and the left rail buckled under the lateral load. During the CEM two-car test the cars remained in-line relative to their mechanically allowable vertical and lateral variations of 3-5 inches. The lead vehicle in the conventional test lifted approximately 6 inches off the track. The lead CEM vehicle rose upward by no more than 2 inches.

Figure 12. Post-test Photographs of Conventional (top) and CEM (bottom) Coupled Connections

Figure 13 shows an overhead view of the still images from the high-speed camera for the conventional and CEM tests. The first photograph shows the cars at the time of impact (indicated by the flash of light). Relative lateral offset of the cars is marked with white lines in the

photographs. In both tests, at the time of impact the cars were offset laterally by approximately 1.5 inches. The second still shows the offset at the time of maximum crush for each test. Sawtooth lateral buckling occurred in the conventional test causing the rail to roll. As can be seen in the left photograph of Figure 12, the cars came to rest approximately 13 inches out-of-line at the end of the collision. Contrastingly, in the CEM test the cars remained in-line as the coupler pushed back and the anticlimbers engaged (indicated by the dotted oval). The test shows that the controlled collapse of the crush zones effectively helps keep the cars in line.

Figure 13. Still Photographs of Coupled Interface for Conventional (top) and CEM (bottom) at Time of Impact (left) and Maximum Crush (right)

The model and the test results show close agreement in the gross motions of the colliding vehicles. The velocity-time history of the single car test results is shown in Figure 14.

The velocity and displacement measurements show very good agreement in the initiation of deceleration, timing of events and the amount of crush. Comparison of the test results (solid line) and model results (dashed line) shows that the model captured the key events of the collision. The initial impact with the wall is indicated by the initial deceleration of the velocity trace. The average deceleration is very closely estimated by the model, as seen by the overlay of the dashed line on the solid line. Overall, the results show that the activation and crush of a CEM crush zone performs as intended.

The CEM design exhibits a faster average deceleration rate than the conventional design. The crushing sequence in the CEM design completes in about 120 milliseconds, while the conventional design takes almost twice as long to rebound off the wall.

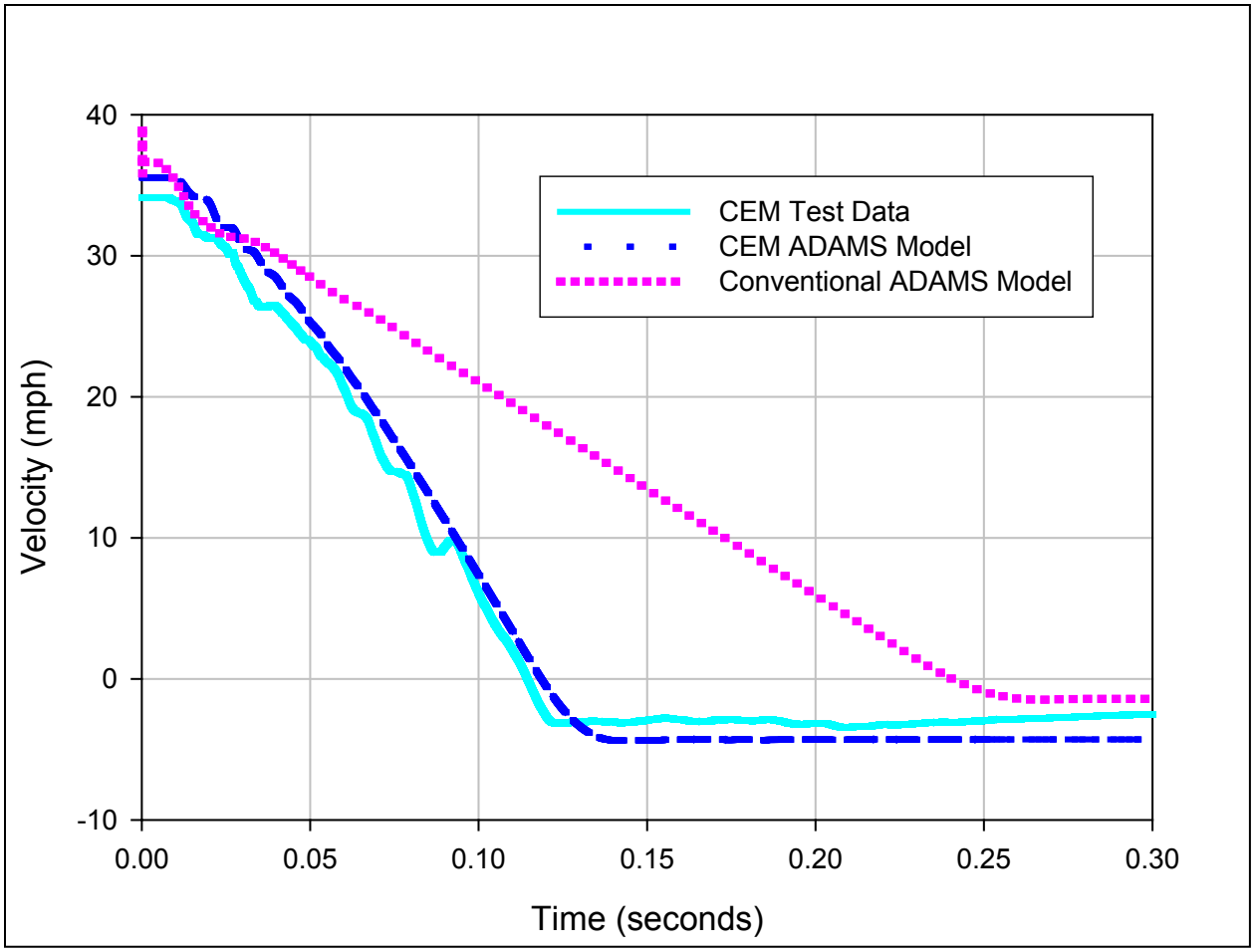

Figure 14. Single-Car Velocity-Time History Plot

Post-test analysis of the force-crush measurements allows for the characteristics of each component to be refined from the initial estimate of the overall force-crush behavior. The results from the single car test indicated that the first two plateaus of the composite force-crush curve required some fine-tuning. Modifications were made to the behavior as shown by the solid line in Figure 4. The crush plateau of the aluminum honeycomb module was increased. The initial peak of the primary energy absorbers was lowered. The plateau of the energy absorbers was replaced by a line with an upward slope. The characteristic for the energy absorbers accounts for the same total energy over the 30 inches of crush length as the previous plateau characteristic. After refining the input force-crush behavior to the collision dynamics model, the velocity-time histories matched the deceleration rates more closely throughout the collision. Appendix D covers the details of measuring the force-crush characteristic.

The two-car test verified the force-crush behavior observed in the single-car test, particularly that the primary energy absorbers require an increasing force to sustain crush. Understanding this behavior improved the overall agreement of the gross motions. With these changes all the important dynamic features were captured in both the single-car and two car tests.

Figure 15 shows the agreement of the model and test data in relation to the sequence of events. The lead car initially decelerates as the pushback coupler crushes. The change in slope indicates the initiation of crush in the primary energy absorbers of the lead crush zone. Crush at the

coupled connection begins at approximately 60 milliseconds. The lead car then rebounds off the wall at around 150 milliseconds, but the trailing car continues moving forward and pins the lead car to the wall until the trailing car comes to a stop. When it rebounds, the trailing car moves away from the wall at a higher speed than the lead car moves away from the wall. This overall behavior differs from the corresponding velocity history of the conventional two-car test. In that case, the lead car sustains nearly all of the crush and the two cars decelerate together as a single mass, so that the velocity-time histories of the two cars overlay for most of the duration of the impact [2].

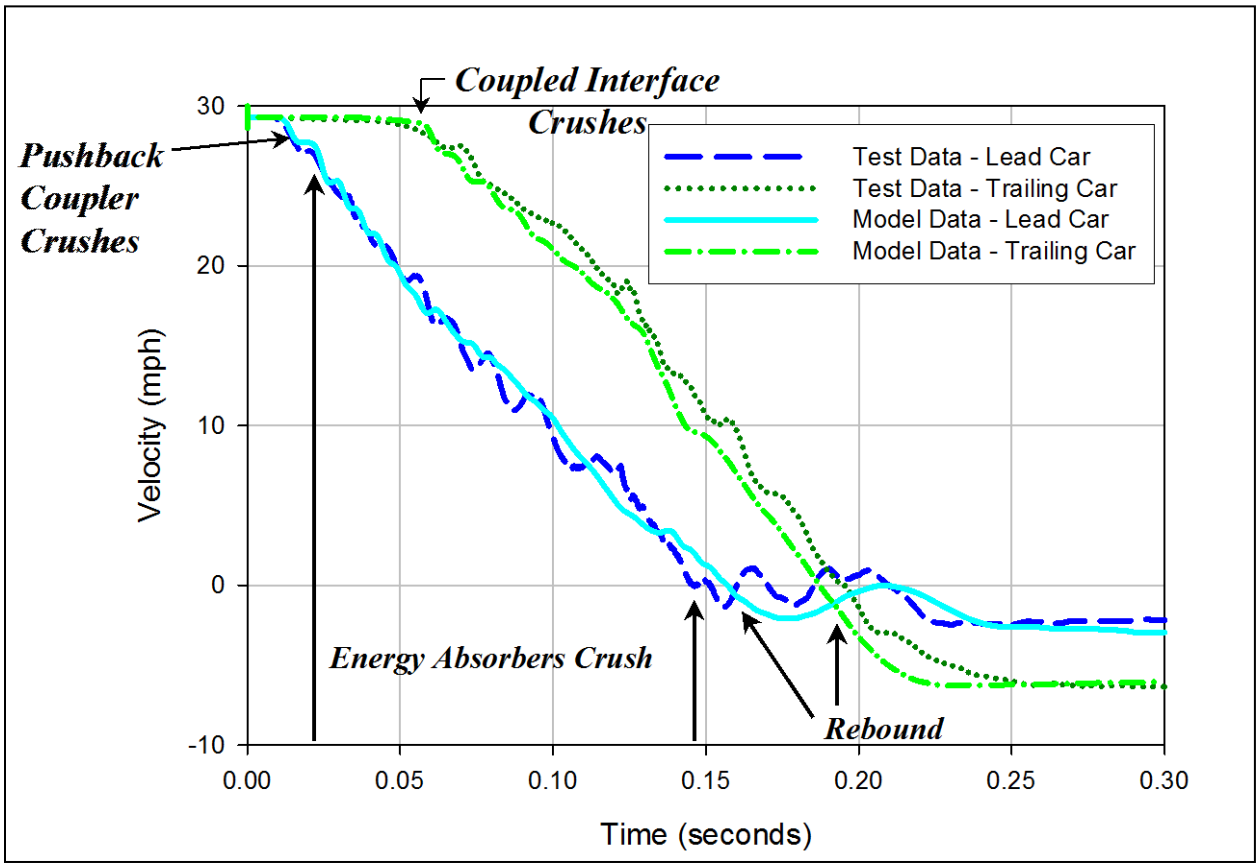

Figure 15. Two-Car Velocity Plots

The velocity plot shows that the model captures proper timing of the initial crush of the pushback coupler, indicated by the matching initial slopes of the lead car. The change in the deceleration of the lead car indicates the crush of the energy absorbers. The results of the single and two-car test have established confidence in how the CEM design functions under varying test conditions.

The slopes of the curves in Figure 14 and Figure 15 represent average accelerations. Figure 14 shows that the CEM single-car test has a more severe occupant environment than its more conventional counterpart. Each of the cars in the two-car test has an average acceleration lower than that in the single-car test. It is anticipated that in the train-to-train test, the presence of additional cars will further reduce the severity of the occupant-environment. The analyses of the interior occupant experiments performed in the two-car test are discussed in a Section 8.

6. Discussion of Structural Test Results

The purpose of this program is to assess and improve occupant protection in passenger trains by evaluating incremental crashworthiness improvements over the current levels. The tests to date in the Equipment Safety Research Program demonstrate that the CEM design has superior crashworthiness performance over the conventional design. The CEM design incorporates a series of crushable elements to absorb the collision energy in a more efficient manner than the conventional design, which was built to meet maximum strength requirements. The two-car test also demonstrates that the crush can effectively be passed back to the subsequent crush zones, thereby distributing the crush to the non-occupied crush zones. In addition, test results show that coupled car interactions can be controlled, and that sawtooth buckling, and consequent derailment, can be successfully minimized.

The collision dynamics models were used to study the kinematic and dynamic response of the individual crush zone components and the resultant car body motions. Utilizing test results and model simulations, modifications were made to the presumed force-crush behavior. Test results suggested a gradually increasing load characteristic for the primary energy absorber. The sloped load characteristic aids in distributing crush to successive crush zones. In both CEM tests, the post-test results show very good agreement between the model and the test results. The combined test and model results are being used to design and construct the cars that will be tested in the train-to-train test of CEM equipment. In the train-to-train test of conventional equipment, crush was focused in the impacting cab car and considerable occupant volume was lost. In addition, the cab car overrode the locomotive. In the train-to-train test of CEM equipment, it is expected that the occupant volumes will all be preserved, including the space for the operator [9] and crush will be distributed to the successive crush zones as demonstrated in the two-car test.

7. Description of Occupant Tests

A collision dynamics model of the two-car CEM impact test indicated that the force/crush behavior of the modified cars would result in a more severe secondary impact environment than in the two-car conventional test [10]. Secondary impact refers to the impact between the occupant and some part of the interior, usually the forward seat, table or bulkhead. While the CEM design was expected to better preserve occupied space, previous analysis [11] has indicated that the secondary impact velocity in a two-car CEM test could be 40-85 percent higher than in a comparable conventional test.

There are three main objectives of interior crashworthiness. It is first necessary to compartmentalize the occupants. Compartmentalization refers to limiting the trajectory of the occupant, usually within the space between the launch seat and the adjacent seat or table. When occupants are compartmentalized, their velocity relative to the car is generally minimized. If compartmentalization fails, the occupant kinematics are less predictable, and increasing risk of striking more hostile surfaces. Compartmentalization has been shown to be an effective occupant protection strategy in rail cars [12].

Second, the loads and accelerations experienced by an occupant during secondary impact must be below maximum injury criteria thresholds. Appropriate design of the force/deflection behavior of the seat backs and tables helps to minimize forces imparted to occupants during contact with these objects.

Third, the seats and tables must remain attached to the rail car, which increases the likelihood of occupant compartmentalization. Also, seat/table attachment prevents these heavy objects from becoming dangerous projectiles during a collision. These three objectives are evaluated in the five occupant experiments.

An underlying objective of the tests was to gather data to refine and validate computer models of each occupant experiment. As more test data are collected on each seat type and configuration, the computer models can be used more reliably to estimate the injury risk in many different collision scenarios.

Three of the occupant experiments (Experiments 1-1, 2-1, and 2-2) included seating arrangements that have been previously evaluated in the conventional full-scale impact tests, as well as in dynamic sled testing. These seats have been modified as determined necessary based on previous tests, as described below. Two of the occupant experiments examine the interaction of an occupant with a workstation table in a facing-seat arrangement. In addition to the aforementioned objectives, these experiments sought to collect information necessary for specifying the design requirements of an improved crashworthiness workstation table.

Occupant experiments were conducted in the two-car test only. A test requirements document (see Appendix F) was prepared to define the test objectives, measurements, and documentation associated with the occupant experiments.

7.1 Experiment 1-1: Forward-Facing Intercity Seats, Two 95th Percentile Male ATDs, Leading Car

Experiment 1-1 consisted of two pairs of forward-facing intercity seats, with a seat pitch of 41 inches. These seats were modified in the same manner as the intercity seats in the two-car and

train-to-train conventional tests, including strengthened seat backs with an energy absorber in the base. These modifications were necessary to ensure compartmentalization of the occupant during a collision. (See Reference [13] for more detail on the intercity seat modifications.) The objective of this experiment was to determine whether these modifications sufficiently protect the occupant in a more severe collision environment.

Two Hybrid III 95th percentile male ATDs were positioned in the rear seat pair. A pre-test photo of Experiment 1-1 is shown in Figure 16. Note that the duct tape shown in these photographs holds the ATDs in their initial positions during the car's approach to the impacted wall, and is perforated so it does not affect their motion during the impact. The experiment was located near the front of the leading cab car that impacted the wall. The ATDs were unrestrained, as were all the ATDs in the two-car CEM test. Both ATDs were instrumented to measure the triaxial head and chest acceleration, axial femur load, shear and axial neck loads, and neck flexion/extension moment. A floor-mounted biaxial accelerometer also measured the longitudinal and vertical car acceleration.

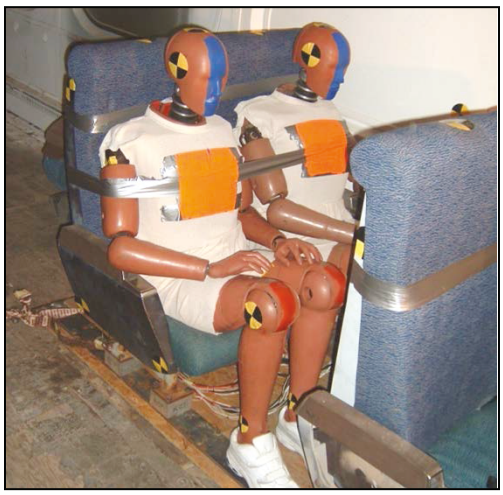

Figure 16. Pre-test Photo of Experiment 1-1

The pre-test MADYMO [14] computer model predicted a high likelihood of exceeding the head, neck and femur injury criteria, with a low probability of exceeding the chest acceleration criterion. While the model predicted about thirty degrees of seat back rotation about the seat base, the occupants were expected to remain compartmentalized.

7.2 Experiment 2-1: Rear-Facing Commuter Seat, One 50th Percentile Male ATD, Trailing Car

Experiment 2-1 consisted of a single modified rear-facing three-person M-Style commuter seat. The seat pedestal and attachment to the floor was strengthened in the same manner as the seat tested in the trailing car of the two-car conventional test [15]. The objectives of this experiment were to ensure that the seat back strength and seat attachments were sufficient to compartmentalize the occupant, and to show that rear-facing seats are an effective occupant protection strategy.

One Hybrid III 50th percentile ATD was positioned in the middle seat position (Figure 17). The experiment was located near the front of the trailing coach car. The ATD was instrumented to

measure triaxial head and chest acceleration, shear and axial neck loads, and neck flexion/extension moment. The pre-test MADYMO computer model predicted a low likelihood of exceeding the head, chest and femur criteria, with a moderate probability of exceeding the neck criterion.

Figure 17. Pre-test Photo of Experiment 2-1

7.3 Experiment 2-2: Forward-Facing Commuter Seat, Three 50th Percentile Male ATDs, Trailing Car

Experiment 2-2 consisted of two forward-facing three-person M-Style commuter seats. The forward seat was modified as described above for Experiment 2-1. Instrumented Hybrid III 50th percentile male ATDs were located in the window and aisle positions of the rear seat. An uninstrumented Hybrid II 50th percentile male ATD was located in the middle seat position (Figure 18). The ATDs in the window and aisle seats were instrumented to measure triaxial head and chest acceleration, axial femur load, shear and axial neck loads, and neck flexion/extension moment. A floor-mounted biaxial accelerometer also measured the longitudinal and vertical acceleration. The pre-test MADYMO computer model predicted a high likelihood of exceeding the head, neck and femur criteria, with a low probability of exceeding the chest acceleration criterion.

Figure 18. Pre-test Photo of Experiment 2-2

7.4 Experiments 1-2 and 1-3: Facing Commuter Seats with Workstation Table

Two new occupant experiments were conducted in this test, using advanced, experimental ATDs seated at workstation tables (Experiments 1-2 and 1-3). The impetus for these experiments was a rail accident in which a MetroLink passenger train collided with a BNSF freight train in Placentia, CA, on April 23, 2002. Many serious injuries and two of the three fatalities were likely caused by abdominal/chest injuries due to impact with a workstation table [16].

The objective of the experiments with tables was to gather information about the crashworthiness behavior of this seating configuration to develop potential countermeasures. In general, abdominal injuries are not as well understood as head, chest, neck and femur injuries. There exist suggested injury criteria but there are no regulatory criteria for abdominal injuries. The standard Hybrid III ATDs do not have instrumentation to measure abdominal forces or penetration.

Another objective of the table experiments was to collect and compare test data from two experimental ATDs subjected to the same collision conditions. The ATDs used in the table experiments were the THOR (Test Device for Human Occupant Restraint) [17] and the Hybrid 3 Rail Safety (3RS) (not currently documented). The 50th percentile male THOR Alpha ATD is a product of the National Transportation Biomechanics Research Center of the National Highway Traffic Safety Administration (NHTSA). Version 1.1 was released in December 2001. It has improved biofidelic features and has significantly enhanced instrumentation capabilities.

Transport Research Laboratory, Limited (TRL, LTD.) developed the Hybrid 3RS test dummy under the direction of the United Kingdom's Rail Safety and Standards Board. The Hybrid 3RS uses the standard Hybrid III head, neck, arms, legs, upper thorax, and several spine components. It incorporates the CRUX thoracic displacement measurement devices, spine flex joint, lower abdomen insert including double-gimballed string potentiometer (DGSP) units, and pelvis from the THOR.

7.4.1 Experiment 1-2: Forward-Facing Commuter Seat with Table, One Hybrid 3RS ATD, Leading Car

Experiment 1-2 consisted of a single Hybrid 3RS ATD seated in the window position of a forward-facing commuter seat, at a workstation table (Figure 19). The pitch of the facing-seat arrangement is 65 inches, with the table centered between the two pairs of seats. The tabletop is 33.5 inches long by 16 inches wide by 1.2 inches thick solid wood. The top of the table is 29.75 inches from the floor. Both the facing seats and table are similar to those on the Metrolink cab car in the Placentia, CA collision. The wall and floor attachments of the table to the car body were strengthened to ensure compartmentalization and allow measurement of the peak load imparted by the occupant. The ATD was instrumented to measure triaxial head and biaxial chest acceleration, axial femur load, shear and axial neck loads, neck flexion/extension moment, bi-lateral three-dimensional displacements of the abdomen, and bi-lateral three-dimensional displacements of the upper and lower rib cage. In addition, the table has multiple transducers to measure force, displacement and acceleration.

A pre-test computer model was not implemented, as a model of the Hybrid 3RS ATD does not exist.

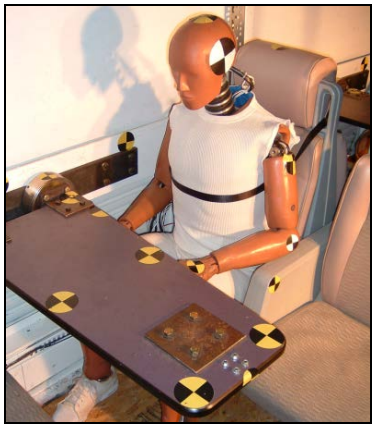

Figure 19. Pre-test Photo of Experiment 1-2

7.4.2 Experiment 1-3: Forward-Facing Commuter Seat with Table, One THOR ATD, Leading Car

Experiment 1-3 consisted of a single THOR ATD seated in the window position of a forward-facing intercity seat, at a workstation table (Figure 20). This seating arrangement is identical to Experiment 1-2. The ATD was instrumented to measure nine-axis head, triaxial chest, and triaxial spine acceleration, axial femur load, shear and axial neck loads, neck flexion/extension moment, upper abdominal acceleration, upper abdominal linear displacement, and bi-lateral three-dimensional displacements of the lower rib cage. In addition, the table has multiple transducers to measure force, displacement and acceleration.

The pre-test MADYMO computer model predicted a high likelihood of exceeding the criteria for abdominal penetration and rate of penetration, as well as peak chest deceleration. The model predicted that the head would strike the top of the table, but the head injury criterion (HIC) and neck injury criterion (Nij) would not be exceeded.

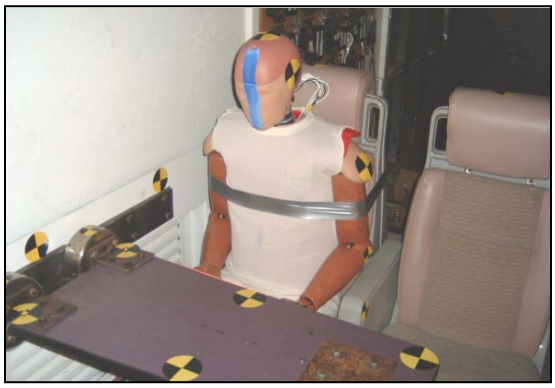

Figure 20. Pre-test Photo of Experiment 1-3

8. Analysis of Occupant Test Results

During an in-line frontal collision, the longitudinal acceleration-time history, or crash pulse, has the most significant influence on the severity of the secondary impact for the occupants. In the two-car CEM test, the force/crush characteristic of the CEM design results in a crash pulse with a relatively high average longitudinal acceleration as compared with the 8 G triangular crash pulse that has been used in sled testing of rail seats [18], and compared to the conventional two-car test results.

The longitudinal acceleration-time history for each car is plotted in Figure 21. The data for each curve were taken from the accelerometer on the center sill near the longitudinal center of the respective cars. The data were then filtered using a CFC 60 filter, as recommended in SAEJ211/1 [19]. There is ringing in the car body acceleration data at less than 100 Hz; however, if filtered at a lower frequency, significant data would be lost. Reference [11] justifies this filter choice.

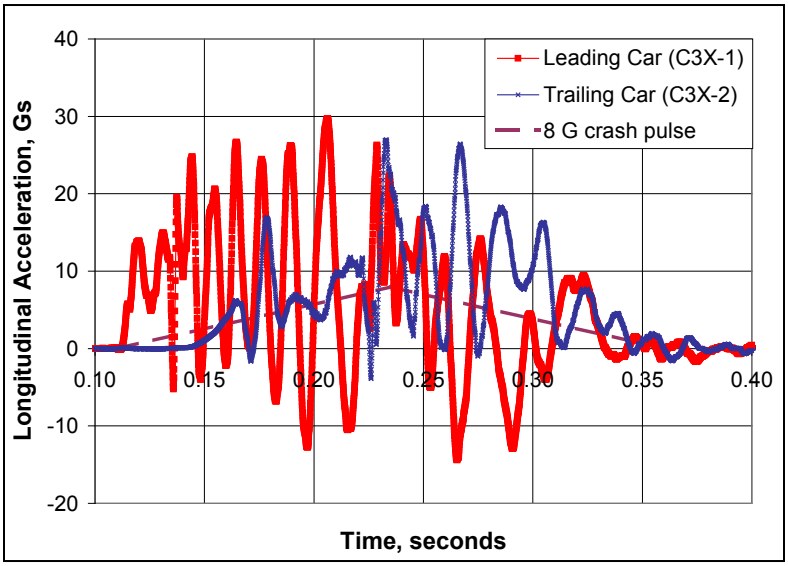

Figure 21. Longitudinal Car Acceleration

As compared to the crash pulses from the conventional two-car test, the initial peak is much lower, but the average peak value increases with time. Another way to look at the influence of the crash pulse is to plot the relative velocity of an occupant with respect to the car against the relative displacement. This plot of relative motion accounts for the whole acceleration time-history, which is more important than the peak values. Relative impact velocity can be used as a simple method to estimate the severity of different collisions with different crash pulses.

In general, the occupant's velocity relative to the car increases with the distance traveled relative to the car within a range of typical seat pitches. At larger relative displacements, the secondary impact velocity reaches an asymptote of roughly the closing speed plus rebound. The higher the secondary impact velocity (SIV), the greater the likelihood of occupant injury. A comparison of SIV for the conventional and CEM designs, shown in Figure 22, suggests the trade-off in performance associated with the higher average accelerations in the CEM design. At 2 feet of travel, the SIV is 13 mph for the conventional design and 22-25 mph for the CEM design. Two

feet is the approximate distance an occupant in the forward-facing commuter seat configuration would travel before impacting the forward seat.

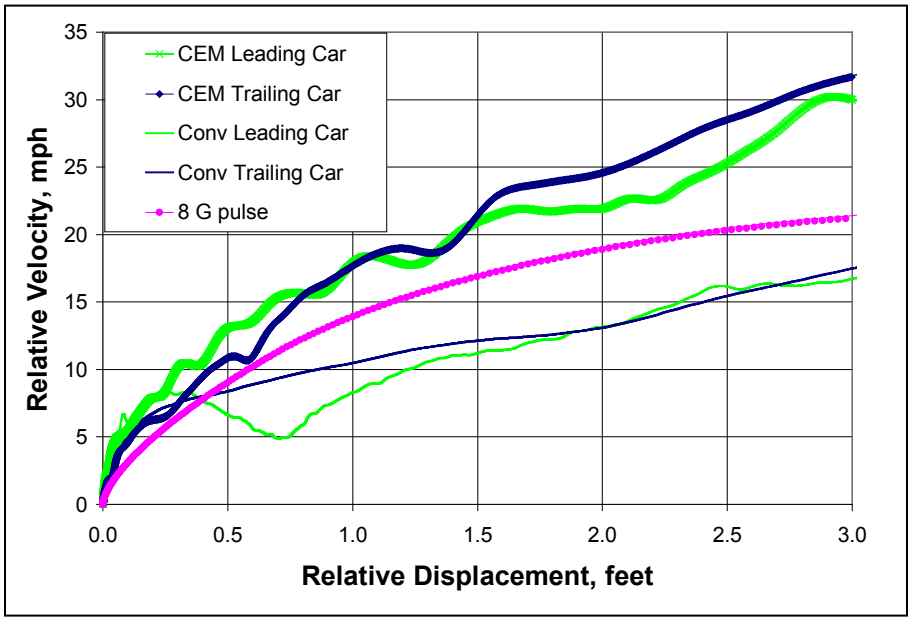

Figure 22. Relative Velocity versus Relative Displacement

As expected, the secondary impact environment was quite severe for the ATDs in this test, when compared to the previous in-line full-scale impact tests. Based on the dummy kinematics, the lateral and vertical car body accelerations appear to be less significant than in the conventional tests. All the ATDs were effectively compartmentalized, with the exception of the ATDs in the forward-facing commuter seats. In this experiment, the forward seat back deformed severely, allowing the ATDs to travel over the top of the forward seat back.

None of the ATDs exceeded the injury criteria for peak tension/compression neck load or axial femur load. Only the ATDs in the workstation table seating arrangements exceeded the injury criterion for chest deceleration. The ATDs in the forward-facing intercity seat exceeded the maximum Head Injury Criterion (HIC). Neither of the ATDs in the seats with table experiments exceeded the suggested injury criteria for abdominal compression and rate of compression. A summary of each occupant experiment, including injury criteria, is given below. Further test results are shown in Appendix H. For comparison, injury results from previous full-scale impact tests are also provided in Appendix H.

8.1 Experiment 1-1: Forward-Facing Intercity Seats, Two 50th-Percentile Male ATDs, Leading Car

As the leading car collided with the wall, the aisle and window dummies began to translate forward, away from the launch seat. The knees impacted the seat back panels, which both deformed severely during the impact. At the same time, the seat backs rotated about the seat base about 15 degrees. At this point, the dummies rotated forward about the pelvis and the heads impacted the top of the seat backs. This caused the seat backs to rotate an additional 10 degrees. The feet and legs of the dummies rose off the ground, and the knees impacted the attachment point of the seat back to the seat base as the dummies fell. The chins also impacted the top of the

seat backs as the dummies fell. A series of pictures taken from high-speed film recorded during the test is shown in Figure 23.

Figure 23. Photo Series for Experiment 1-1: Forward-Facing Intercity Seats, Leading Car

Both dummies remained compartmentalized, and the seats remained attached to the car during the collision. The HIC was exceeded by both the aisle and window dummies. The Nij criteria indicated a high risk of neck injury in the compression-flexion case for both dummies. The peak Nij occurred as the head first impacted the seat back. The face remained in contact with the seat back as the body continued to translate forward and rotate upward about the knee contact, bringing about compression and flexion of the neck. The chest acceleration criterion was relatively low in both dummies. The femur loads approach but do not exceed the maximum criteria value. (See Table 3 for measured injury results.)

Table 3. Experiment 1-1: Injury Results for 95th Percentile Male

Criteria	**Injury Threshold** [21]	**95th Percentile Male, Window Seat**	**95th Percentile Male, Aisle Seat**
HIC15 (Window)	700	2,600 (3.3 ms)	3,849 (1.6 ms)
Nij	1.0	0.39 (Ntf) 0.60 (Nte) 0.85 (Ncf) 0.11 (Nce)	0.43 (Ntf) 0.32 (Nte) 0.77 (Ncf) 0.19 (Nce)
Peak Neck Fz, lbf	+1,131/-1,089	+409/-935	+422/-465
Chest G	55	19.8	26.4
Femur Load, lbf	2,850	1,090 1,976	2,056 1,444

There was plastic deformation of the seat back panels in both of the impacted seats. The panels caved inwards when impacted by the knees of the dummies and began to pull out the rivets at the bottom of the seatback. The seat pedestal itself did not deform, but the seat track bowed roughly half an inch upward at the rear pedestal attachment and downward at the front pedestal attachment.

The results from this experiment show that the modified seat back of the intercity seat is sufficient to compartmentalize the occupants under this more severe occupant environment. The seat back deflection absorbed some energy during the impact; however, additional padding is necessary at the top of the seat back to reduce the risk of head injury. The high HIC values measured require further analysis; one questionable aspect is the extremely small time window of the peak head accelerations.

8.2 Experiment 2-1: Rear-Facing Commuter Seat, One 50th-Percentile Male ATD, Trailing Car

The rear-facing seat experiment was the most benign of all the experiments in the two-car CEM impact test. The sole ATD in the middle seat was already in contact with the seat back and therefore did not develop a significant velocity with respect to the seat. The ATD fell onto the floor after the impact, but had there been another row of seats in front, he likely would have remained sitting on the launch seat. The injury criteria shown in Table 4 are all well below the injury thresholds.

Table 4. Experiment 2-1: Injury Results

Criteria	Injury Threshold [22]	50th Percentile Male, Middle Seat
HIC15	700	94
Nij	1.0	0.07 (Ntf) 0.62 (Nte) 0.05 (Ncf) 0.10 (Nce)
Peak Neck Fz, lbf	+937/-899	+430/-94
Chest G	60	14
Femur Load, lbf	2250	N/A

The seat remained attached and there was minimal deformation of the seat attachment brackets at the wall mount. There was no visible deformation of the floor pedestal. The inertia from the combined mass of the ATD and the seat caused a moderate degree of permanent bending of the vertical frame members in the seat back.

The results from this experiment demonstrate that a single occupant is compartmentalized in the rear-facing commuter seat. There is a potential concern that the seat back may not have been strong enough to provide compartmentalization had the seat been loaded by three ATDs rather than just one. The injury risk due to the occupant interaction with the seat is fairly low, indicating that rear-facing seats are an effective occupant protection strategy.

A series of pictures taken from high-speed film recorded during the test is shown in Figure 24. In the middle slide it is observed that the seat back is not tall enough to support the ATD's head properly, resulting in a moderate tension-extension neck load. This injury mode could be improved with the addition of a headrest or a taller seat back.

Figure 24. Photo Series for Experiment 2-1: Rear-Facing Commuter Seat, Trailing Car

8.3 Experiment 2-2: Forward-Facing Commuter Seats, Three 50th-Percentile Male ATDs, Trailing Car

During the collision, the ATDs slid forward in the seat until the knees struck the back of the forward row of seats, instigating severe deformation of the seat back. Next the heads and chests struck the seat back as it continued to deform, resulting in relatively low head and chest impact forces. The ATDs' forward motion took them over the top of the forward seat back. The tethers tying the ATDs to the floor prevented them from traveling further. The time-sequence of pictures shown in Figure 25 was taken from an overhead camera. Side-view pictures were not available because that camera was damaged during the test.

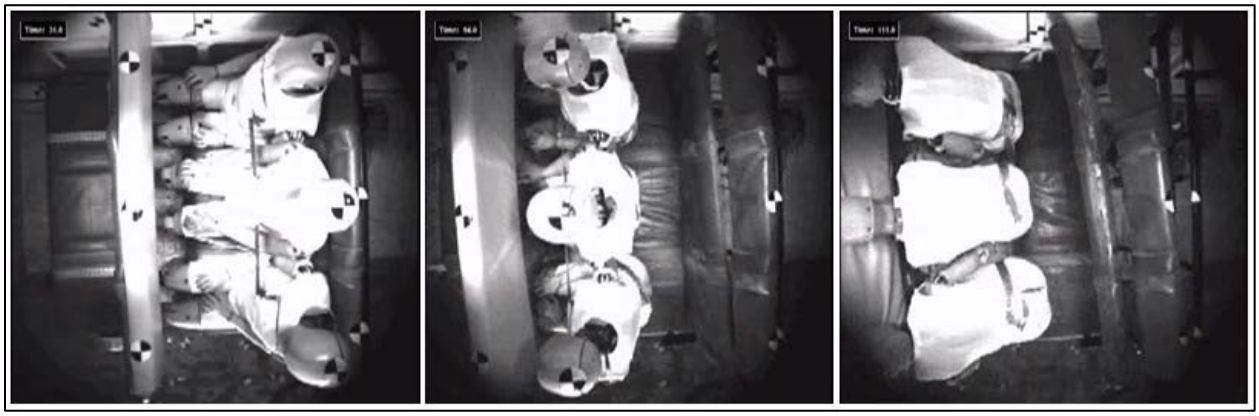

Figure 25. Time-Sequence for Experiment 2-2, Forward-Facing Commuter Seat, Trailing Car

Although the seats remained attached to the car in this experiment, none of the occupants were compartmentalized. Because the seat back deformed severely and provided little resistance, the injury criteria are all quite low. The ATDs did not impact other interior structures because the additional seats were removed and tethers limited the travel of the ATDs. Since the first necessary element to occupant protection, i.e., compartmentalization, was not achieved, the injury criteria measurements are disregarded.

As manufactured, the continuous steel frame members running vertically down the seat back and longitudinally under the seat base formed an interior angle of approximately 110 degrees. After deforming under the load of the ATDs, the angle between the seat back and seat base was reduced to about 45 degrees. The seat base and pedestal were mostly intact. The forward wall-mounting bracket collapsed while the rear bracket fractured. The square tube connecting the seat back to the seat base on the wall side failed just in front of the gusset. All of the seat cushions from the rear seat as well as the cushions from the seat back of the forward seat detached from the seat frames and became hazardous projectiles.

The results of this experiment show that the forward-facing commuter seats require modification on order to provide adequate collision protection in a collision of this severity. The seat back needs to be strengthened to prevent gross deformation.

8.4 Experiment 1-2: Forward-Facing Intercity Seats with Table, One Hybrid 3RS ATD, Leading Car

Upon impact, the Hybrid 3RS ATD translated directly forward in the longitudinal direction. There was little or no vertical or lateral motion. The dummy's shoes initially began to slide along the floor, and then dragged enough to cause rotation about the knee. The knees contacted the facing seat pan at the same time as the upper abdomen impacted the table. Upon impact with the table, the upper abdomen compressed nearly half the depth of the dummy. As this compression occurred, the upper body rotated forward and down toward the table, while the pelvis and legs rotated slightly upward toward the table. At the point of maximum compression, the dummy slid backward and returned to the initial seating position (see Figure 26 for photos of the time-response).

Figure 26. Photo Series for Experiment 1-2: Hybrid 3RS with Table, Leading Car

The HIC, Nij, peak neck tension/compression, chest acceleration, and femur loads were all below the maximum injury criteria values. Results show a high peak abdominal load and significant abdominal compression and rate of compression. These measurements are consistent with the photometric evidence illustrated in Figure 26. See Table 5 for measured injury results. Note that an abdominal compression of 50 percent corresponds to a 25 percent probability of an abdominal injury ≥4 on the abbreviated injury scale (AIS) [23].

Table 5. Experiment 1-2: Injury Results for Hybrid 3RS

Criteria	Injury Threshold	Hybrid 3RS Male, Window Seat
HIC15	700	215
Nij	1.0	0.34 (Ntf) 0.60 (Nte) 0.07 (Ncf) 0.32 (Nce)
Peak Neck Fz, lbf	+937/-899	+558/-93
Chest G	60	45.8
Femur Load, lbf	2,250	417/652
Upper Abdomen Compression Ratio [23]	50%	37.1%
Upper Abdomen V*C (m/s) [24]	1.98	1.08

There were no signs of failure in any of the seat or table attachments. The displacement of the table was minimal, and it returned to its original position after the impact. The peak table load measured at the location of the impact was 6,490 pounds. While this seating arrangement was

successful in compartmentalizing the occupant, the injury risk associated with the table impact is very high. Thus, an occupant seated at a workstation table is not sufficiently protected during a collision of this severity.

8.5 Experiment 1-3: Forward-Facing Intercity Seat with Table, One THOR ATD, Leading Car

As the THOR impacted the workstation table, the rotation of the upper body about the point of impact was severe. The head pitched downward and struck the forward edge of the table. Since the dummy's jacket was wedged between the upper and lower abdominal inserts after the impact, it is likely that the table edge initially contacted the upper abdomen insert, then slid into the gap between the upper and lower abdomen inserts and impacted the spine. This event brought about a high chest acceleration peak. See Figure 27 for photos of the time-response.

Figure 27. Photo Series for Experiment 1-3, THOR with Table, Leading Car

Aside from the peak chest acceleration, the measured injury criteria values were within survivable limits. The abdominal compression and rate of abdominal compression were below the suggested maximum injury criteria values. However, the validity of this measurement as an index of injury is questionable in this case. The measured compression was lower than the total compression of the upper abdomen, due to the fact that the table edge penetrated between the upper and lower abdominal inserts and below the lowest rib, where the lower thoracic bilateral displacement transducer is attached. Photometric evidence suggests an upper abdominal compression of at least 50 percent. Had the table impact remained squarely on the upper abdominal insert, the penetration of the table into the abdominal cavity would have been reduced, and the spine would not have been impacted. See Table 6 for measured injury results.

As in experiment 1-2, the table was minimally displaced during the impact, and returned to its original position afterwards. The peak table load measured at the location of the impact was above 6,813 pounds. There were no signs of failure in any of the seat or table attachment point. Again, while this seating arrangement compartmentalizes the occupant, the injury risk associated with the table impact is very high.

The kinematics of the Hybrid 3RS and the THOR ATDs differed greatly. In the impact with the table, both ATDs showed upper body rotation down towards the top of the table, and lower extremity and pelvis rotation up towards the bottom of the table. However, the THOR rotations were large enough that the head impacted top of the table and the knees impacted the bottom of the table. Thus, the THOR measured higher HIC and Nij values than the Hybrid 3RS. The peak chest acceleration was also higher for the THOR, as the table edge bypassed the abdominal inserts and directly impacted the spine. The Hybrid 3RS includes a bib made of

polytetrafluoroethylene (PTFE) between the abdomen and rib cage to prevent such intrusion from occurring. See reference [25] for a more detailed comparison of these experimental test devices.

Table 6. Experiment 1-3 Injury Results for THOR

Criteria	Injury Threshold	Hybrid Male, Window Seat
HIC15	700	530
Nij	1.0	0.36 (Ntf) 0.41 (Nte) 0.16 (Ncf) 0.73 (Nce)
Peak Neck Fz, lbf	+937/-899	+585/-209
Chest G	60	94
Femur Load, lbf	2,250	904/1,328
Upper Abdomen Compression Ratio [23]	50%	30.2%
Upper Abdomen V*C (m/s) [24]	1.98	1.30

9. Discussion of Occupant Tests

Five interior occupant experiments were conducted as part of the two-car impact test of crash energy management equipment. Three of these experiments were similar to those conducted in previous full-scale impact tests such that injury results could be compared for impact tests involving conventional and CEM equipment. Two new experiments were conducted using tables and advanced experimental dummies to analyze the risk of abdominal injury for occupants seated at tables.

The impact test described in this report is the first in the series that utilized instrumented ATDs in CEM equipment. Based on computer modeling results, it was anticipated that the two-car CEM test would produce the most severe secondary impact environment of any test in the series. Test results confirm that the secondary impact environment in the two-car CEM test is indeed more severe than that of the previous tests. By quantifying the dynamic environment, interior modifications to mitigate the severity can be proposed, tested and evaluated. The rear-facing commuter seat experiment confirms the success of one potential remedy.

In spite of the severe collision environment, the measured injury results were generally lower than expected. Only a few injury thresholds were exceeded. No injury criteria were exceeded in the rear-facing seating configuration resulting in the lowest likelihood of injury among any of the configurations tested. While no injury criteria were exceeded in the forward-facing commuter seat experiment, the load imparted by the three ATDs was sufficient to cause severe deformation of the seat back, resulting in a loss of compartmentalization. Both ATDs in the forward-facing intercity seats exceeded the head injury criteria.

The THOR and Hybrid 3RS experimental test dummies in the workstation table experiments provided information on the interaction of the abdomen with the table edge. These test dummies measured the abdominal compression and rate of compression, which will be used to estimate abdominal injury risk. The table was instrumented to measure the peak loads imparted by the occupant, which will be used to form standards for an improved table design. The THOR ATD exceeded the injury threshold for chest deceleration. Suggested injury criteria for abdominal compression and rate of compression were not exceeded, however these measurements were still quite high for both the THOR and Hybrid 3RS ATDs.

In addition to rear-facing seating, other steps can be taken to reduce the effects of the more severe CEM crash pulse. Modifications to the seats and tables can make the interiors less hostile during a collision. A reinforced commuter seat back will provide more resistance to deformation and increase the likelihood of compartmentalization. A taller seat back on the commuter seat will minimize neck loads in the rear-facing seat configuration. Additional seat padding on the intercity seat back will reduce the severity of head and neck injuries. An improved table design will limit and distribute the abdominal load while ensuring compartmentalization of the occupant.

The final test in the series of full-scale impact tests—a train-to-train test using crash energy management-equipped passenger equipment—is planned for 2006. This test will incorporate all the occupant experiment configurations described in this report. The recommended seat and table modifications described above will be incorporated in the train-to-train test of CEM equipment, such that improved crashworthiness can be measured and evaluated.

10. Conclusion

The Federal Railroad Administration's one-car and two-car tests of CEM equipment were the first of three tests intended to define the performance of equipment designed with improved-crashworthiness in in-line collisions. The first test consisted of a single passenger car impacting a fixed barrier, with the principal objective of measuring the force required to cause significant crush of the car and observing the geometry of the crushed structure. The second test consisted of two-coupled passenger cars impacting a fixed barrier, with the principal incremental objective of measuring the interaction of the coupled cars, i.e., the kinematics of the coupling during the impact and the influence of the trailing car on the leading cars' deceleration.

Other tests based on the in-line train-to-train collision scenario included single-car and two-car tests of conventional equipment [1, 2]. In the single car test of conventional equipment, the car crushed approximately 6 feet and the wheels of the lead truck lifted off the rails by 9 inches as it crushed. In contrast, the CEM car crushed by 3 feet and all the wheels remained on the track. In the two-car test of conventional equipment, the impacting car was crushed by about 6 feet and rose vertically about 9 inches, while the impacting CEM car was crushed about 3 feet and its wheels remained on the rails. In the two-car test of conventional equipment, the coupled cars sawtooth-buckled, and the trucks immediately adjacent to the coupled connection derailed. In the two-car test of CEM equipment, the cars remained in-line, and none of the trucks derailed. These tests demonstrated that CEM equipment can successfully distribute the crush to unoccupied areas of multiple CEM vehicles and minimize both the lateral and vertical motions of the cars.

In the train-to-train test of conventional equipment, the colliding cab car crushed by approximately 22 feet and overrode the locomotive [3]. The space for the operator's seat and for approximately ten rows of passenger seats was lost. The passenger equipment to be used in the subsequent test is designed to preserve the space for the operator and passengers by dispersing the structural crush into unoccupied areas of the train. Computer simulations of the train-to-train test of equipment with crush zones indicated that the cab car will crush by approximately 3 feet, and that override will be prevented [27, 28]. Structural crush will be distributed back to all of the coach car crush zones, and all of the crew and passenger space will be preserved. The train-to-train test of CEM equipment, planned for March 2006, would be expected to confirm these predictions.

The impact tests described in this report are the first in FRA's series that utilized instrumented ATDs in CEM equipment. Conventional seats and workstation tables, with some modifications for increased strength, were used in the occupant experiments carried out as part of the two-car test of CEM equipment. Test results confirmed that the secondary impact environment in the two-car test of CEM equipment was somewhat more severe than in the two-car test of conventional equipment. By quantifying the dynamic environment, interior modifications to mitigate the severity can be proposed, tested and evaluated. To reduce injury risks to the occupants in a more severe environment, modifications to the interior fixtures were made to keep secondary impact forces and decelerations within survivable limits.

In 2005, designs incorporating features for increased occupant protection for workstation tables and commuter passenger seats were being developed [25, 26]. Examples of these designs would be included in the train-to-train test of CEM equipment. Five occupant protection experiments would be included on the train-to-train tests of CEM equipment to measure the occupant

response in modified versions of previously-tested seating arrangements: forward-facing intercity seats, forward- and rear-facing commuter seats, and facing commuter seats with intervening tables. These modifications are expected to minimize injury risks to the occupants.

References

1. Tyrell, D., Severson, K., & Perlman, A.B. (2000). *Single passenger rail car impact test. Volume I. Overview and selected results* (DOT/FRA/ORD-00/02.1). Washington, DC: U.S. Department of Transportation.

2. Tyrell, D., Severson, K., & Perlman, A.B. (2002). *Passenger rail two-car impact test. Volume I. Overview and selected results* (DOT/FRA/ORD-01/22.I). Washington, DC: U.S. Department of Transportation.

3. Tyrell, D., Severson, K., Perlman, A.B., & Rancatore, R. (2002). Train-to-train impact test: Analysis of structural measurements. American Society of Mechanical Engineers. Paper No. IMECE2002-33247.

4. Jacobsen, K., Tyrell, D., & Perlman, A.B. (2003). Grade-crossing impact tests: Collision dynamics. ASME/IEEE Paper No. RTD2003-1655.

5. Jacobsen, K., Tyrell, D., & Perlman, A.B. (2004). Impact test of a crash energy management passenger rail car. RTD2004-66045.

6. Mayville, R.A., Johnson, K.N., Stringfellow, R.G., & Tyrell, D.C. (2003). The development of a rail passenger coach car crush zone. ASME/IEEE Paper No. ASME RTD 2003-1653.

7. Severson, K., Parent, D., & Tyrell, D. (2004). Crash energy management impact tests: Occupant tests. American Society of Mechanical Engineers. Paper No. IMECE2004-61249.

8. Severson, K., Tyrell, D., & Perlman, A.B. (2000). Rail passenger equipment collision tests: Analysis of structural measurements. American Society of Mechanical Engineers. RTD-Volume 19.

9. Tyrell, D.C., & Perlman, A.B. (2003). Evaluation of rail passenger equipment crashworthiness strategies. Transportation Research Record No. 1825, pp. 8-14. National Academy Press.

10. Jacobsen, K., Tyrell, D., & Perlman, A.B. (2004). Impact tests of crash energy management passenger rail cars: Analysis and structural measurements. American Society of Mechanical Engineers. Paper No. IMECE2004-61252.

11. Severson, K., Tyrell, D., & A. B. Perlman. (2003). Collision safety comparisons of conventional and crash energy management passenger rail car designs. JRC2003-1657. ASME/IEEE Joint Railroad Conference. Chicago, IL.

12. Tyrell, D.C., Severson, K.J., & Marquis, B.J. (1995). Analysis of occupant protection strategies in train collisions. ASME International Mechanical Engineering Congress and Exposition. AMD-Vol. 210, BED-Vol. 30, pp. 539-557.

13. VanIngen-Dunn, C. (2003). *Passenger rail train-to-train test. Volume II: Summary of occupant protection program* (DOT/FRA/ORD-03/17.2). Washington, DC: U.S. Department of Transportation.

14. TNO Road-Vehicles Research Institute. (2003). MADYMO 3D, Release 6.0/6.1. Delft, The Netherlands.

15. VanIngen-Dunn, C. (2002). *Passenger rail two-car impact test. Volume II: Summary of occupant protection program* (DOT/FRA/ORD-01/22.II). Washington, DC: U.S. Department of Transportation.

16. National Transportation Safety Board. (2003). Collision of Burlington Northern Santa Fe freight train with Metrolink passenger train, Placentia, California, April 23, 2002. (Railroad Accident Report NTSB/RAR-03-04).

17. Haffner, M., et al. (2001). Foundations and elements of the NHTSA THOR Alpha ATD design. Paper 458 presented at the 17th International Technical Conference on the Enhanced Safety of Vehicles, Amsterdam, Netherlands.

18. *Standard for the design and construction of passenger railroad rolling stock* (APTA SS-C&S-034-99). (2004). Washington, DC: American Public Transportation Association.

19. Surface vehicle recommended practice: Instrumentation for impact tests. (1995). SAE J211-1.

20. Severson, K., Tyrell, D., & Perlman, A.B. (2000). Rail passenger equipment collision tests: Analysis of structural measurements. *Rail Transportation*, American Society of Mechanical Engineers. RTD-Vol. 19.

21. Eppinger, R., Sun, E., Kuppa, S., & Saul, R. (2000). Development of improved injury criteria for the assessment of advanced automotive restraint systems II. Washington, DC: Supplement to NHTSA Docket No. 1998-4405-9.

22. Standard 208 Occupant Crash Protection. (2002). Code of Federal Regulations. Title 49, Part 571.

23. Rouhana, S.W., Viano, D.C., Jedrzejczak, E.A., & McCleary, J.D. (1989). Assessing submarining and abdominal injury risk in the Hybrid III family of dummies. SAE Technical Paper No. 892440. Proceedings of the 33rd Stapp Car Crash Conference, pp. 257-279.

24. Wallace, W.A., Srinivasan, S.C.M. (2002). *Rail Passenger & Crew Survivability Studies: Part 2*.

25. Parent, D., Tyrell, D., Perlman, A.B., & Matthews, P. (2005). Evaluating abdominal injury in workstation table impacts. Compendium of Papers, 84th Annual Meeting, Transportation Research Board.

26. Severson, K., Tyrell, D., & Rancatore, R. (2005). Crashworthiness requirements for commuter rail passenger seats. American Society of Mechanical Engineers. Paper No. IMECE2005-82643.

27. Tyrell, D., Jacobsen, K., Parent, D., & Perlman, A.B. (2005). Preparations for a train-to-train impact test of crash-energy management passenger rail equipment. American Society of Mechanical Engineers, Paper No. IMECE2005-70045.

28. Martinez, E., Tyrell, D., Rancatore, R., Stringfellow, R., & Amar, G. (2005). A crush zone design for an existing passenger rail cab car. ASME, Paper No. IMECE2005-82769.

29. ADAMS, Version 2003.0.0, Mechanical Dynamics, Inc. Ann Arbor, Michigan.

30. VanIngen-Dunn, C. (2003). *Commuter rail seat testing and analysis of facing seats* (DOT/FRA/ORD-03/06). Washington, DC: U.S. Department of Transportation.

31. VanIngen-Dunn, C., & Manning, J. (2002). C*ommuter rail seat testing and analysis* (DOT/FRA/ORD-01/06). Washington, DC: U.S. Department of Transportation.

Abbreviations and Acronyms

ATD	Anthropomorphic Test Devices
BNSF	Burlington Northern Santa Fe
CEM	Crash Energy Management
DGSP	Double-Gimballed String Potentiometer
FRA	Federal Railroad Administration
HIC	Head Injury Criterion
SIV	Secondary Impact Velocity
THOR	Test Device for Human Occupant Restraint
TTC	Transportation Technology Center
TTCI	Transportation Technology Center Inc.
Volpe Center	Volpe National Transportation Systems Center

Appendix A. Retrofit of Existing Budd Pioneer Cars with CEM Crush Zones

One challenging aspect of the test program was the retrofit of existing single-level equipment with the newly developed CEM crush zone designs. The test vehicles were a pair of Budd Pioneer cars also used in other full-scale tests. The integration of new components onto the existing car structures was accomplished in three steps: fabrication of the new components, preparation of the existing carbody structure for introduction of new components, and integration of the new components onto the test vehicle. Figure A1 is a schematic of the process.

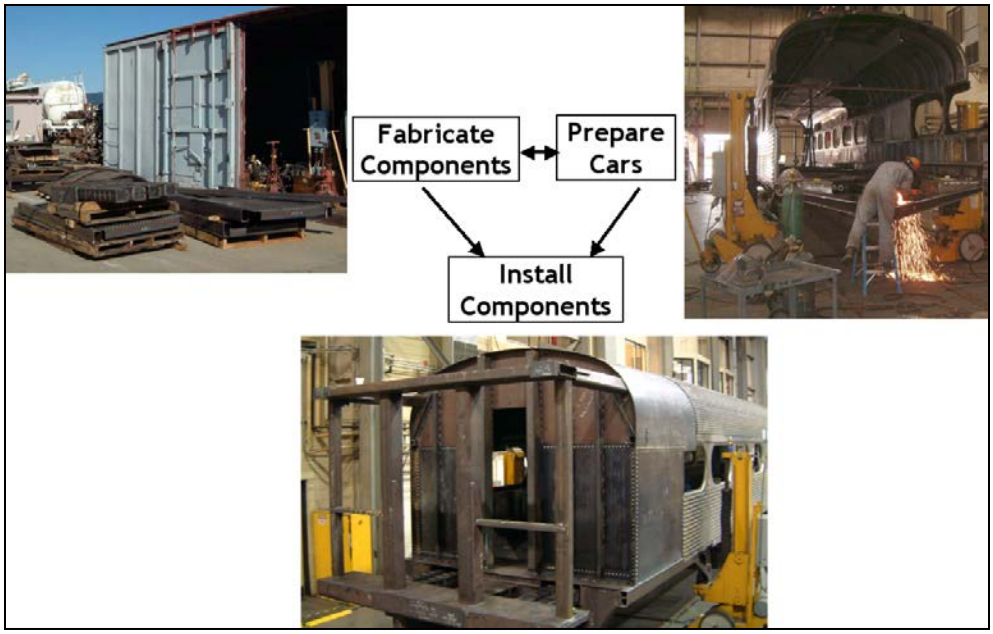

Figure A1. Flow Chart, Retrofit of Crush Zones onto Existing Conventional Cars

The crush zones were fabricated at a separate rail shop and shipped to the Transportation Technology Center. Part and assembly drawings were sent to the rail shop and the materials were ordered, formed, and welded per the drawings. The major assemblies included: the fixed sill, the sliding sill, the pushback coupler, the end frame, the energy absorbers, the partition wall, the front and rear reaction groups, and several roof members. Prior to shipment of the completed assemblies and other parts, several fit-up procedures were followed to assure that key components were capable of sliding the full stroke length.

Figure A2 shows several of the key assemblies constructed. Starting at the top left of the figure, this is a photograph of the fixed sill assembly. This assembly will be attached to the body bolster of the existing car. Within the fixed sill, the sliding sill assembly is drilled and bolted into place. On the sliding sill photograph note the (8 total but 4 visible) shear bolts associated with the connection between the pushback coupler and the sliding sill. The pushback coupler assembly is shown in the bottom right-hand photograph. The sliding buff lug is visible behind the coupler yoke and draft gear as is the honeycomb energy absorber. The primary energy absorbers are mounted onto reaction groups and serve as the principal mechanism for controlled energy absorption once the sliding sill has triggered and pushes back uniformly into the fixed sill. The roof absorbers act like a plunger system where the inner tube compresses a series of honeycomb

cartridges as it pushes back. It is very important to maintain good QA/QC procedures at this stage to prevent subsequent problems at the integration stage.

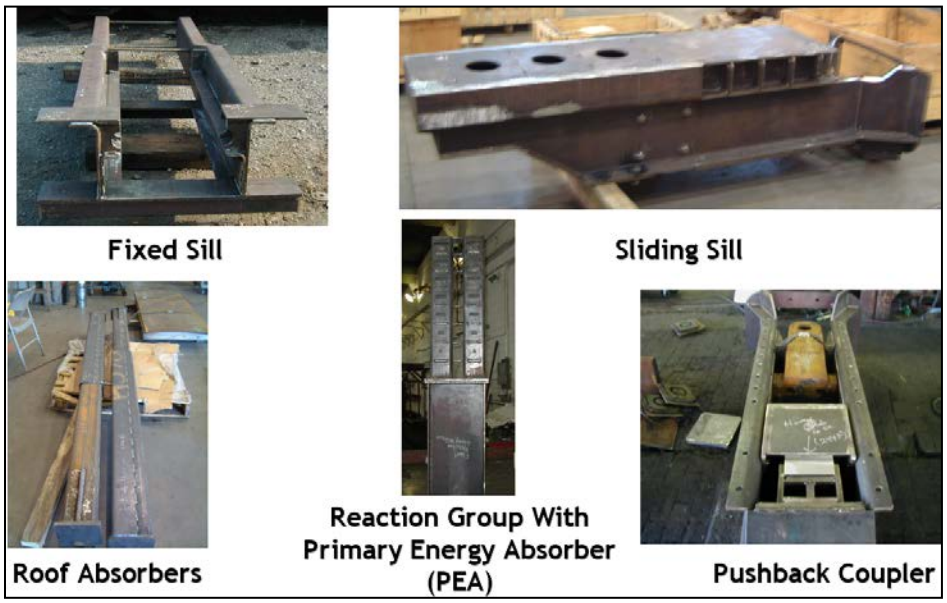

Figure A2. Example Assemblies Fabricated at Rail Car Shop

While the crush zones were being constructed, the Pioneer car had to be prepared for installation. A cutout sequence was developed for use by the assembly team. The damaged ends of the cars from previous tests were removed and the edges on the cut-out planes were smoothed. Figure A3 is a pre-integration photograph of one of the prepared Pioneer cars. There are a limited number of attachment points available on the existing vehicle where load is passed back into the main carbody structure. The most important connections are those at the level of the floor into the body bolster and into the side sills. A majority of the load is reacted through the floor in this CEM design. Additionally some load is reacted through the sidewalls and the roof. The load from the roof absorbers is reacted in shear through the roof sheathing between the cant/roof rail and the purlins located at the top of the roof.

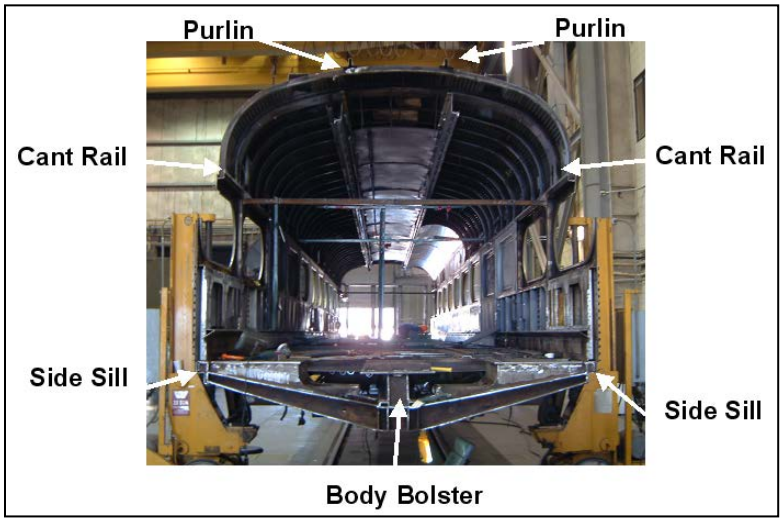

Figure A3. Pre-integration Photograph of a Budd Pioneer Car

In order for the crush zone to act as intended, it is vitally important to assure that no crush be passed back into the occupied volume. Considerable design work was required to distribute the impact load into longitudinal members capable of resisting such loads. The intention of the retrofit design was not to change existing structure on the vehicle aft of the body bolster. The goal was to demonstrate that the prototype design could be implemented on existing equipment that meets both current federal regulations and industry standards.

Integration Sequence

The first step was to reinforce the existing body bolster by closing the bolster box sections and adding additional channel sections longitudinally above the center sill through the body bolster. Lateral stiffeners were added to the vertical face of the tapered channel sections that make up the bolster as well as vertical plates to close the bolster channels facing the end of the car. Figure A4 shows both a half view of the model developed as well as photographs of the car taken during this stage of car preparation and integration.

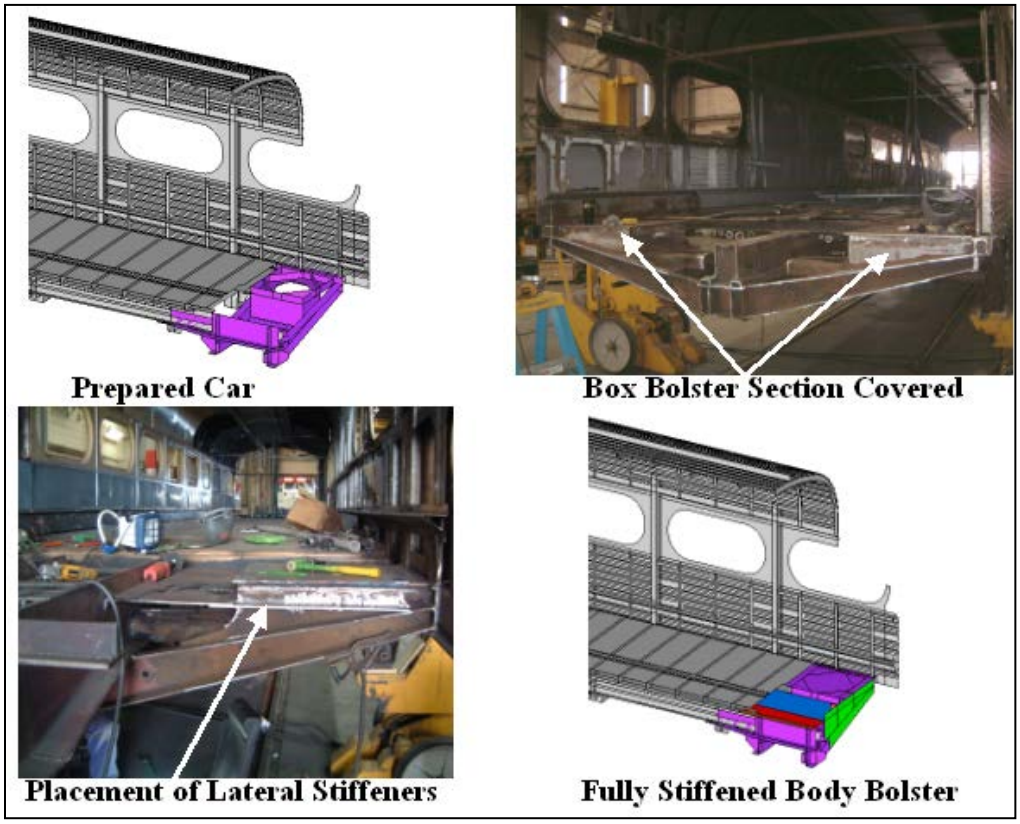

Figure A4. Reinforcing the Existing Body Bolster

After the body bolster was strengthened, the side sills were reinforced and extended a distance forward to the end of the rear vestibule wall. The cant rail was also extended and supported by a set of hydraulic jacks. To leave room to work the trucks were removed. Figure A5 depicts the half-model view and a photograph of the car.

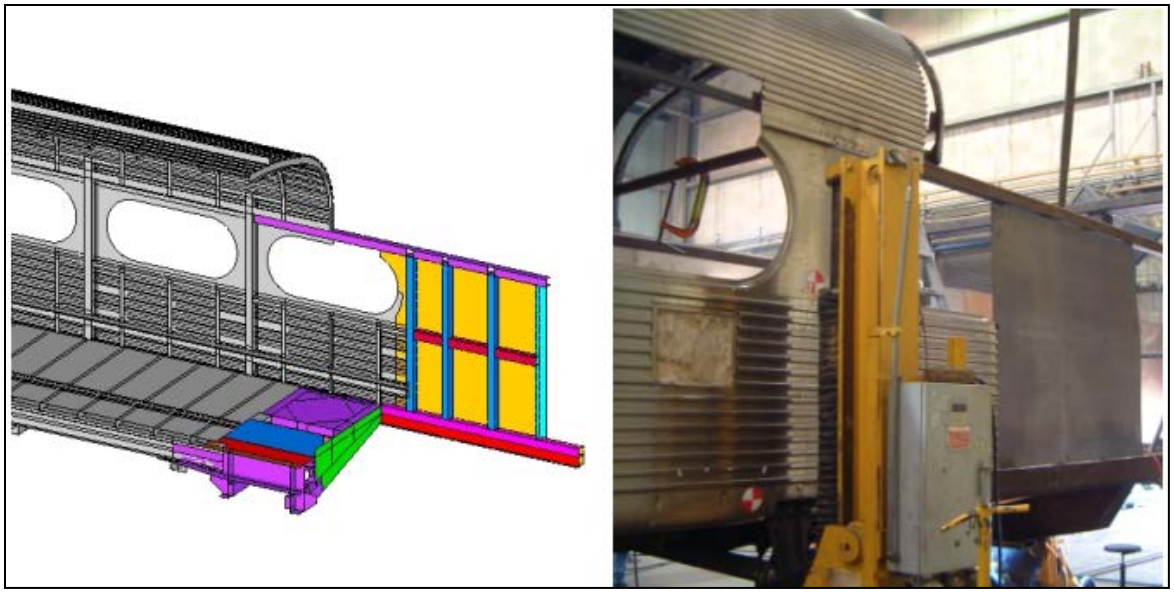

Figure A5. Reinforcing the Existing Side Sills and Extending the Cant/Roof Rails

After the side sills were reinforced and the sidewalls and cant/roof rails extended, the fixed sill connection with the body bolster was put in place. As mentioned previously, rather than welding up a series of small pieces, complete assemblies were fabricated and shipped. The completed unit was then attached. To laterally brace the fixed sill, additional cross braces were added. Figure A6 depicts a half model view and photographs of one end of a car at this stage of integration.

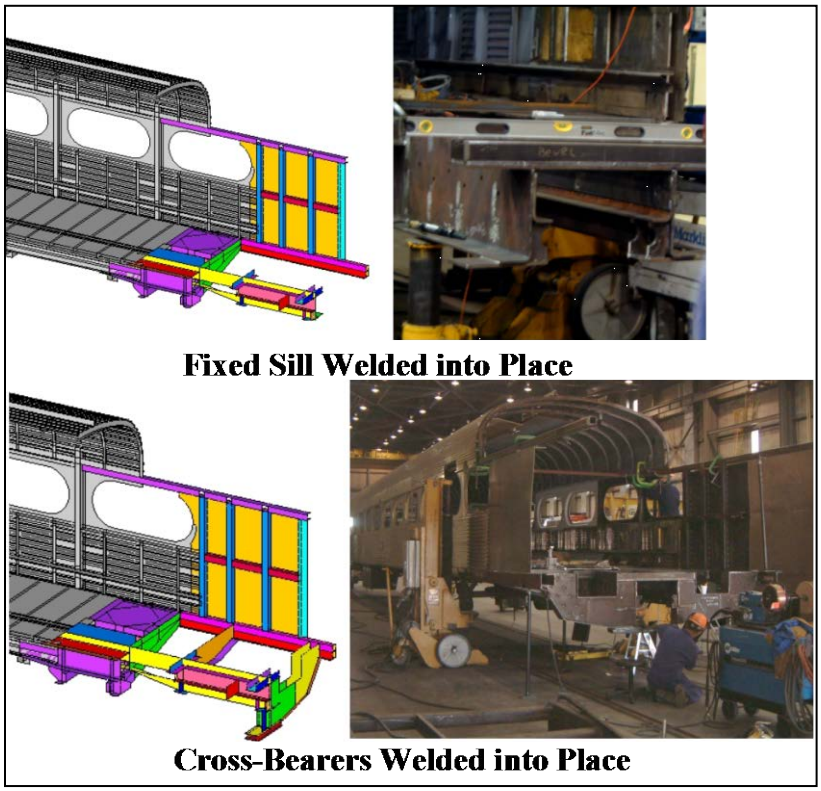

Figure A6. Fixed Sill and Cross-Bearers Installed

Next, the sliding sill was put in place. The holes for the shear bolts were drilled. The sliding sill was then bolted to the fixed sill. Figure A7 depicts the final placement of the sliding sill in the fixed sill as well as a photograph of the shear bolt holes being drilled and the final shear bolt layout.

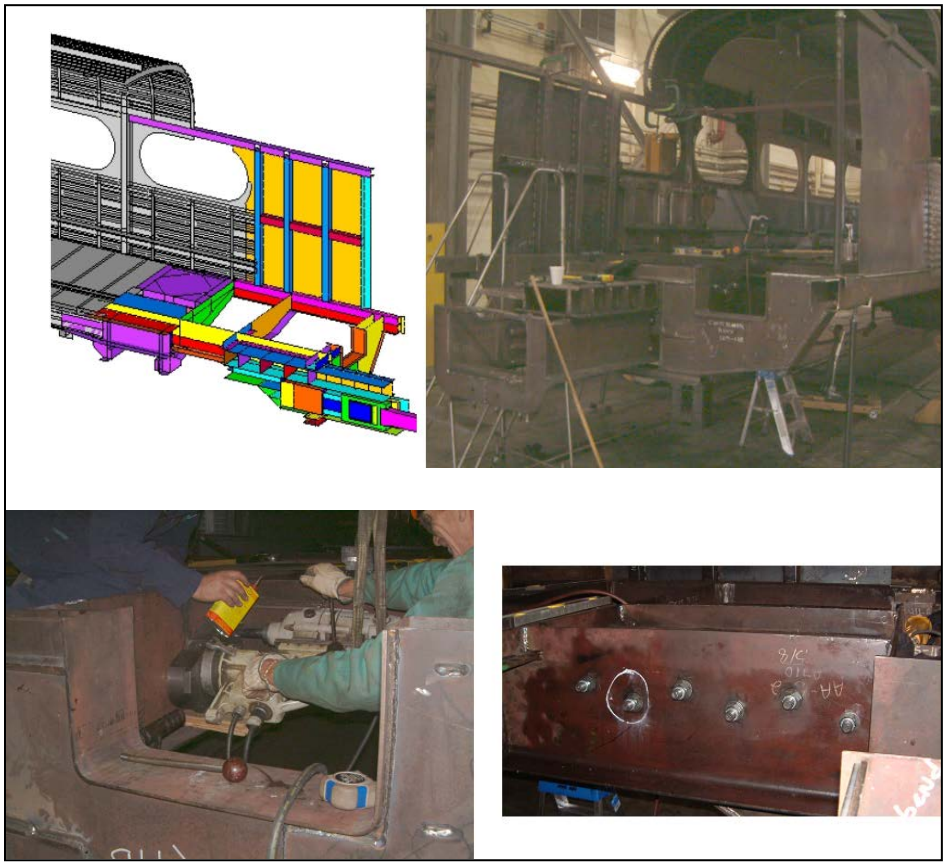

Figure A7. Integration of the Sliding Sill into the Fixed Sill

After the sliding sill was located, drilled, and installed, the next step was to place and weld in the end frame. Careful attention was placed on accurately aligning these large components. Small misalignments in the placement of the end frame can be greatly magnified resulting in problems with the attachment of the roof energy absorbers. Figure A8 shows the half model view and a photograph of the end frame welded into place.

Upon successful installation of the end frame, the primary energy absorbers and reaction groups were placed. The floor plates were then welded into place. Figure A9 shows those two stages of the integration process. The final steps were to situate and weld in the partition wall and the roof structure, as depicted in Figure A10.

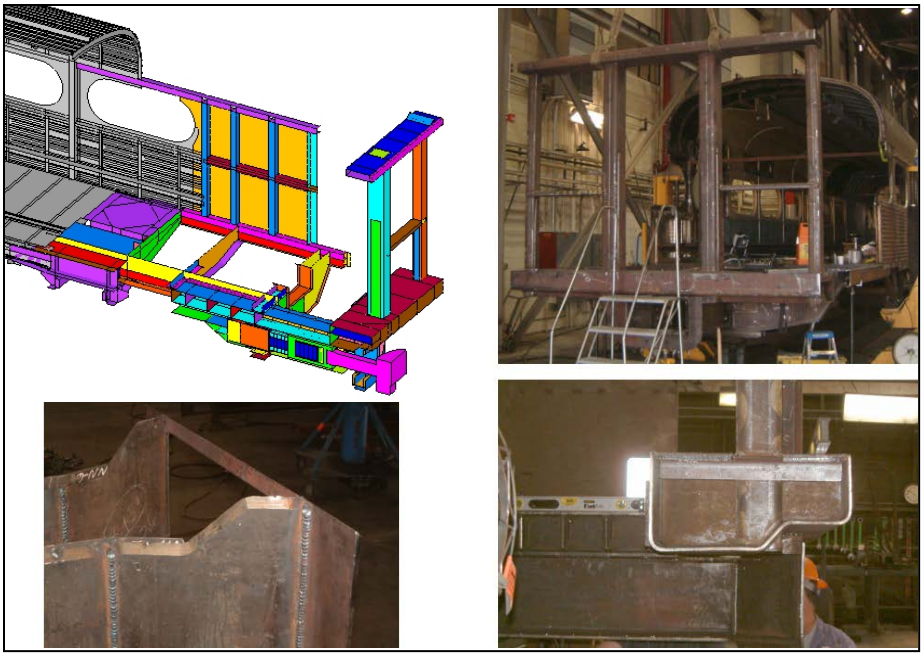

Figure A8. Placement of End Frame onto Sliding Sill

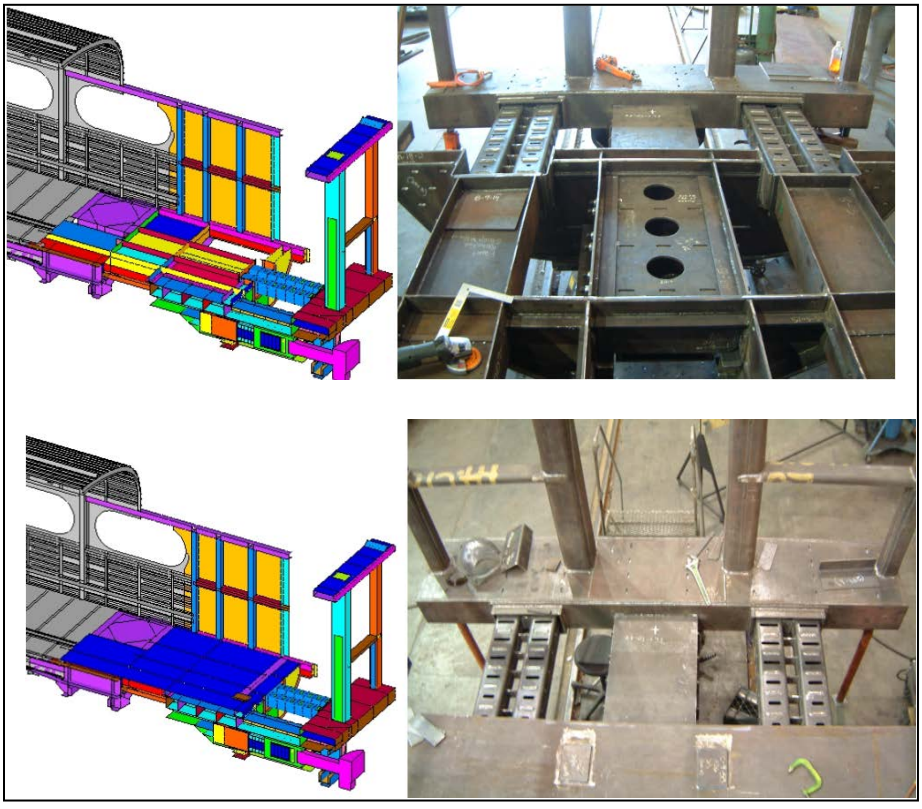

Figure A9. Placement of the Primary Energy Absorbers and Floor Plates

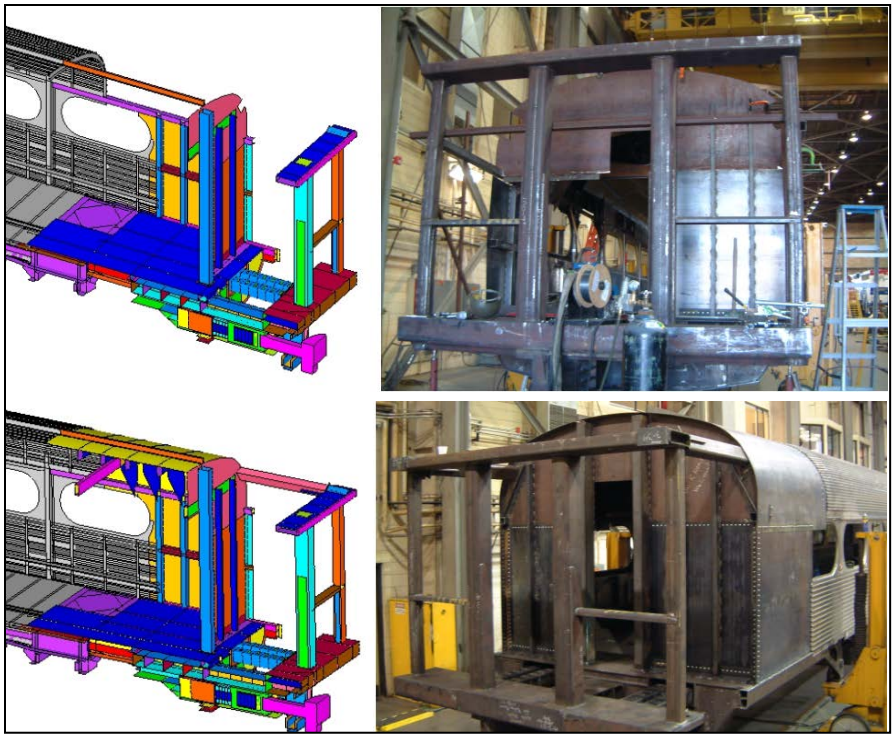

Figure A10. Final Assembly Stage: Placement of Partition Wall and Roof

Lessons Learned

For both the one- and two-car CEM rigid barrier tests, it was necessary to prepare existing passenger rail vehicles for introduction of newly designed components. After the final crush zone designs were developed, sets of engineering drawings were sent to a typical rail car fabrication shop. The rail fabrication shop constructed both large assemblies as well as all the other necessary parts and packaged them for shipment. A set of QA/QC procedures were implemented during the construction phase of the new components and several trips were made to oversee various stages of the fabrication process. Issues raised at this stage were documented to assist in the possible retrofit of new components for additional tests later.

The Budd Pioneer test cars chosen for retrofit were previously used in other full-scale impact tests. In the course of those tests the cars had experienced some damage to the ends of the vehicles. Every end was unique due to distortions experienced during prior testing. Such distortions required special fit-up of new components at key connection locations. The distance from these attachment points to the end frame is large such that small errors in the placement of long structural elements become magnified. As a result, it was sometimes necessary to re-fabricate some components or change the placement of backing bars to assure good fit-up.

In summary, the four crush zones were successfully integrated onto the two Budd Pioneer test vehicles. Car 244 was successfully tested in the single car impact into the rigid barrier test. This car was then used as the trailing vehicle for the two-car impact test where Car 248 was used as the lead vehicle. The undamaged end of car 244 was coupled to the B-end of Car 248. Figure A11 shows a pair of photographs of the design, looking down and from the side of the test wall.

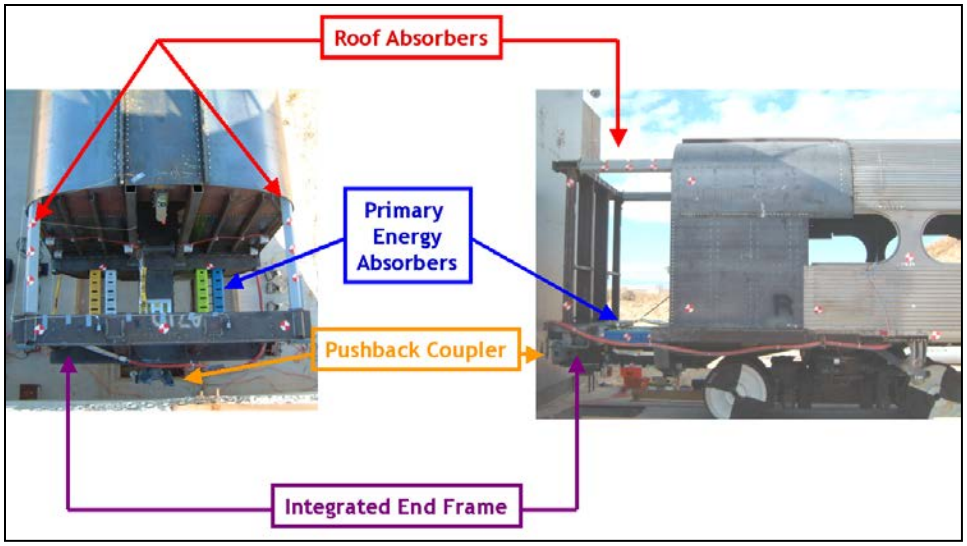

Figure A11. Retrofitted Design Against Rigid Barrier Test Wall

The goal of retrofitting existing single level equipment with crush zones without having to make any changes between the body bolsters of the equipment was accomplished. The prototype designs demonstrated that the collision loads could be sustained and damage to the equipment was restricted to those components designed to crush.

Appendix B. Structural Instrumentation

The instrumentation used to develop information about the kinematics and dynamics of the coupled car crush zones during impact with a rigid wall were chosen based upon pre-test analysis. The pre-test analyses provide information about likely places to locate certain types of instrumentation as well as to range the instrumentation appropriately. The instrumentation ranges and locations used were typical of both the single car and two-car tests. Therefore this Appendix will focus on the implementation of the two-car test. The following types of instrumentation were used: accelerometers, strain gauges, string potentiometers, and high-speed cameras. Figure B1 depicts a schematic of the two-car test layout. The test vehicles were oriented such that the A-end of coach car 248 impacted the rigid test barrier and the B-end was coupled to the B-end of coach car 244.

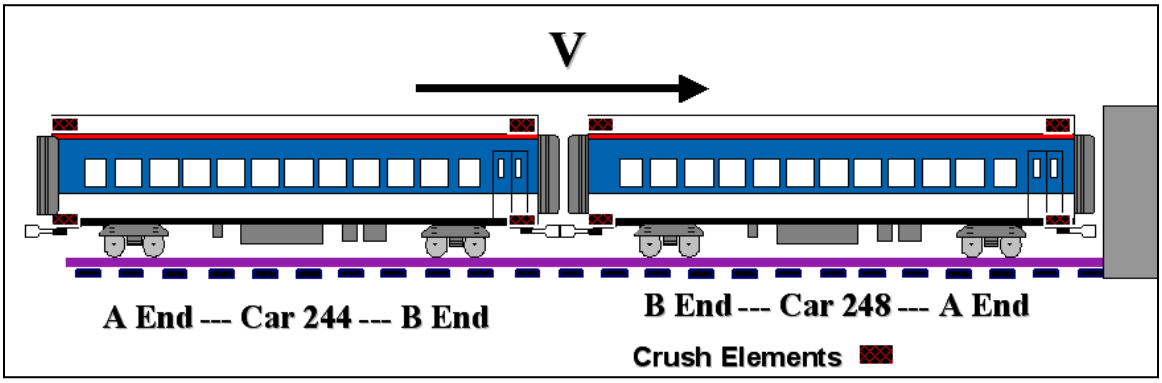

Figure B1. Schematic of CEM Two Car Impact into a Rigid Barrier Test Layout

The objective of the structural instrumentation was to measure the performance of the crush zone at the colliding interface with the rigid barrier as well as at the coupled interfaces. Specifically, detailed information was desired about the triggering of the push-back coupler, the crush of the honeycomb energy absorber behind the push-back coupler, the triggering of the fixed sill/sliding sill shear bolts, and the subsequent crush of the primary energy absorbers and the roof energy absorbers. In addition, the instrumentation was used to develop a better assessment of the change in load path through the crush zone into the occupied compartment. This information would help in better developing a composite force crush characteristics of each crush zone and to determine the influence of the trailing car on the lead crush zone performance.

The accelerometers are used to develop information about the dynamic motions of the vehicles as well as to decompose the force differentials. The string potentiometers and the strain gauges are used to measure both local deformations as well as the load path. Finally, the high-speed film was used as an additional means to develop both kinematic and dynamic information that could be compared against the other measured quantities as a check. Special care was taken to ensure some redundancy in the manner that information was obtained due to the severe loading environment that can cause instrumentation failure.

Accelerometers

Forty-six accelerometers were used to fully instrument the two-coupled cars with their respective crush zones. Each crush zone was instrumented with duplicate accelerometers placed

symmetrically across the longitudinal centerline of the car to assure that at least one channel of data survived the severe shock loading conditions. Two 5000g piezo-electric accelerometers were placed on the push-back coupler. An additional two 5000g piezo-electric accelerometers were placed on the sliding sill. In addition to the crush zone components, two accelerometers were placed symmetrically on the end/buffer beam as well as the anti-telescoping plate. Figure B2, Figure B3, and Figure B4 show photographs taken of the instrumentation placed on a representative end of one of the test vehicles.

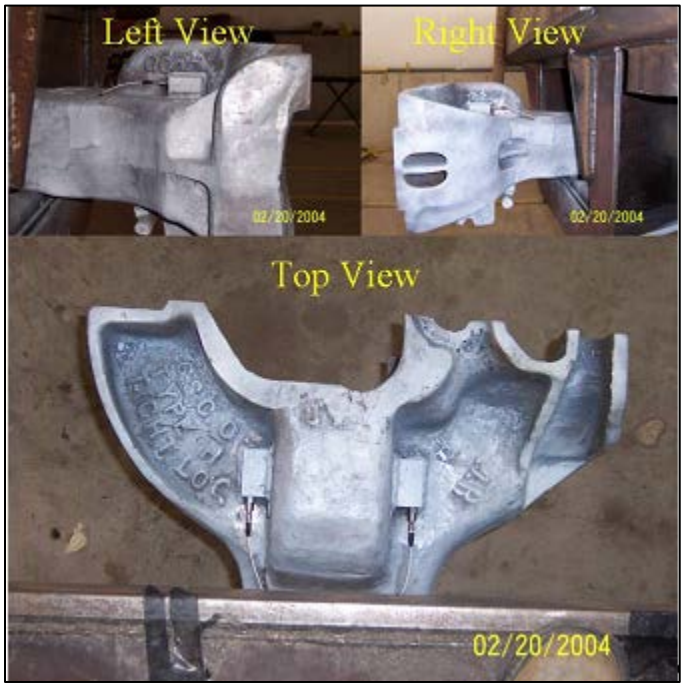

Figure B2. Typical Placement of Push-Back Coupler Accelerometers

Figure B3. Typical Placement of Accelerometers on the Sliding Sill

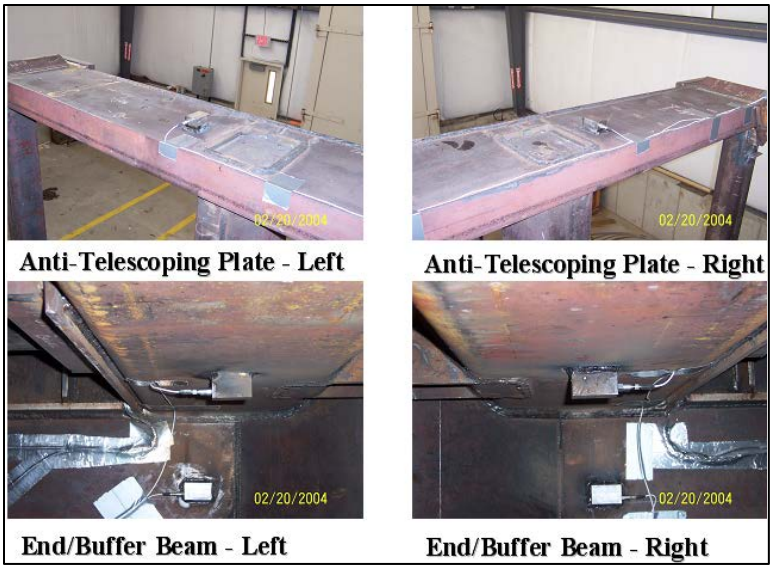

Figure B4. Typical Placement of Accelerometers on End/Buffer Beam and Anti-Telescoping Plate

Additional accelerometers were placed along the center sill at the body bolsters and near the longitudinal center of gravity (CG) of the car. These were triaxial accelerometers and ranged for decelerations between 200 and 400 g. At the longitudinal CG of the car two additional biaxial accelerometers were mounted onto the side sills of the car to measure both longitudinal and vertical decelerations. Each truck had a 400-g accelerometer mounted to measure vertical accelerations. Figure B5 and Figure B6 show the typical placement of the accelerometers on a test vehicle.

Figure B5. Typical Placement of Accelerometers mounted on the Body Bolster and Truck

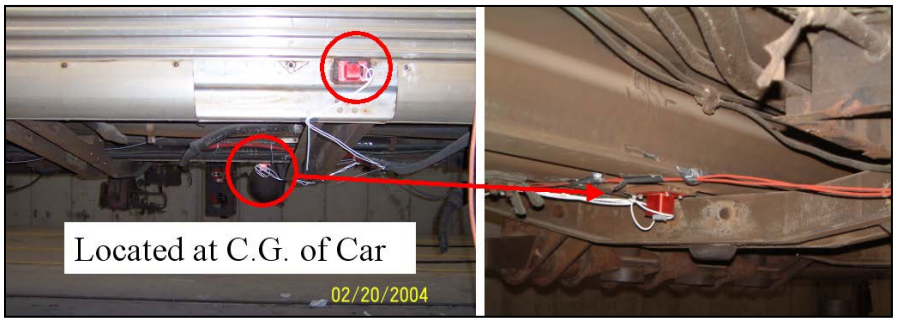

Figure B6. Typical Placement of Accelerometers Mounted at Longitudinal CG of Coach Car

Table B1 lists the accelerometers used on both test vehicles. Included in the table is information about the orientation, the range, and the location of mounting. The associated locations for the accelerometer placement are shown for each car in Figures B7 through B12.

Table B1. Summary of Accelerometer Channels on the Lead Vehicle

Location	Orientation	Channel Name		
		Range	Lead Car # 248	Trailing Car # 244
EL1 – Left side buffer beam	X-Longitudinal	5000g	EL1-AX	N/A
ER1 – Right side buffer beam	X-Longitudinal	5000g	ER1-AX	N/A
EL2 – Left side AT Plate	X-Longitudinal	5000g	EL2-AX	N/A
ER2 – Right side AT Plate	X-Longitudinal	5000g	ER2-AX	N/A
C2 – Center sill, about even with leading body bolster	X-Longitudinal	—	C2-AX (400g)	C2-AX2 (200g)
	Y-Lateral	200g	C2-AY	C2-AY2
	Z-Vertical	200g	C2-AZ	C2-AZ2
L3 – Left side, centered longitudinally	X-Longitudinal	200g	L3-AX	L3-AX2
	Z-Vertical	200g	L3-AZ	L3-AZ2
C3 – Center sill, centered longitudinally	X-Longitudinal	200g	C3-AX	C3-AX2
	Y-Lateral	200g	C3-AY	C3-AY2
	Z-Vertical	200g	C3-AZ	C3-AZ2
R3 – Right side, centered longitudinally	X-Longitudinal	200g	R3-AX	R3-AX2
	Z-Vertical	200g	R3-AZ	R3-AZ2
C4 – Center sill, about even with trailing body bolster	X-Longitudinal	200g	C4-AX	C4-AX2
	Y-Lateral	200g	C4-AY	C4-AY2
	Z-Vertical	200g	C4-AZ	C4-AZ2
B1 – Leading Bogie	Z-Vertical	400g	B1-AZ	B1-AZ2
B2 – Trailing Bogie	Z-Vertical	400g	B2-AZ	B2-AZ2
PBCL1 – Push Back Coupler, left side, leading end	X-Longitudinal	5000g	PBCL1-AX	PBCL1-AX2
PBCR1 – Push Back Coupler, right side, leading end	X-Longitudinal	5000g	PBCR1-AX	PBCR1-AX2
SLSL1 – Sliding Sill, left side, leading end	X-Longitudinal	5000g	SLSL1-AX	SLSL1-AX2
SLSR1 – Sliding Sill, right side, leading end	X-Longitudinal	5000g	SLSR1-AX	SLSR1-AX2
PBCL2 – Push Back Coupler, left side, trailing end	X-Longitudinal	5000g	PBCL2-AX	N/A
PBCR2 – Push Back Coupler, right side, trailing end	X-Longitudinal	5000g	PBCR2-AX	N/A
SLSL2 – Sliding Sill, left side, trailing end	X-Longitudinal	5000g	SLSL2-AX	N/A
SLSR2 – Sliding Sill, right side, trailing end	X-Longitudinal	5000g	SLSR2-AX	N/A

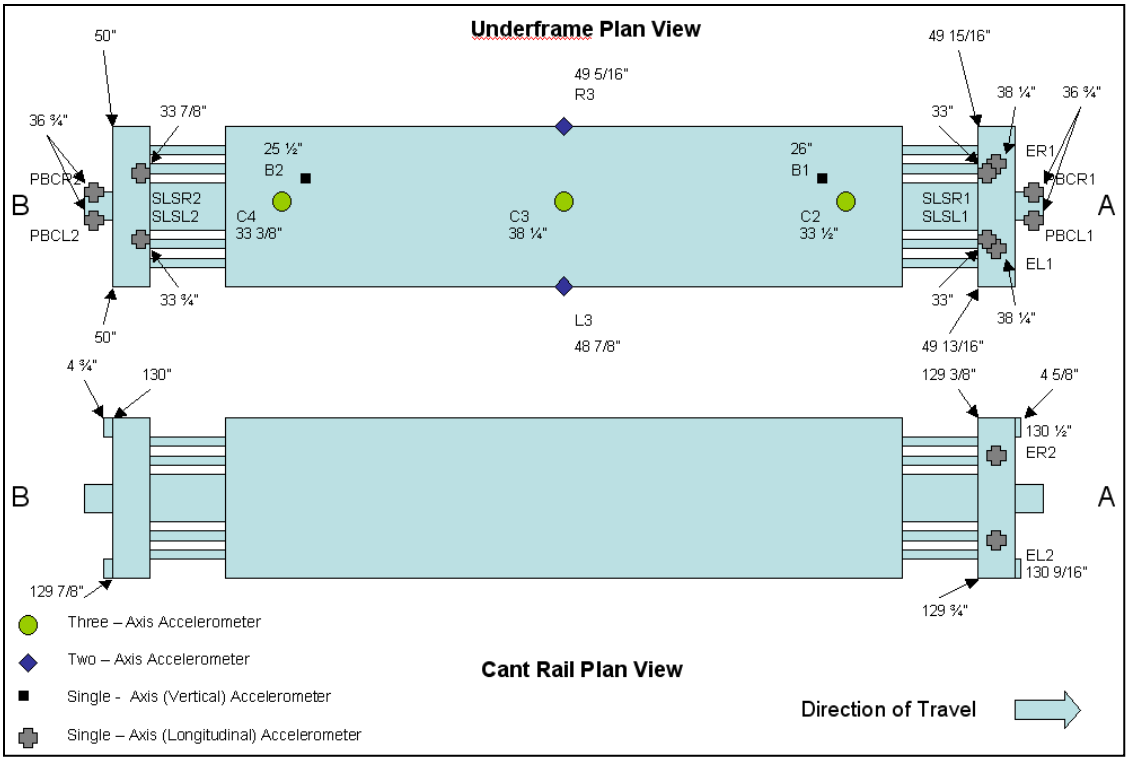

Figure B7. Vertical View of Car 248 (Leading) Accelerometer Pre-Test Measurement Layout

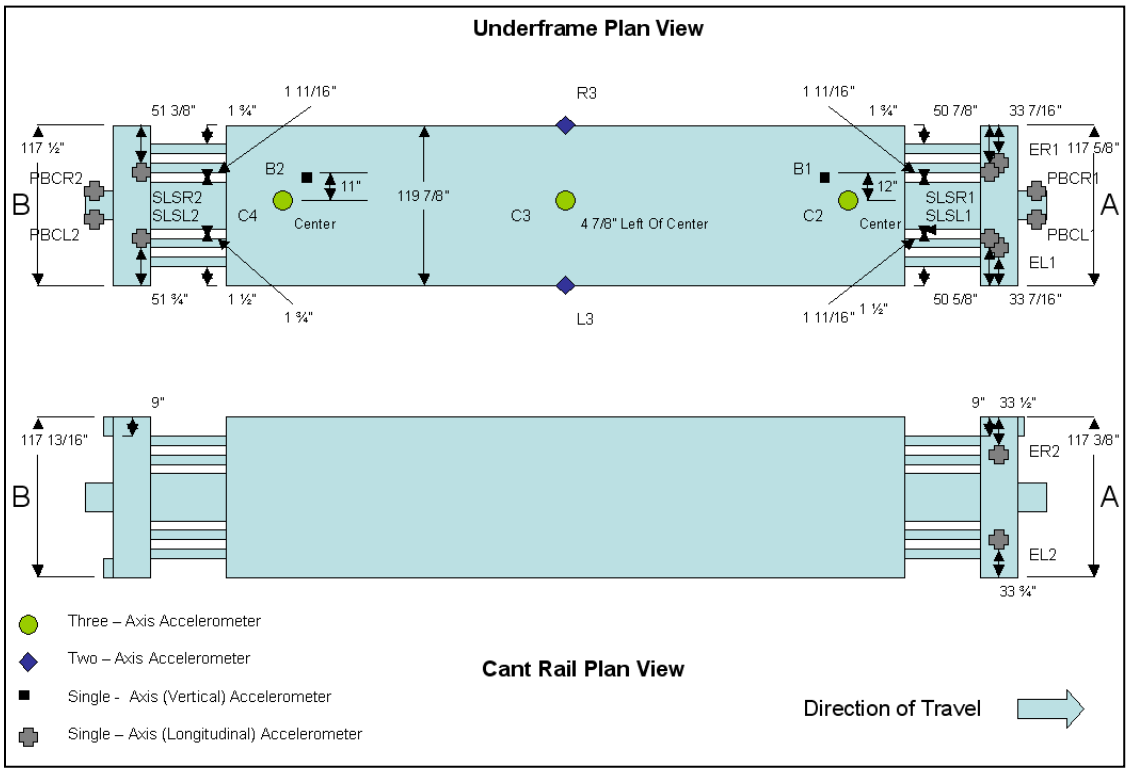

Figure B8. Lateral View of Car 248 (Leading) Accelerometer Pre-Test Measurement Layout

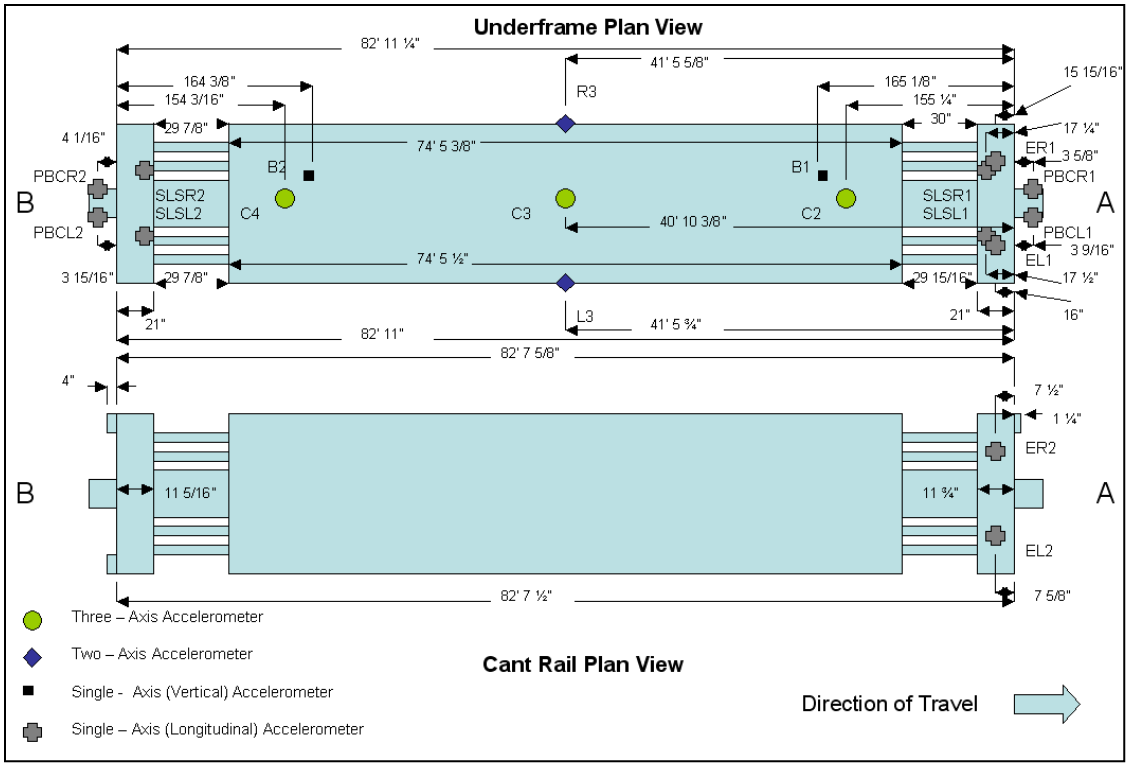

Figure B9. Longitudinal View of Car 248 (Leading) Accelerometer Pre-Test Measurement Layout

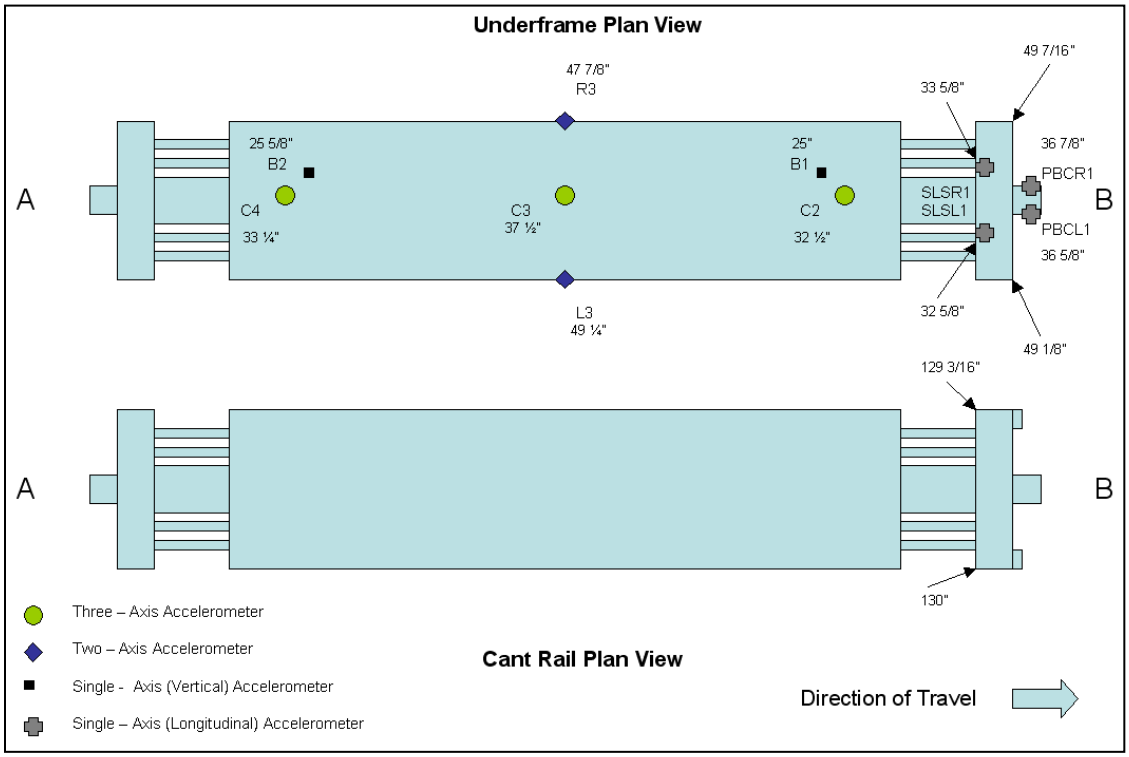

Figure B10. Vertical View of Car 244 (Trailing) Accelerometer Pre-Test Measurement Layout

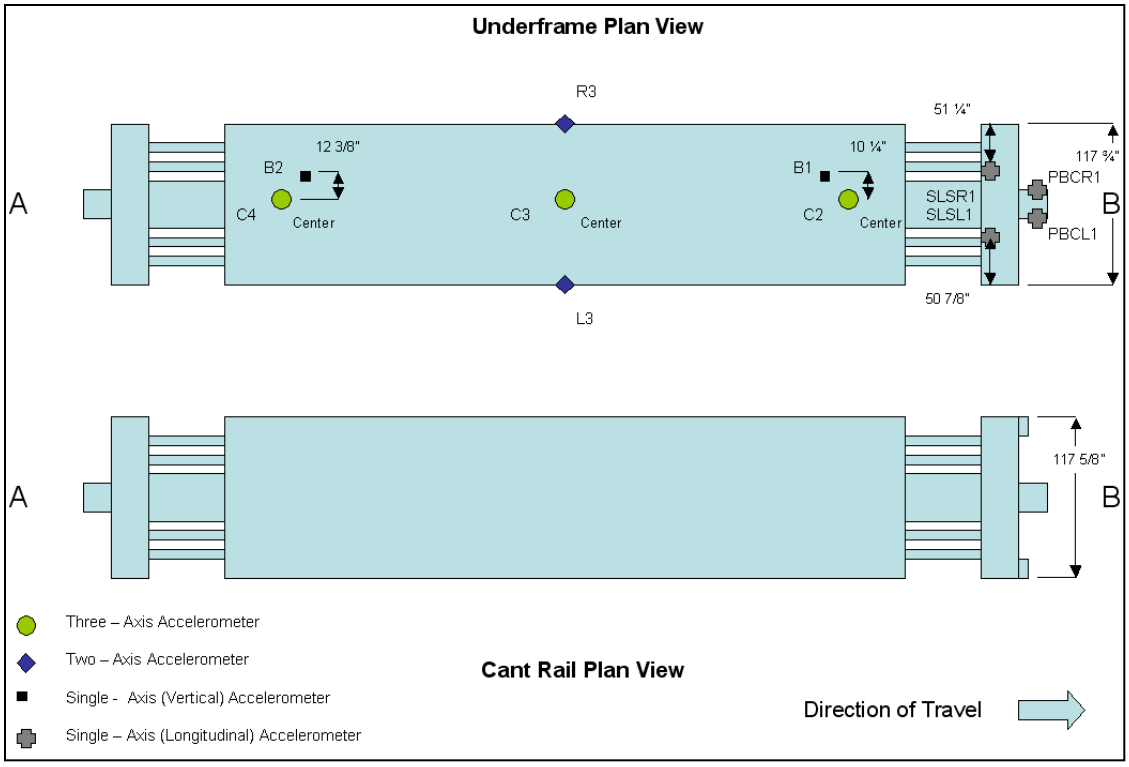

Figure B11. Lateral View of Car 244 (Trailing) Accelerometer Pre-Test Measurement Layout

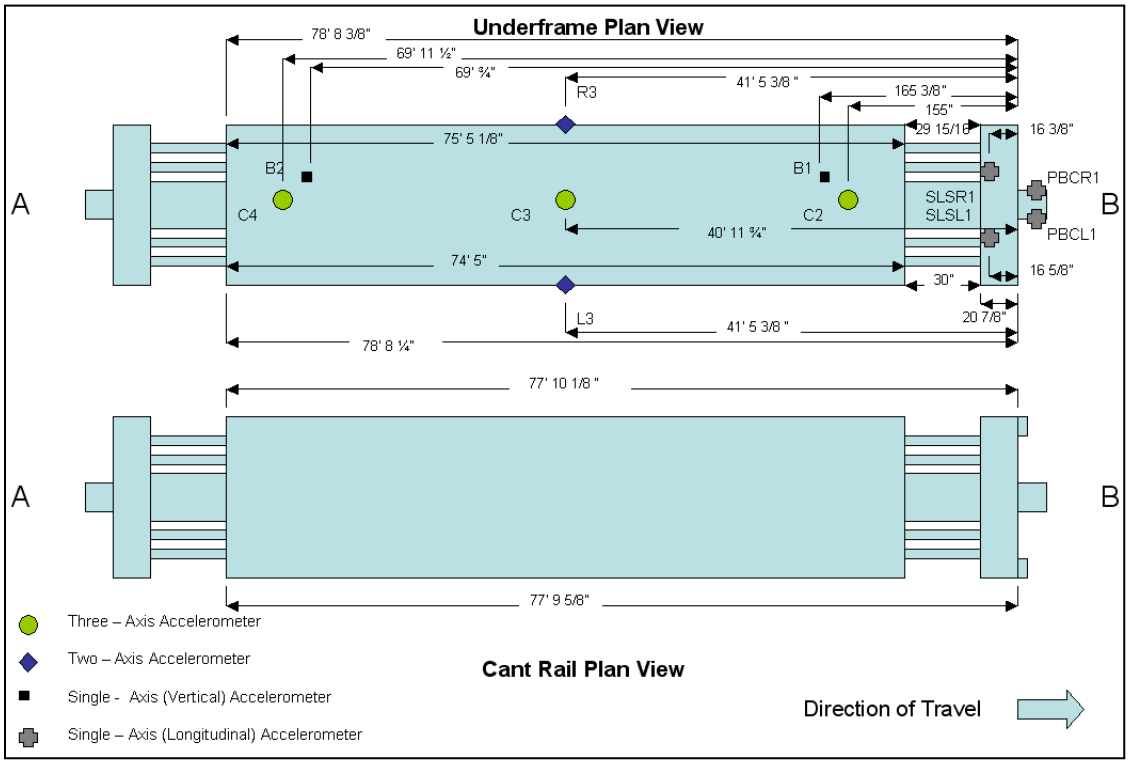

Figure B12. Longitudinal View of Car 244 (Trailing) Accelerometer Pre-Test Measurement Layout

Strain Gauges

Strain gauges were used to measure how the load enters each car end and how it is then transmitted through the car. Some strain gauges were used to determine the timing of triggering events in the push-back coupler and at the fixed/sliding sill connection. The strain was measured at 56 locations total (see tables below for breakdown on cars). The location of the strain measurements was broken down into the following categories:

- Strain gauges on the car body:
  - Roof absorbers (4 uniaxial gauges/end)
  - Draft/Center sill (4 uniaxial gauges/end + 4 uniaxial gauges at the CG location of car 248)
  - Side sill (2 uniaxial gauges/end)
- Strain gauges on the crush zone
  - Coupler Trigger (2 uniaxial gauges/end; actual gauges on sliding sill)
  - Sliding sill (3 uniaxial gauges/impacting end only)
  - Fixed sill (4 uniaxial gauges/end)
- Strain gauges on coupler between cars
  - Instrumented coupler (1 uniaxial gauge)

Strain measurements were made with single element gauges with ½ inch gauge lengths and a maximum range of up to 5 percent. All strain gauge channels were configured to measure a nominal range of ±5,000 micro-strain (με) with a resolution of about ±5με. The actual range and resolution will depend on the gauge factors of the individual strain gauges. Table B2 lists the strain gauge channels placed on the car bodies. Table B3 lists the strain gauge channels placed on the crush zones.

Table B2. Strain Gauge Placement on the Test Cars: Carbody

Component	Detailed Location	Channel Name		
		Lead Car A-End 248	Lead Car B-End 248	Trailing Car B-End 244
Center Sill	Center sill just behind body bolster, left side, top edge	CS-L1T-SXA	CS-L1T-SXB	CS-L2T-SXB
	Center sill just behind body bolster, right side, top edge	CS-R1T-SXA	CS-R1T-SXB	CS-R2T-SXB
	Center sill just behind body bolster, left side, bottom flange	CS-L1B-SXA	CS-L1B-SXB	CS-L2B-SXB
	Center sill just behind body bolster, right side, bottom flange	CS-R1B-SXA	CS-R1B-SXB	CS-R2B-SXB
	Center sill at **CG** location, left side, top edge	CS-L1T-SXC	N/A	N/A
	Center sill at **CG** location, right side, top edge	CS-R1T-SXC	N/A	N/A
	Center sill at **CG** location, left side, bottom edge	CS-L1B-SXC	N/A	N/A
	Center sill at **CG** location, right side, bottom edge	CS-R1B-SXC	N/A	N/A
Left Side Sill	Left side sill, centered, outside	LSS-1-SXA	LSS-1-SXB	LSS-2-SXB
Right Side Sill	Right side sill, centered, outside	RSS-1-SXA	RSS-1-SXB	RSS-2-SXB
Left Roof Absorber	Left cant rail, centered, location 2, inside	LRA-P2-SX1A	LRA-P2-SX1B	LRA-P2-SX2B
	Left cant rail, centered, location 3, outside	LRA-P3-SX1A	LRA-P3-SX1B	LRA-P3-SX2B
Right Roof Absorber	Right cant rail, centered, location 2, outside	RRA-P2-SX1A	RRA-P2-SX1B	RRA-P2-SX2B
	Right cant rail, centered, location 3, outside	RRA-P3-SX1A	RRA-P3-SX1B	RRA-P3-SX2B

Table B3. Strain Gauge Placement on the Test Cars: Crush Zone

Component	Detailed Location	Channel Name		
		Lead Car A-End 248	Lead Car B-End 248	Trailing Car B-End 244
Coupler Trigger (gauges on sliding sill)	Push back coupler, 1.5” ahead of forward bolts, left side	PBC-L-SX1A	PBC-L-SX1B	PBC-L-SX2B
	Push back coupler, 1.5” ahead of forward bolts, right side	PBC-R-SX1A	PBC-R-SX1B	PBC-R-SX2B
Sliding Sill	Sliding Sill, top, centered, between 1st and 2nd box	SLS-TC-SX	N/A	N/A
	Sliding Sill, left side, centered on 3rd box	SLS-SL-SX	N/A	N/A
	Sliding Sill, right side, centered on 3rd box	SLS-SR-SX	N/A	N/A
Fixed Sill	Fixed sill, left side, 1.5” behind 1st bolt	FS-1BL-SX1A	FS-1BL-SX1B	FS-1BL-SX2B
	Fixed sill, left side, 1.5” behind 6th bolt	FS-6BL-SX1A	FS-6BL-SX1B	FS-6BL-SX2B
	Fixed sill, right side, 1.5” behind 1st bolt	FS-1BR-SX1A	FS-1BR-SX1B	FS-1BR-SX2B
	Fixed sill, right side, 1.5” behind 6th bolt	FS-6BR-SX1A	FS-6BR-SX1B	FS-6BR-SX2B

Figures B13 through B15 show the locations of strain gauges on the fixed and sliding sills. Figures B16 through B18 show the strain gauges on side and center sills. The strain gauges on the cant rail are shown in Figure B19.

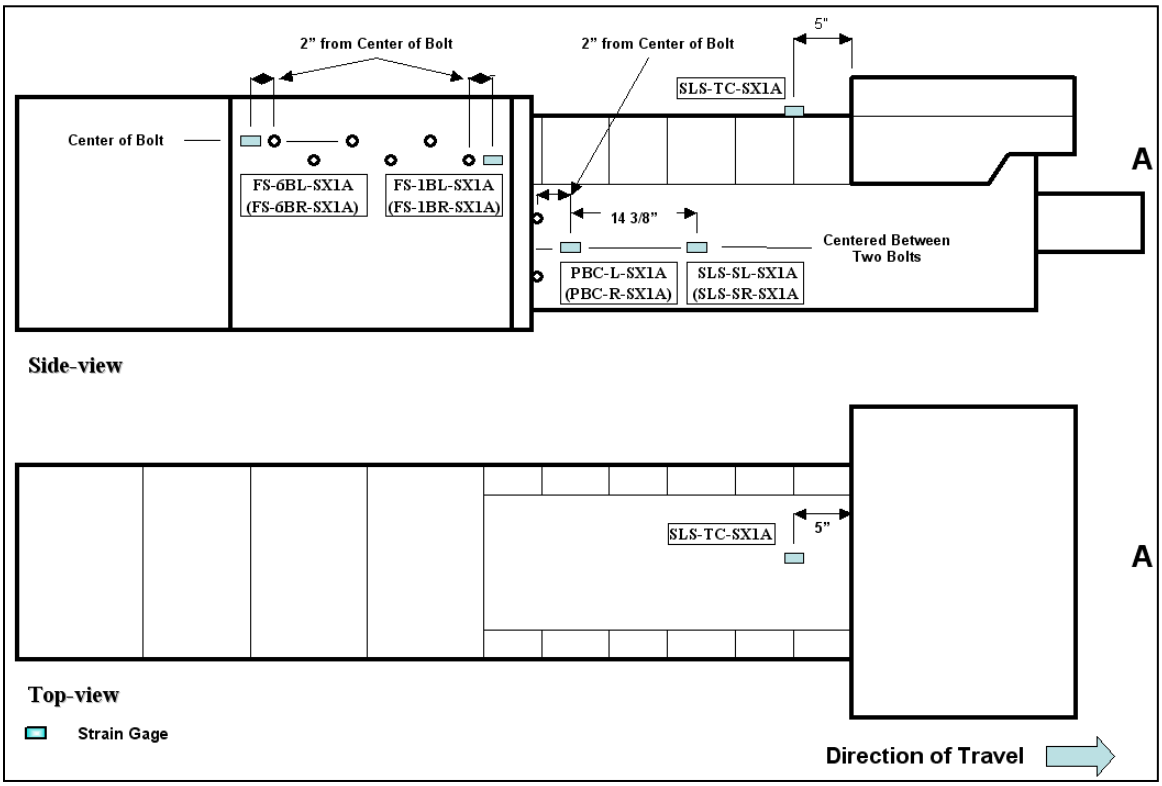

Figure B13. Strain Gauge Layout on Car 248 (Leading) End Fixed/Sliding Sill

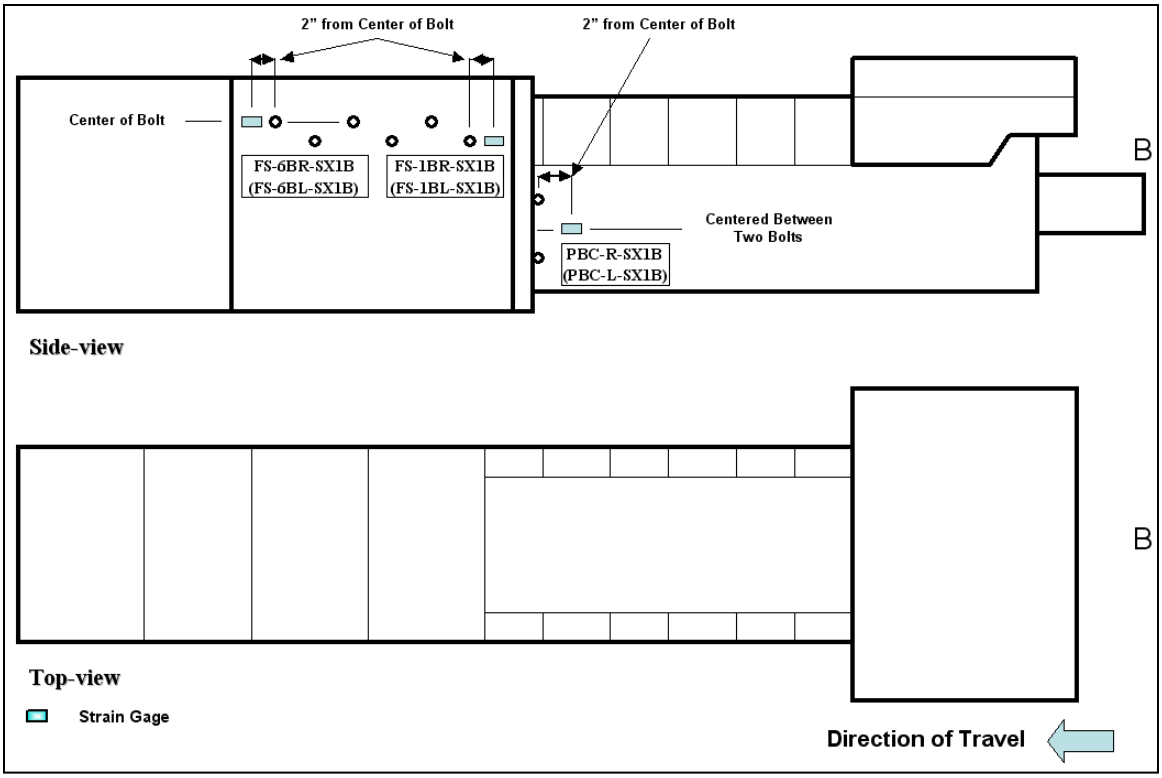

Figure B14. Strain Gauge Layout on Car 248 (Trailing) End Fixed/Sliding Sill

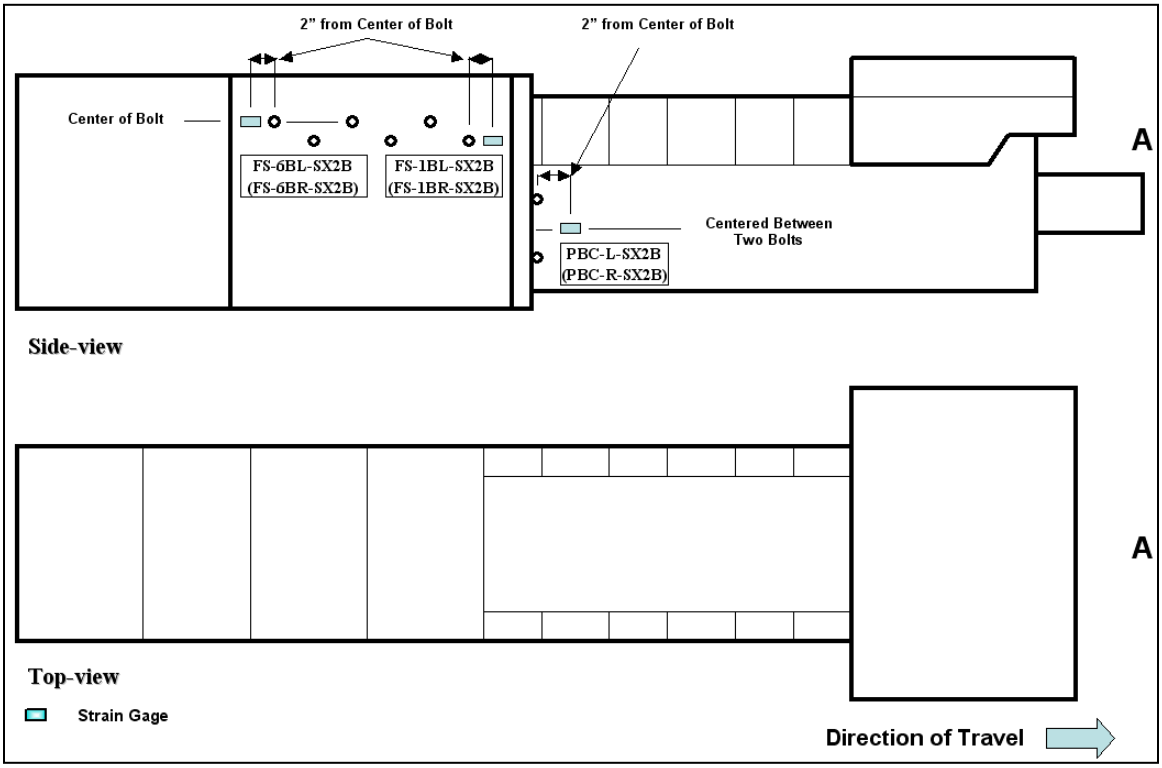

Figure B15. Strain Gauge Layout on Car 244 (Leading) End Fixed/Sliding Sill

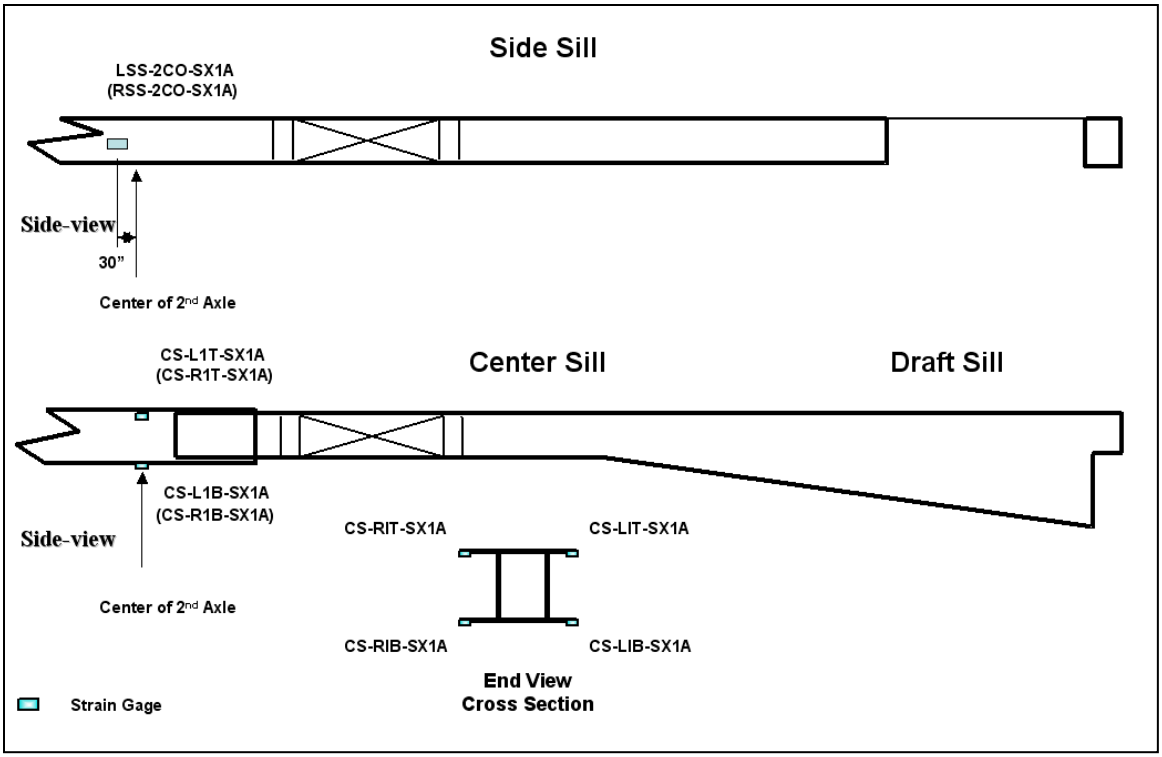

Figure B16. Strain Gauge Layout on Car 248 (Leading) Center and Side Sills

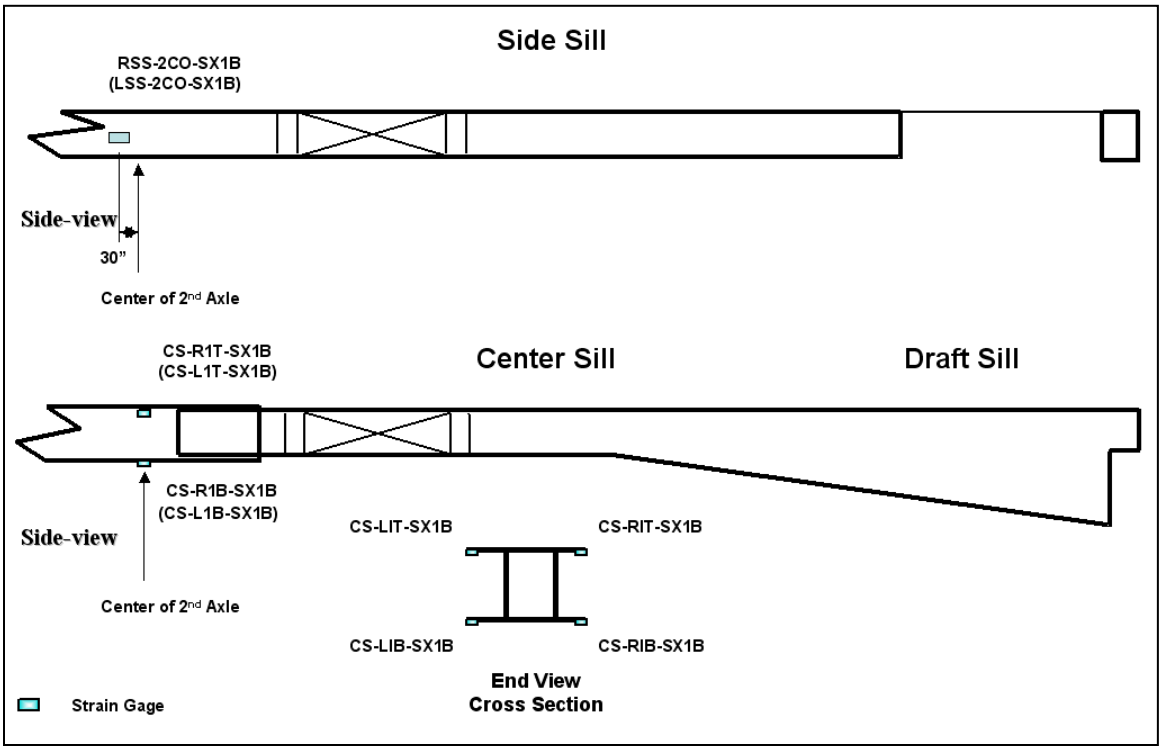

Figure B17. Strain Gauge Layout on Car 248 (Trailing) Center and Side Sills

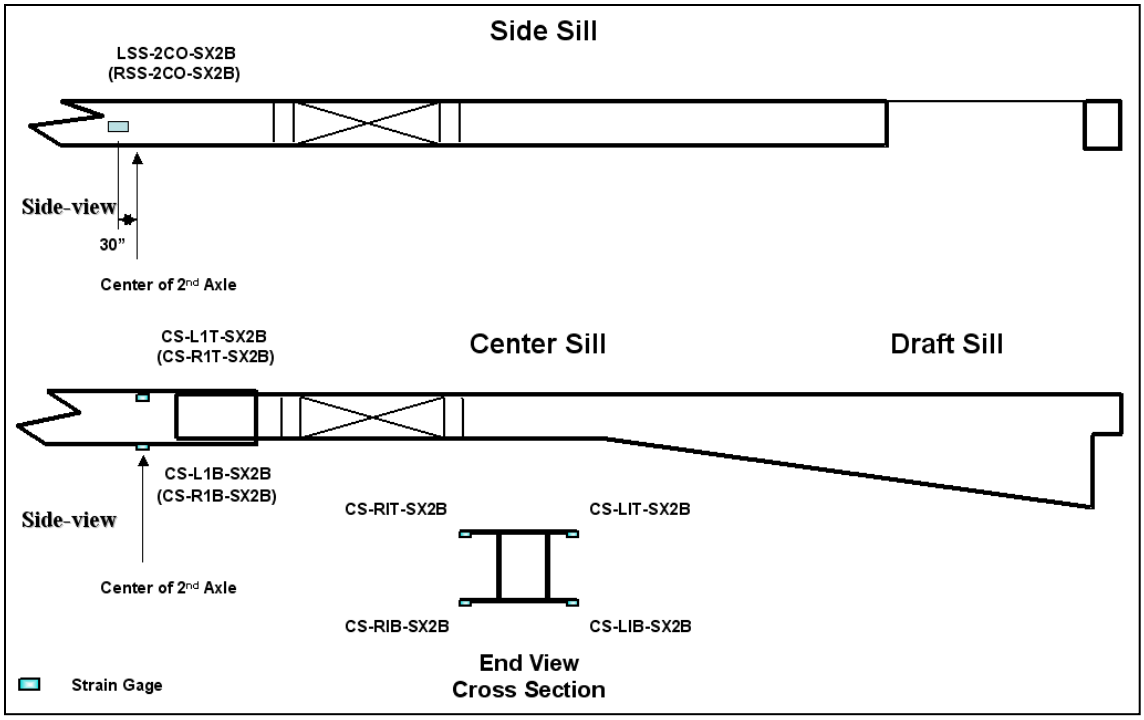

Figure B18. Strain Gauge Layout on Car 244 (Leading) Center and Side Sills

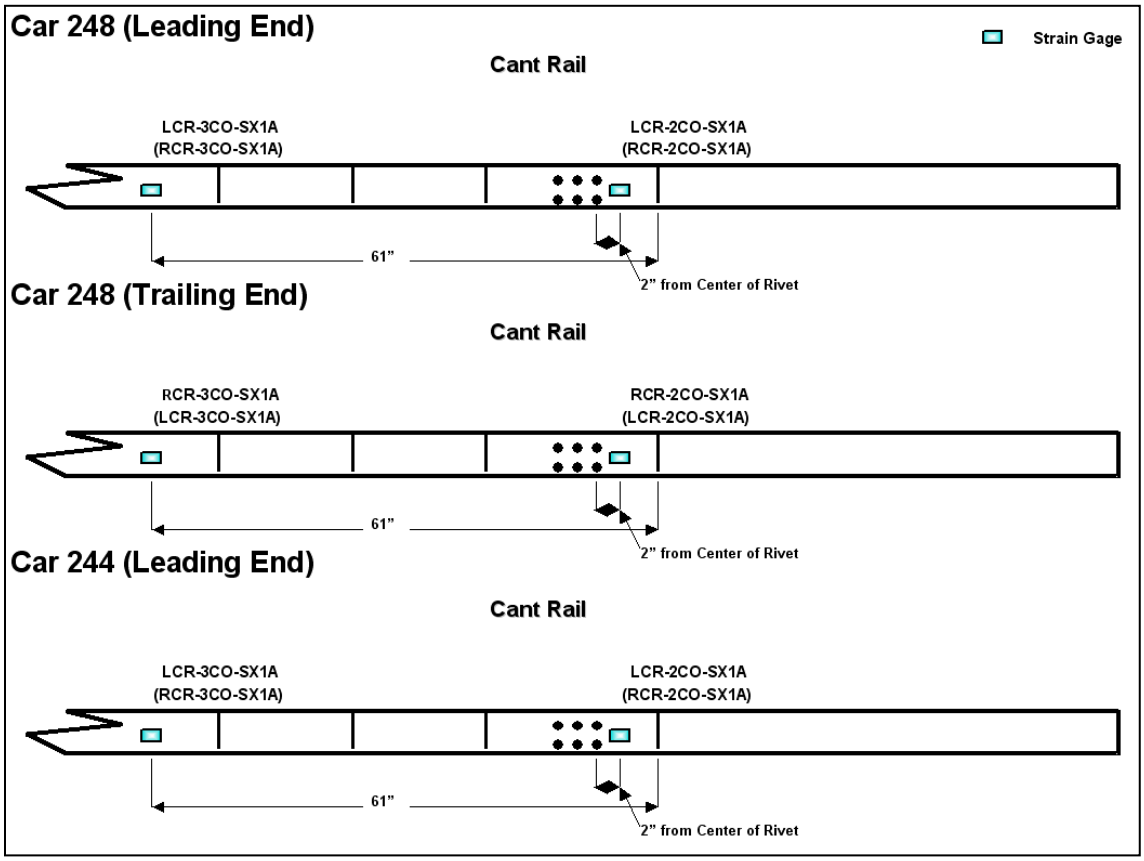

Figure B19. Strain Gauge Layout on Cars 248 and 244 Cant Rails

String Potentiometers

String potentiometers were used to measure differential movement between fixed and sliding components to assist in better assessing the degree of planar pushback of sliding components into fixed components. The information obtained from the differential displacements is helpful in developing the cross plot of force versus displacement between major assemblies. Longitudinal and vertical displacement was measured at 38 locations during the test. Eight string potentiometers were positioned to measure the vertical secondary suspension displacement, one on each side of each truck. Four string potentiometers were positioned to measure the longitudinal crush between the end frame of each car and the corresponding car body. Four string potentiometers were positioned on each crush zone. Table B4 lists the string potentiometers used on the two cars.

Table B4. Summary of String Potentiometers Used for Two-Car Test

Location	Orientation	Range	Channel Name	
			Leading Car	Trailing Car
Leading bogie, left Side, truck bolster to car body	Vertical	10” (±5”)	B1-L-DZ1	B1-L-DZ2
Leading bogie, right Side, truck bolster to car body	Vertical	10” (±5”)	B1-R-DZ1	B1-R-DZ2
Trailing bogie, left Side, truck bolster to car body	Vertical	10” (±5”)	B2-L-DZ1	B2-L-DZ2
Trailing bogie, right side, truck bolster to car body	Vertical	10” (±5”)	B2-R-DZ1	B2-R-DZ2
Car body to AT plate, left side	Longitudinal	50 (0 to 50”)	ATP-L-DX1A	ATP-L-DX2A
Car body to AT plate, right side	Longitudinal	50 (0 to 50”)	ATP-R-DX1A	ATP-R-DX2A
Car body to buffer beam, left side	Longitudinal	50” (0 to 50”)	BB-L-DX1A	BB-L-DX2A
Car body to buffer beam, right side	Longitudinal	50” (0 to 50”)	BB-R-DX1A	BB-R-DX2A
Car body to AT plate, left side, trailing end	Longitudinal	50” (0 to 50”)	ATP-L-DX1B	N/A
Car body to AT plate, right side, trailing end	Longitudinal	50” (0 to 50”)	ATP-R-DX1B	N/A
Car body to buffer beam, left side, trailing end	Longitudinal	50” (0 to 50”)	BB-L-DX1B	N/A
Car body to buffer beam, right side, trailing end	Longitudinal	50” (0 to 50”)	BB-R-DX1B	N/A
Sliding sill to coupler, top	Longitudinal	10” (0 to 10”)	PBC-T-DX1A	PBC-T-DX2A
Sliding sill to coupler, bottom	Longitudinal	10” (0 to 10”)	PBC-B-DX1A	PBC-B-DX2A
Fixed sill to sliding sill, top	Longitudinal	50” (0 to 50”)	SLS-T-DX1A	SLS-T-DX2A
Fixed sill to sliding sill, bottom	Longitudinal	50” (0 to 50”)	SLS-B-DX1A	SLS-B-DX2A
Sliding sill to coupler, top, trailing end	Longitudinal	10” (0 to 10”)	PBC-T-DX1B	N/A
Sliding sill to coupler, bottom, trailing end	Longitudinal	10” (0 to 10”)	PBC-B-DX1B	N/A
Fixed sill to sliding sill, top, trailing end	Longitudinal	50” (0 to 50”)	SLS-T-DX1B	N/A
Fixed sill to sliding sill, bottom, trailing end	Longitudinal	50” (0 to 50”)	SLS-B-DX1B	N/A
Coupler	Vertical	20” (0 to 20”)	CDZ1B	CDZ2A
Coupler	Lateral	20” (0 to 20”)	CDY1B	CDZ2A
Coupler	Longitudinal	20” (0 to 20”)	CDX1B	CDZ2A

Figures B20 through B22 show the vertical, lateral and longitudinal locations of the string potentiometers on the lead car (248). Figures B23 through B25 show the vertical, lateral and longitudinal locations of the string potentiometers on the trailing car (244). Figure B26 shows the inter-car string potentiometer layout.

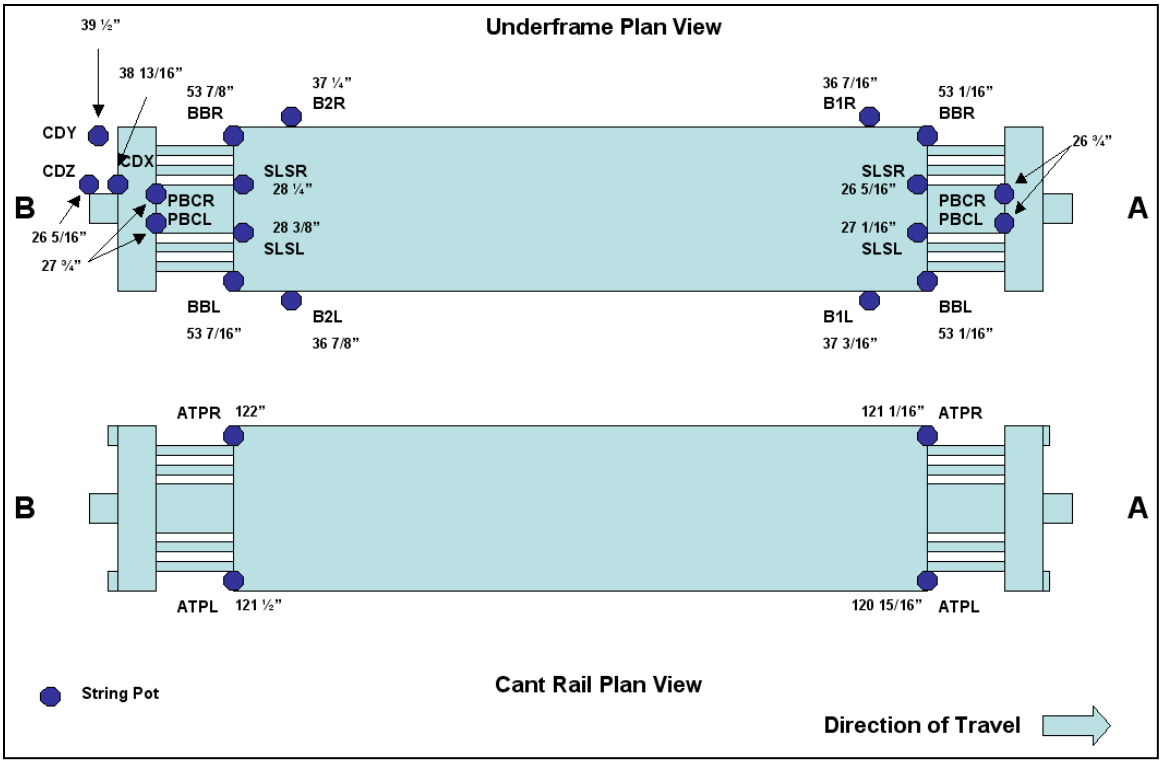

Figure B20. Vertical Location of String Potentiometers on Leading Car 248

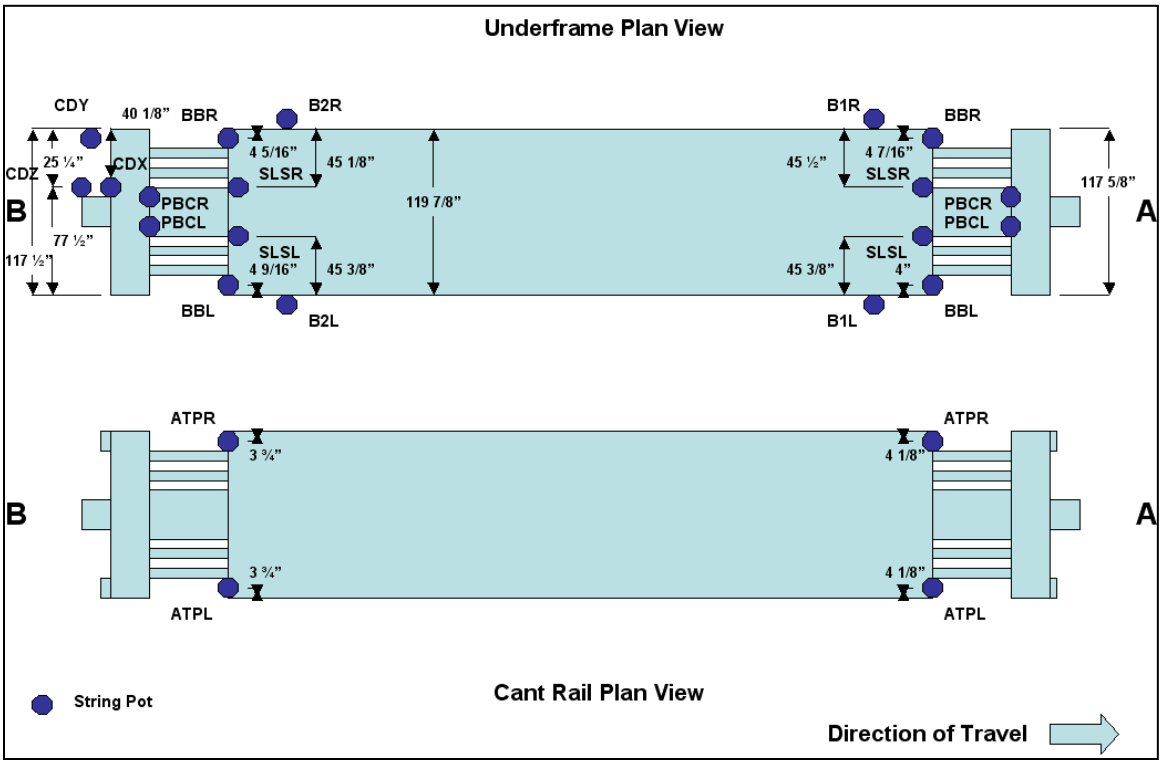

Figure B21. Lateral Location of String Potentiometers on Leading Car 248

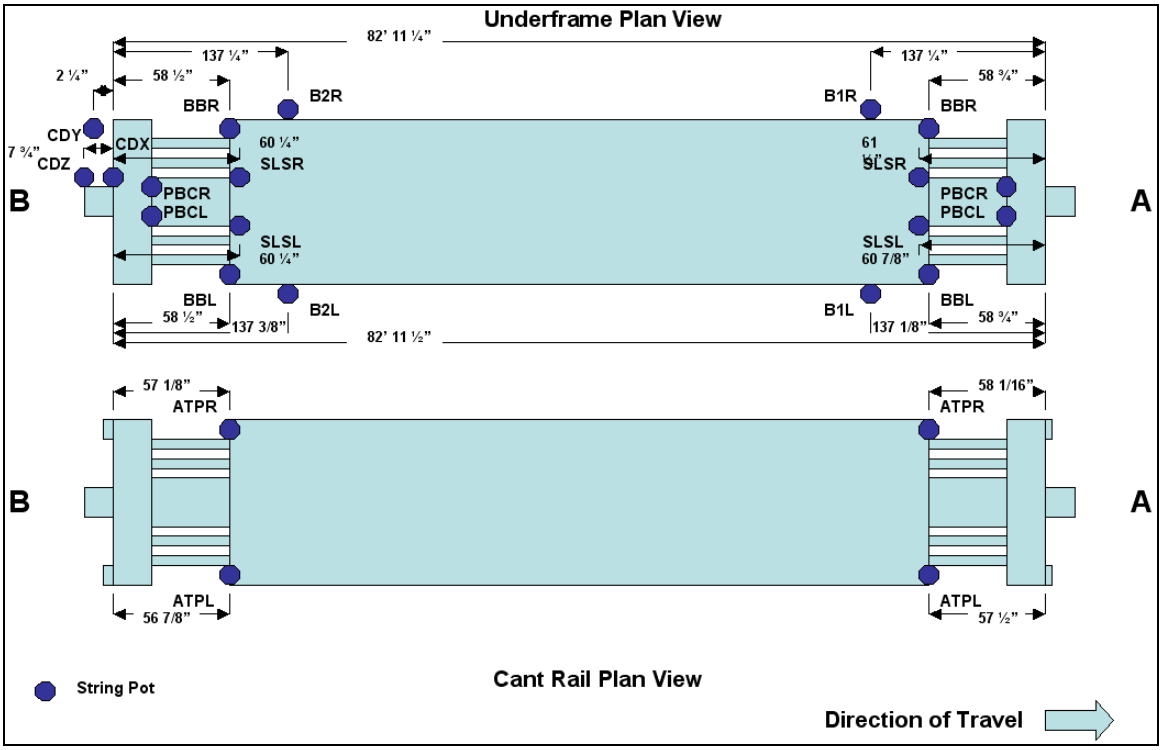

Figure B22. Longitudinal Location of String Potentiometers on Leading Car 248

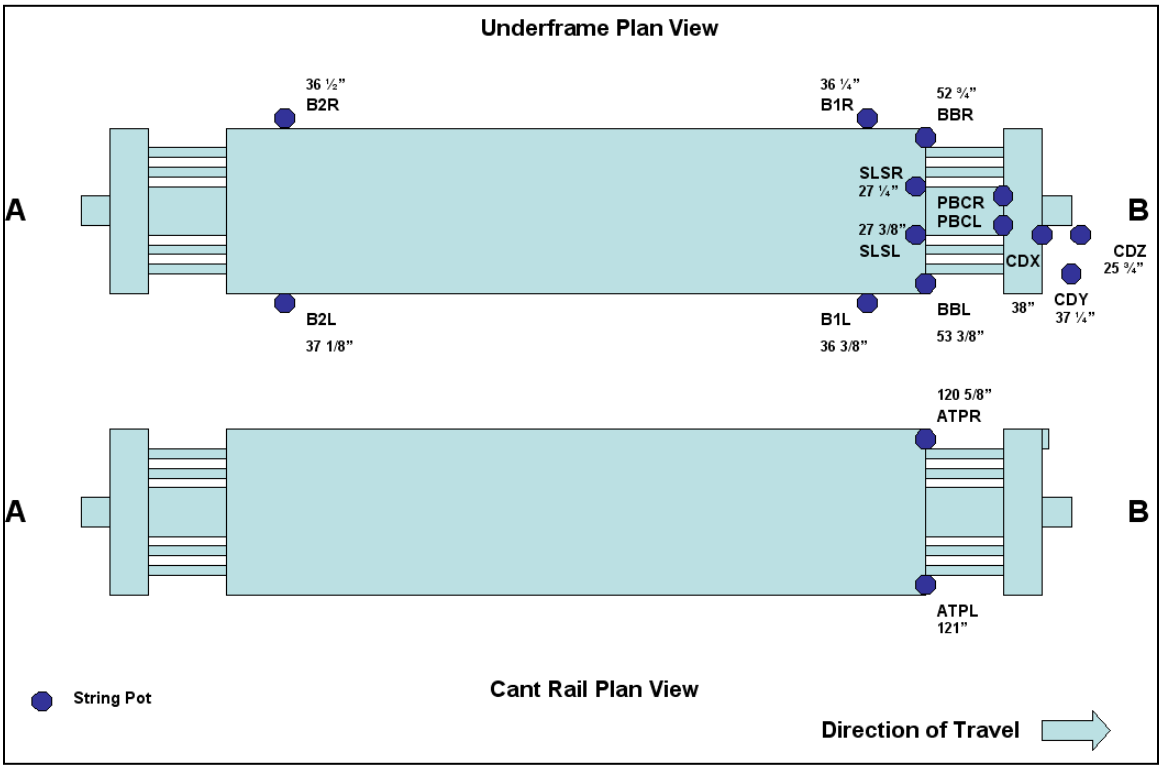

Figure B23. Vertical Location of String Potentiometers on Leading Car 244

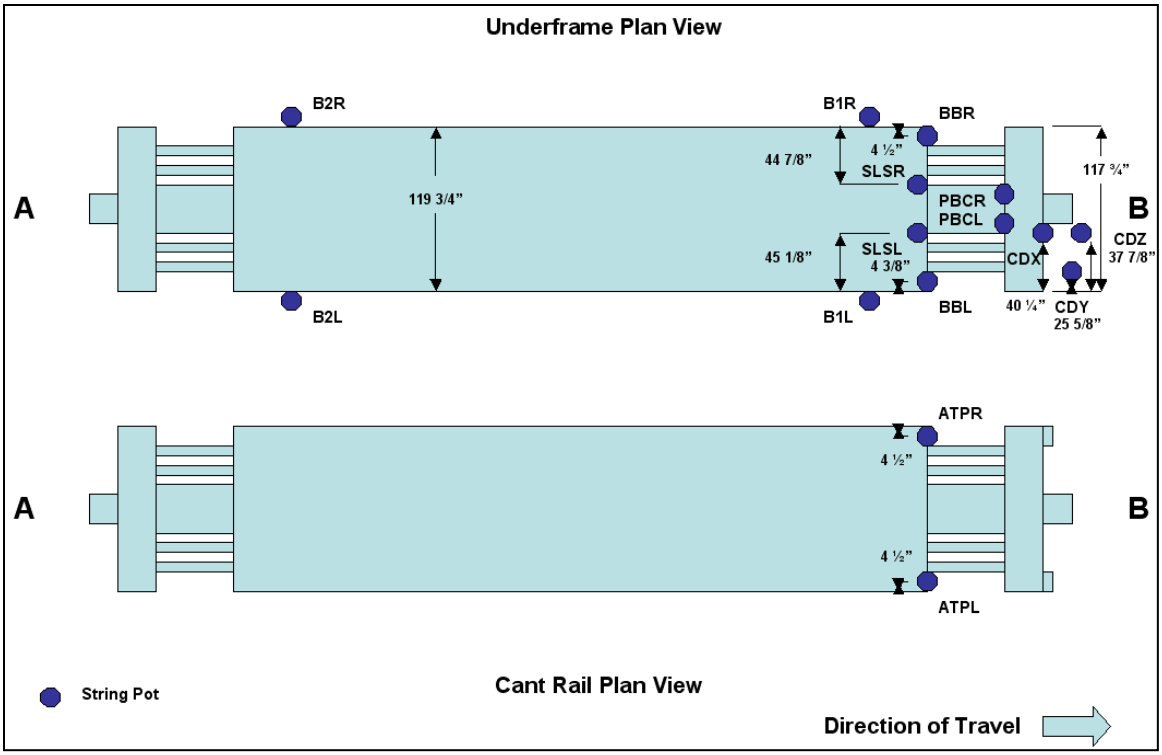

Figure B24. Lateral Location of String Potentiometers on Leading Car 244

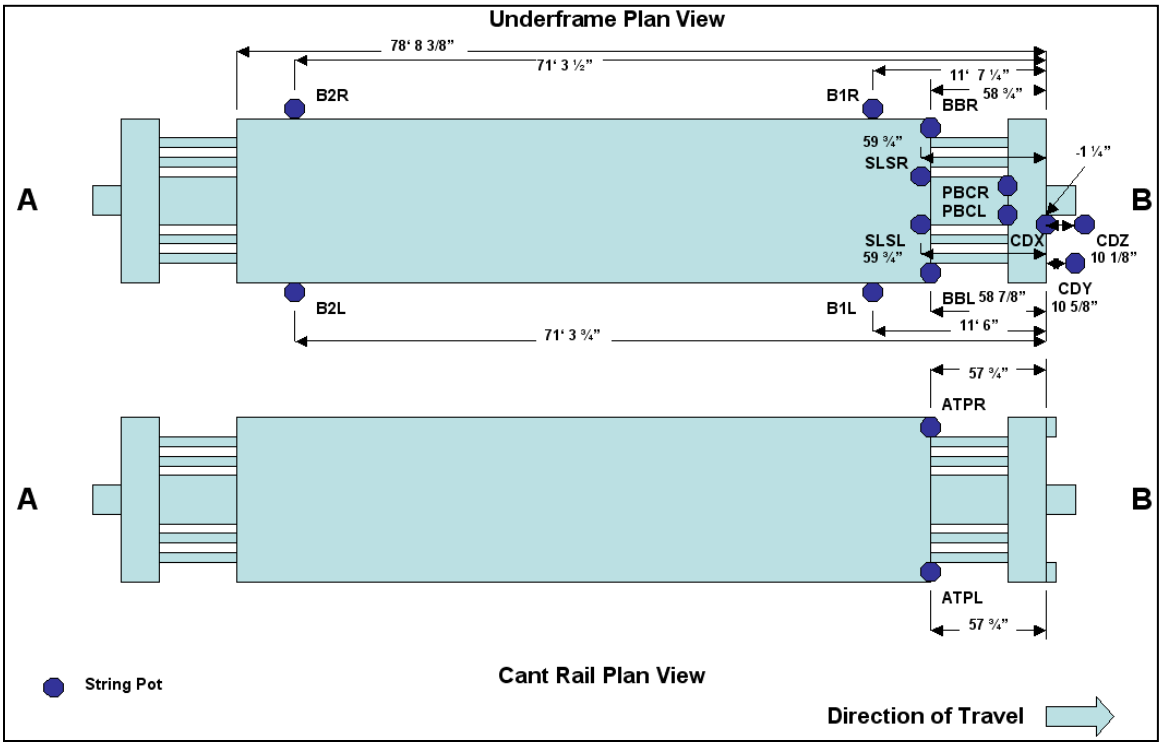

Figure B25. Longitudinal Location of String Potentiometers on Leading Car 244

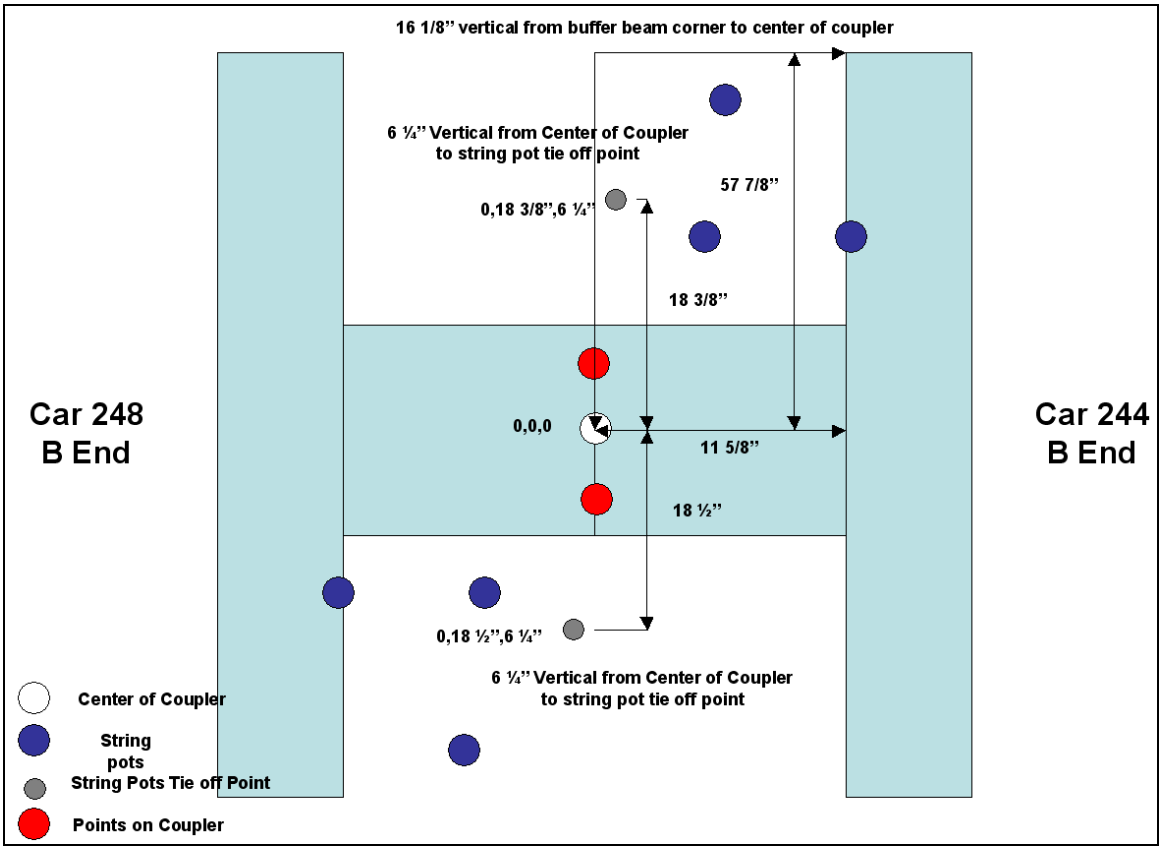

Figure B26. Inter-Car Location of String Potentiometers

High-Speed Cameras and Video

The high-speed film cameras and video cameras were used to provide post-test footage to better assess the timing of key events during the test. Thirteen high-speed film cameras and four video cameras were used to document the test. Figure B27 shows the positions of the cameras. A 100-Hz reference signal was placed on the high-speed film to assist in post-test film analysis. Targets were placed on the vehicles and on the ground to facilitate post-test film analysis to determine speed and displacement during the test. The targets are divided into four quadrants with adjacent colors contrasting to provide good visibility. Large diameter targets were used. Figure B28 schematically shows the locations of the targets on the lead car (248). Figure B29 depicts side view schematics of the locations of the targets used at the lead end of car 248. Figure B30 depicts the side schematics of the locations of the targets used on the trailing end of car 248. Figures B31 and B32 show the locations of the targets used for the trailing car 244.

Filming with the ground-based cameras was started manually. The cameras ran at nominal speeds between 300 and 500 frames per second for about 8 seconds before the 100-ft film reel was entirely exposed. Onboard digital cameras were used (see Appendix D).

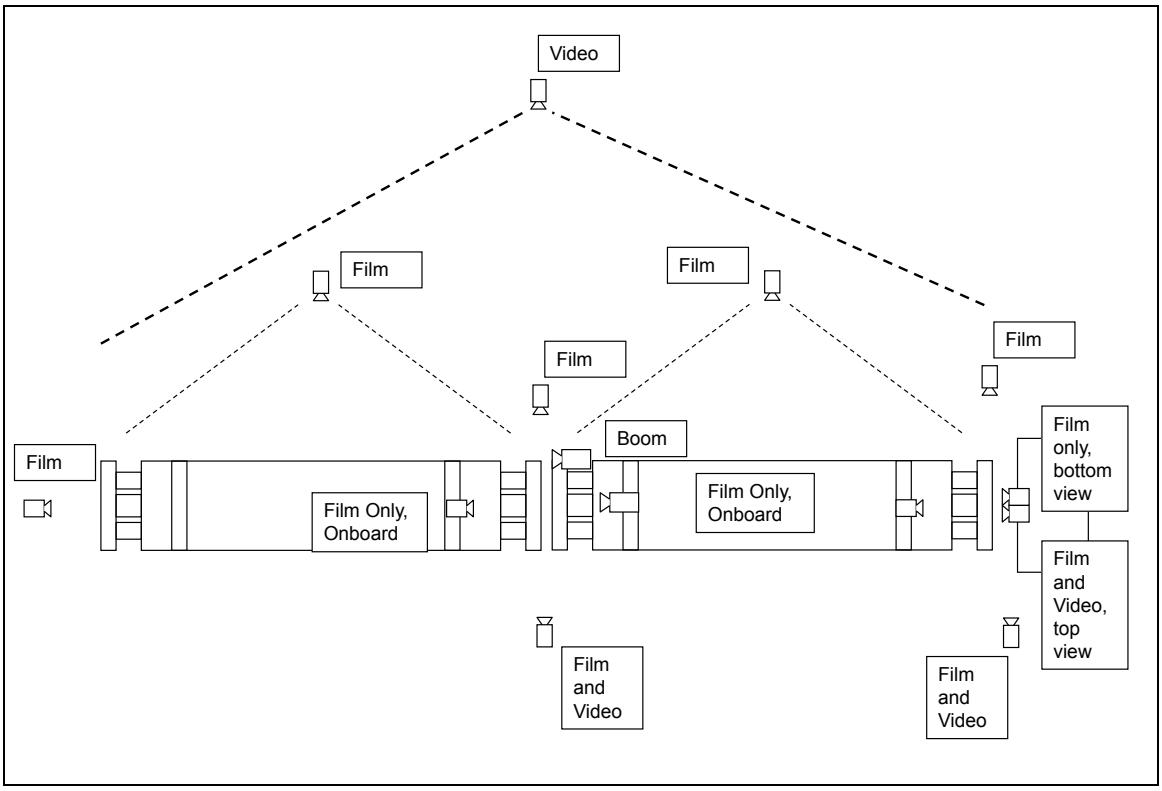

Figure B27. Schematic of Exterior Camera Locations

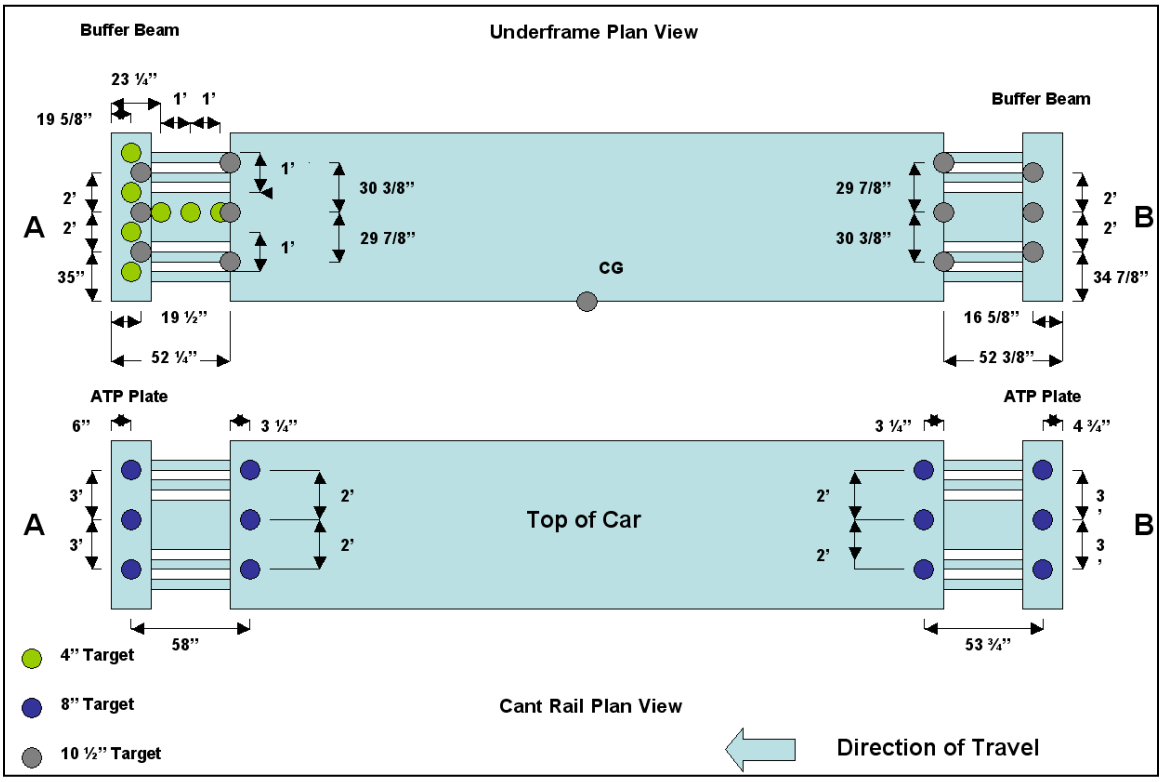

Figure B28. Top View of Target Locations on Lead Car 248

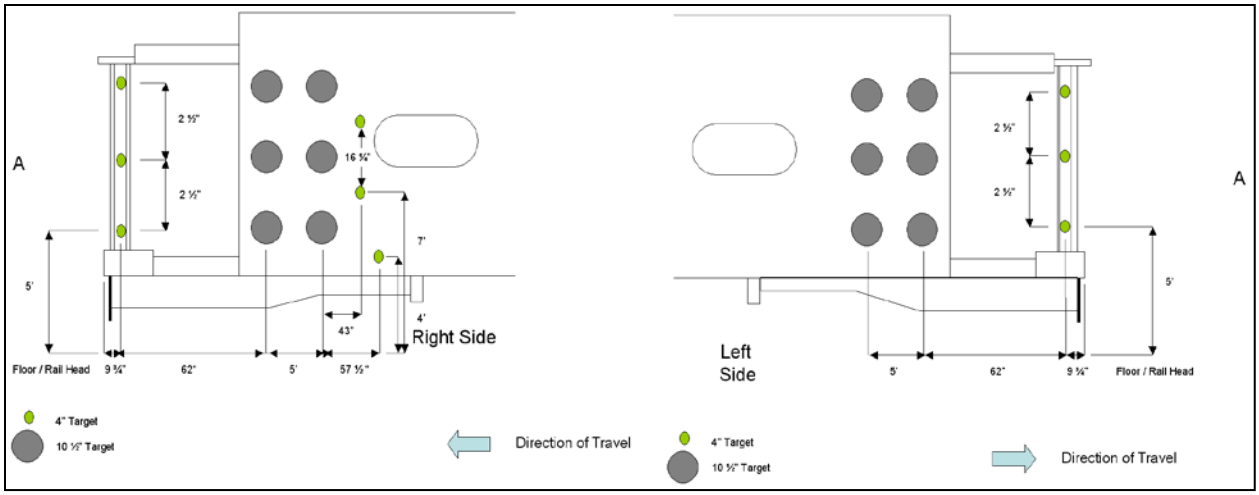

Figure B29. Side View of Target Locations on Test Lead Car 248: Lead End

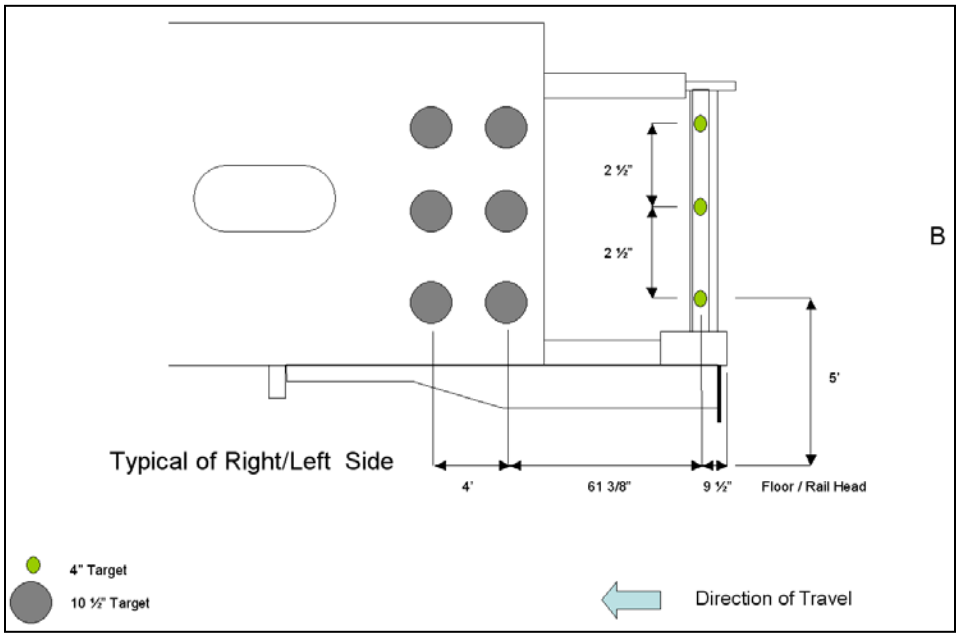

Figure B30. Side View of Target Locations on Test Lead Car 248: Trailing End

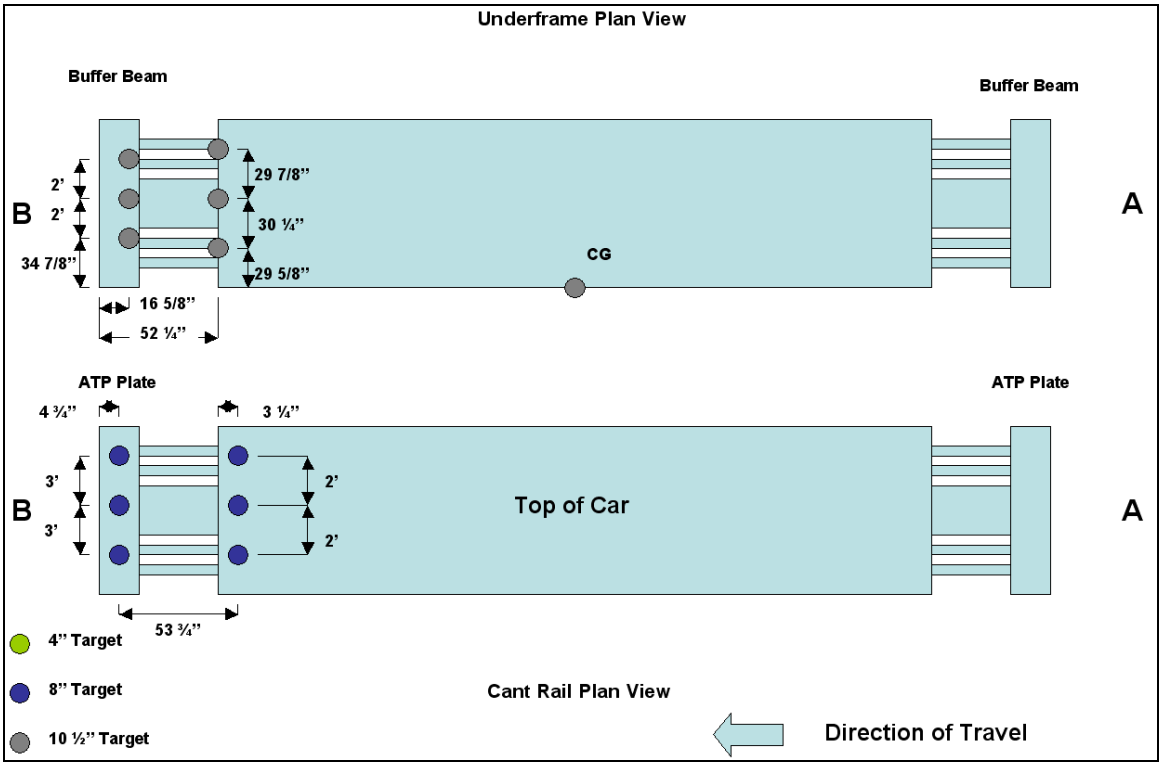

Figure B31. Top View of Target Locations on Car 244

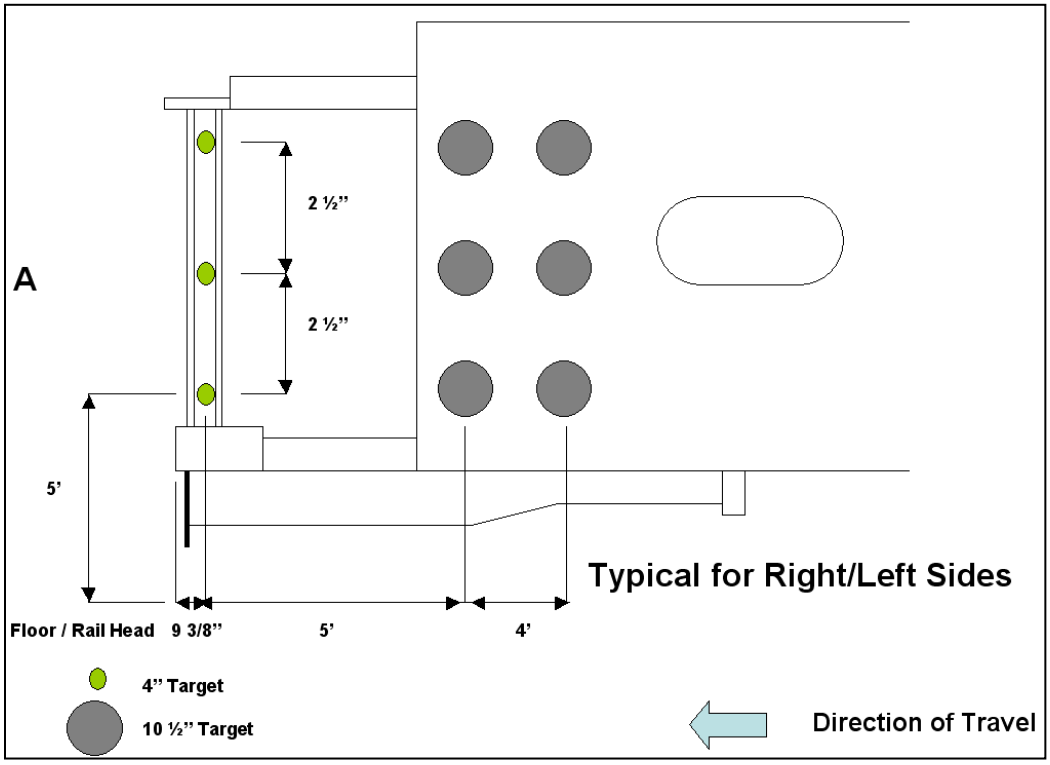

Figure B32. Side View of Target Locations on Car 244

Data Acquisition

The sample rate used for all the instrumentation was 12,800 Hz. A pre-sample filter was used, which was a low-pass corner frequency at 1735 Hz. The system was pre-triggered to record 12,800 samples prior to initial contact with the test wall. This equates to 1.0 seconds of pre-trigger data. A total of 51,200 samples were taken as the post-trigger data, which equates to 4.0 seconds of data.

Appendix C. Collision Dynamics Modeling

Single-Car Model Description

One-dimensional and three-dimensional models were developed to make pre-test predictions, determine initial conditions, specify instrumentation and evaluate the single car test results. This lumped-mass model simulates the gross motions of the coach car test vehicle and the longitudinal crush of the impacting interface. The collision dynamics model was developed using ADAMS software [29].

Initially, a one-dimensional model was used to predict the test results using an idealized composite force-crush characteristic to represent the intended structural behavior of the CEM crush zone (see Figure 4). The car body of the one-dimensional model was constrained to ground with a translational joint, which allows for movement in the longitudinal direction only. The model was expanded to represent the key components of the crush zone, while continuing to limit the bodies to longitudinal motions. This model was used to examine the forces required to activate each component in the crush zone. To further prepare for the single-car test, a three-dimensional model was developed, as shown in Figure B1 and described further below.

As shown in Figure C1, the model is a system of masses and springs that represent the key movements in the carbody in relation to the wall and ground. The trucks are restrained to move along the ground with a point-to-curve connection and transmit force in the vertical, lateral and longitudinal directions. The car body suspension is characterized by linear spring-damper connections for small displacements (+/-2 inches) with compression and tension forces and vertical and lateral gauges.

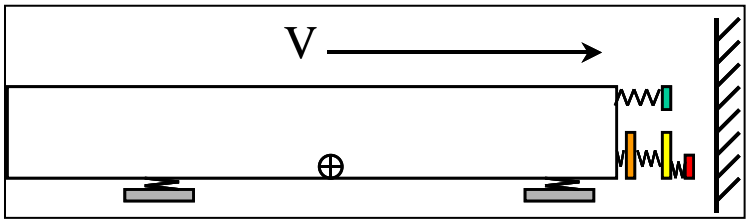

Figure C1. Single Car Lumped Mass Model Schematic

A series of masses and non-linear springs characterize the force-crush response of each of the key components in the crush zone: shearback coupler, sliding sill, roof absorbers, and the fixed sill. Characterizing each component of the crush zone provides estimates of the individual force contribution and dynamic behavior of each. The corresponding input parameters for each spring are shown in Figure C2.

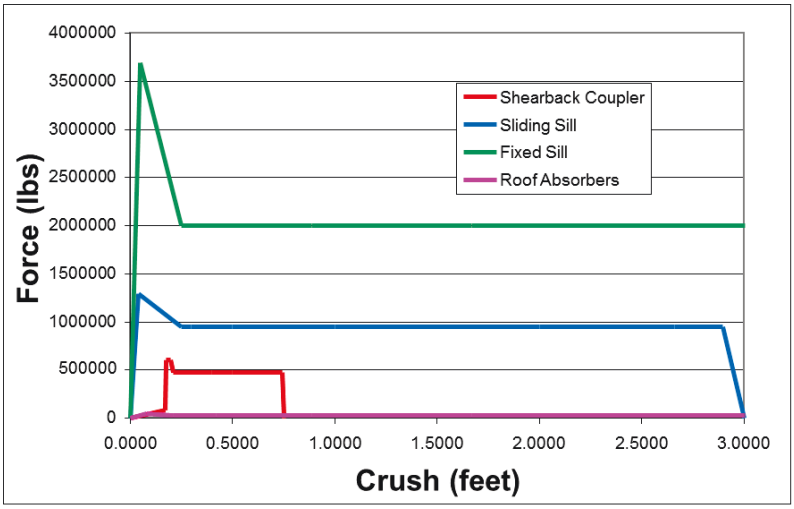

Figure C2. Component Force-Crush Characteristics

The combination of spring characteristics shown in Figure C2 defines the structural modes of deformation that the CEM coach car crush zone experiences during an impact. The composite force-crush characteristic is shown in the main body of the paper (see Figure 4).

A surface-to-surface impact force is activated when the coupler mass first contacts the rigid wall at its initial velocity. The impact stiffness and damping coefficients are 7.0E+07 lb/ft and 2.0E+04 lb/ft, respectively. The test vehicle weighed a total of 71,650 lbm and the individual mass properties for each body in the model are shown in Table C1. The vertical center of gravity of the carbody is located approximately one foot above the coach car floor height (approximately 5.25 feet above the top of rail).

Table C1. Vehicle Mass Properties

Property	Car Body	Truck	Coupler	Sliding Sill	Fixed Sill
Mass (lbm)	51,242	7,700	638	1,636	2,534
Centroidal Roll (lbm-ft^2)	9.67E+05	3.55E+04	41.4	4.2	4.2
Centroidal Pitch (lbm-ft^2)	2.22E+07	1.08E+05	26.1	4.1	4.1
Centroidal Yaw (lbm-ft^2)	2.25E+07	9.28E+04	26.1	1,734.0	1,725.0

Two-Car Model Description

The two-car model was developed from the single-car three-dimensional collision dynamics model. Crush zones were added to both car ends, and the two crush zones were mated by a simplified coupler connection. Figure C3 shows a schematic of the full model and a close-up of the coupled interfaces.

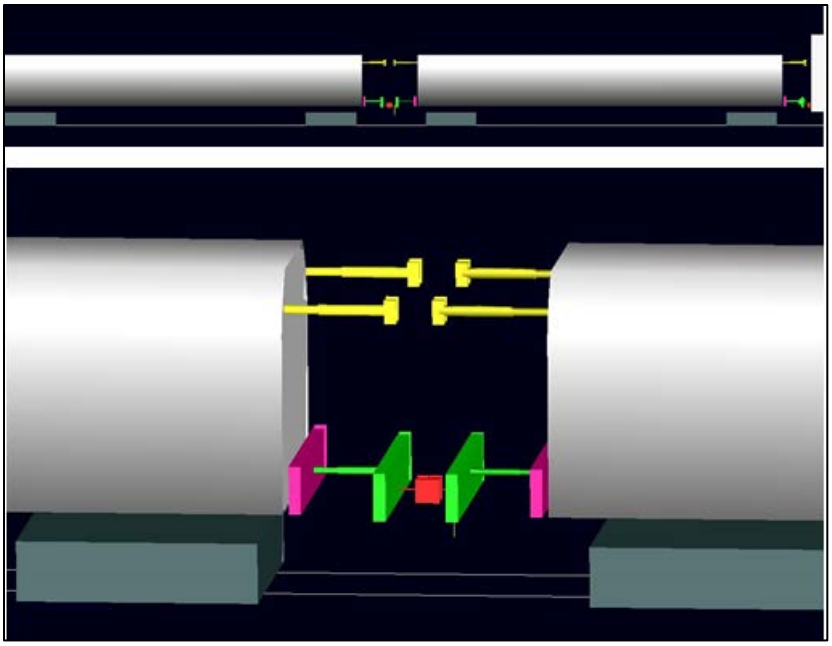

Figure C3. Schematic of Two-Car Three-Dimensional Model (Top) and Close-up of Coupled Ends (Bottom)

The test vehicles used in the two-car test each weighed approximately 75,000 lbm. Mass properties were the same as used in the single-car test, except the car body mass was 49,584 lbm, as a result of the different vehicle weights and crush zones retrofitted on both ends of each car (Table C2).

Table C2. Vehicle Mass Properties

Property	Car Body	Truck	Coupler	Sliding Sill	Fixed Sill	Roof Absorbers
Mass (lbm)	49,584	7,700	638	1,636	2,534	100
Centroidal Roll (lbm-ft^2)	9.67E+05	3.55E+04	41.4	4.2	4.2	41.4
Centroidal Pitch (lbm-ft^2)	2.22E+07	1.08E+05	26.1	4.1	4.1	26.2
Centroidal Yaw (lbm-ft^2)	2.25E+07	9.28E+04	26.1	1,734.0	1,725.0	26.2

Selected Results

Selected single-car and two-car test results are shown in Appendix D (Data Reduction) and Appendix E (Force-Crush Analysis).

Figure 14 shows the longitudinal car body motions predicted by the lumped-mass model. The model estimates the deceleration of the single coach car with very close agreement with the data from the accelerometers on the main car body. Key features of the impact are captured in this plot: initiation of the crush zone, deceleration of the car body and the overall collision energy.

As mentioned in the main body of the report, the CEM design limits the vertical and lateral motions. Vertical (pitch) and lateral (yaw) motions were negligible in comparison to the conventional test. Less than 2 inches vertically and 2 inches laterally fall within the allowable range of motion of the carbody suspension.

Appendix D. Data Reduction

Single-Car Test

Photometric Data

High-speed film was taken at different angles for the one car test. For the data shown here, a right-side view of the impacting end was used (Figure D1). This video was taken at a speed of 500 frames per second. When the photometric data was taken, the lower two points on the end frame, the car body and the wall were marked. The lower two markers were chosen because they are shown in the high-speed film, while the top markers are not shown. The data are initially collected in both the lateral and the vertical direction. Data were processed only for the lateral direction. To help correct for error, the lateral position of the two end frame markers at each time step was averaged, and the same was done for the lateral position of the wall and the car body. To correct for movements of the camera, the lateral position of the wall was subtracted from the lateral position of the end frame and car body. Once the positions of the end frame and car body were corrected for the wall, trendlines were used to smooth the data.

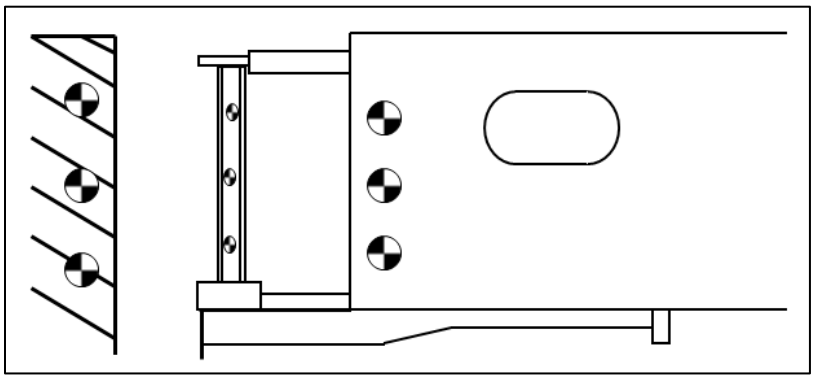

Figure D1. Right Side View of Impacting End

Accelerometer Data

The accelerometer data were taken from accelerometers mounted on the coupler, sliding sill and the car body. The accelerometer data are collected at a rate of 12,800 data points per second. The data were filtered using a Butterworth filter. The coupler data were filtered at a bandwidth of 1,000 Hz, while the car body and the end frame data were filtered at 100 Hz. The acceleration data are filtered, and integrated twice to get a displacement time history. The direction of the accelerometers was noted and verified as part of the installation and test set up. As needed, directions were verified with video and other data. The following graphs show the influence of the filter bandwidth on the measured coupler response. Additional graphs compare the data retrieved from the accelerometers with the photometric data.

Figure D2 shows the influence of the filter bandwidth. The results obtained using the 2,000 Hz, 1,500 Hz, and 1,000 Hz filters overlay one another. When the filter bandwidth is dropped to 750 Hz, the result is less accurate. For the coupler accelerometer data, 1,000 Hz is used as the cutoff frequency.

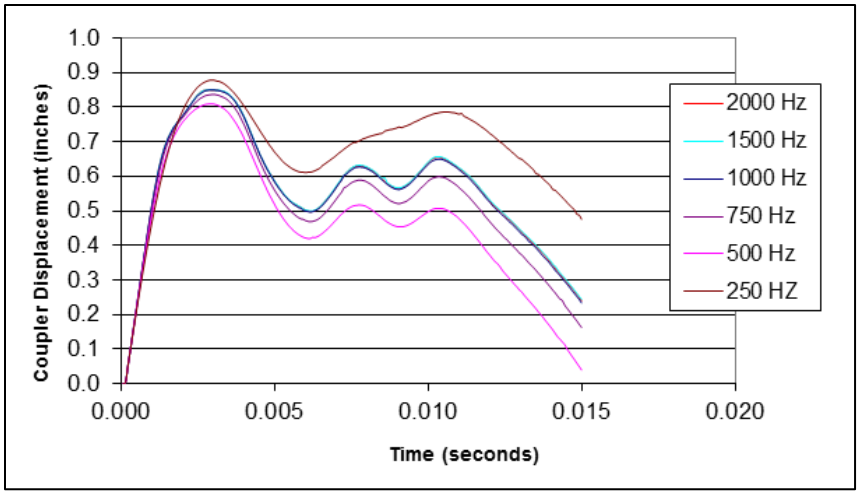

Figure D2. Influence of Filter Bandwidth on Accelerometer Results for Coupler Longitudinal Displacement

Figure D3 shows the position of the coupler, and Figure D4 shows the position of the end frame, with respect to time. The accelerometer data were filtered at 100 Hz. The photometric data match the accelerometer very well.

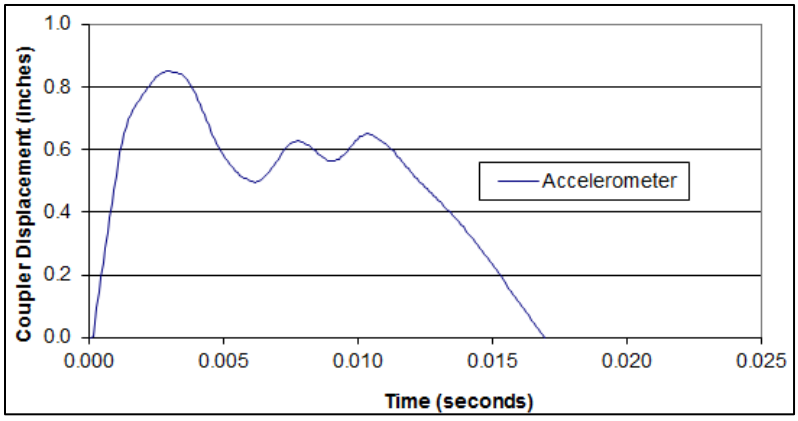

Figure D3. Coupler Longitudinal Displacement Time History

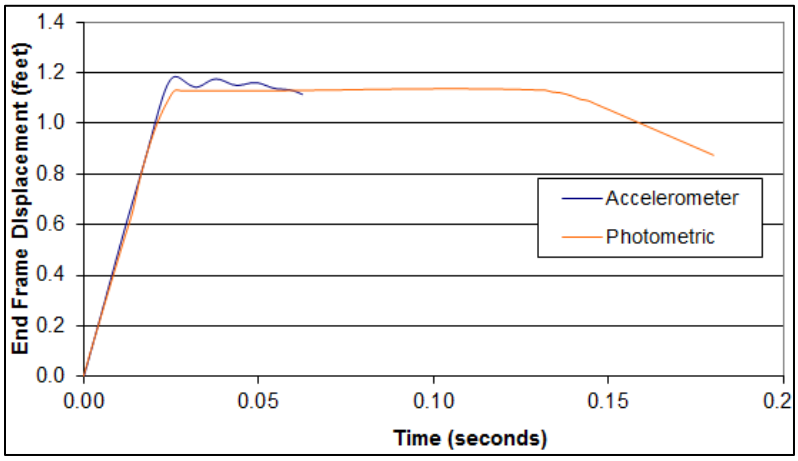

Figure D4. End Frame Longitudinal Displacement Time History

Figure D5 compares the position of the car body with respect to time for the accelerometer and photometric data. In this graph the photometric data match the accelerometer data closely.

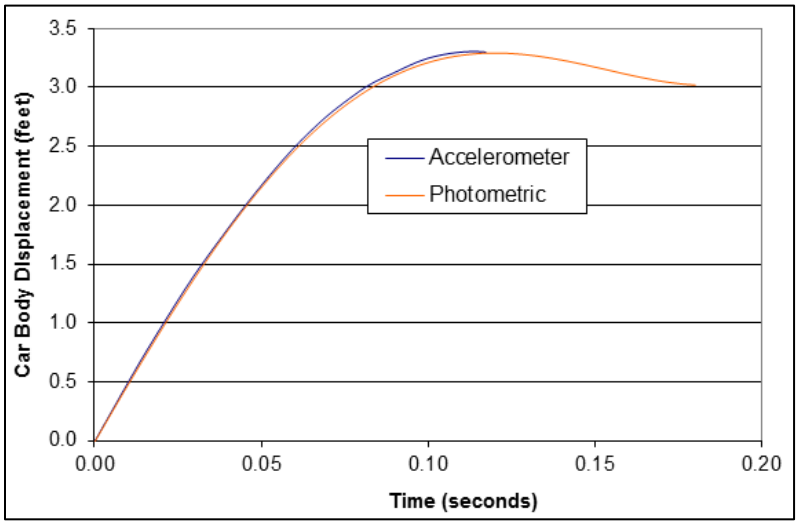

Figure D5. Car Body Longitudinal Displacement Time History

Two-Car Test

Photometric Data

High-speed film was taken at different angles for the two-car test. For the data shown here, a right side view of the impacting end was used, and a right side view of the collision between the cars was used(Figure D6). For the collision between the two cars, video was taken both from a side view and a top view. All the videos were taken at a speed of 1,000 frames per second. When the photometric data were taken, the lower two points on the end frames, the car bodies and the wall were marked. The lower two markers were chosen because they are shown in the high-speed film, while the top markers are not shown. The data are initially collected in both the lateral and the vertical directions. Data were processed only for the lateral direction. To help correct for error, the lateral position of the two end frame markers at each time step was averaged, and the same was done for the lateral the car body. To correct for movements of the camera, the lateral position of the wall was subtracted from the lateral position of the end frame and car body. Once the positions of the end frame and car body were corrected for the wall, trendlines were used to smooth the data.

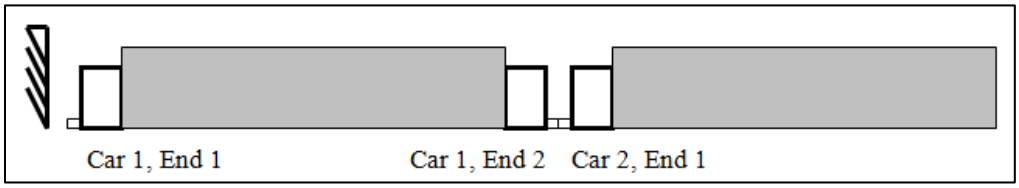

Figure D6. Schematic of Test, Elevation View of Left Side

Accelerometer Data

The accelerometer data were taken from accelerometers mounted on the couplers, sliding sills, and both car bodies. The data were filtered using a Butterworth filter. The coupler data were filtered at a bandwidth of 1,000 Hz, while the car body and the end frame data were filtered at 100 Hz. After filtering, it is integrated twice to get a displacement vs. time graph. The accelerometer data are collected at a rate of 12,800 data points per second. The following graphs compare the data retrieved from the accelerometers with the data taken photometrically.

Figure D7 shows the position of the first car body with respect to time. This graph has accelerometer data and two sets of results from the photometric data. The photometric data were adjusted to compensate for the delay between initial contact of the coupler with the wall and the display of the photo flash. The time of the photometric data was adjusted forward by 0.01 sec, and the displacement was moved forward 0.4 feet. 0.4 feet is the distance the car moved in 0.01 seconds with 29.3 mph velocity. Once the photometric data are adjusted, they match the accelerometer data. In this graph, the car body moves forward 3.25 feet after the coupler hits the wall. This accounts for the crush of the coupler and the end frame.

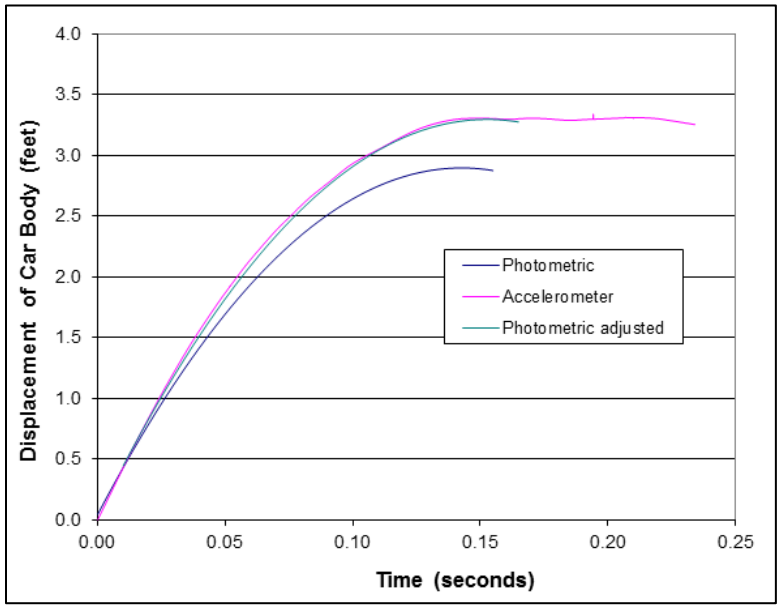

Figure D7. Position of the First Car Body with Respect to Time

Figure D8 shows the displacement of the end frame on the front end of the first car with respect to time. Once again, the photometric data were adjusted for a time delay of 0.1 second and a displacement of 0.4 feet. Once this adjustment is made, the photometric data match the accelerometer data. Once the coupler hits the wall, the end frame moves forward approximately 1.1 feet and comes to a gauge.

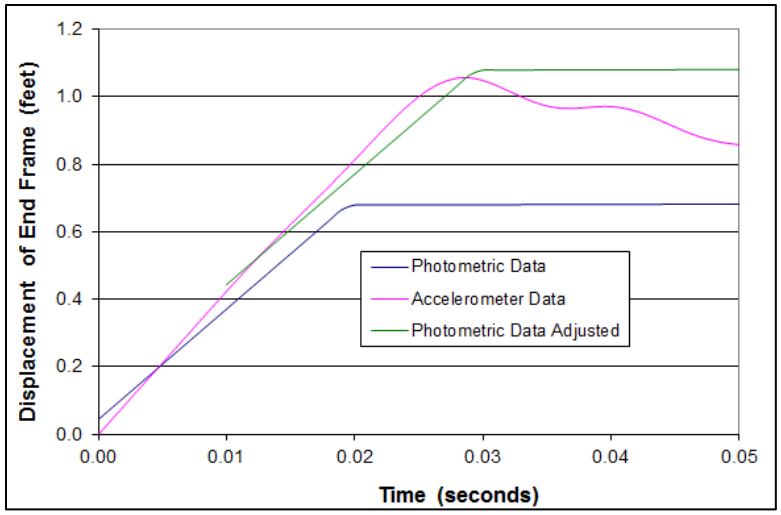

Figure D8. Position of the End Frame, at Car 1 and End 1, with Respect to Time

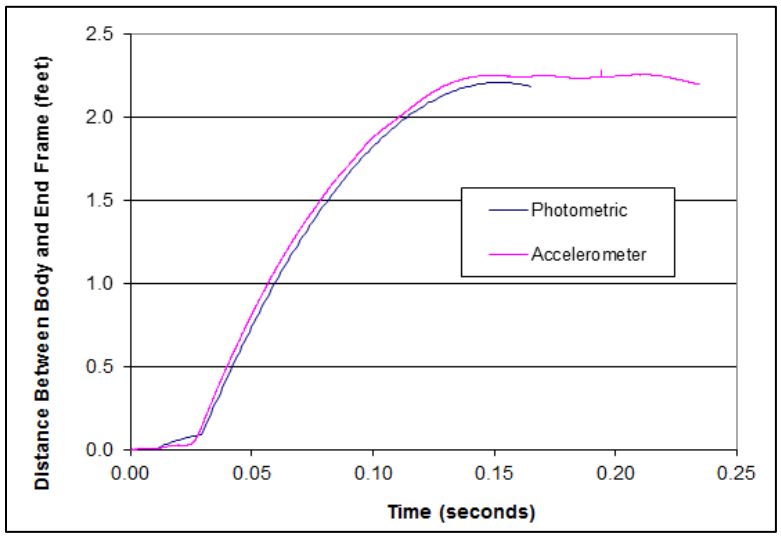

Figure D9. Relative Displacement Between the First End Frame and the First Car Body

Figure D10 shows the relative displacement between the two car bodies. Again, the photometric data starting point has been adjusted. This change in displacement accounts for the crushing of the two couplers and the two end frames at the second interface.

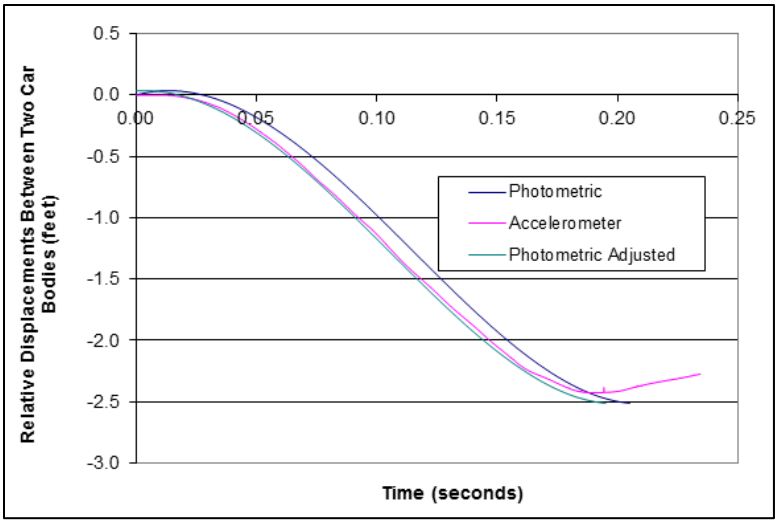

Figure D10. Relative Displacements of the Two Car Bodies with Respect to Time

Appendix E. The Crash Zone Force/Crush Characteristic

Introduction

One challenge to be addressed in processing the test measurements into a force/crush characteristic is that there is significant overlap in frequency of the acceleration signals and noise. The kinematics of the crush zone, with the pushback coupler and primary energy absorber trigger mechanism, introduces much noise. These trigger or initiation mechanisms closely approximate delta functions for the force acting on the car, and ring the car structure to which the accelerometers are mounted.

The force/crush characteristic has been developed in segments from the test measurements based on the kinematic behavior of the crush zone. During the test, the coupler first pushes back on the draft gear. After the gear bottoms out, the shear bolts of the pushback coupler mechanism are loaded, and then shear. The energy absorber of the shearback coupler then crushes until the coupler is pushed back and the load into the wall is now reacted by the end frame. The shear bolts of the primary energy absorber and the shear rivets of the roof absorbers are now loaded, until they shear. The roof and primary energy absorbers then crush, until the car rebounds from the wall.

The idealized force/crush characteristic was developed in segments. The timing of the shear-back coupler and sliding sill fuses was determined from strain gauge measurements in the vicinity of the respective shear-bolts. This timing was then used to determine the crush at which the shear back coupler and sliding sill triggered.

The shear-back coupler energy absorber and primary/roof energy absorber force/crush characteristics were assumed to be flat, i.e., straight lines on the force/crush characteristic. The straight line assumption was made because that was the design target and because the one-dimensional model is not sensitive to short-wavelength variations. The draft gear characteristic was assumed to be a linear spring, with 40 kips of force at 3.5 inches of travel. These values are based on information from the manufacturer.

Crush Zone Force/Crush Characteristic

Figure E1 shows the idealized force/crush characteristic for the coach car crush zone, based on the test data. Used as input to a one-degree-of-freedom model, this force crush curve closely reproduces the displacement and velocity time histories of the carbody, and approximates the acceleration time histories for the measurements made during the single-car and two-car tests of CEM equipment.

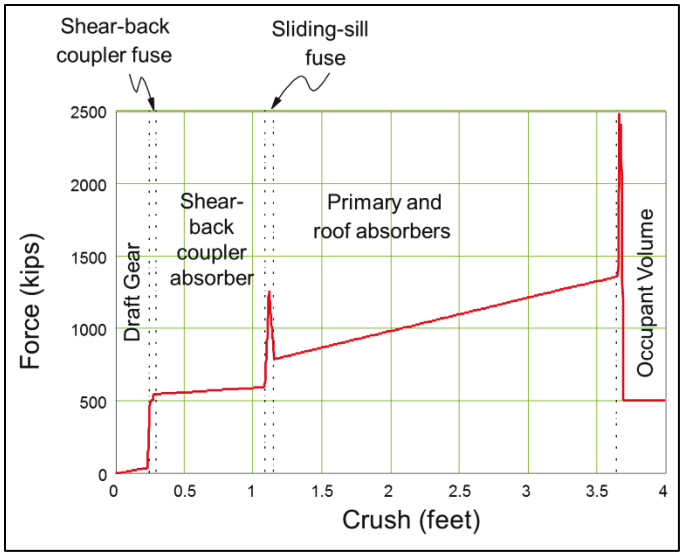

Figure E1. Idealized CEM Force/Crush Characteristic

Shear-Back Coupler and Sliding Sill Fuses

Figure E2 shows the measurements made by the strain gauges on the left and right side of the sliding sill, approximately 1.5 inches ahead of the shear bolts for the buff lug. Time zero corresponds with the coupler first contacting the wall. About 0.003 seconds after the coupler first contacts the wall, an increase in the measured strain is recorded. This change in strain indicates that the shear bolts have failed. The car has traveled approximately 2 inches since the coupler first contacted the wall.

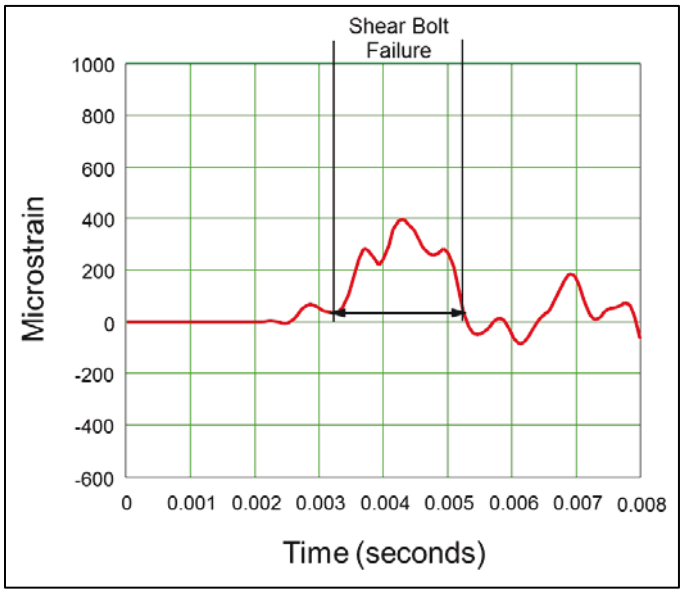

Figure E2. Strains in Sliding Sill Near Shear-back Coupler Fuse Bolts

Figure E3 shows the average strain in the fixed sill just ahead of the fuse bolts, from two strain gauges on the right side and two strain gauges on the left side. The change in strain caused by the triggering of the shear-back coupler fuse bolts can be seen at approximately 0.0035 seconds. The change in strain caused by the triggering of the sliding sill fuse bolts can be seen at approximately 0.023 seconds. The car has traveled approximately 13.5 inches since first contacting the wall.

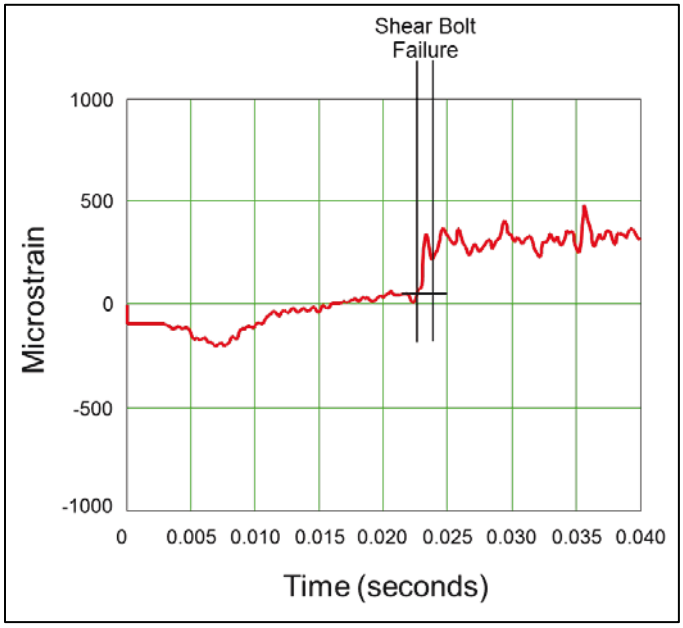

Figure E3. Strains in Fixed Sill Near Sliding-Sill Fuse Bolts

The energy absorber of the pushback coupler crushed during the time period from 0.006 seconds to .023 seconds. At 0.006 seconds, the sliding sill and car have travelled 0.27 feet toward the wall, from initial contact of the coupler with the wall. At 0.023 seconds the sill and car have travelled 1.10 feet toward the wall. The draft gear has reached its maximum excursion toward the wall before 0.006 seconds, so that the crush in the pushback coupler energy absorber is the difference in position of the sliding sill at these two points in time. Figure E4 shows the pushback coupler energy absorber crush force calculated from the test measurements and the idealized pushback coupler crush force. The force is idealized as a straight line, computed as a least-squares best fit. The force is approximated as a straight line because this was the design target and the one-dimensional model is not sensitive to the short wavelength variations.

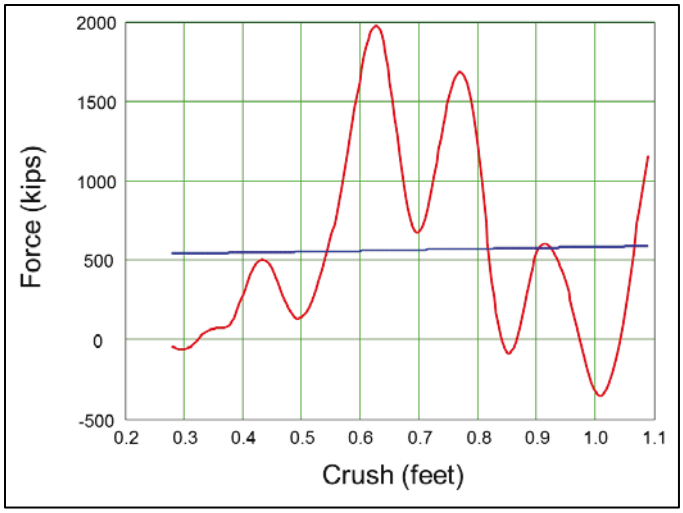

Figure E4. Measured and Idealized Force from Crush of Pushback Coupler Energy Absorber

Primary Energy Absorber

The energy absorber of the pushback coupler crushed from 0.024 seconds to 0.120 seconds. At 0.024 seconds, the carbody has travelled 1.15 feet toward the wall, from initial contact of the coupler with the wall. At 0.120 seconds the carbody has travelled 3.29 feet toward the wall. The sliding sill has reached its maximum excursion toward the wall by 0.024 seconds, so that the crush in the energy absorbers is the difference in position of the carbody relative to the wall. Figure E5 shows the energy absorber force calculated from the test measurements and the idealized energy absorber crush force. The force is idealized as a straight line, computed as a least-squares best fit.

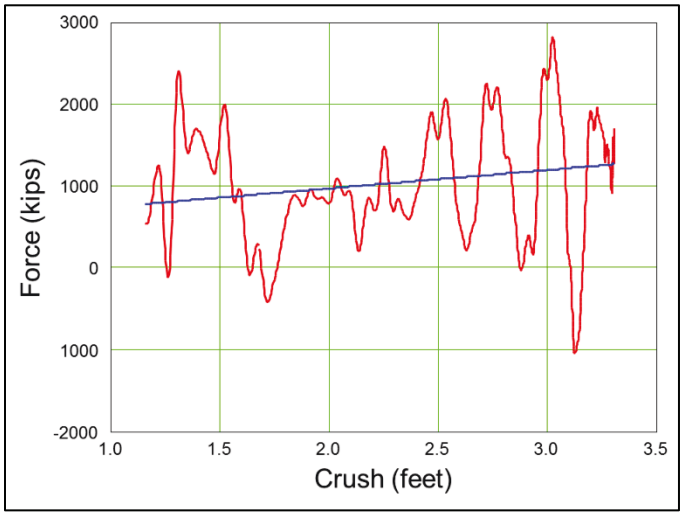

Figure E5. Measured and Idealized Force from Crush of Primary and Roof Energy Absorbers

One-Dimensional Single Degree-of-Freedom Model

Figure E6 shows a one-dimensional single degree-of-freedom model of the coach cars impacting the wall. For this model, the car is assumed to act as a single mass, including the trucks and all of the carbody. During the test, the coupler and end frame decelerate at a greater rate than the carbody; however, this difference is neglected in this model. The coupler and end frame account for about 3 percent of the car mass. The overall error in this approximation is estimated to be about half the mass percentage.

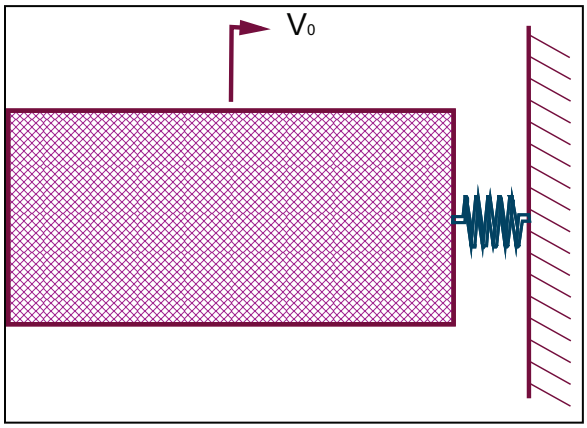

Figure E6. One-Dimensional Single Degree-of-Freedom Model

Acceleration Time-History

Figure E7 shows the deceleration time history for the car, and includes the test measurement and model prediction. The test measurement was made with accelerometer R3-X, located on the right side sill near the longitudinal center of the car. (Appendix B includes schematics and photos of this and other accelerometers.) Both the test measurement and the model result were filtered with the SAE CFC 300 filter. Such a simple model cannot capture the high-frequency details of the signal measured during the test, but it does capture the low-frequency features. The test measurement signal has a strong component at approximately 80 Hz. This component is likely due to carbody vibrations. The model result does not include rebound from the wall. During the test, the car rebounded off the wall at a speed of approximately 4 mph.

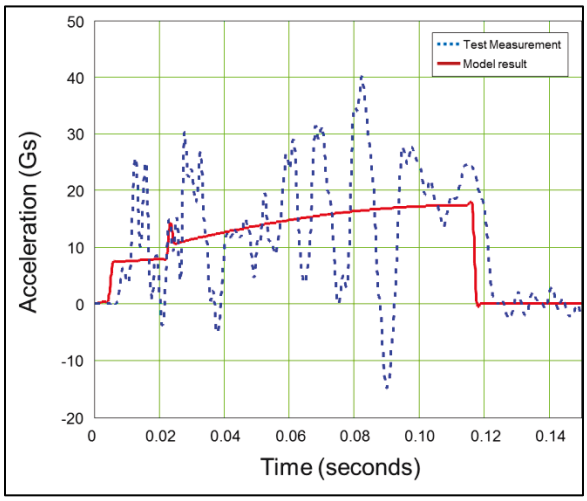

Figure E7. Car Acceleration Time History, Test and Model Results

Figure E8 shows the velocity time history for the car, including the test measurement and model prediction. The test results are calculated from accelerometer R3-X and from motion-analysis of the high-speed film. (See Appendix D for other results from high-speed film analysis.) Although the model does not capture the fine details of the acceleration time history, it does closely capture the velocity time-history. The model does not include rebound. During the test, the car rebounded off the wall at a speed just less than 4 mph.

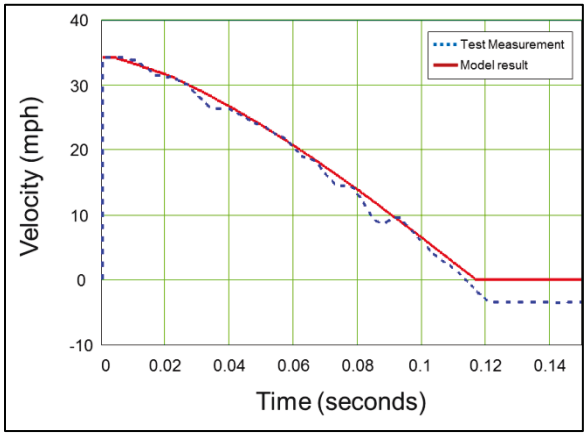

Figure E8. Car Velocity Time History, Test and Model Results

Displacement Time Histories

Figure E9 shows the car's displacement time history, again with model and test results. The model and test results are nearly identical from zero up to the maximum displacement. After the maximum displacement, the test results decrease, owing to the rebound of the car from the wall, which is not accounted for in the model.

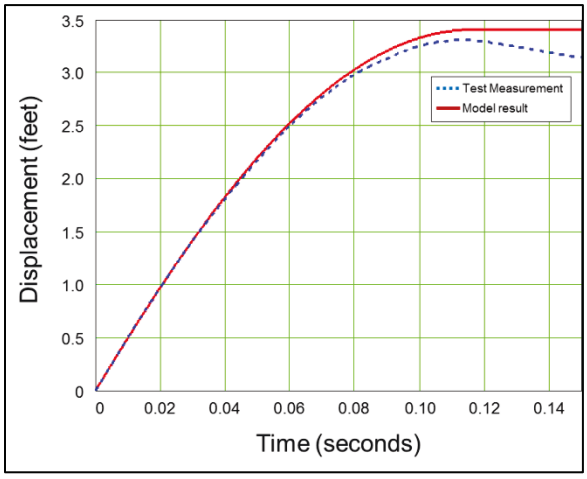

Figure E9. Car Displacement Time History, Test and Model Results

Force

Figure E10 shows the force acting on the wall, as calculated from the carbody acceleration. Time histories from both test measurements and model results are shown. Both model results and test

measurements were filtered with a CFC 300 filter. For a short distance at about 3.2 feet, the force calculated from the measurements is negative.

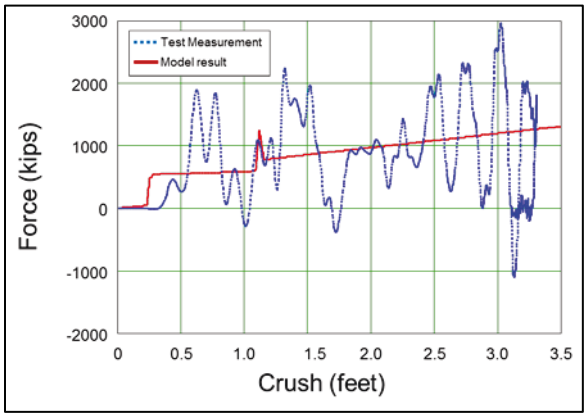

Figure E10. Force/Displacement Characteristic, Calculated from Test Measurements and Model Results

One-Dimensional Three Degree-of-Freedom Model

Figure E11 shows the one-dimensional three degree-of-freedom model. Figure E6 (above) shows a one-dimensional single degree-of-freedom model of the coach car's impact with the wall. For this model, the car is assumed to act as three masses: a coupler mass, a sliding sill and end frame mass, and a mass representing the carbody and trucks. The individual accelerations of the coupler and end frame are accounted for in this model.

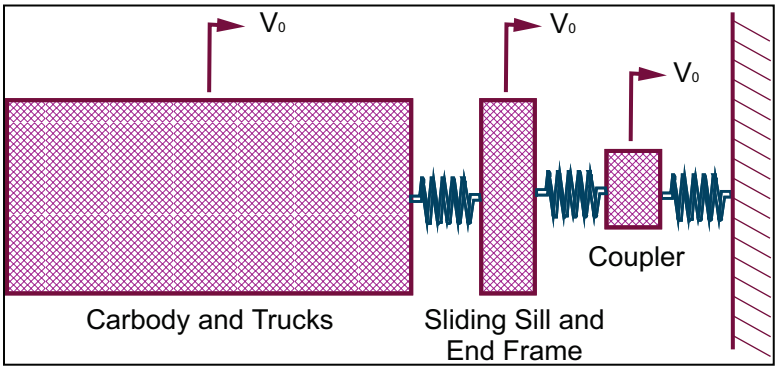

Figure E11. One-Dimensional Three-Degree-of-Freedom Model

Figure E12 shows the force displacement characteristics acting between the wall and the coupler mass, between the coupler and sliding sill and end frame masses, and between the sliding sill and end frame and the carbody and truck masses. These force/crush characteristics are the components that make up the composite force/crush characteristic shown in Figure E1.

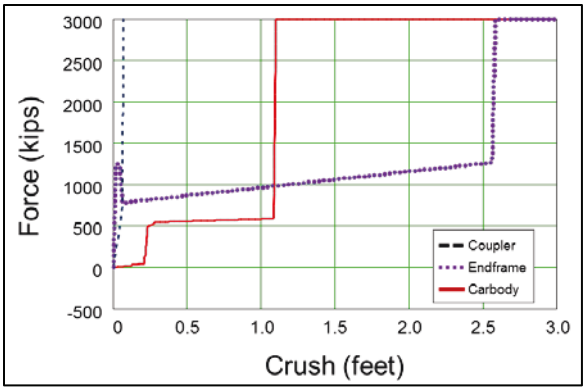

Figure E12. Component Force/Crush Characteristics for Three-Degree-of-Freedom Model

Acceleration Time-Histories

Figure E13 shows the acceleration time histories for the three masses in the model and for measurements made during the single car test. Overall, there is reasonable agreement, but the model does not capture the high-frequency content present in the test measurements.

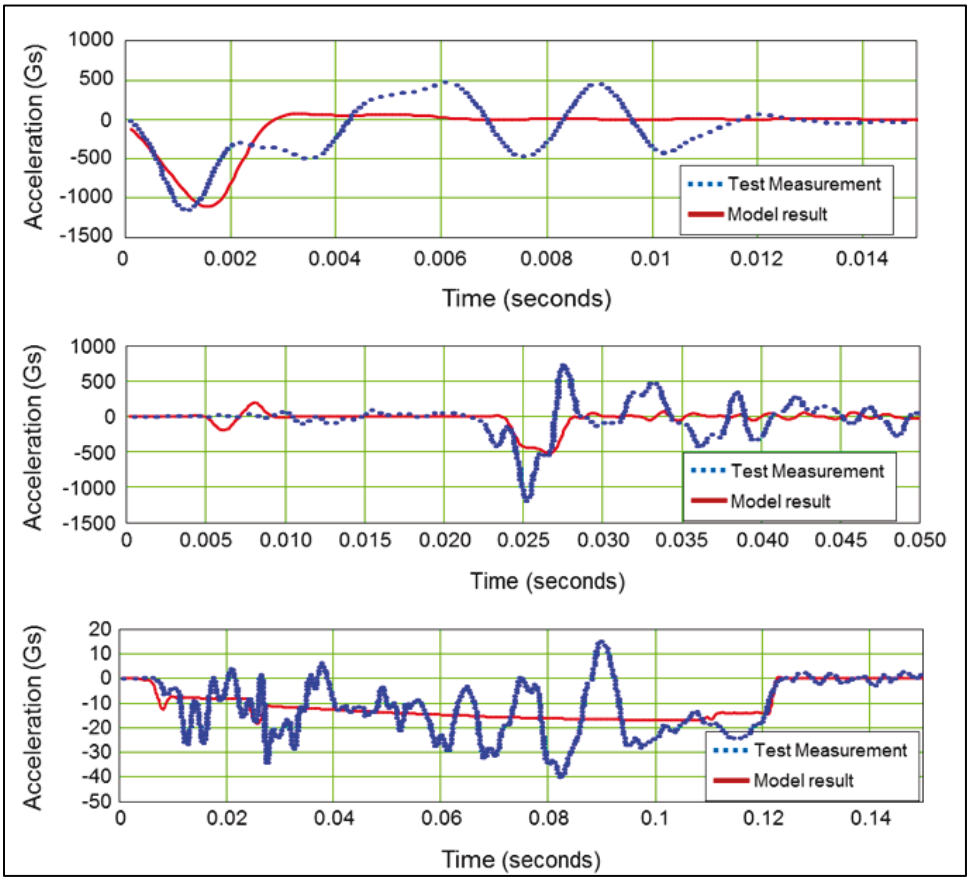

Figure E13. Model and Test Results for Accelerations of the Coupler (top), Sliding Sill and End Frame (center), and Carbody and Truck (bottom) Masses

Velocity Time-Histories

Figure E14 shows the velocity time histories for the three masses in the model and for calculations from measurements made during the single car test. Overall, there is close agreement, although the model does not capture the high-frequency ringing of the coupler and sliding sill and frame masses.

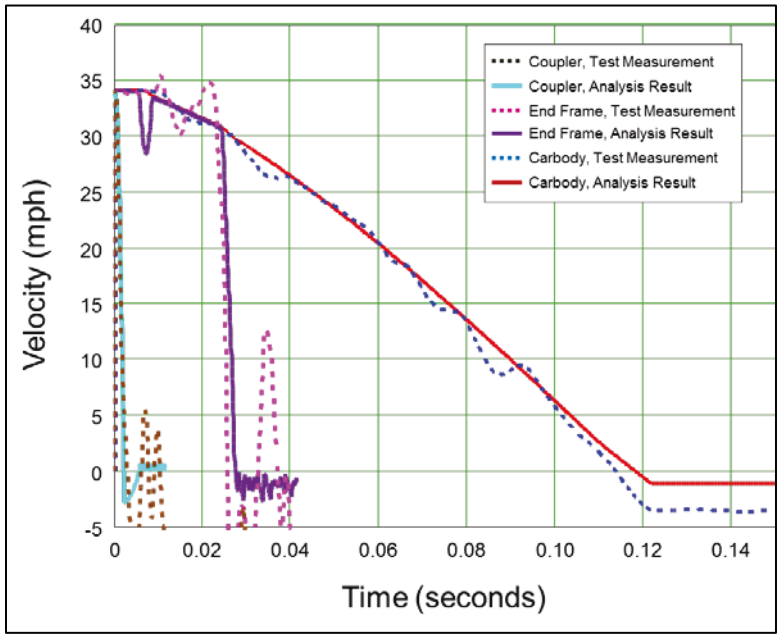

Figure E14. Model and Test Results for the Velocities of the Coupler, Sliding Sill and End Frame, and Carbody and Truck Masses

Displacement Time-History

Figure E15 shows the displacement time histories for the three masses in the model and for calculations from measurements made during the single car test. Overall, there is very close agreement. The high-frequency content of the acceleration has little influence on the displacement of the masses.

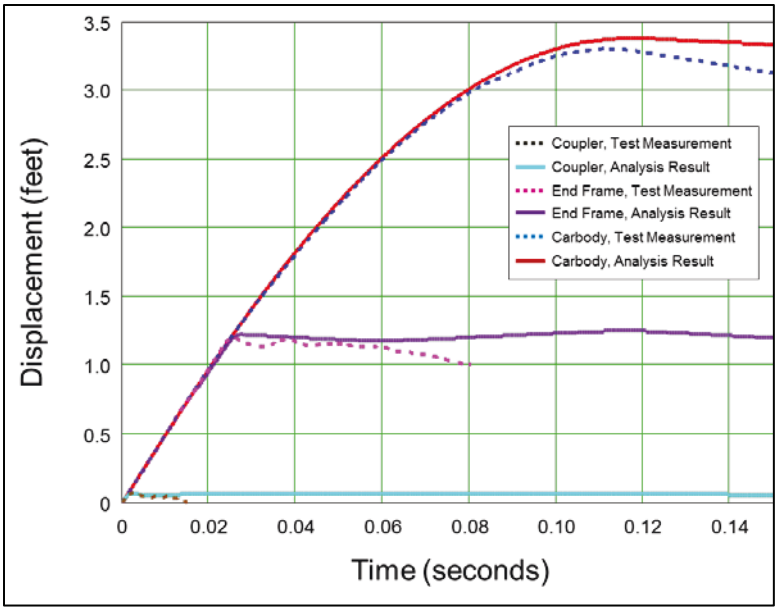

Figure E15. Model and Test Results for the Displacements of the Coupler, Sliding Sill and End Frame, and Carbody and Truck Masses

Forces

Figure E16 shows the force/crush characteristic calculated from the accelerations of the carbody and trucks, end frame and sliding sill, and coupler masses. Both the accelerations measured from the test (blue) and computed with the model (red) are shown in the figure.

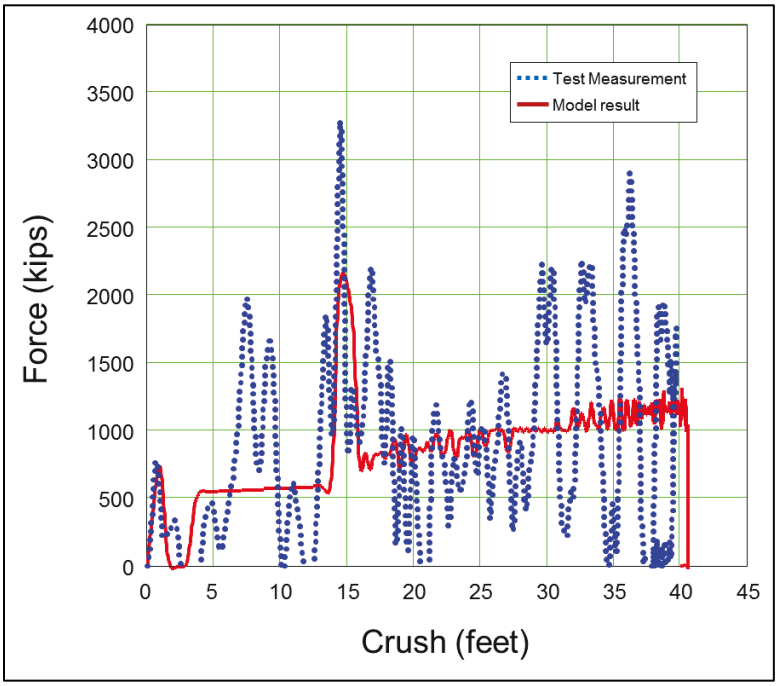

Figure E16. Model and Test Results for CEM Force/Crush Characteristic, Calculated from Component Accelerations

Appendix F. Occupant Test Requirements

Background Information

As part of the ongoing study of passenger rail crashworthiness, a series of occupant experiments were conducted as part of the full-scale collision tests. These occupant experiments utilized anthropomorphic test devices (ATDs, or test dummies) to measure the occupant kinematics and kinetics, which were used to predict injury risk. This quantification of occupant response allows an evaluation of the crashworthiness performance of various passenger seating configurations. Occupant experiments have included crash test dummies positioned in forward- and rear-facing intercity and commuter seats (Table F1).

Table F1. Previous and Planned Occupant Experiments Performed on Board Full-Scale Collision Tests of Conventional and CEM Equipment

	Conventional			CEM		
	One-Car	Two-Car	Train-to-Train	One-Car	Two-Car	Train-to-Train
Forward-Facing Commuter	●	● ●	● ●		●	●
Rear-Facing Commuter	●	●			●	●
Unrestrained Intercity	●	●	●		●	●
Three-point Belt Intercity	●	●	●			
Workstation Table					● ●	● ●
Locomotive/ Cab Operator			●			

Legend: ● **Previous Test** ● **Planned Test**

In the single-car test of CEM equipment, occupant experiments were not conducted, because the environment was predicted to be more severe than the two-car and train-to-train full-scale tests of CEM equipment, and not representative of an actual train collision in terms of carbody deceleration. In the two-car test of CEM equipment conducted on February 26, 2004, five occupant experiments were conducted:

1-1. Forward-facing inter-city seats

1-2. Facing seats with workstation table

1-3. Facing seats with workstation table

2-1. Rear-facing M-Style commuter seat

2-2. Forward-facing M-Style commuter seats.

Tests similar to 1-1, 2-1, and 2-2 were conducted in all three previous full-scale in-line collision tests of conventional equipment. These three experiments allow a comparison of the occupant

response and injury risk in conventional and CEM passenger equipment. Tests 1-2 and 1-3 have not been conducted in previous full-scale collision tests, although there have been sled tests of the facing seats with workstation table configuration. The workstation table experiments examine the occupant response in a similar environment to that of the METROLINK April 2002 passenger train collision in in Placentia, CA. The experiments with the workstation tables utilize advanced ATDs (Hybrid 3RS and THOR), which are described in more detail below. In the full-scale train-to-train collision test of CEM equipment, which was conducted on March 23, 2006, all five of these experiments were included with modifications to incorporate occupant protection strategies.

Test Objectives

The primary objective of each occupant experiment was to quantify the occupant response using high-speed video to record the occupant kinematics, on-board test dummy instrumentation to record the forces and accelerations imparted on the occupant, and additional instrumentation of the seating environment to measure the seat and table performance. Crashworthiness performance was then evaluated by determining the level of compartmentalization of the occupants, the injury risk to the instrumented ATDs, and the ability of the seats and tables to withstand secondary impact without unintended structural failure.

A secondary objective of these experiments was to build an understanding of the performance of workstation tables during collision conditions similar to those in the Placentia, CA, train collision. The table stiffness and attachment strength can affect the kinematics of the occupant during impact of the table, particularly the potential for head impact with the tabletop and the bending of the spine.

Test Requirements

Occupant Experiment Layout

Experiments 1-1, 1-2, and 1-3 are to be installed on the lead car in the two-car consist. Experiment 1-1 is to be installed on the left-hand side of the front half of the lead car, while experiments 1-2 and 1-3 are to be installed adjacently on the right-hand side of the rear half of the lead car (Figure F1). Experiments 2-1 and 2-2, respectively, are to be installed on the front left and rear right of the trailing car (Figure F2).

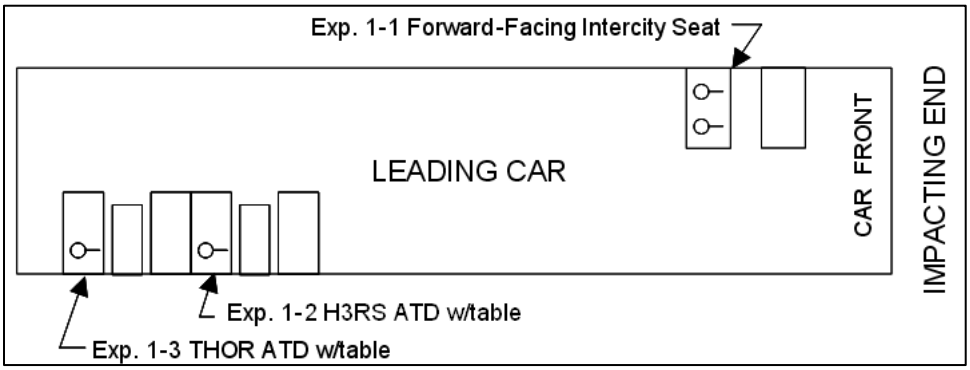

Figure F1. Location of Leading Car Occupant Experiments

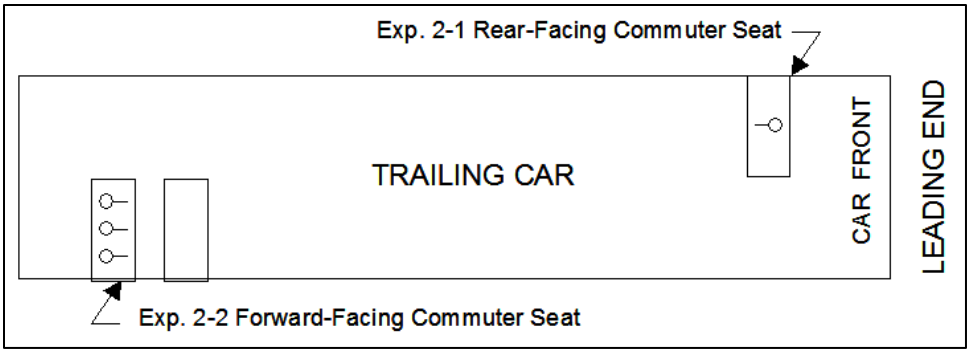

Figure F2. Location of Trailing Car Occupant Experiments

Forward-facing Inter-city Seats

Experiment 1-1 consists of two pairs of forward-facing inter-city seats, with a seat pitch of 41 inches, with two unrestrained Hybrid III 95th percentile large male ATDs initially positioned in the rear seat pair. These seats were modified in the same manner as the inter-city seats in the two-car and train-to-train conventional tests, including strengthened seat backs with an energy absorber in the base. These modifications were necessary to ensure compartmentalization of the occupant during a collision. The objective of this experiment was to determine if these modifications sufficiently protect the occupant in a more severe collision environment.

Facing Seats with Intervening Workstation Table

Experiments 1-2 and 1-3 each consist of a forward-facing window-side occupant seated at a workstation table. These two experiments are identical save for the type of test dummy. Experiment 1-3 utilizes a THOR (Test Device for Human Occupant Restraint) dummy, which is an experimental dummy developed by the National Transportation Biomechanics Research Center of the National Highway Traffic Safety Administration (NHTSA) to research the complex interaction of the occupant with state-of-the-art restraint systems including air bags and seat belts. Experiment 1-2 utilizes a Hybrid 3 Rail Safety (3RS) test dummy, which was developed by Transport Research Laboratory, Limited (TRL, Ltd.) under the direction of the United Kingdom's Rail Safety and Standards Board (RSSB) to investigate rail-specific injuries. The Hybrid 3RS is a specialized version of the standard Hybrid III dummy that incorporates many of the biofidelity and instrumentation improvements of the THOR, specifically the ability to measure triaxial thoracic and abdominal deflection.

Both experiments 1-2 and 1-3 position the test dummy in the window position of a forward-facing commuter seat at a workstation table. The pitch of the facing-seat arrangement is 65 inches, with the table centered between the two pairs of seats. The tabletop is 33.5 inches long by 16 inches wide by 1.2 inches thick and is made of solid wood. The top of the table is 29.75 inches from the floor. Both the facing seats and table are similar to those on the Metrolink cab car in the Placentia, CA, collision. The wall and floor attachments of the table to the car body are to be strengthened to ensure compartmentalization and allow measurement of the peak load imparted by the occupant.

Rear-facing M-Style Commuter Seat

Experiment 2-1 consists of one Hybrid III 50th percentile male ATD seated in the middle position of a three-passenger rear-facing M-Style commuter seat similar to the seat tested in the trailing car of the two-car conventional test. The seat shall be modified to include a strengthened floor pedestal/attachment and frame stiffeners between the seat back and seat base.

Forward-facing M-Style Commuter Seat

Experiment 2-2 consists of three ATDs seated in a pair of forward-facing three-person M-Style commuter seats with a pitch of 32 inches. The forward seat is to be modified as described above for Experiment 2-1. Instrumented Hybrid III 50th-percentile male ATDs are to be seated in the window and aisle positions of the rear seat. An un-instrumented Hybrid II 50th-percentile male ATD is to be located in the middle seat position.

Required Test Measurements

For each experiment, high-speed video equipment shall be used to record the occupant motion from at least the top and side views (Figure F3). In each camera view, photo targets on the walls, seats, and ATDs shall be visible. The targets' placement locations (Figure F4) shall include the top and side of each seat back, the top and side of each ATD head, and six wall targets within the field of view of the side-view camera. The position of each marker shall be measured and documented.

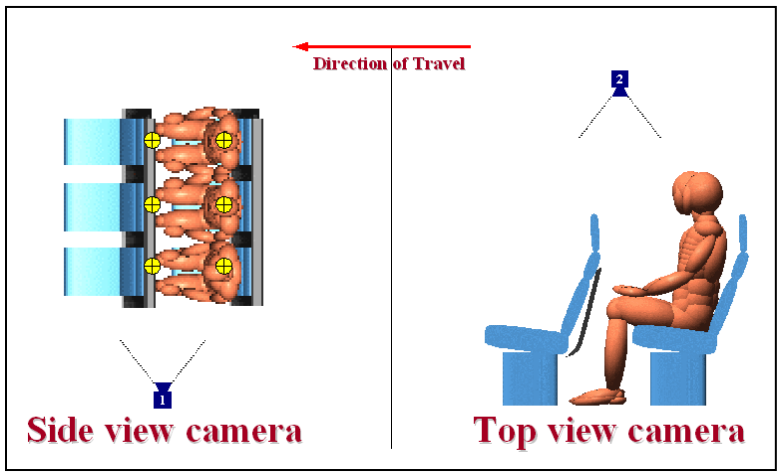

Figure F3. Placement of High-Speed Video Cameras and Photo Targets in the Experiments Without Workstation Tables

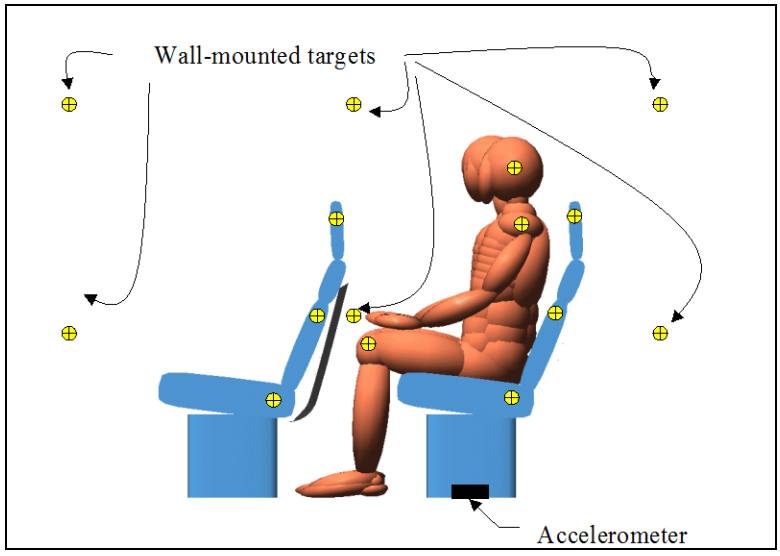

Figure F4. Placement of Photo Targets Visible to the Side-View Camera in the Experiments Without Workstation Tables

Note the placement of the floor-mounted accelerometer.

Each instrumented ATD shall measure the triaxial acceleration-time histories of the head and chest, the force-time histories of upper neck tension/compression and longitudinal shear, the force-time histories of axial compression of each femur, and the moment-time history of the extension/flexion moment of the upper neck. Forces and accelerations are to be recorded and processed in accordance with SAE-J211/1. From these measurements, the injury assessment values of head injury criterion (HIC), chest acceleration, neck injury criterion (Nij), peak upper neck tension/compression, and peak femur load shall be reported in accordance with 49 CFR 571.208. Additionally, an accelerometer is to be installed on the floor near each experiment to record the triaxial acceleration-time history of the local car body structure.

The required data channels for experiments 1-1, 2-1, and 2-2 are listed in Table F2.

Table F2. Summary of Data Channels for Experiments 1-1, 2-1, and 2-2

Required Instrumentation	Number of Data Channels		
	1-1 Forward-Facing Inter-City Seats	2-1 Rear-Facing Commuter Seat	2-2 Forward-Facing Commuter Seats
Accelerometers			
Triaxial Head	6	3	6
Triaxial Chest	6	3	6
Triaxial Floor	3	3	3
Load Transducers			
Upper Neck Force (Fx, Fz)	4	2	4
Upper Neck Moment (M_y)	2	1	2
Uniaxial Femur Force	4	0	4
Total	**25**	**12**	**25**

Required Test Measurements, Table Experiments

For each table experiment, high-speed video equipment shall be used to record the occupant motion from at least the top, side, and front views (Figure F5). In each camera view, photo targets on the walls, seats, table, and ATDs shall be visible. The targets' placement locations are shown in Figure F6, and shall include the top and side of each seat back, the top and side of each table, the top and side of each ATD head, the top and side of each ATD shoulder, the side of each ATD pelvis, and six wall targets within the field of view of the side-view camera. The position of each marker shall be measured and documented.

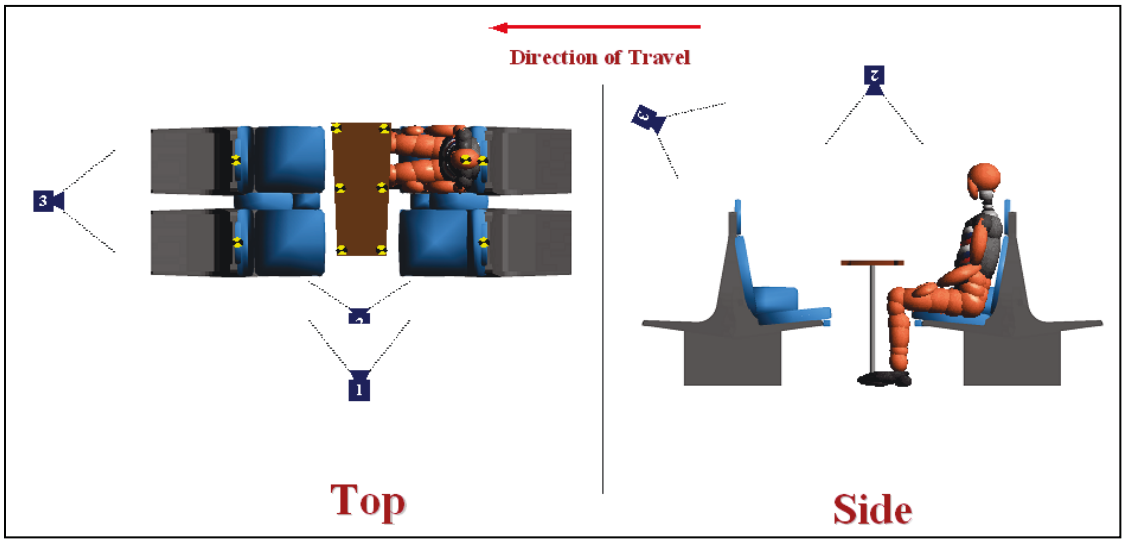

Figure F5. Placement of High-Speed Video Cameras and Photo Targets in the Experiments with Workstation Tables

Figure F6. Placement of Photo Targets Visible to the Top- and Side-View Cameras in the Experiments with Workstation Tables

Accelerometers, shown as green cubes, are placed on the aisle-side edge of the tabletop and the floor near the table leg.

For experiments 1-2 and 1-3, additional measurements are necessary. Load cells are to be installed between the each table and the floor and wall attachment locations, a total of four points for each table (Figure F7). For each load cell, the force-time history of two of the three axes (those parallel to the longitudinal axis of the rail car and normal to the load cell) shall be recorded. Three linear displacement transducers shall be installed to measure the displacement-time history of the aisle, middle, and window position of each table with respect to the car body structure. The triaxial acceleration-time history of the aisle side of the tabletop shall be recorded.

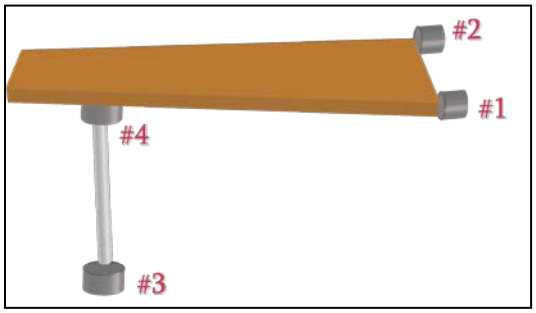

Figure F7. Load Cell Installation Positions for Experiments 1-2 and 1-3

In addition to the ATD measurements listed above, the THOR and Hybrid 3RS dummies are capable of recording the deflection-time histories of the thorax and upper abdomen. For both ATDs, the lower CRUX triaxial bilateral displacement-time history shall be recorded. In the THOR experiment, the uniaxial displacement-time history and acceleration-time history of the upper abdomen shall be recorded. If available, the triaxial acceleration-time history of the spine at vertebra T12 shall be recorded as well. Along with the previously specified injury metrics, the additional measurements of the thorax and abdomen of the THOR and Hybrid 3RS shall be used to calculate the viscous criterion of the chest and upper abdomen. Due to a limitation in the number of available channels, the triaxial acceleration of the car body structure between the two table experiments is not recorded. The data channels required for occupant experiments 1-2 and 1-3 are detailed in Table F3 and Table F4, respectively.

Table F3. Summary of Data Channels for Experiment 1-2

	Hybrid 3RS	Channels	Seats/Table	Channels
Displacement Transducers	Upper abdomen, uni-directional, bi-lateral	2	Tabletop, three (uni-directional)	3
	Lower thorax CRUX, triaxial, bi-lateral	12		
	Abdominal DGSP, bi-lateral	6		
Accelerometers	Head, triaxial	3	Floor, biaxial	2
	Chest, biaxial	2	Tabletop, uniaxial	1
Load Transducers	Neck load, biaxial (Fz, Fx)	2	Table Attachment Loads, four (4) biaxial (longitudinal, lateral)	8
	Neck moment, uniaxial (M_y)	1		
	Femur load, uniaxial	2		
Totals	**Hybrid 3RS:**	**30**	**Seats/Table:**	**14**
			Total requested channels per experiment:	**44**

Table F4. Summary of Data Channels for Experiment 1-3

	THOR 50th	Channels	Seats/Table	Channels
Displacement Transducers	Upper Abdomen, uniaxial	1	Tabletop, three (uni-directional)	3
	Lower thorax CRUX, triaxial, bi-lateral	6		
Accelerometers	Head, three triaxial	9	Tabletop, triaxial	1
	Chest, triaxial	3		
	Spinal T12, triaxial	3		
	Upper abdomen, uniaxial	1		
Load Transducers	Neck load, biaxial (Fz, Fx)	2	Table Attachment Loads, four (4) triaxial (take parallel to track, normal to load cell at each)	8
	Neck moment, uniaxial (M_y)	1		
	Neck cable load, uniaxial	2		
	Femur load, uniaxial	2		
Other	Head rotation sensor	1		
Totals	**THOR 50th:**	**31**	**Seats/Table:**	**12**
			Total requested channels per experiment:	**43**

Test Documentation

At the completion of the test, the results shall be thoroughly documented. Each recorded data channel shall be filtered and de-biased in accordance with SAE-J211/1, and each time-history shall be presented in a plot including the values and times of occurrence of each peak. Injury metrics shall be calculated in accordance with 49-CFR571.208 for, where applicable, HIC, chest acceleration, Nij, thoracic viscous criterion, abdominal viscous criterion, peak upper neck tension/compression force, and peak femur loads. Pre- and post-test measurements of each photo target location shall be documented relative to the location of each high-speed camera. Video from each high-speed camera shall be presented, along with still photographs taken directly before and after the collision test. Table F5 summarizes the deliverables.

Table F5. Summary of Deliverables

Deliverables	Experiment Number				
	1-1	1-2	1-3	2-1	2-2
ATD Measurements					
Head acceleration	●	●	●	●	●
Chest acceleration	●	●	●	●	●
Spinal acceleration			●		
Upper abdominal acceleration			●		
Upper abdominal displacement		●	●		
Lower CRUX displacement		●	●		
Lower abdominal displacement		●			
Neck tension/compression force	●	●	●	●	●
Neck shear force	●	●	●	●	●
Neck flexion/extension moment	●	●	●	●	●
Neck cable force			●		
Femur force	●	●	●		●
Head rotation			●		
Calculated Injury Metrics					
HIC	●	●	●	●	●
Nij	●	●	●	●	●
Peak neck tension/compression	●	●	●	●	●
Chest acceleration (3ms clip)	●	●	●	●	●
Chest viscous criterion (V*C(t))		●	●		
Upper abdomen viscous criterion (V*C(t))		●	●		
Peak femur axial load	●	●	●		●
Seat/Table/Environment Measurements					
Car body acceleration near experiment	●	●		●	●
Table attachment forces		●	●		
Table displacement		●	●		
Tabletop acceleration		●	●		
Video/Photos					
High-speed video, top	●	●	●	●	●
High-speed video, side	●	●	●	●	●
High-speed video, front		●	●		
Pre-test photo target measurements	●	●	●	●	●
Post-test photo target measurements	●	●	●	●	●
Pre-test still photos	●	●	●	●	●
Post-test still photos	●	●	●	●	●

Appendix G. Occupant Model Descriptions

Experiment 1-1. Forward-Facing Intercity Seats

Experiment 1-1 consisted of two Hybrid III 95th-percentile male anthropomorphic test devices (ATDs) seated side-by-side in forward-facing intercity seats (Figure G1). The experiment included two rows of seat pairs: the rear ("launch") seats and the forward ("struck") seats. The launch seats were unmodified from the in-service hardware. The struck seats incorporated strengthened seatbacks and energy absorbers. These modified seats were included in previous full-scale tests [1, 2, 3].

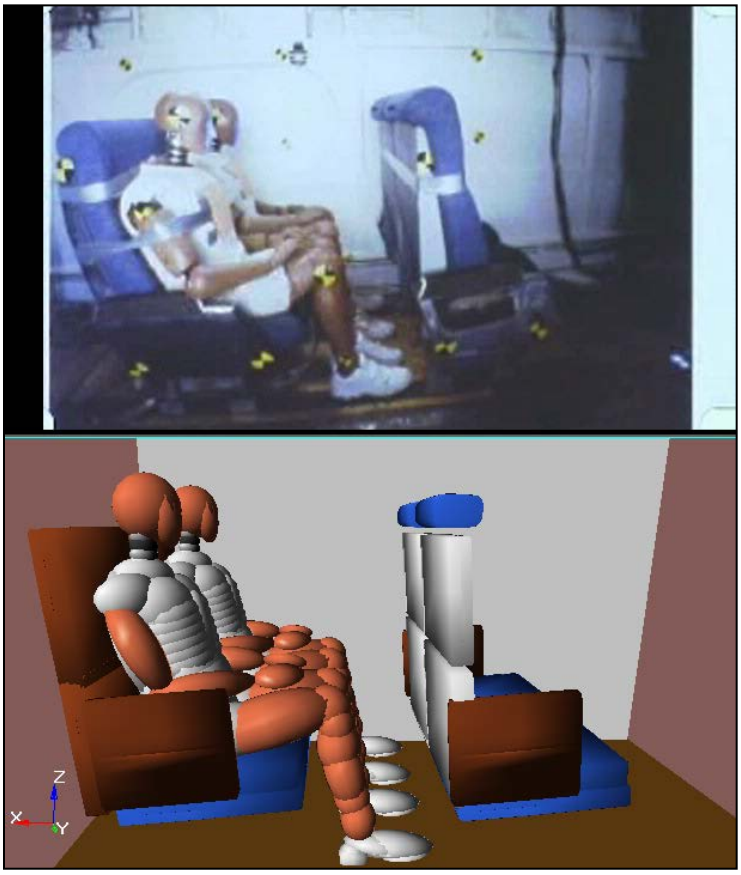

Figure G1. Test Photograph and Model Depiction of Forward-Facing Intercity Seat Experiment

The model was developed prior to the full-scale test, and used to make predictions of the test results. After the full-scale test was run, the model was refined to achieve better agreement with the test measurements. This refinement included several aspects:

1. **Occupant environment:** In the pre-test simulation, the acceleration pulse applied to the occupant environment was determined from a collision dynamics model of the full-scale two-car test. The actual acceleration was measured during the test, and replaces this acceleration pulse in the refined post-test simulation. The most suitable longitudinal acceleration pulse was taken from the accelerometer at the center of gravity of the lead car, labeled C3X [10].

The measured lateral and vertical acceleration during the impact was negligible, and thus not applied to the model.

2. **Initial position:** The ATDs in the test were sitting with a more supine posture and resting firmly against the seatback. The model was adjusted to match this seated posture.
3. **Seatback deformation:** The pre-test model did not allow any deformation of the lower seatback at the point of impact of the knees. In the test, there was significant deformation at this point, up to 15 inches for the aisle side ATD. The model was adjusted to allow such deformation. Also, the pre-test simulation underestimated the overall seatback rotation, thus changes were made to the seatback moment-rotation characteristic in the refined model.
4. **Contact characteristics:** Since the physical characteristics of the impact surfaces have not been individually tested, the contact characteristics are derived based on the measured response of the ATD. For instance, in the full-scale test, the heads of the ATDs strike the rigid seatback below the headrest cushions of the struck seats, making for a more severe head acceleration measurement than in the pre-test simulation. The contact characteristics were adjusted accordingly.

Model Description

The model consists of five multi-body systems. The systems are described in detail in the same order:

1. **Lead Car:** The first system represents the lead car body itself. This system serves as a reference frame for the motion of the seats and the occupants. The floor and the wall are rigidly attached to the lead car body.
2. **Launch Seat:** The occupants are initially positioned in the launch seat pair, which is facing the impacted end of the lead car. There are two seats, window and aisle, which each consist of a seat back, seat base, and seat cushion. The seat bases are attached to the lead car body through point restraints representing load cells.
3. **Struck Seat:** The struck seat is located forty inches forward of the launch seat. The seat backs of the struck seat pair are more detailed than launch seat pairs in order to accurately represent the impact of the occupants during the collision. The struck seat bases are also attached to the lead car body through point restraints representing load cells.
4. **Window Occupant:** The window occupant is a Hybrid III 95th percentile male ATD, seated on the left seat (facing the impacted end of the car) of the pair. This occupant is unrestrained.
5. **Aisle Occupant:** The aisle occupant is a Hybrid III 95th percentile male ATD, seated on the right seat (facing the impacted end of the car) of the pair. This occupant is unrestrained.

System 1. Lead Car

The lead car is represented by a lumped mass of 34,000.0 kg in a translational joint parallel to the x-axis in the global reference frame. The body begins at rest, and a prescribed displacement is applied at t_0. This prescribed displacement represents the deceleration of the car body upon impact with the rigid wall. The longitudinal deceleration pulse measured at the center of gravity of the lead car in the CEM two-car full-scale impact test (C3X) is integrated twice to obtain this prescribed displacement. Figure G2 shows the measured acceleration, relative velocity, and relative displacement of the lead car body.

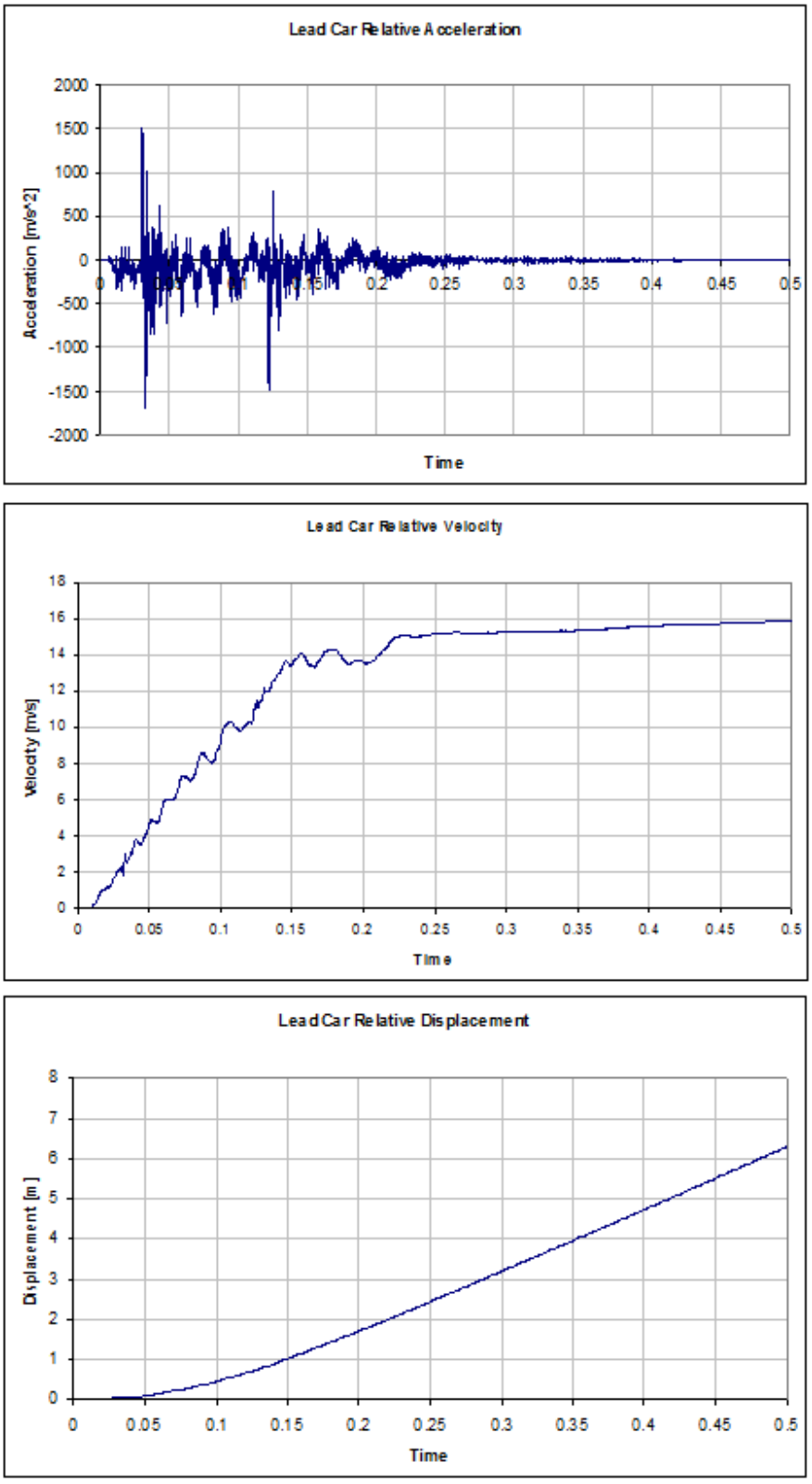

Figure G2. Measured Acceleration, Relative Velocity, and Relative Displacement of the Lead Car Body

Planes representing the wall and the floor of the car are fixed to the car body. Contact Characteristic A (Figure G3) is applied to both of these surfaces.

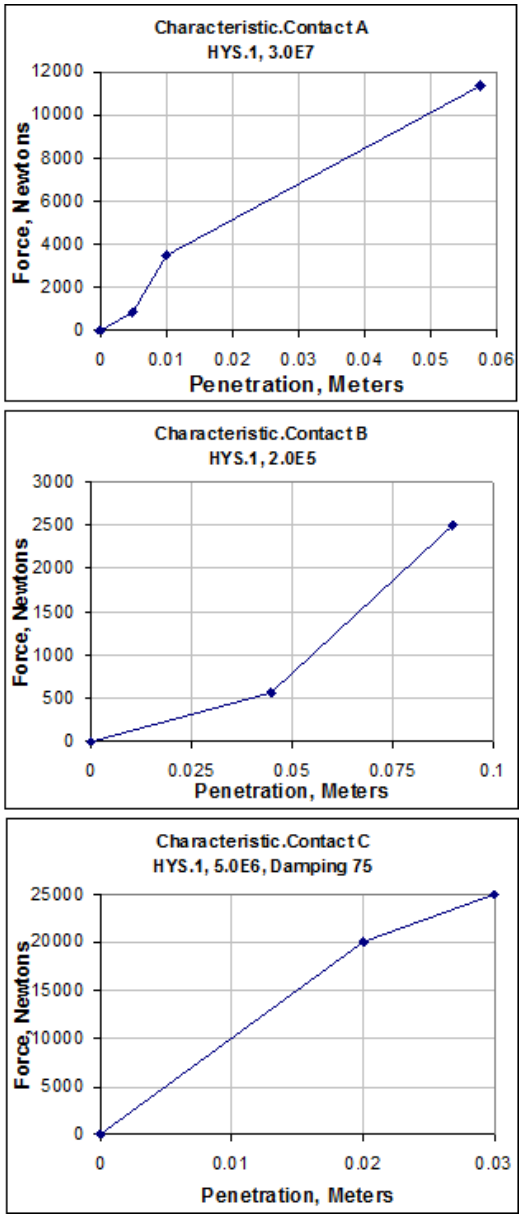

Figure G3. Contact Characteristics A, B, and C for MADYMO Model of Experiment 1-1

System 2. Launch Seat

The launch seat consists of four bodies: the seat back, the seat base, and two seat cushions. Although the individual seatbacks can move independently of each other, this property was not included in the launch seat for the sake of simplicity, as there are no impacts with the launch seat back during the collision. The seat back is attached to the seat base via a revolute joint parallel to the global y-axis, which is in turn attached to the lead car body by four point restraints. These point restraints, which use Load Characteristic A (Figure G4), can be used to output the seat attachment loads during the impact, which have been measured in previous experiments. The

cushions are attached to the seat base by free joints, which are initially locked. If the x-component of the joint constraint load reaches 2,000 N, the free joints will unlock and allow the cushions to detach. The moment-rotation characteristic of the seat back has been determined from quasi-static testing. It has been provided by Simula and is applied as a joint restraint with Load Characteristic B at the revolute joint connecting the seat back to the seat base.

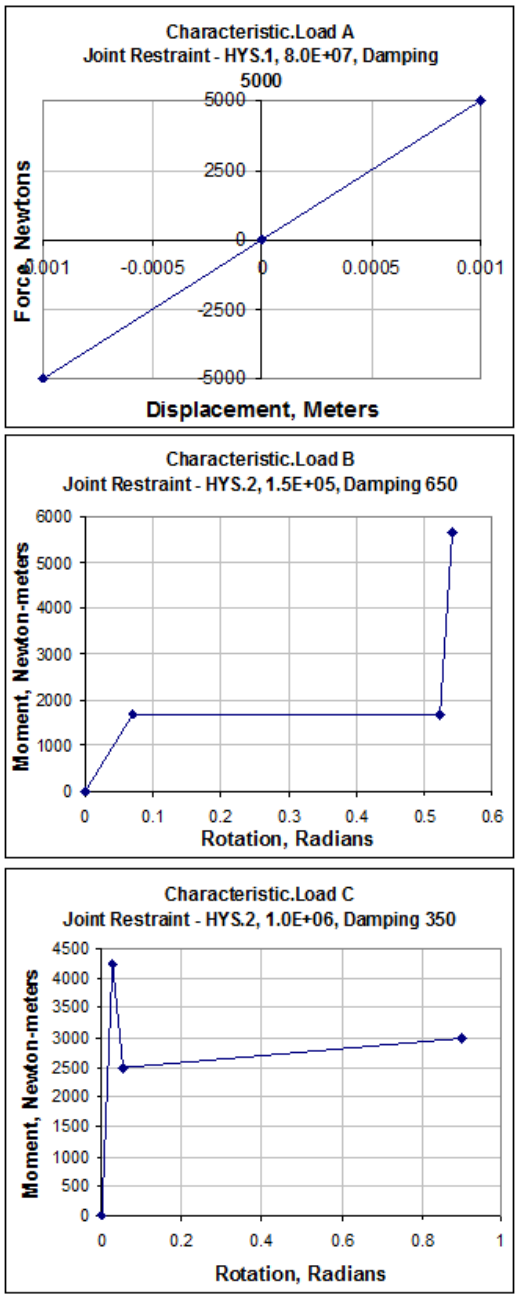

Figure G4. Load Characteristics A, B, and C for MADYMO Model of Experiment 1-1

System 3. Struck Seat

The model of the struck seat (Figure G5) is more detailed than the launch seat. First, the aisle and window seat backs each deformed to a different degree, thus lumping them together would not allow agreement with the test results. Second, the impact of the knees caused deformation of the lower seatback that was independent of the overall rotation of the seatback, thus each seatback was divided into two bodies. Finally, the portion of the seatback cushion of the stuck seat that wraps around the back of the headrest detached when the heads of the ATDs impacted the upper seatbacks, which contributed to the shape and peak of the measured head accelerations and neck loads.

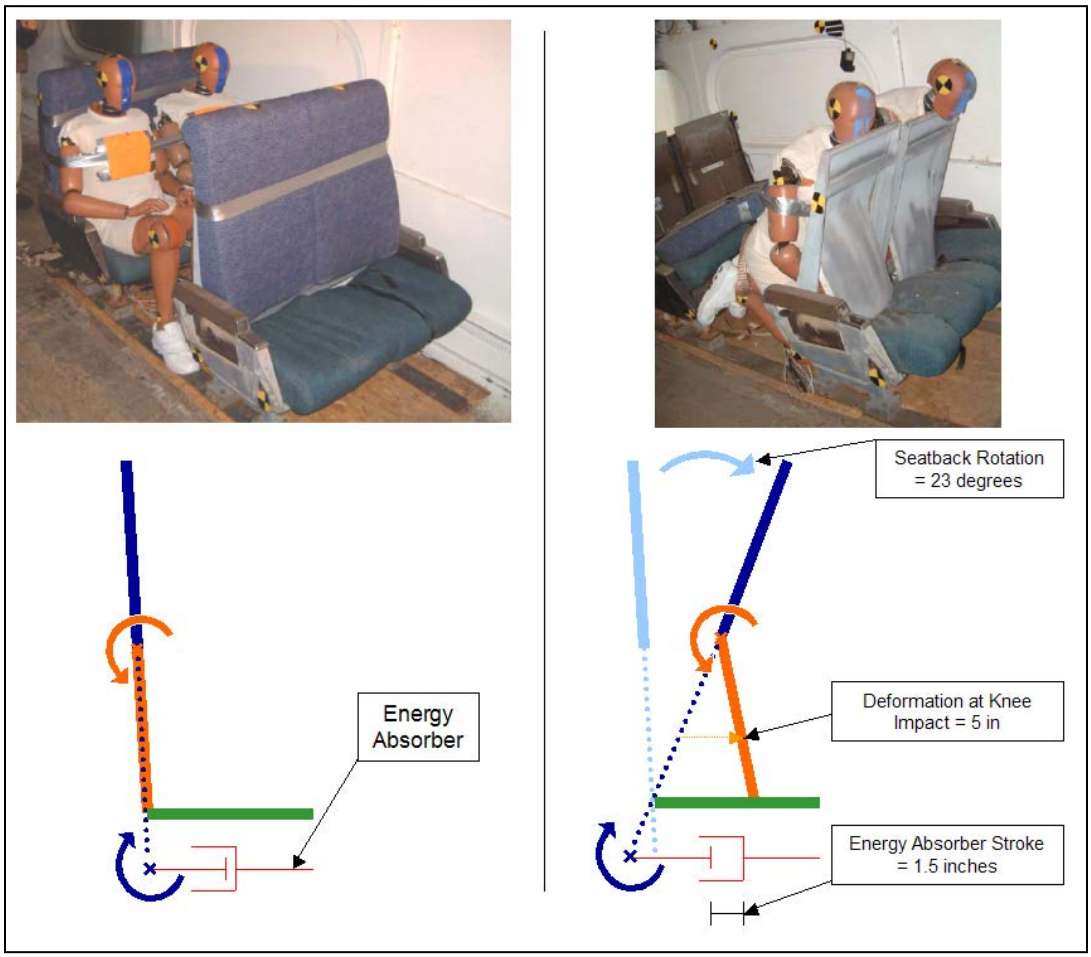

Figure G5. Struck Seat Model

The moment-rotation characteristic of the seat back, provided by Simula, has been determined from quasi-static testing and is applied as a joint restraint with Load Characteristic B (see Figure G4) at the revolute joint connecting the seat back to the seat base. There is also an energy absorber at this joint, which is reflected in the high damping coefficient in the joint restraint specification. This characteristic applies to the rigid frame of the seatback, as it remains connected to the seat base throughout the impact. However, there is deformation of the sheet metal at the point where the knees impact the seatback, which can be seen in Figure G6. The seatback indentation was modeled as a revolute joint parallel to the global y-axis at a point above

the impact of the knees, using a joint restraint with Load Characteristic C (see Figure G4). This characteristic was determined iteratively, making sure that the femur loads, overall seatback deformation, and occupant kinematics matched the recorded test data.

Figure G6. Seatback Deformation

The struck seat system also includes the portion of the seat cushions that wraps around the headrest, as seen in Figure G7. This detail was included to accurately model the contact interaction between the heads of the ATDs and the seatback. The upper seat cushions of the struck seat are attached to the seatback with a locked free joint, which unlocks once a load of 1,000N is reached. Contact Characteristic B (see Figure G3) is used for the upper seat cushions. The upper seatback itself uses the much stiffer Contact Characteristic C (see Figure G3), since there is no padding below the upper seat cushion.

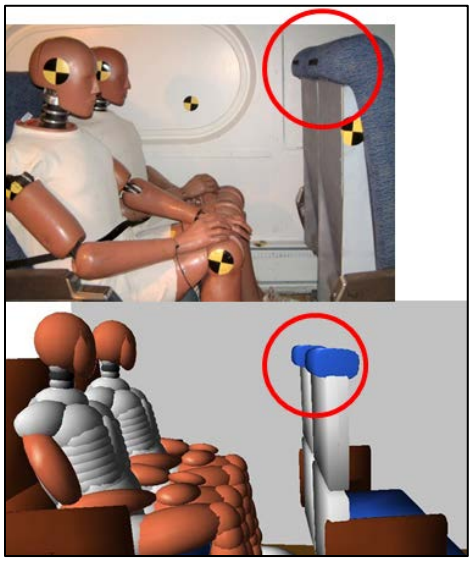

Figure G7. Struck Seat System

Systems 4 and 5. Window Occupant and Aisle Occupant

The occupants are represented by the 95th percentile Hybrid III (sitting) male dummy in MADYMO, ellipsoid model version 4.0 (created March 19, 2001). The ATDs are initially sitting in the launch seat pair, with the window ATD on the left-hand side and the aisle ATD on the right-hand side (facing the impacted end of the car). The initial position of the ATDs has been adjusted to match the pre-test measurements and photographs.

An additional modification to the ATD models entailed increasing the joint restraint friction of the knee joints in order to match the ATD kinematics from the test. The Q1 component of the friction load, which corresponds to rotation about the global Y-axis, was increased from 32.7 Nm to 150 Nm. All other ATD model parameters remained unchanged.

Experiment 1-2: Facing Commuter Seats with Intervening Workstation Table, Hybrid III Railway Safety ATD

Experiment 1-2 consisted of a Hybrid III Railway Safety ATD seated in a facing commuter seat configuration with an intervening workstation table (Figure G8). The ATD is located on the window side of the seat pair facing the impacted end of the lead car. This seating arrangement has been previously tested during a series of sled tests with a standard HIII 50th-percentile ATD [29].

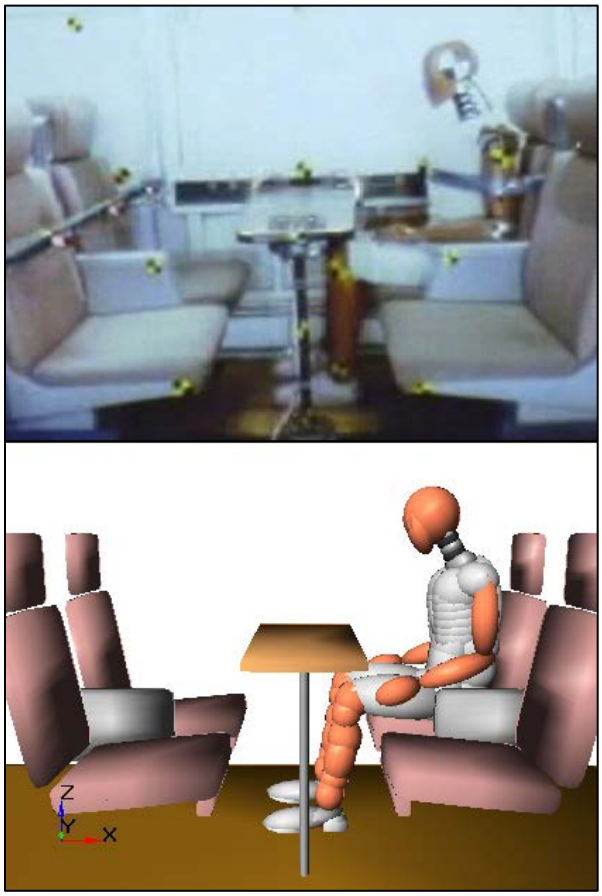

Figure G8. Test Photograph with H3RS ATD and Model Depiction with HIII ATD of Facing Seat Experiment with Workstation Table

The Hybrid III Railway Safety ATD (Hybrid 3RS) is a modified version of the stock Hybrid III 50th-percentile male ATD, aimed at characterizing injuries perceivable in rail collisions, specifically with fixed tables in seating bays and with seat back tables. The development of the Hybrid 3RS was directed and funded by the United Kingdom's Rail Safety and Standards Board, with the assistance of Transport Research Laboratory, Ltd., along with GESAC, Inc. and AEA Technology Rail, as well as the Millbrook and MIRA test facilities. The Hybrid 3RS is an experimental ATD, and there is currently only one in existence.

Since the Hybrid 3RS ATD is relatively new, and the only one of its kind, there is no MADYMO model currently in existence. For this reason, a pre-test prediction simulation was not run. However, analysis of the test results suggested that implementing the standard Hybrid III 50th-percentile male MADYMO model in a simulation would yield relatively accurate correlations between model predictions and test results.

Model Description

The model consists of four multi-body systems. The systems will be described in detail in the same order:

1. **Lead Car:** The first system represents the lead car body itself. This system serves as a reference frame for the motion of the seats and the occupants. The floor and the wall are rigidly attached to the lead car body.
2. **Launch Seat:** The ATD is initially positioned on the window side of the launch seat pair, which is facing the impacted end of the lead car. There are two seats, window and aisle, which each consist of a seat back, headrest, and seat cushion. Both seats are attached to a seat base, which also includes an armrest between the two seat cushions. The seat base is attached to the lead car body through point restraints representing load cells.
3. **Struck Seat:** The struck seat is located sixty-five inches forward of the launch seat. The portion of the struck seat that is represented by ellipsoids is facing the launch seat. There are two seats, window and aisle, which each consist of a seat back, headrest, and seat cushion. Both seats are attached to a seat base, which also includes an armrest between the two seat cushions. The seat base is attached to the lead car body through point restraints representing load cells.
4. **Window Occupant:** The window occupant is a Hybrid III 50th percentile male ATD, seated on the right seat (facing the impacted end of the car) of the pair. This occupant is unrestrained.

System 1. Lead Car

The lead car is represented by a lumped mass of 34,000.0 kg in a translational joint parallel to the x-axis in the global reference frame. The body begins at rest, and a prescribed displacement is applied at t_0. This prescribed displacement represents the deceleration of the car body upon impact with the rigid wall. The longitudinal deceleration pulse measured at the center of gravity of the lead car in the CEM two-car full-scale impact test (C3X) is integrated twice to obtain this prescribed displacement. Figure G9 shows the measured acceleration, relative velocity, and relative displacement of the lead car body.

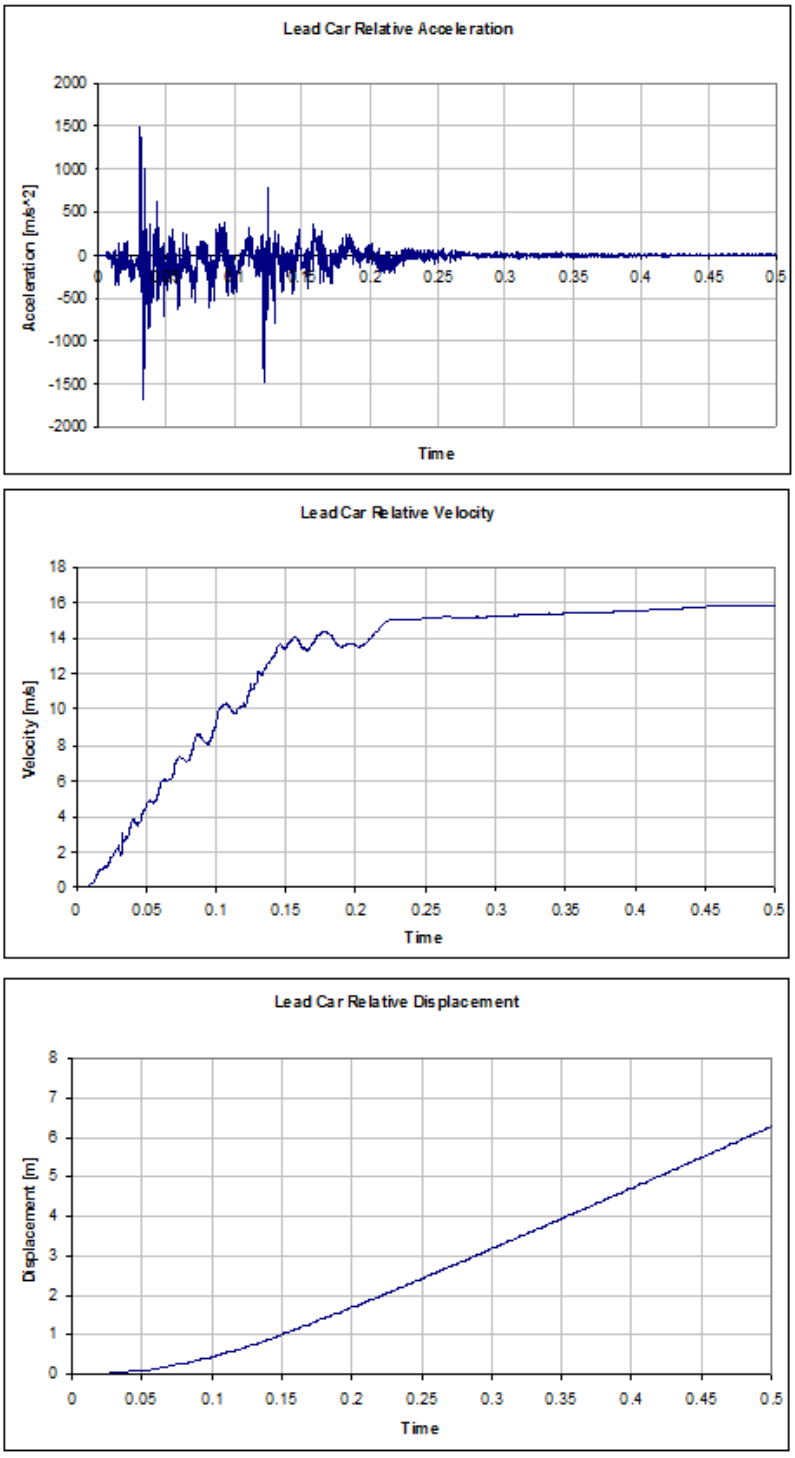

Figure G9. Measured Acceleration, Relative Velocity, and Relative Displacement of the Lead Car Body

An ellipsoid representing the floor of the car is fixed to the car body. Contact Characteristic A (Figure G10) is applied to this surface.

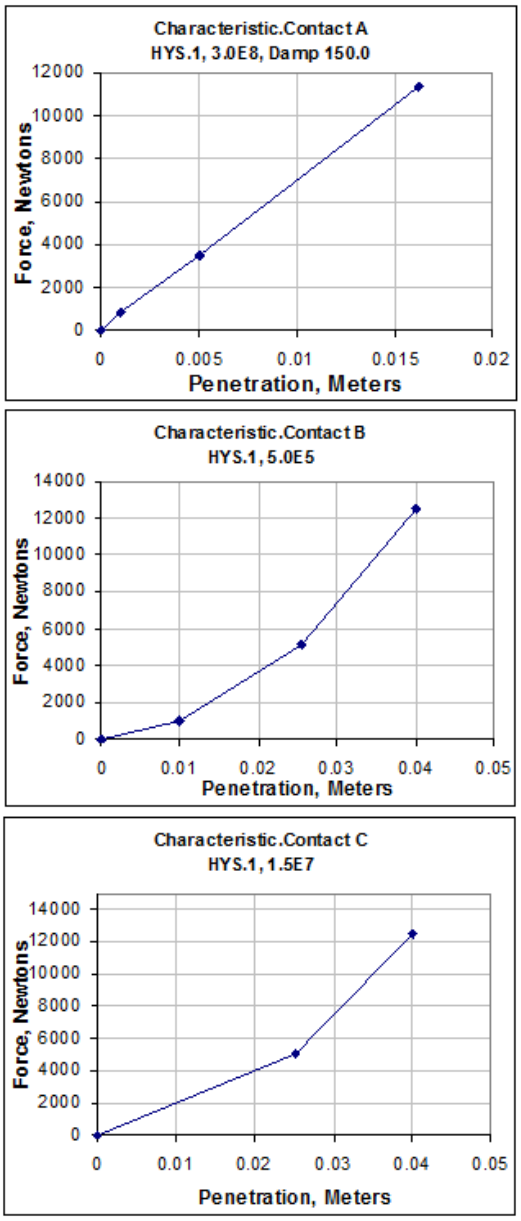

Figure G10. Contact Characteristics for MADYMO Model of Experiment 1-2

The lead car system also includes the workstation table. In the original MADYMO model created during the sled testing of facing commuter seats, the table was represented by a faceted surface. However, this model was never validated,because the table detached from the wall attachment during the sled test. The faceted surface was since replaced with an ellipsoid for several reasons: first, the surface was represented by over one thousand elements, which took up a disproportionate amount of processor time; second, the table did not deform in previous tests and was not expected to deform in the CEM two-car test; and finally, comparative simulations showed that the effect of the tapered edge of the table was negligible. Since the table is assumed

to be significantly more rigid than the impacting elements of the ATD, the contact characteristics built into the Hybrid III model are used to define the contact of the ATD with the table.

The table is attached to the car body by four point restraints: two at the wall, one between the table and the leg, and one between the table and the floor. These point restraints can be used to output the load cell measurements, which can be compared directly to the test data. Load Characteristic A (Figure G11) is used to define these point restraints.

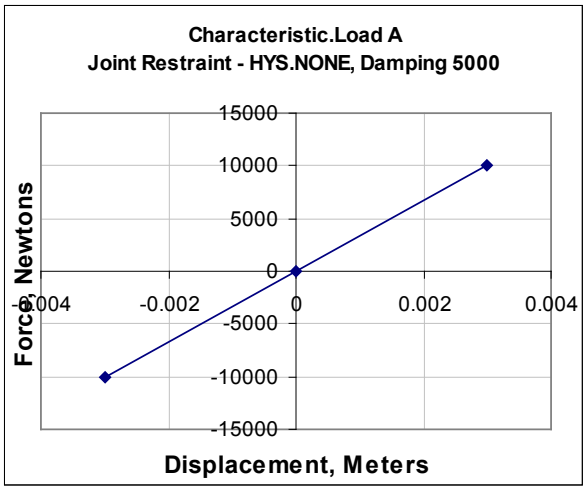

Figure G11. Load Characteristics for MADYMO Model of Experiment 1-2

System 2. Launch Seat

All the facing commuter seats were provided by Metrolink. They were arranged in back-to-back pairs attached to a common seat pedestal. This experiment included two such arrangements, which allowed for a total of eight seating positions. Only four seating positions were included in the model (the two pairs that face each other, straddling the table), as the other four seating positions faced outward and did not see any interaction with the occupant (Figure G12).

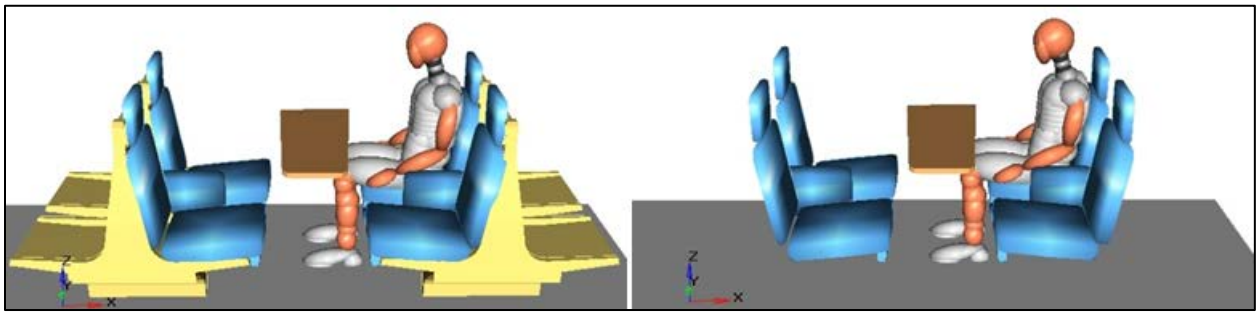

Figure G12. MADYMO Model of Experiment 1-2

The launch seat is modeled as one rigid body, since there is only minor interaction of the occupant with the launch seat. The seat base is attached to the lead car body by four-point restraints. Load Characteristic A (see Figure G11) is used to define the point restraints. The point restraint loads can be output and compared to load cell measurements collected in previous experiments. Contact Characteristic B(see Figure G10) is used to define the contact of the seated

ATD with the seat cushion. This is important to achieve correlation with the initial kinematics from the test.

System 3. Struck Seat

The struck seat is identical to the launch seat, except that it is facing away from the impacted end of the lead car. The struck seat has been simplified from an earlier model of the facing seat configuration without an intervening table. This earlier model included a breakaway headrest and detailed contact characteristics for different locations of the seat. Since the only contact between the occupant and the struck seat is the interaction of the tibias and knees with the seat pan, this unnecessary detail has been removed. Contact Characteristic C (see Figure G10) is used to represent the lower portion of the seat cushion as well as the stiffer seat pan directly behind it.

System 4. Window Occupant

The occupant is represented by a 50th-percentile Hybrid III (sitting) male dummy in MADYMO, ellipsoid model version 6.6 (created February 24, 2003). The ATD is initially sitting on the right-hand side (facing the impacted end of the lead car) of the launch seat pair. The initial position of the ATD was modified to match the initial position of the Hybrid 3RS in the test, and additional output definitions were added (such as upper abdominal displacement) to compare to the data measured in the test. All other ATD model parameters remained unchanged.

Experiment 1-3: Facing Commuter Seats with Intervening Workstation Table, THOR ATD

Experiment 1-3 consisted of a Test Device for Human Occupant Restraint (THOR) ATD, seated in a facing commuter seat configuration with an intervening workstation table (Figure G13). The ATD is located on the window side of the seat pair facing the impacted end of the lead car. This seating arrangement has been previously tested during a series of sled tests [29].

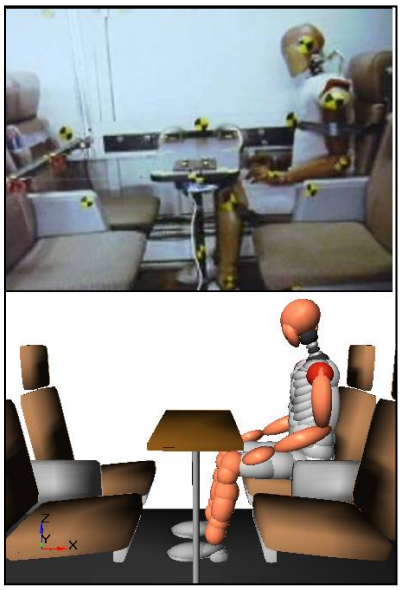

Figure G13. Test photograph and Model Depiction of Facing Seat Experiment with Workstation Table with THOR ATD

The THOR ATD, which represents a 50th-percentile male, was developed by the National Transportation Biomechanics Research Center of the National Highway Traffic Safety Administration [17]. The THOR was originally developed to investigate the injury risk associated with restraints, such as seat belts and airbags, to the thorax and abdomen. The THOR ATD, like the Hybrid 3RS, is an experimental test device; it is currently at the Alpha level of development, and there are several in existence.

The model representing this experiment was created in MADYMO Version 6.1 and exercised prior to the full-scale test. The purpose of this simulation was to make predictions of the test results, which aids in determining the proper instrumentation types, locations, and ranges. After the full-scale test was run, the model was refined to achieve better agreement with the test measurements. This refinement included several aspects:

1. **Occupant environment:** In the pre-test simulation, the acceleration pulse applied to the occupant environment was determined from a collision dynamics model of the full-scale two-car test. The actual acceleration was measured during the test, and replaces this acceleration pulse in the refined post-test simulation. The most suitable longitudinal acceleration pulse was taken from the accelerometer at the center of gravity of the lead car, labeled C3X [10]. The measured lateral and vertical acceleration during the impact was negligible, and thus not applied to the model.
2. **Initial position:** The ATD in the test was sitting more upright than in the pre-test simulation. The model was adjusted to match this seated posture.
3. **Contact Characteristics:** Several contact characteristics were modified to enhance correlation with test results. For instance, friction was increased between the shoes of the ATD and the floor to match the kinematics from the test.
4. **THOR Model:** In the pre-test simulation, the rotation of the upper body towards the tabletop and the pelvis and femurs towards the bottom of the table was not as pronounced as in the full-scale test. The measurements of the abdominal response to the table impact, however, were more severe than those measured in the test in all categories except for chest acceleration. Refinement of the simulation entailed making changes to the MADYMO THOR model to allow the magnitude of rotation about the table contact point. The most significant change to the THOR was to allow rotation about the lumbar spine pitch change joint, which was fractured during the test. This allowed the THOR upper body to rotate about the table contact point close to the extent seen in the high-speed film.

Model Description

The model consists of four multi-body systems. The systems will be described in detail in the same order:

1. **Lead Car:** The first system represents the lead car body itself. This system serves as a reference frame for the motion of the seats and the occupants. The floor and the wall are rigidly attached to the lead car body.
2. **Launch Seat:** The ATD is initially positioned on the window side of the launch seat pair, which is facing the impacted end of the lead car. There are two seats, window and aisle, which each consist of a seat back, headrest, and seat cushion. Both seats are attached to a seat

base, which also includes an armrest between the two seat cushions. The seat base is attached to the lead car body through point restraints representing load cells.

3. **Struck Seat:** The struck seat is located sixty-five inches forward of the launch seat. The portion of the struck seat that is represented by ellipsoids is facing the launch seat. There are two seats, window and aisle, each of which consist of a seat back, headrest, and seat cushion. Both seats are attached to a seat base, which also includes an armrest between the two seat cushions. The seat base is attached to the lead car body through point restraints representing load cells.
4. **Window Occupant:** The window occupant is a THOR ATD, seated on the right seat (facing the impacted end of the car) of the pair. This occupant is unrestrained.

System 1. Lead Car

The lead car is represented by a lumped mass of 34,000.0 kg in a translational joint parallel to the x-axis in the global reference frame. The body begins at rest, and a prescribed displacement is applied at t_0. This prescribed displacement represents the deceleration of the car body upon impact with the rigid wall. The longitudinal deceleration pulse measured at the center of gravity of the lead car in the CEM two-car full-scale impact test (C3X) is integrated twice to obtain this prescribed displacement. Figure G14 shows the measured acceleration, relative velocity, and relative displacement of the lead car body. An ellipsoid representing the floor of the car is fixed to the car body. Contact Characteristic A is applied to this surface (Figure G15).

The lead car system also includes the workstation table. In the original MADYMO model created during the sled testing of facing commuter seats, the table was represented by a faceted surface. However, this model was never validated, since the table detached from the wall attachment during the sled test. The faceted surface was since replaced with an ellipsoid for several reasons: first, the surface was represented by over one thousand elements, which took up a disproportionate amount of processor time; second, the table did not deform in previous tests and was not expected to deform in the CEM two-car test; and finally, comparative simulations showed that the effect of the tapered edge of the table was negligible. Since the table is assumed to be significantly more rigid than the impacting elements of the ATD, the contact characteristics built into the Hybrid III model are used to define the contact of the ATD with the table.

The table is attached to the car body by four point restraints: two at the wall, one between the table and the leg, and one between the table and the floor. These point restraints can be used to output the load cell measurements, which can be compared directly to the test data. Load Characteristic A is used to define these point restraints (Figure G16).

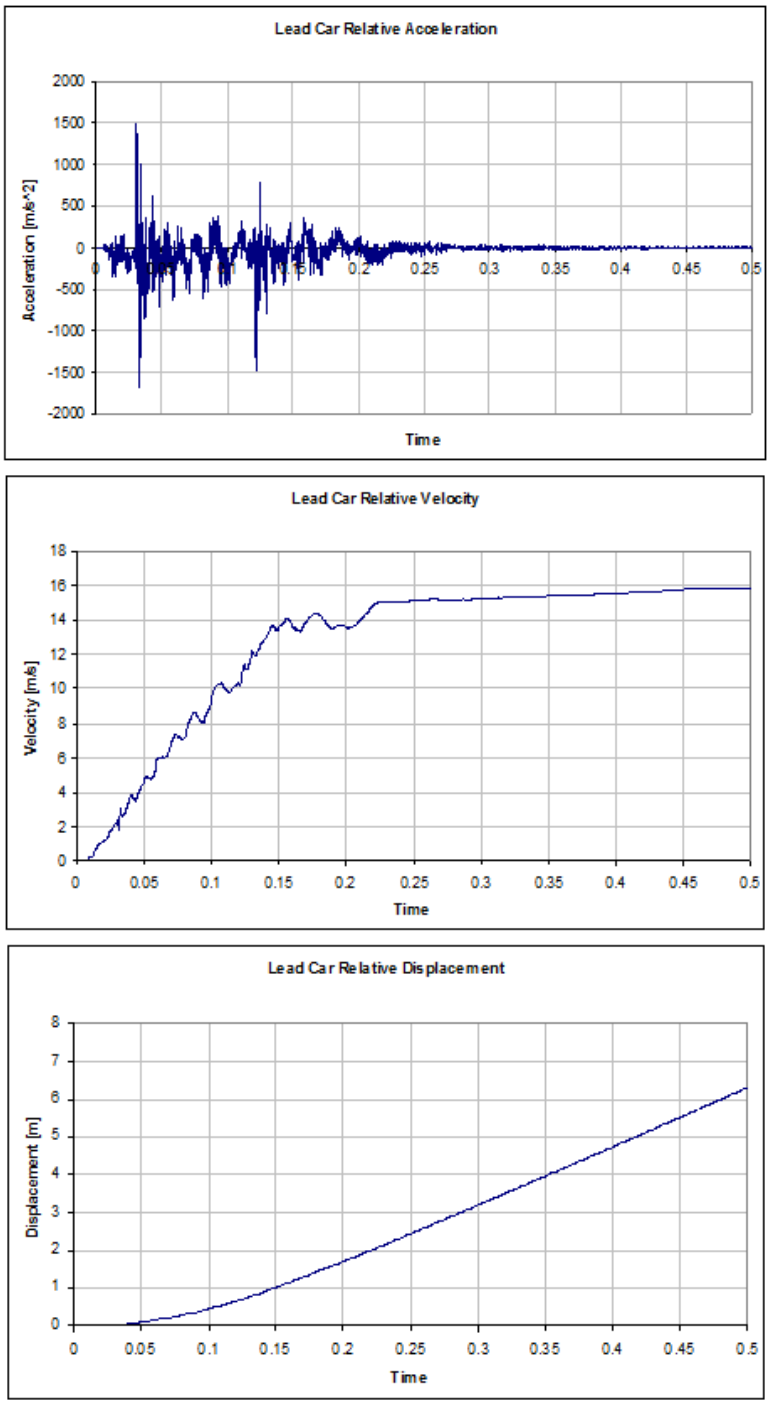

Figure G14. Measured Acceleration, Relative Velocity, and Relative Displacement of the Lead Car Body

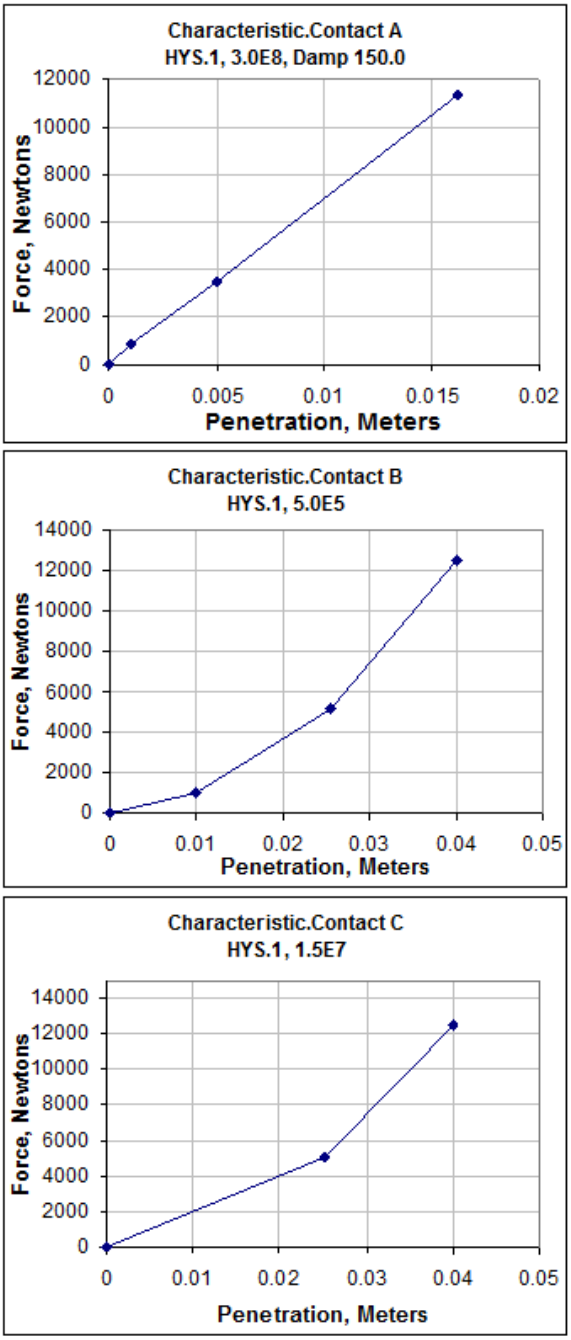

Figure G15. Contact Characteristics for MADYMO Model of Experiment 1-3

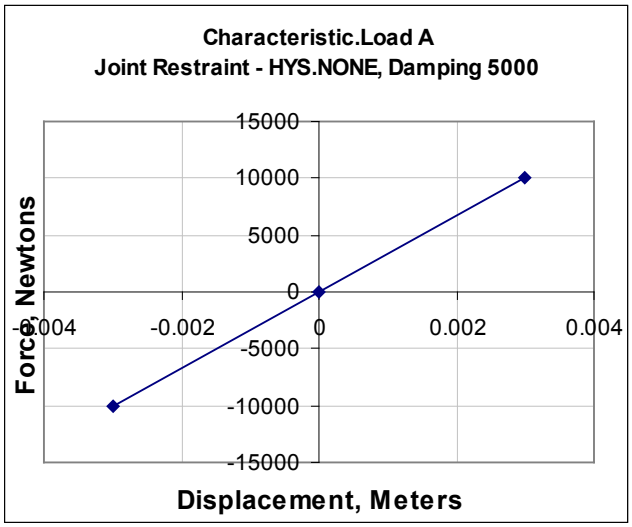

Figure G16. Load Characteristics for MADYMO Model of Experiment 1-3

System 2. Launch Seat

All the facing commuter seats were provided by Metrolink. These seats are arranged in back-to-back pairs attached to a common seat pedestal. This experiment included two such arrangements, which allowed for a total of eight seating positions. Only four seating positions are included in the model (the two pairs that face each other, straddling the table), as the other four seating positions face outward and do not see any interaction with the occupant (Figure G17).

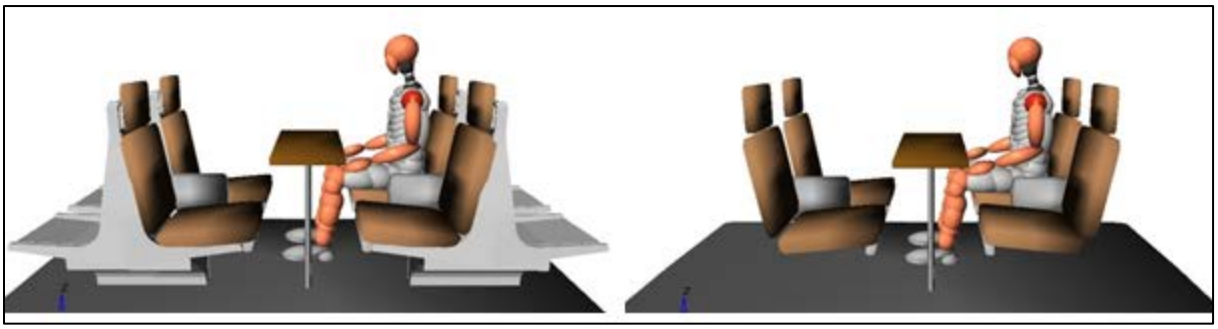

Figure G17. MADYMO Model of Experiment 1-3

The launch seat is modeled as one rigid body, since there is only minor interaction of the occupant with the launch seat. The seat base is attached to the lead car body by four point restraints. Load Characteristic A is used to define the point restraints. The point restraint loads can be output and compared to load cell measurements collected in previous experiments.

Contact Characteristic B (see Figure G15) is used to define the contact of the seated ATD with the seat cushion. This is important to achieve correlation with the initial kinematics from the test.

System 3. Struck Seat

The struck seat is identical to the launch seat, except that it is facing away from the impacted end of the lead car. The struck seat has been simplified from an earlier model of the facing seat

configuration without an intervening table. This earlier model included a breakaway headrest and detail contact characteristics for different locations of the seat. Since the only contact between the occupant and the struck seat is the interaction of the tibias and knees with the seat pan, this unnecessary detail has been removed. Contact Characteristic C (see Figure G15) is used to represent the lower portion of the seat cushion as well as the stiffer seat pan directly behind it.

System 4. Window Occupant

The occupant is represented by a 50th percentile THOR alpha version dummy in MADYMO, ellipsoid model version 1.3 (created November 10, 2003). The ATD is initially sitting on the right-hand side (facing the impacted end of the lead car) of the launch seat pair. The initial position of the ATD was modified to match the initial position of the THOR in the test.

In the pre-test simulation, the rotation of the upper body towards the tabletop and the pelvis and femurs towards the bottom of the table was not as pronounced as in the full-scale test. This occurred partly because the lumbar spine pitch change bracket fractured during the impact of the ATD with the table. A review of the test data showed that this event occurred at 109 ms after t_0 (impact of the lead car with the wall). Thus, in the simulation, the lumbar spine pitch change joint is unlocked at t = 109 ms. This allowed the THOR upper body to rotate about the table contact point close to the extent seen in the high-speed film. All other ATD model parameters remained unchanged.

Experiments 2-1 and 2-2: Rear- and Forward-Facing Commuter Seats

Experiment 2-1 consisted of a single modified rear-facing three-person M-Style commuter seat. The seat pedestal and attachment to the floor were strengthened in the same manner as the seat tested in the trailing car of the two-car conventional test. One Hybrid III 50th-percentile ATD was positioned in the middle seat position (Figure G18). The experiment was located in the front of the trailing coach car on the left side.

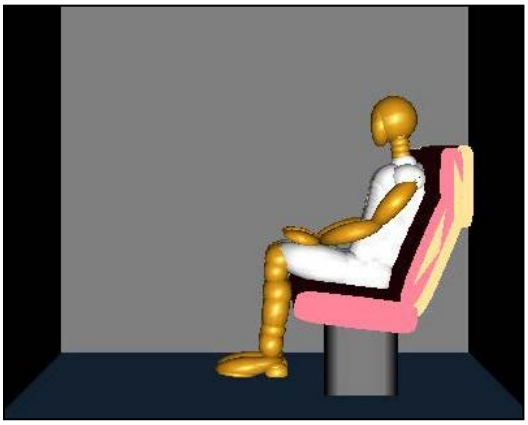

Figure G18. Hybrid III 50th-Percentile ATD in the Middle Seat Position

Experiment 2-2 consisted of two forward-facing three-person M-Style commuter seats. The forward seat was modified as described above for Experiment 2-1. Instrumented Hybrid III 50th-percentile male ATDs were located in the window and aisle positions of the rear seat. An uninstrumented Hybrid II 50th-percentile male ATD was located in the middle seat position (Figure G19).

Figure G-19. Uninstrumented Hybrid II 50th-Percentile Male ATD in the Middle Seat Position

The computer model of the commuter seat was based on a model developed by Simula Technologies, Inc. in conjunction with static and dynamic testing of the M-Style commuter seat [31]. The commuter seat model was modified to reflect structural modifications made to the seats used in previous full-scale tests. The rear-facing and forward-facing seat/occupant models were exercised prior to the test to predict results from the two-car CEM test. Subsequent to the test, the parameters have been modified to achieve better agreement between the test and model results, in terms of occupant kinematics, load and acceleration time-histories, and injury criteria.

Model Description

Each model is made up of several systems representing the car body, the seats, and the occupants. Each system is described in detail below.

System 1: Reference Space (Car Body)

The trailing coach car is represented by the reference space. Surface planes representing the floor and side wall are attached to the reference space. The motion of all systems is described with respect to this space.

An acceleration time history is applied to the reference space. This acceleration time history represents the motion of the trailing car during impact. Prior to the test, the occupant model used acceleration data that was calculated from a separate rigid body dynamics model of the two-car CEM test. After the test, the acceleration data was replaced with actual test data measured from accelerometers mounted to the car body.

System 2: Seats

The rear-facing occupant model has one three-passenger commuter seat, which is the launch seat. It is facing away from the impact, towards the rear of the car. The forward-facing occupant model has two identical rows of three-passenger commuter seats. They are placed 32 inches apart, and face the front of the car. Each seat is made up of two rigid bodies, a seat base, and a seat back. Each seat base is attached to the floor and wall by means of point restraints, which act as very stiff springs (k = 1.0E+08) that calculate the triaxial load at the seat attachment points. These loads can be compared to those measured with triaxial load cells during previous full-scale tests. A revolute joint connects the seat base and seat back to one another. Cylinders,

representing cushions and seat contact surfaces (Figure G20), are attached to the rigid bodies and have prescribed force vs. crush characteristics.

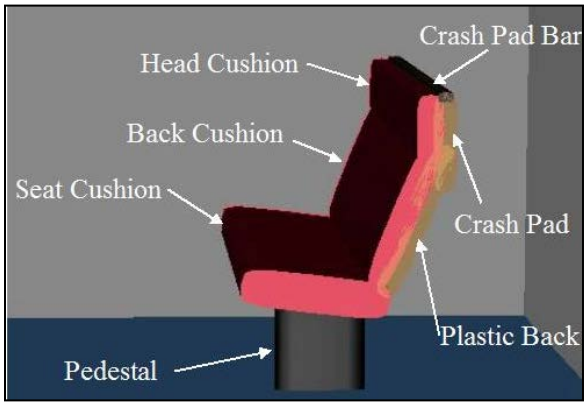

Figure G20. Cylinder Identification

The force vs. crush characteristics for the head cushion, back cushion, seat cushion, and plastic seat back are shown in Figure G21. The force vs. crush characteristic for the crash pad bar is linear with k = 1.0E+05 N/m. The force vs. crush characteristic for the crash pad is also linear with k = 3.33E+04 N/m. The moment vs. rotation characteristic for the revolute joint between the seat base and seat back is shown in Figure G22.

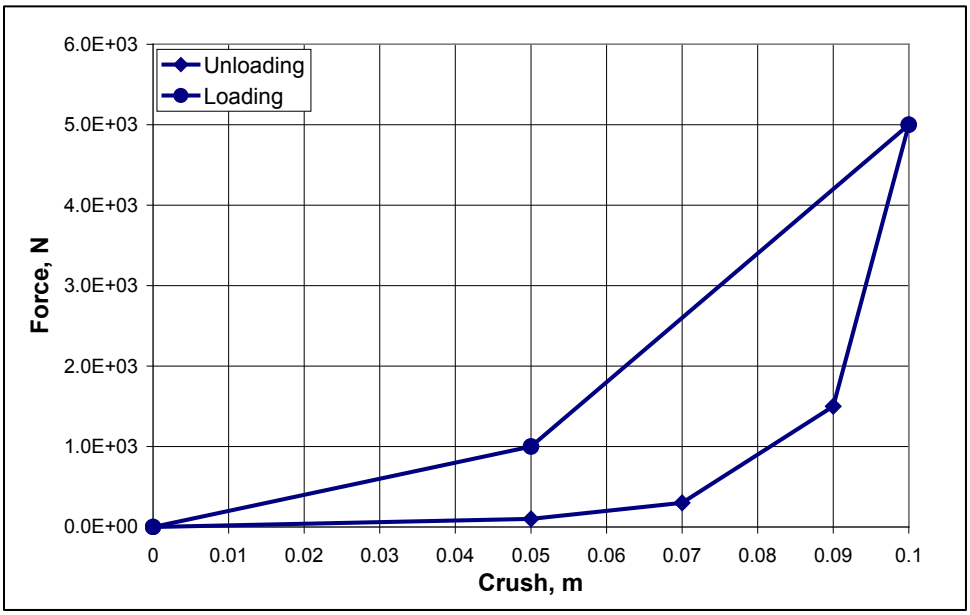

Figure G21. Force vs. Crush of Contact Surfaces

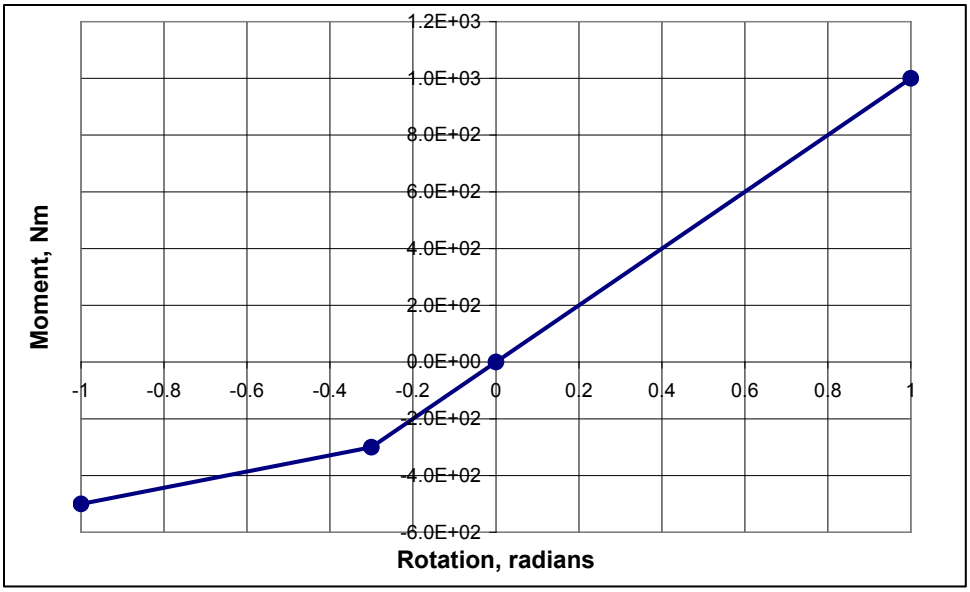

Figure G22. Moment vs. Rotation of Seat Back

The seat components represented by the various cylinders are self-evident based on the name identification, except possibly the crash pad bar. At the top of the seat back is a steel bar that runs along the top of the entire seat, which is covered by a thin layer of padding. The load and acceleration time-histories measured from the rear-facing ATD during the test indicate that the head makes contact with this bar. The head acceleration time history measured in the test was used to calibrate the effective stiffness of this contact surface at the top of the seat back. In the forward-facing commuter seat experiment, the ATDs' heads strike the face of the crash pad and do not appear to make contact with the steel crash pad bar.

System 3: Occupants

The rear-facing commuter seat experiment had a single Hybrid III 50th-percentile male ATD positioned in the middle seat position. The forward-facing commuter seat experiment had three 50th-percentile male ATDs: two Hybrid III ATDs were positioned in the aisle and window positions, and a Hybrid II was in the middle seat. The HIII has a more biofidelic neck capable of measuring and evaluating neck injury.

The ellipsoid models of the 50th-percentile ATDs were developed by TNO Automotive, © 2001. The ATD models were not modified for the commuter seat models. The initial joint positions and orientations were modified to match the initial joint positions and orientations of the ATDs in the CEM test.

Appendix H. Occupant Modeling and Test Results

Experiment 1-1. Forward-Facing Intercity Seats

Dynamics

The following section contains plots of the force, acceleration, and displacement time-histories recorded from two Hybrid III 95th percentile male ATDs seated in forward-facing intercity seats. The experiment was located near the front of the lead car. The corresponding time-histories from the ATDs in the MADYMO model of Experiment 1-1 are plotted against the test data for direct comparison. The CFC filter frequency (in accordance with SAE J211-1) is indicated on each plot. The HIC injury criteria calculated from the test and model results are located on the head resultant acceleration plots. The chest injury criteria (3 ms clip) are located on the chest resultant acceleration plots. The neck injury criteria (Nij) are located on the neck bending M_y moment plots.

Aisle Occupant

Acceleration Time-Histories

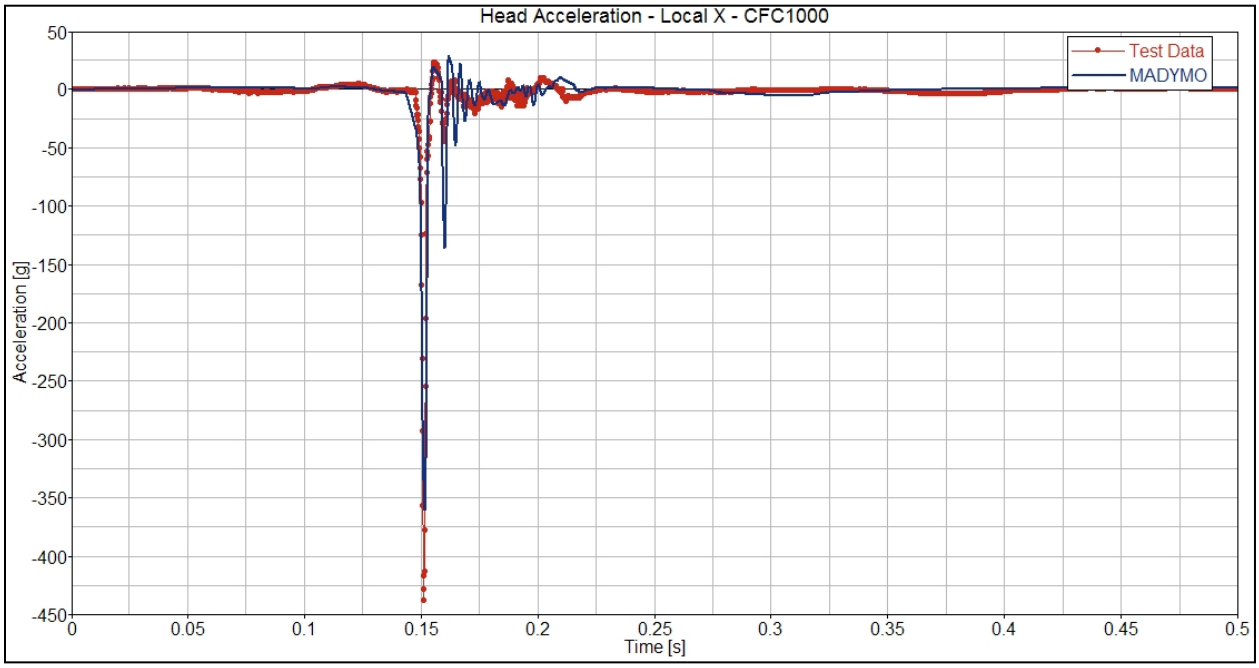

Figure H1. Head CG Acceleration, Local X

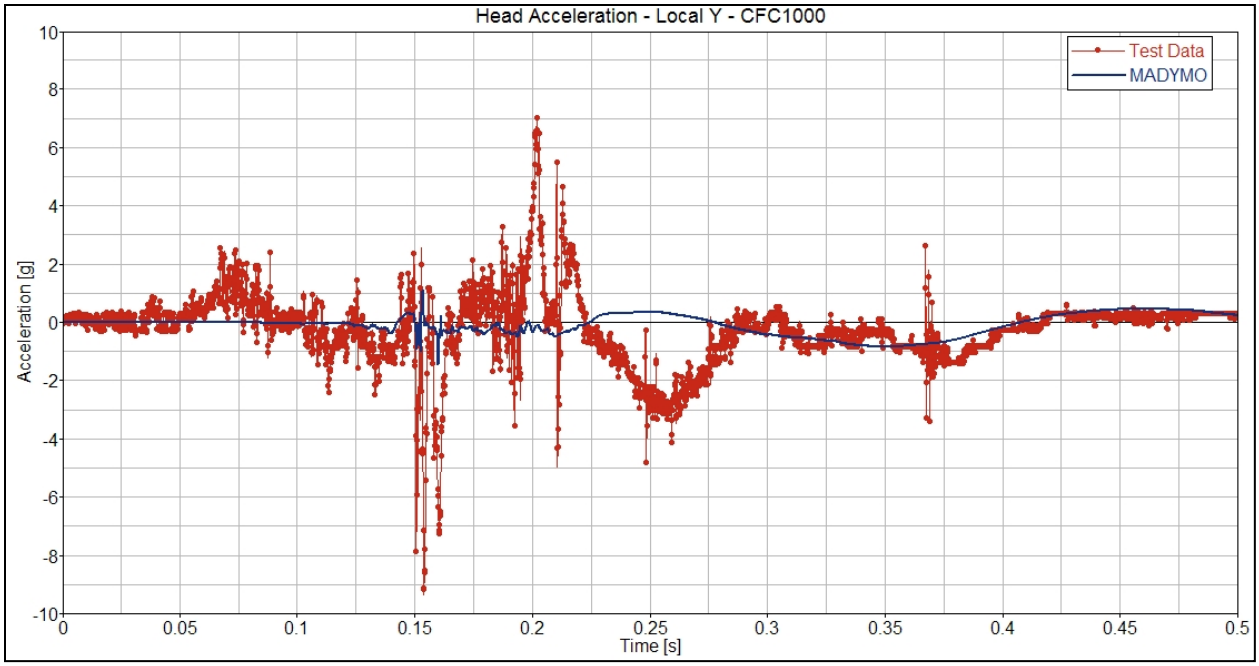

Figure H2. Head CG Acceleration, Local Y

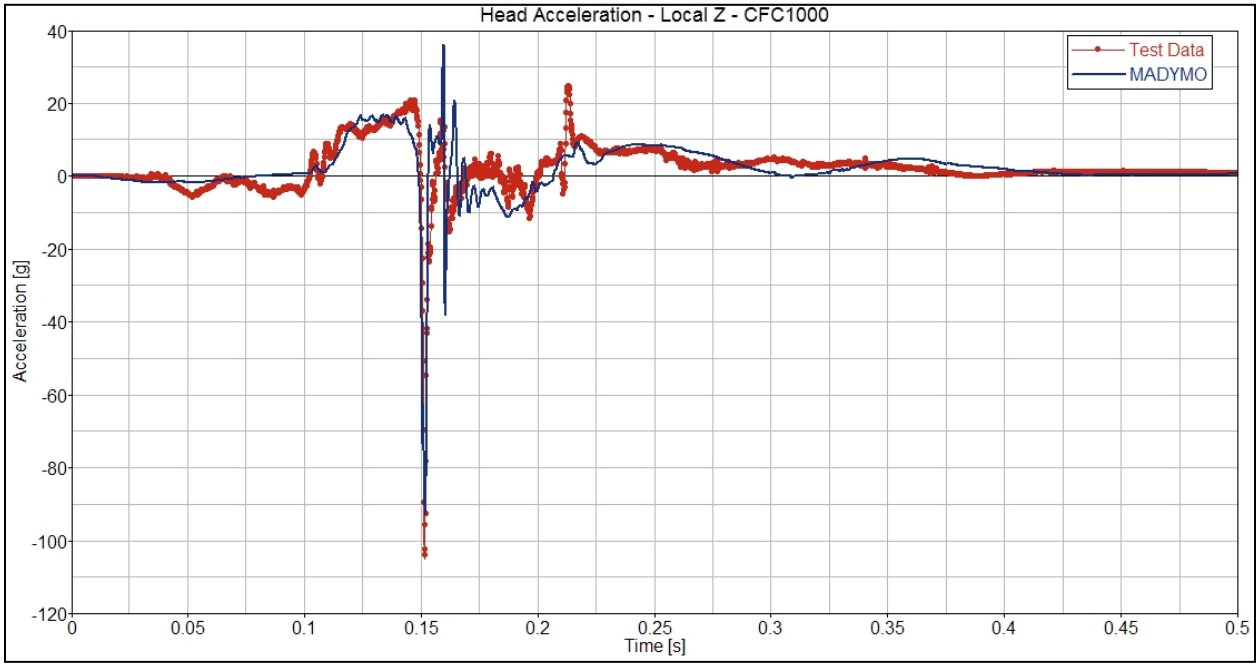

Figure H3. Head CG Acceleration, Local Z

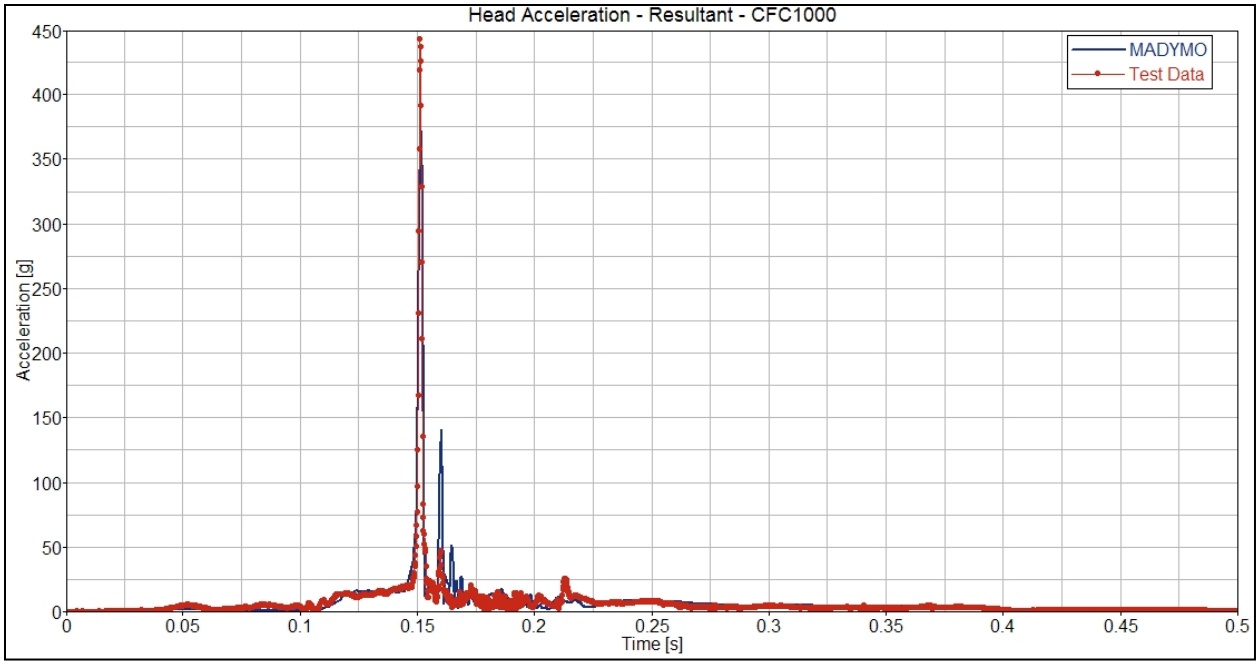

Figure H4. Head CG Acceleration, Resultant

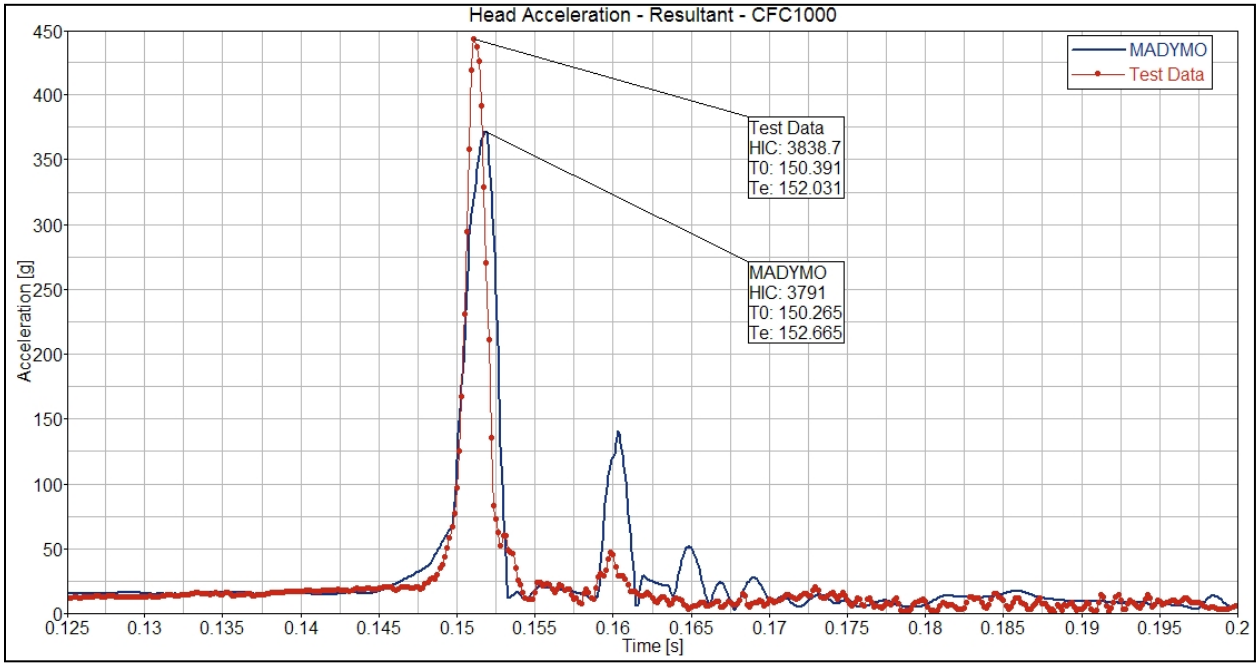

Figure H5. Head CG Acceleration, Resultant

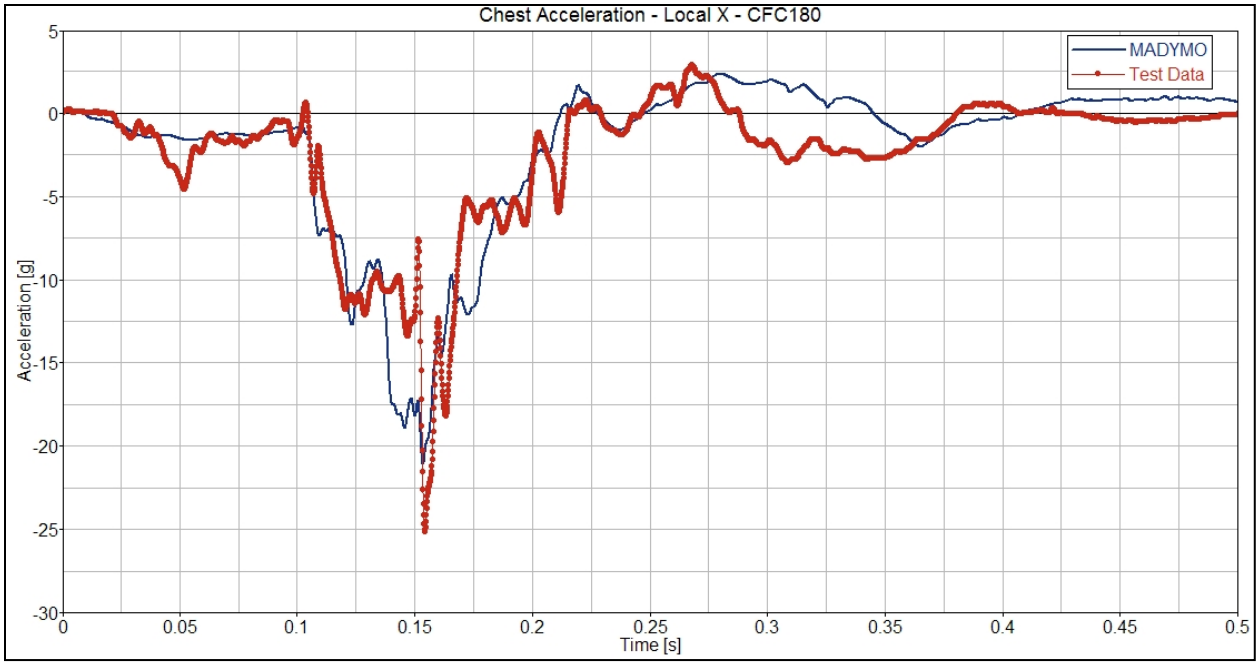

Figure H6. Chest Acceleration, Local X

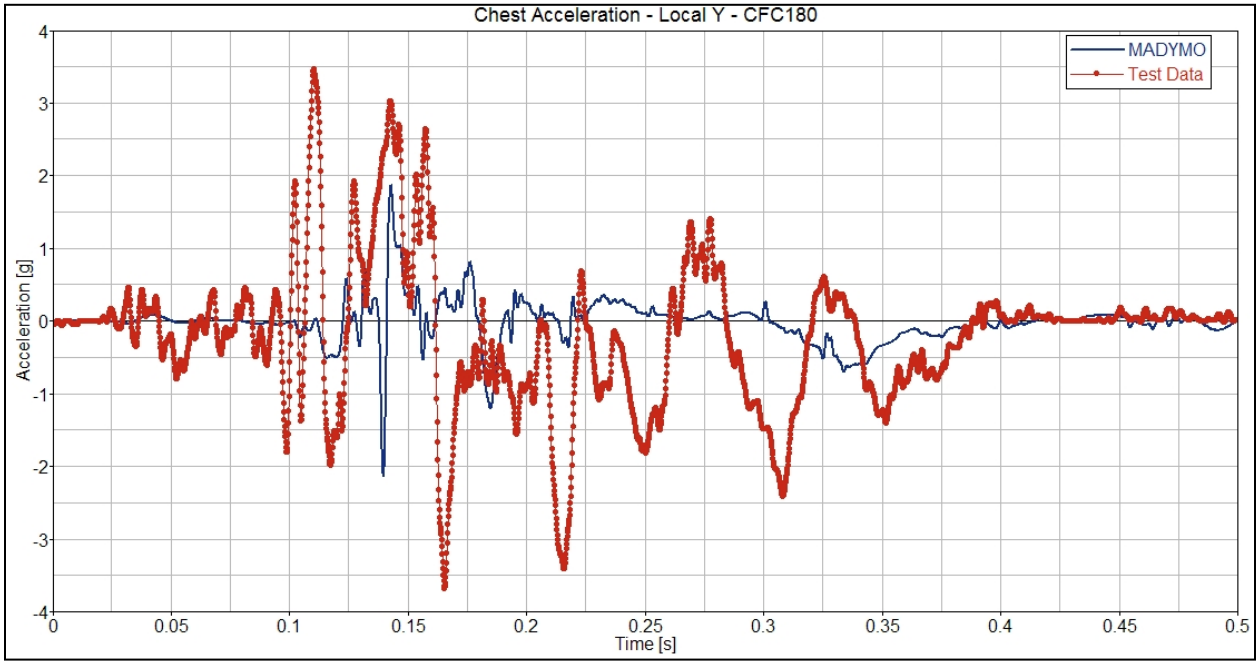

Figure H7. Chest Acceleration, Local Y

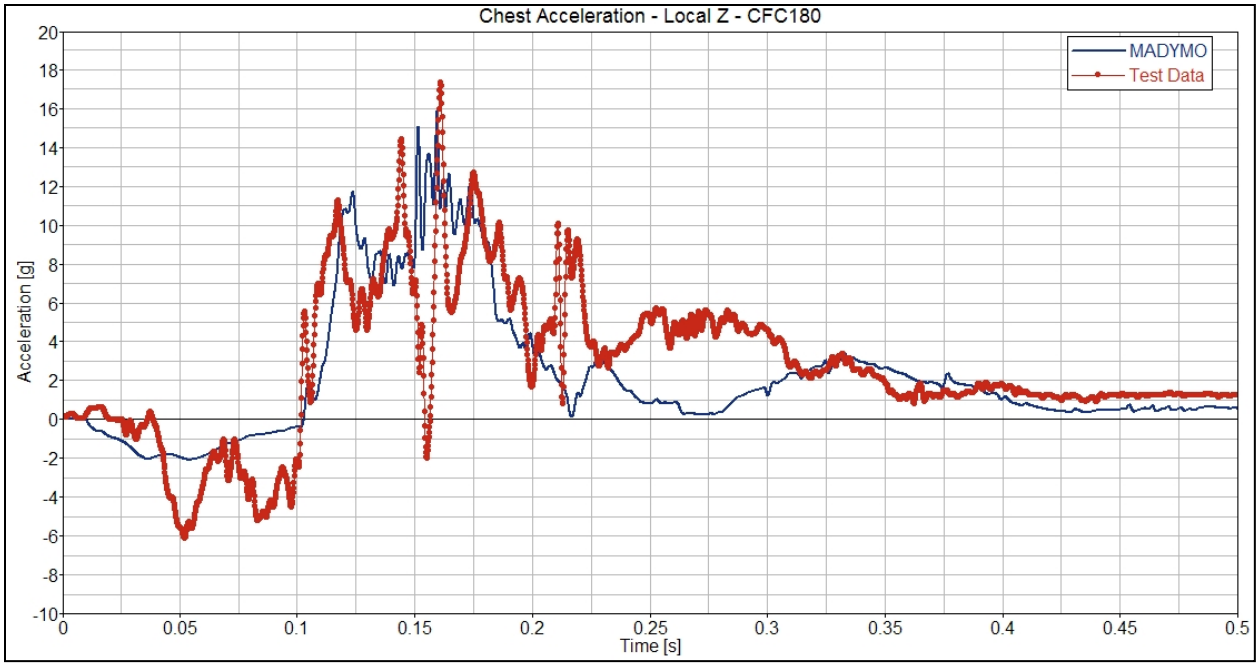

Figure H8. Chest Acceleration, Local Z

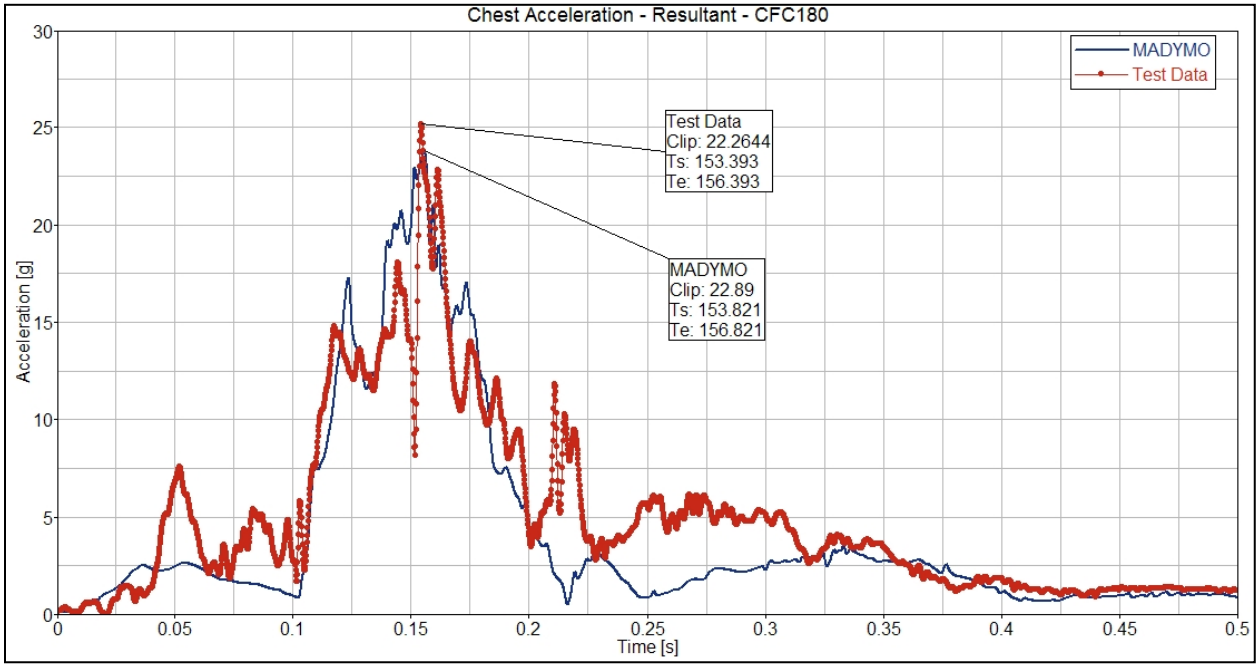

Figure H9. Chest Acceleration, Resultant

Force Time-Histories

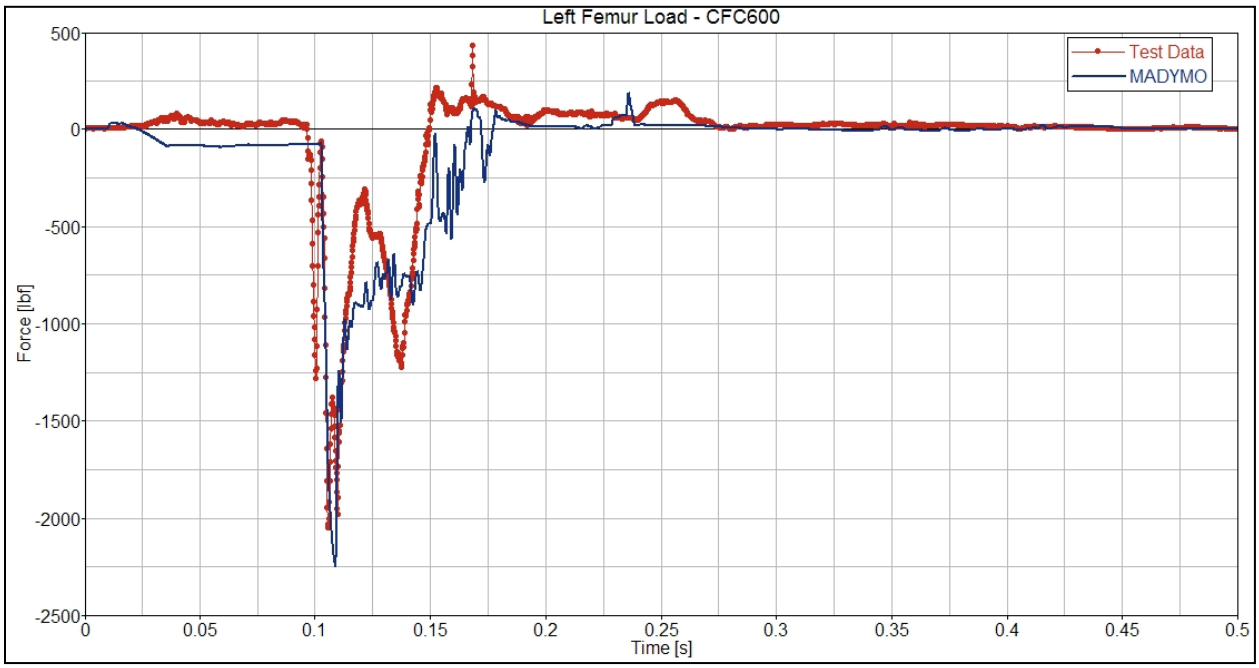

Figure H10. Left Femur Force, Local X

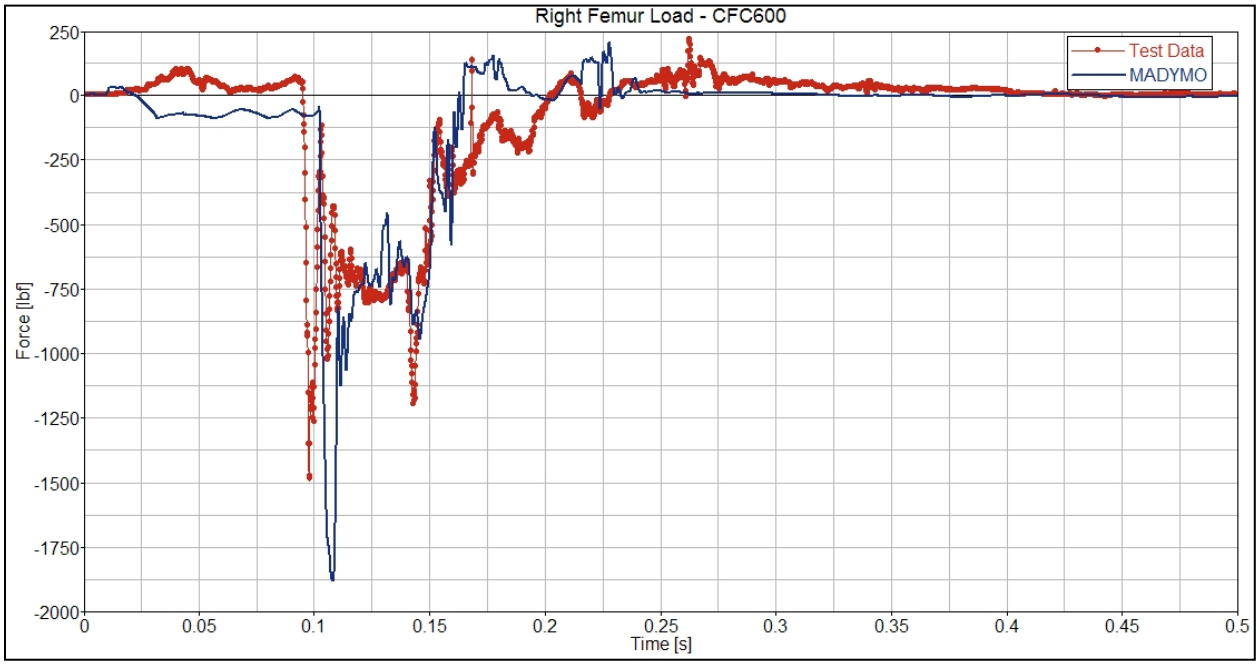

Figure H11. Right Femur Force, Local X

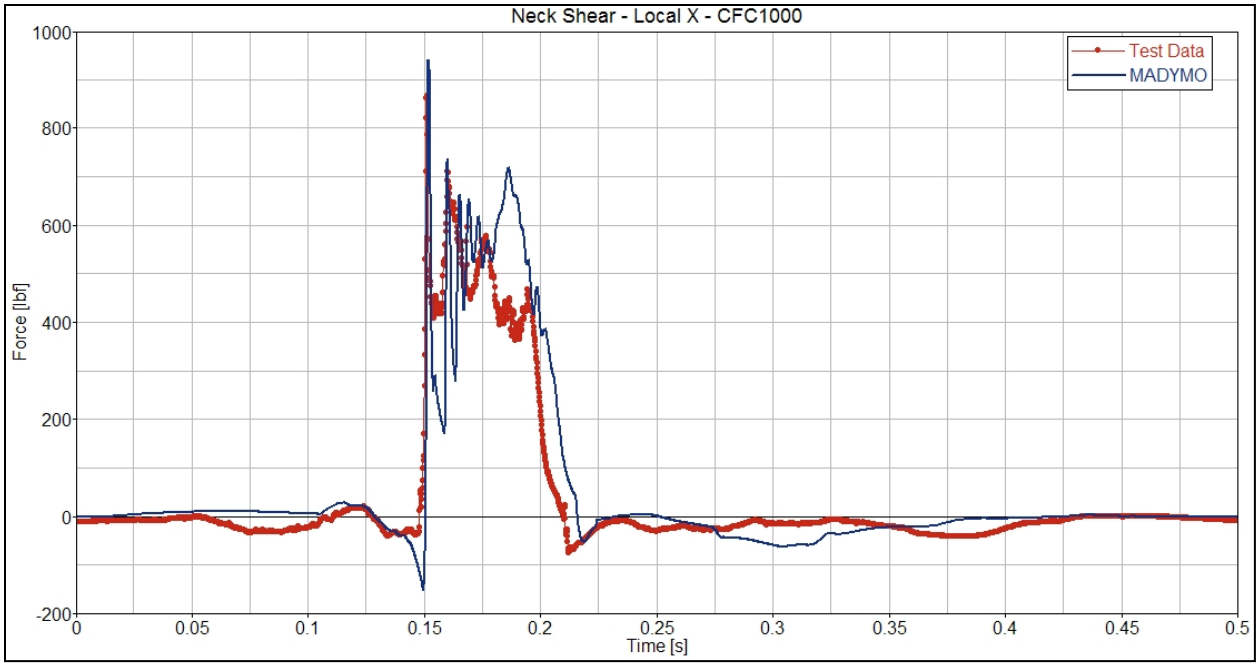

Figure H12. Upper Neck Shear Force, Fx

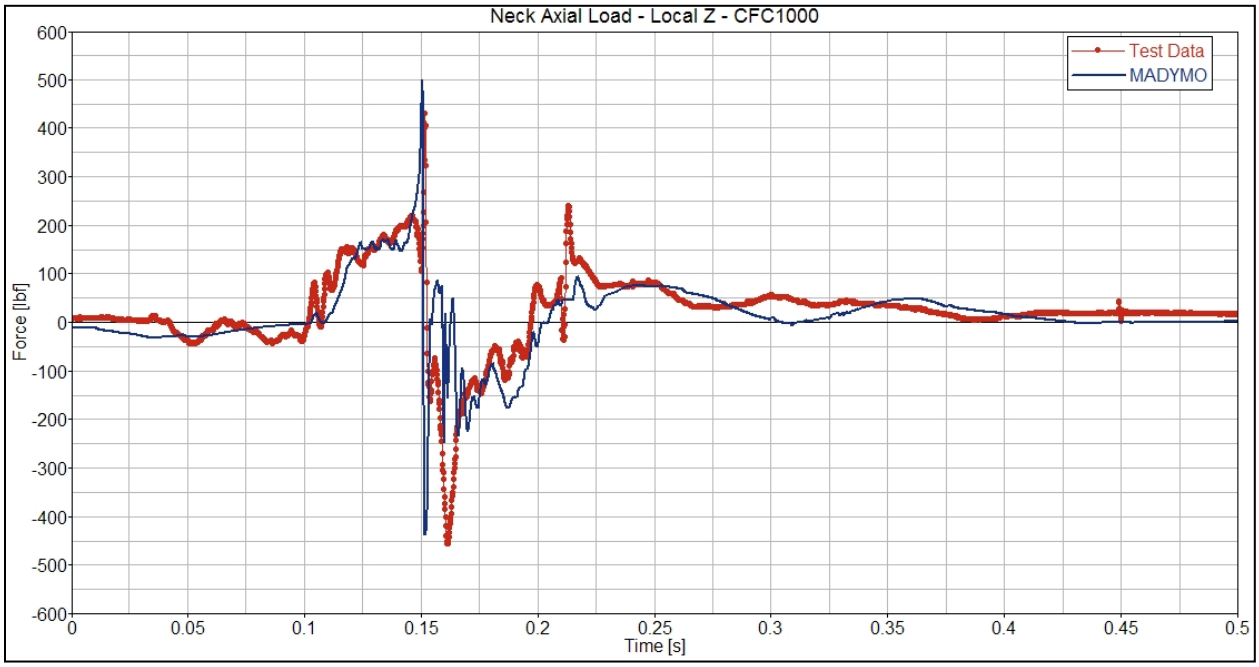

Figure H13. Upper Neck Axial Force, Fz

Moment Time-Histories

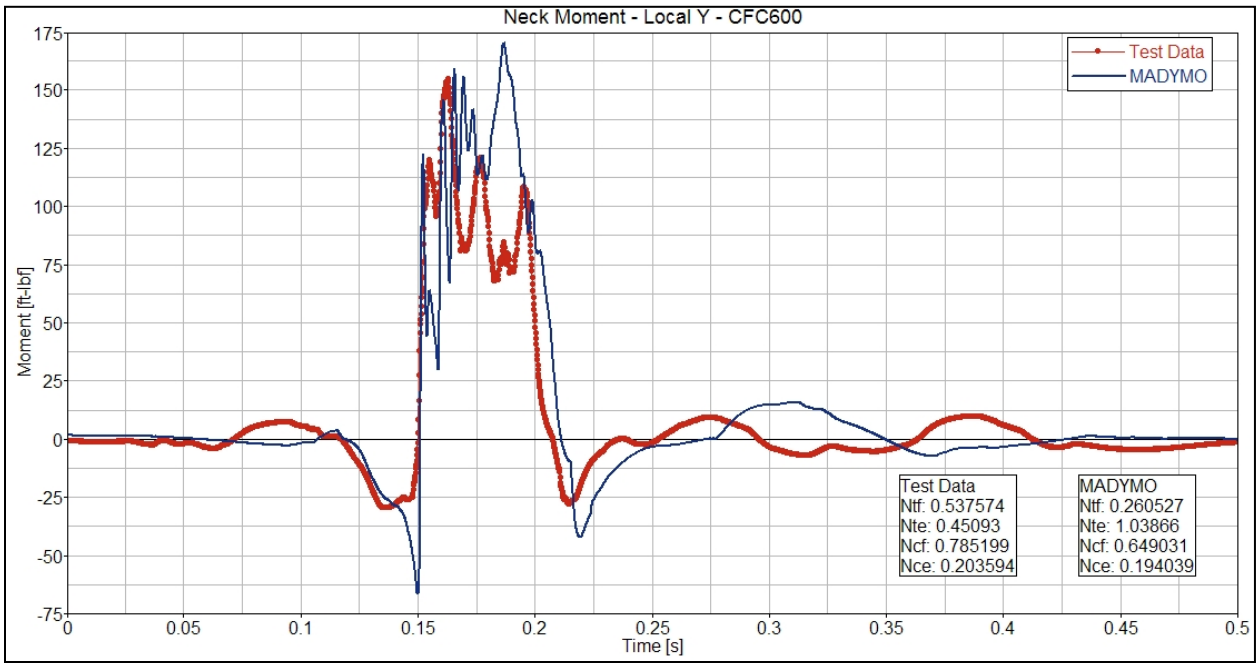

Figure H14. Upper Neck Occipital Condyle Bending Moment, M_y

Window Occupant

Acceleration Time-Histories

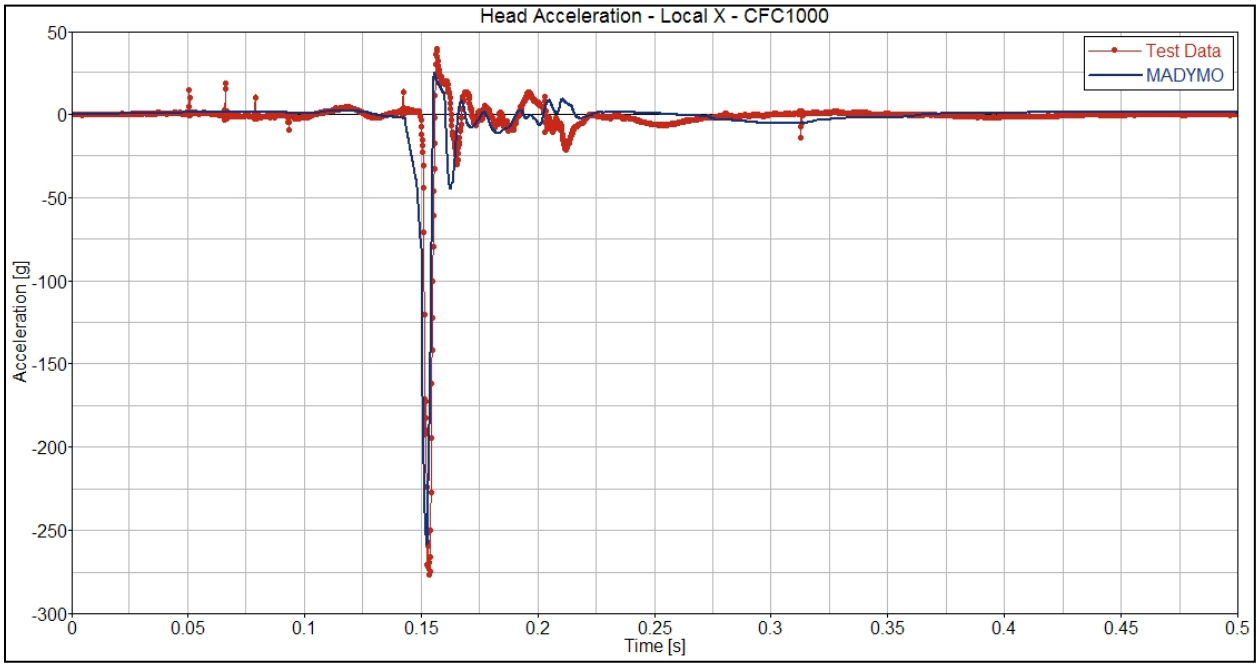

Figure H15. Head CG Acceleration, Local X

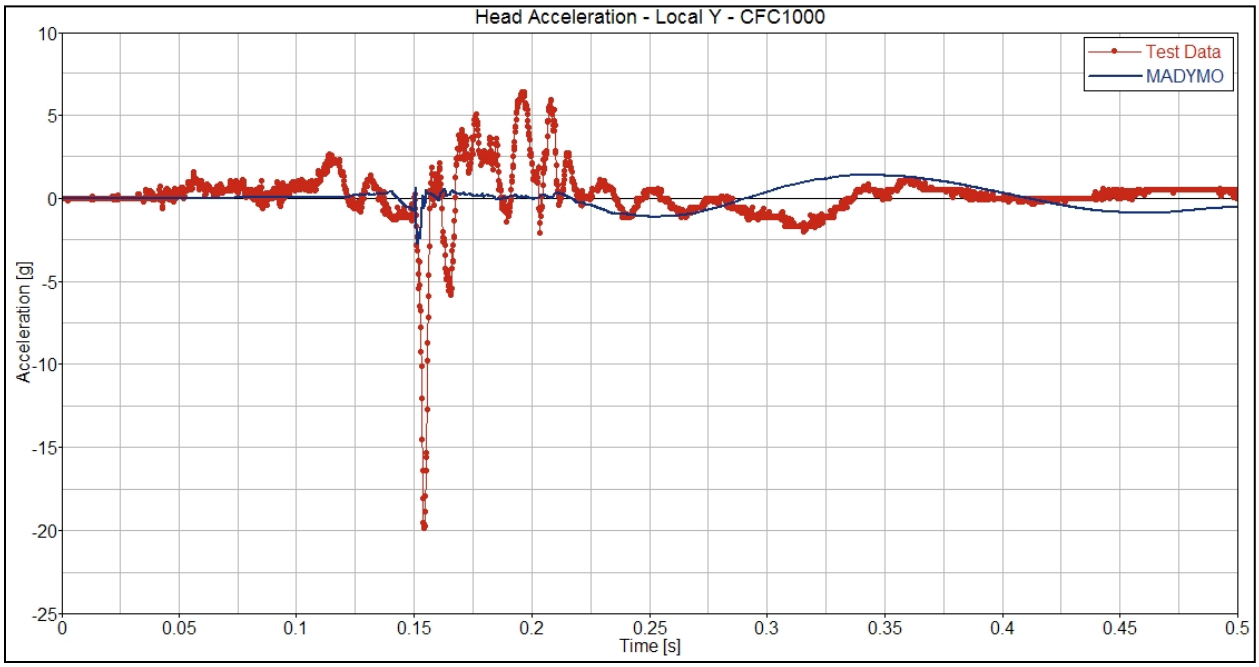

Figure H16. Head CG Acceleration, Local Y

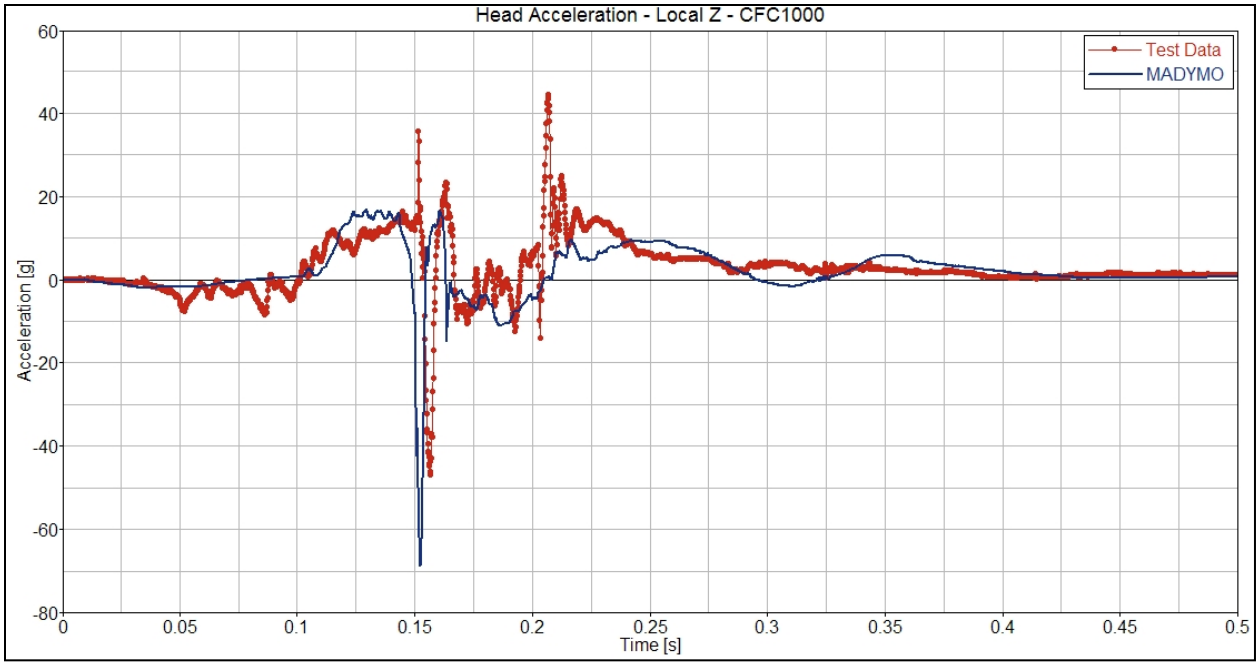

Figure H17. Head CG Acceleration, Local Z

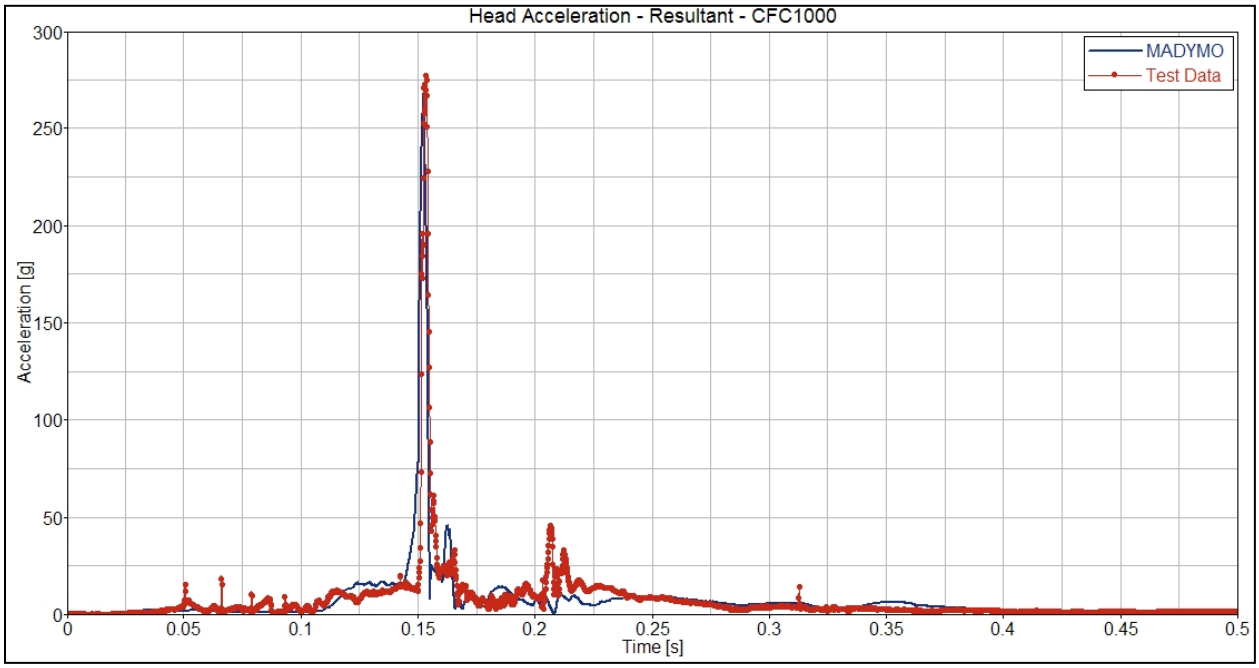

Figure H18. Head CG Acceleration, Resultant

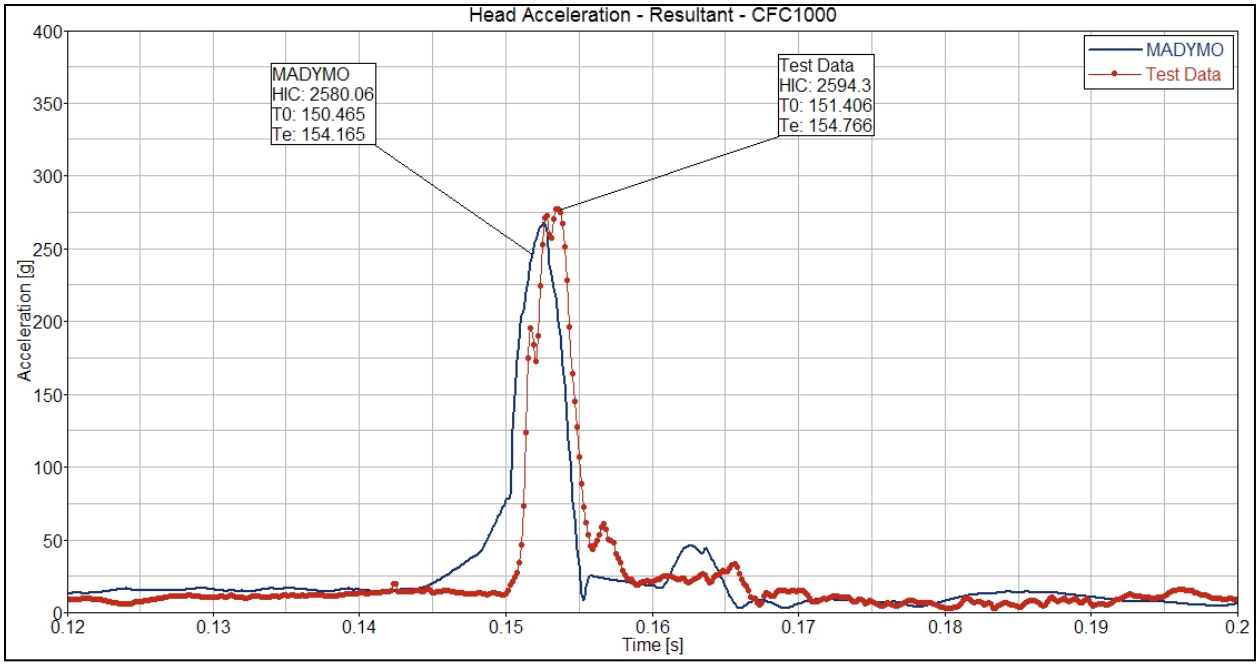

Figure H19. Head CG Acceleration, Resultant

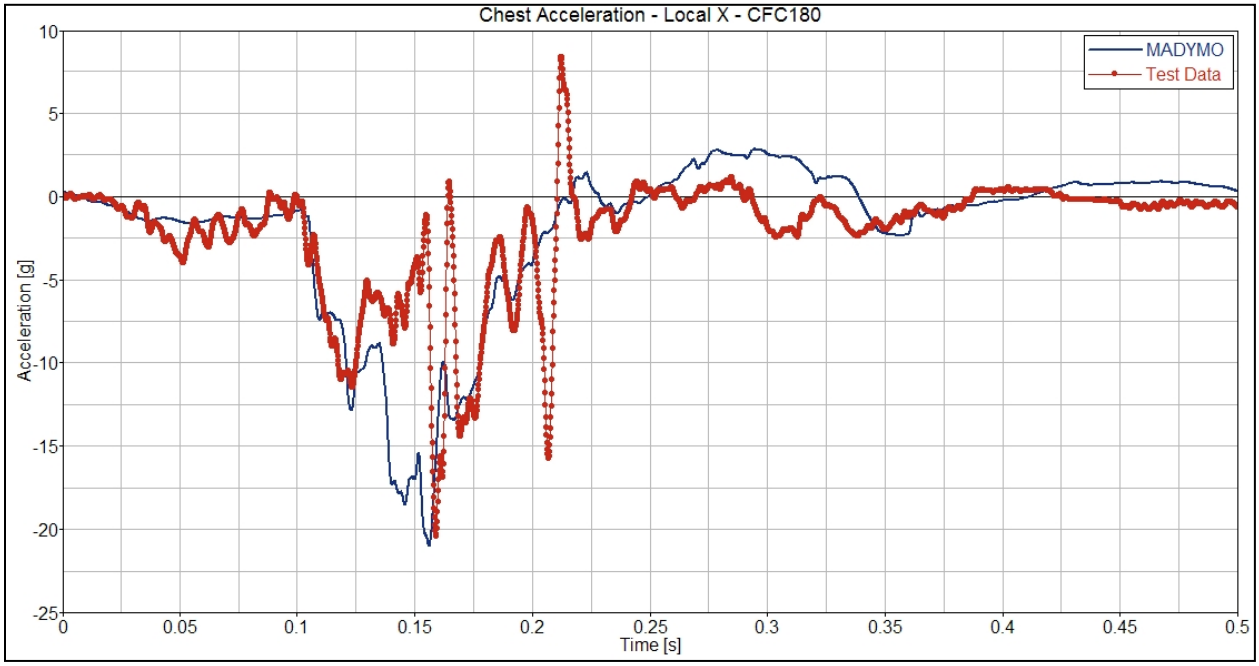

Figure H20. Chest Acceleration, Local X

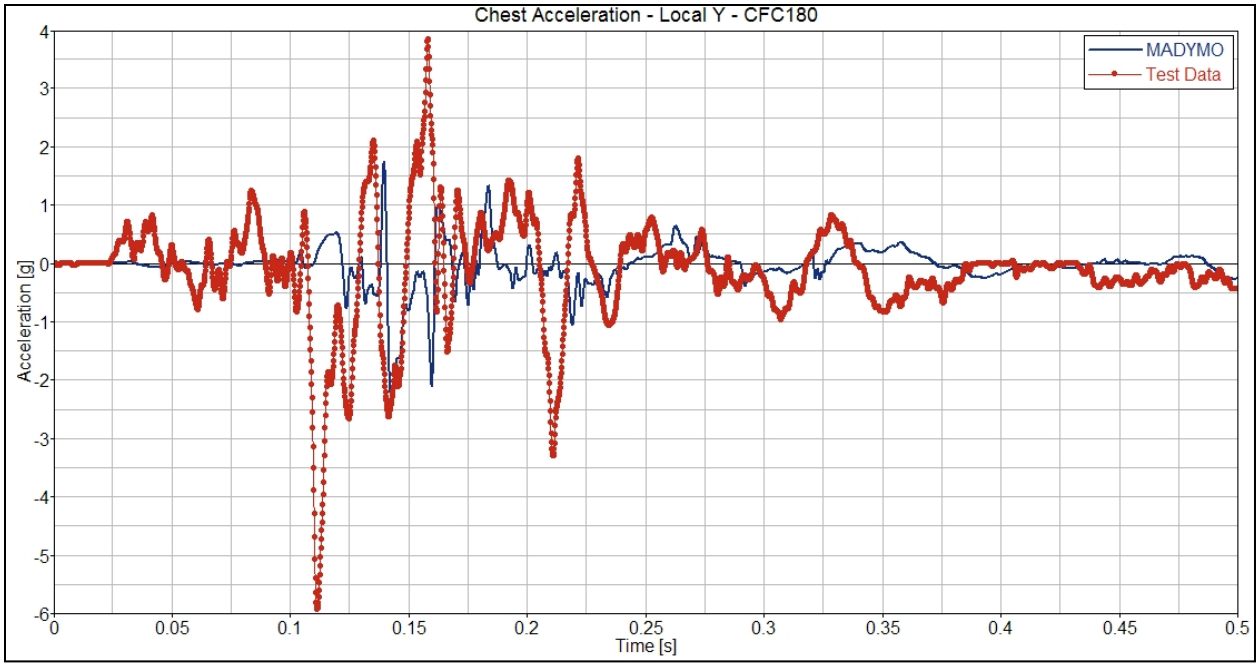

Figure H21. Chest Acceleration, Local Y

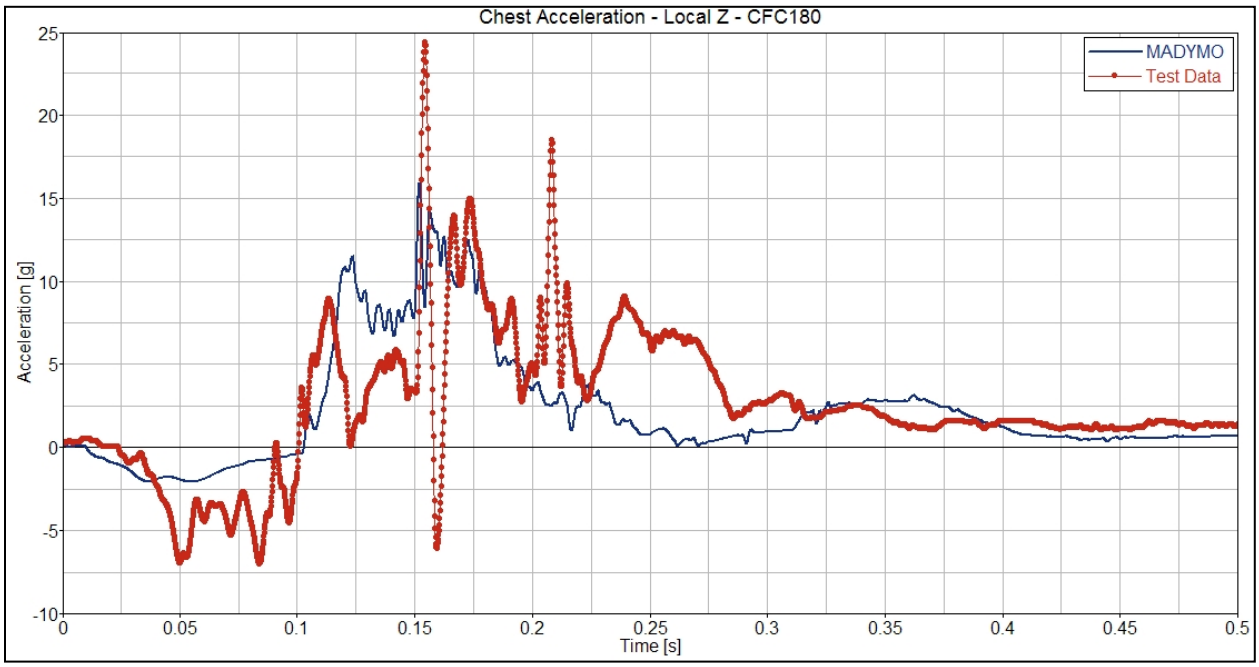

Figure H22. Chest Acceleration, Local Z

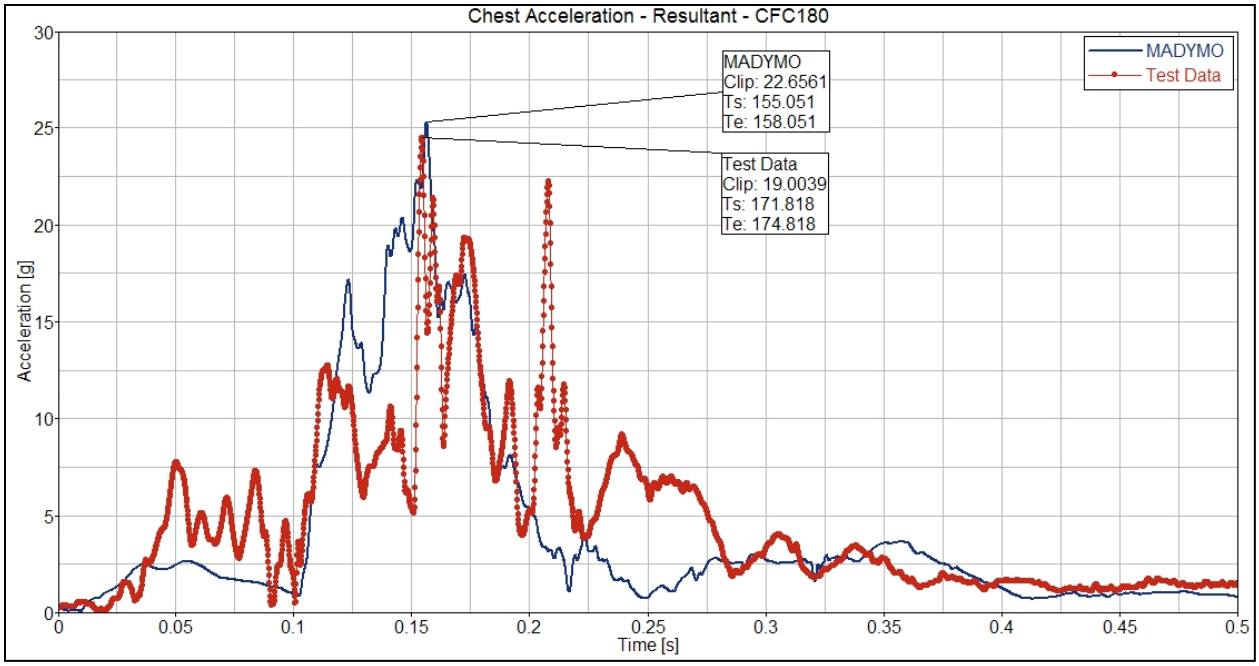

Figure H23. Chest Acceleration, Resultant

Force Time-Histories

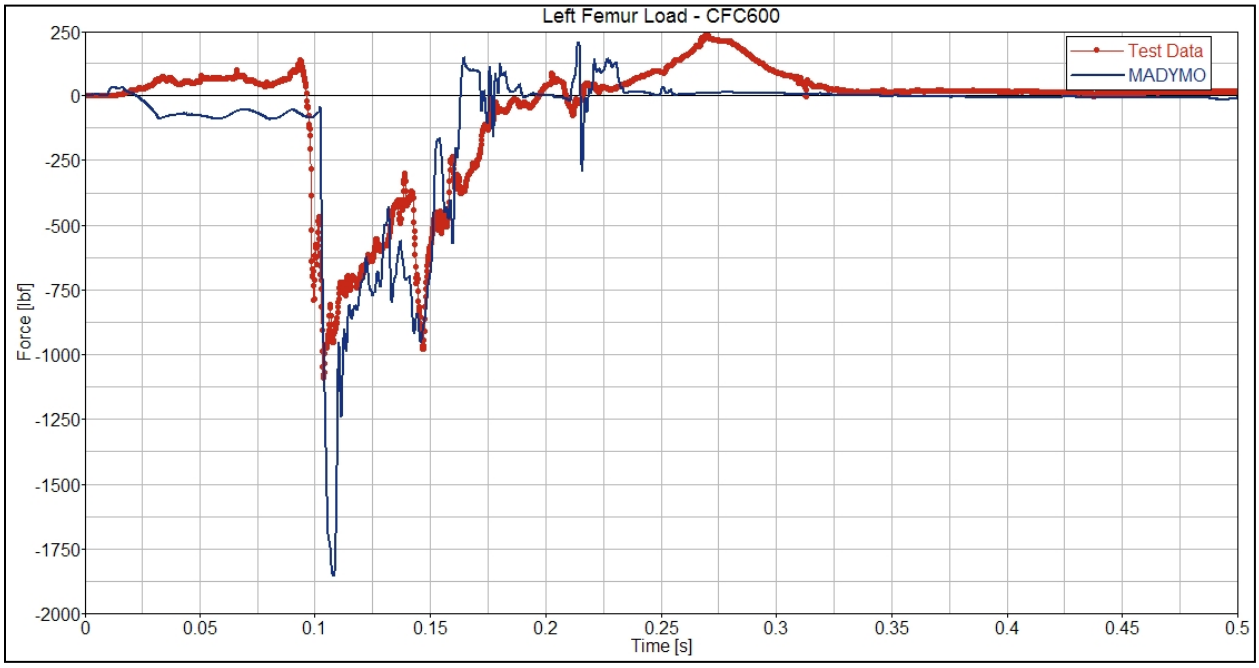

Figure H24. Left Femur Force, Local X

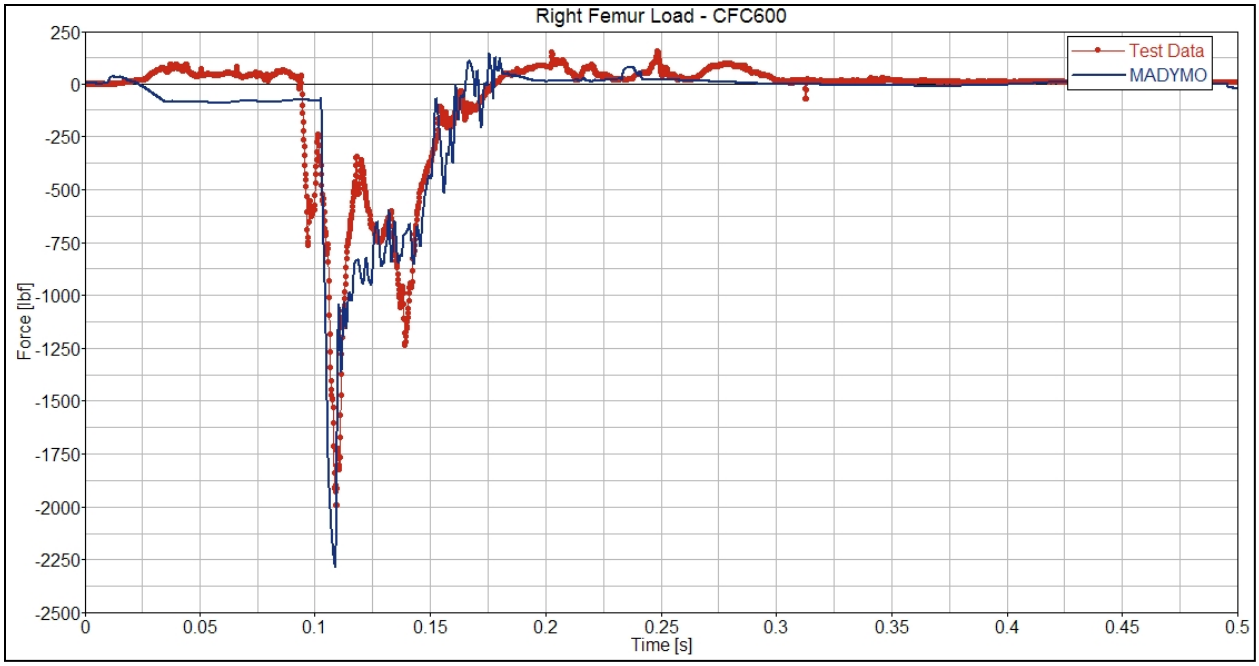

Figure H25. Right Femur Force, Local X

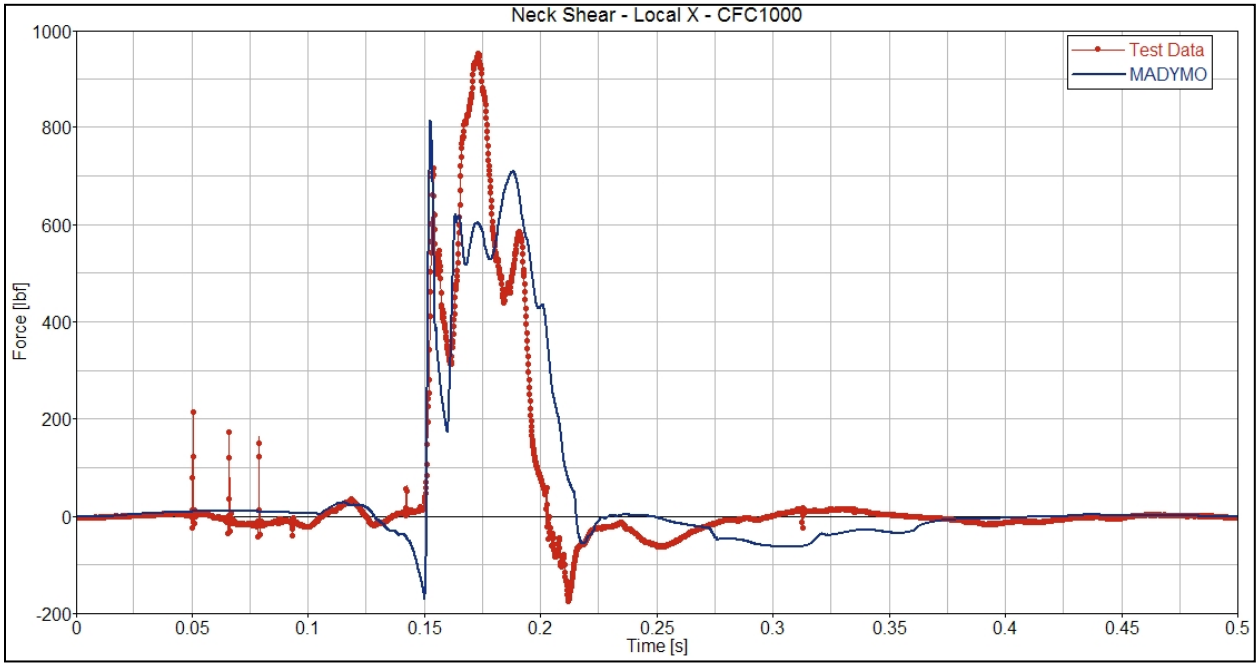

Figure H26. Upper Neck Shear Force, Fx

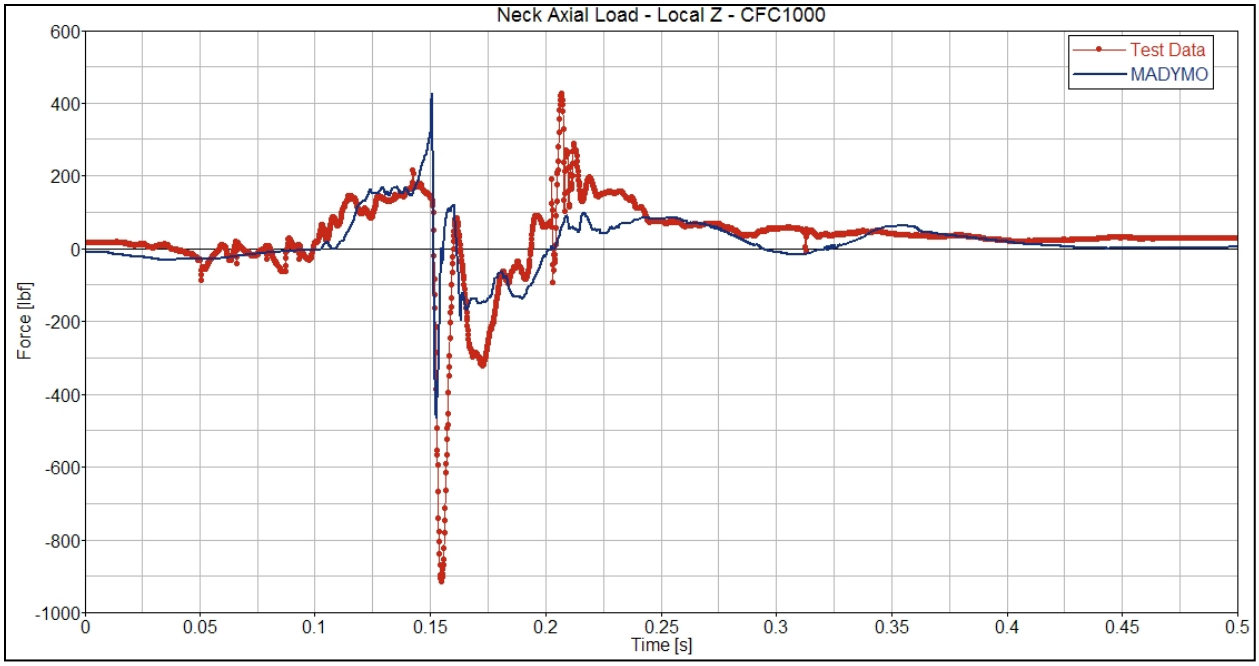

Figure H27. Upper Neck Axial Force, Fz

Moment Time-Histories

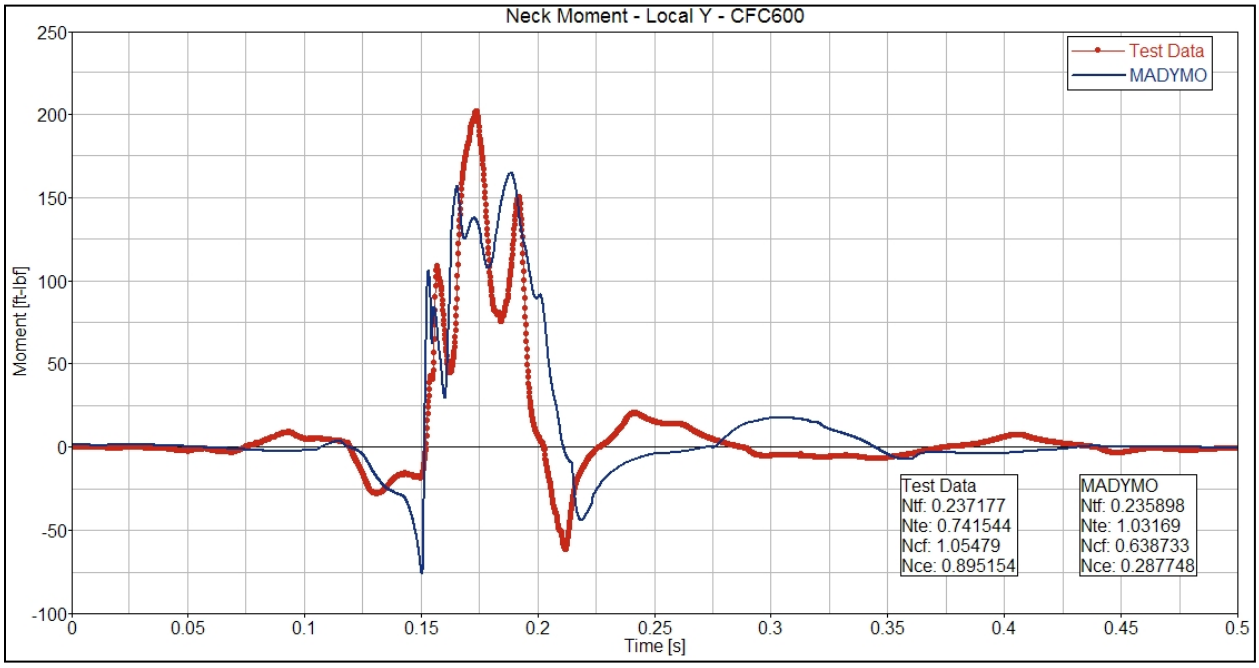

Figure H28. Upper Neck Occipital Condyle Bending Moment, M_y

Kinematics

A series of time-sequence pictures of the ATD kinematics are presented in this section. The pictures are taken from the test video and the MADYMO model output and presented together for comparison.

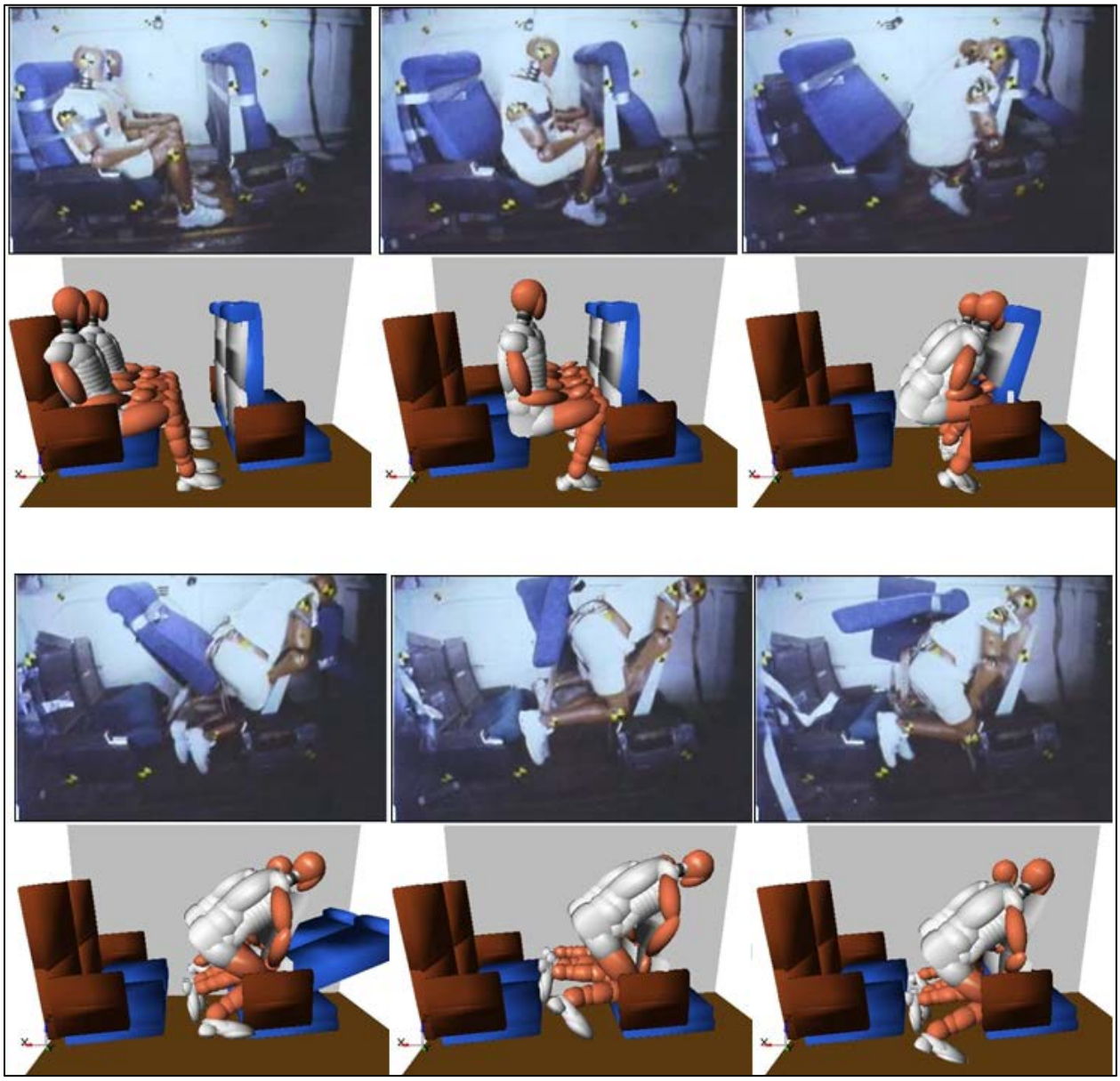

Figure H29. Test Dummy Kinematics in Forward-Facing Rows of Seats, Simulation Results and Test Observations

Experiment 1-2. Facing Seats with Workstation Table

Dynamics

The following section contains plots of the force, acceleration, and displacement time-histories recorded from the Hybrid III Railway Safety (Hybrid 3RS) ATD seated in the window seat position of the facing commuter seats with intervening workstation table. The experiment was located near the rear of the lead car. The corresponding time-histories from the ATD in the MADYMO model of Experiment 1-2 are plotted against the test data for direct comparison. The CFC filter frequency used in accordance with SAE J211-1 is indicated on each plot. The HIC injury criteria calculated from the test and model results are located on the head resultant acceleration plots. The chest injury criteria (3 ms clip) are located on the chest resultant acceleration plots. The neck injury criteria (Nij) are located on the neck bending M_y moment plots.

Acceleration Time-Histories

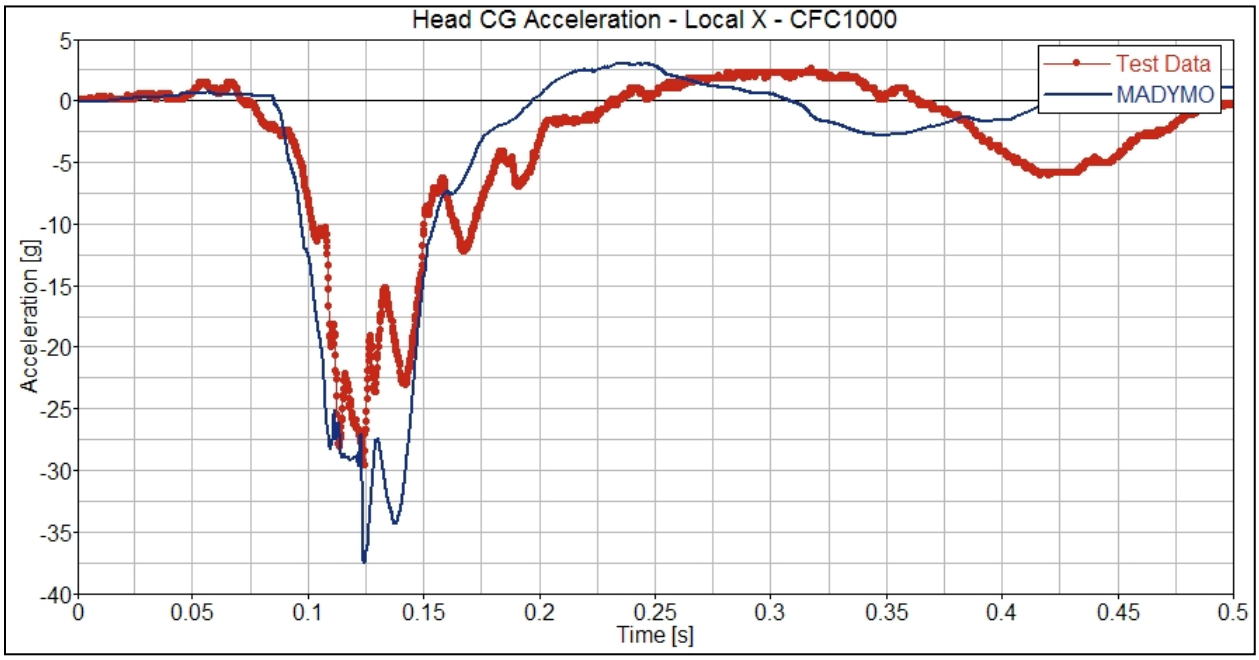

Figure H30. Head CG Acceleration, Local X

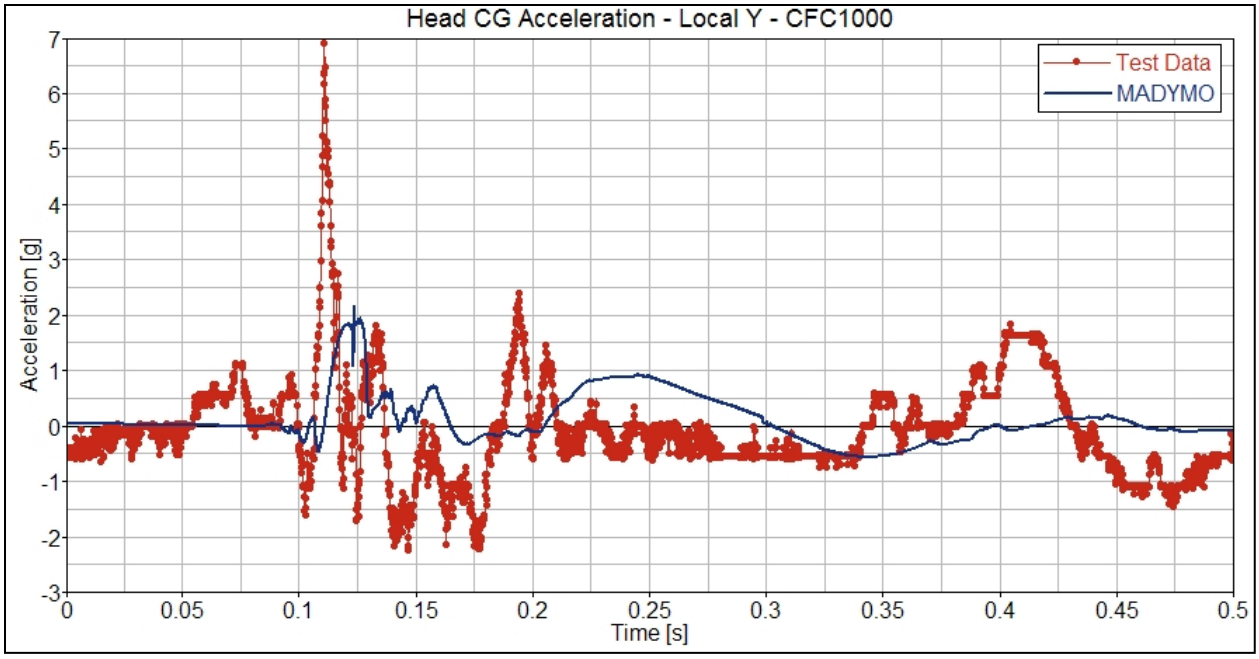

Figure H31. Head CG Acceleration, Local Y

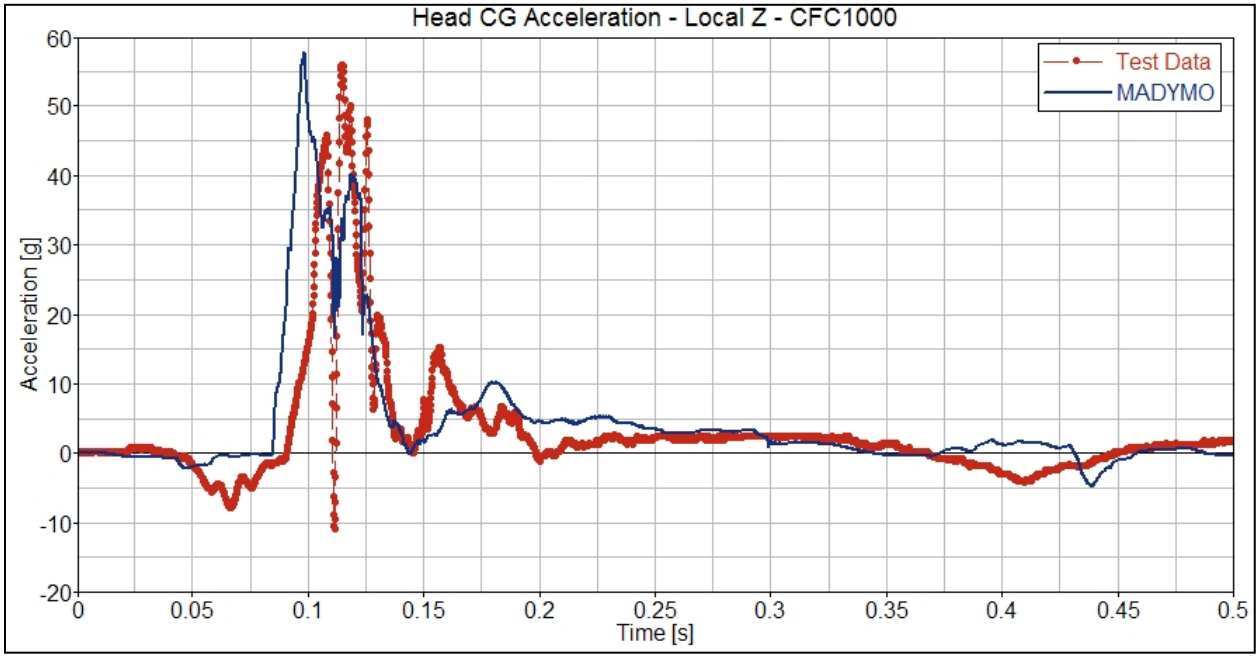

Figure H32. Head CG Acceleration, Local Z

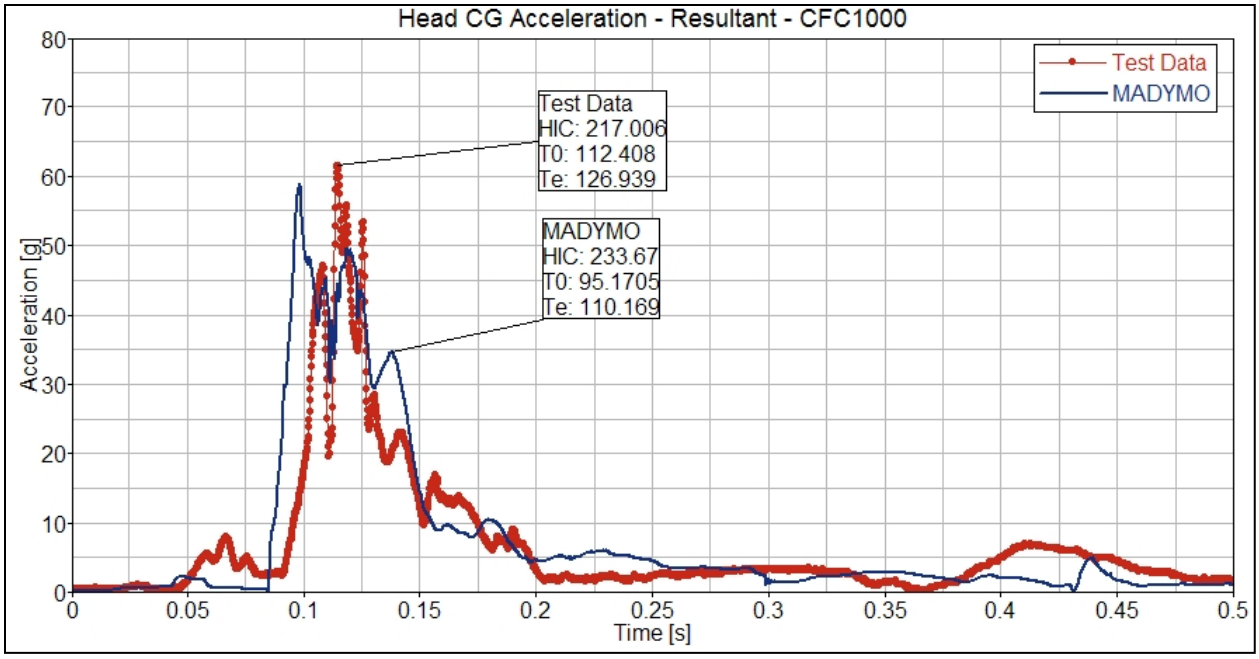

Figure H33. Head CG Acceleration, Resultant

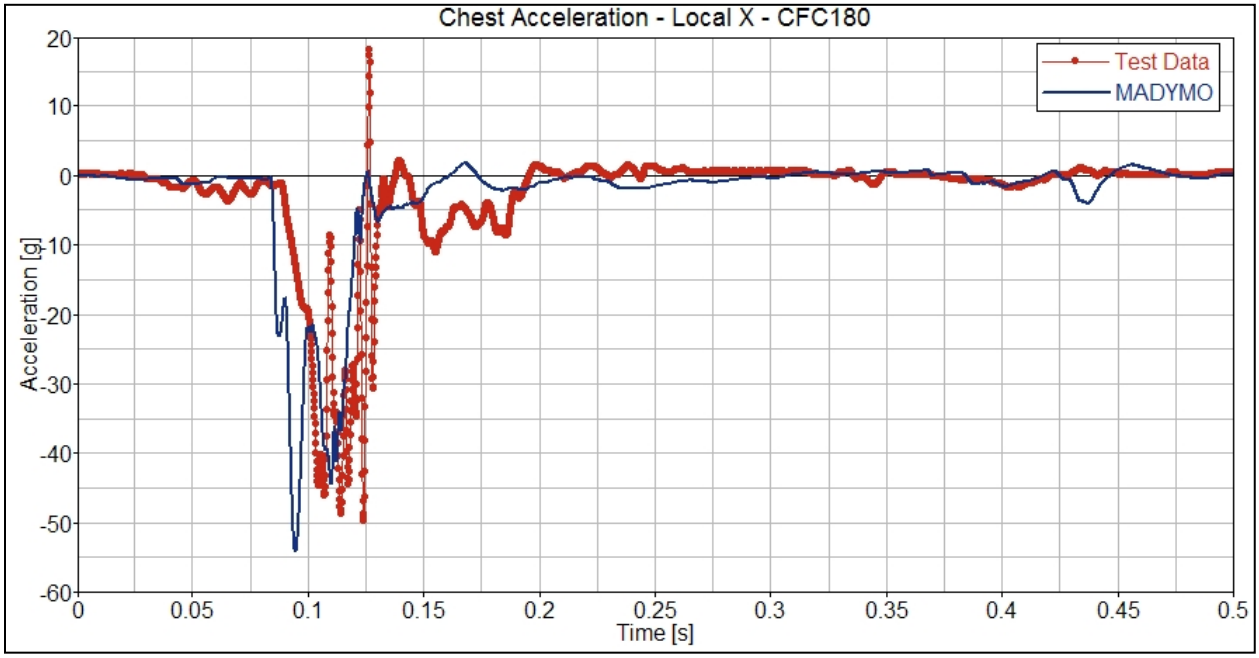

Figure H34. Chest Acceleration, Local X

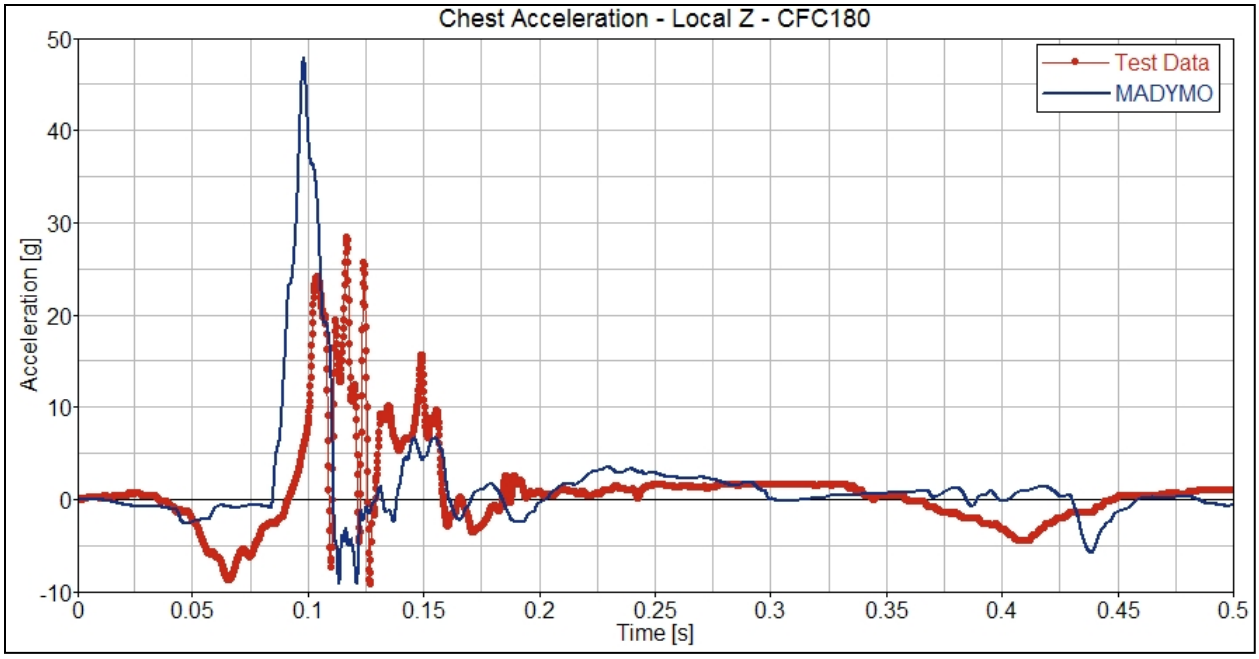

Figure H35. Chest Acceleration, Local Z

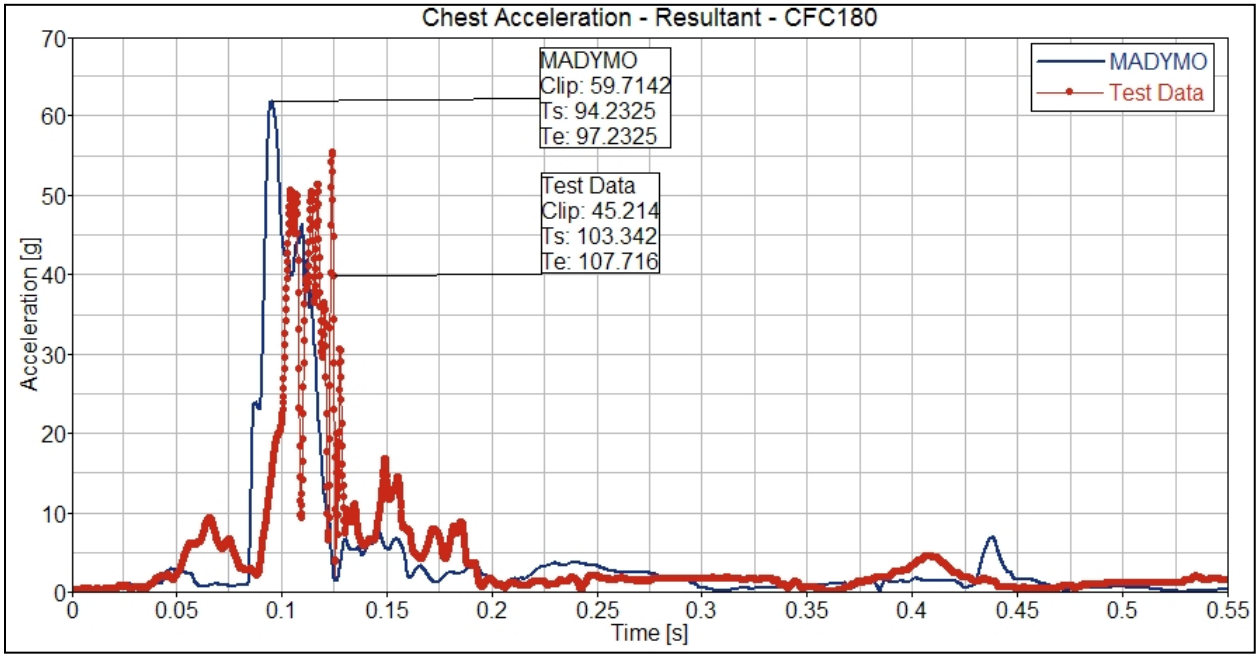

Figure H36. Chest Acceleration, Resultant

Displacement Time-Histories

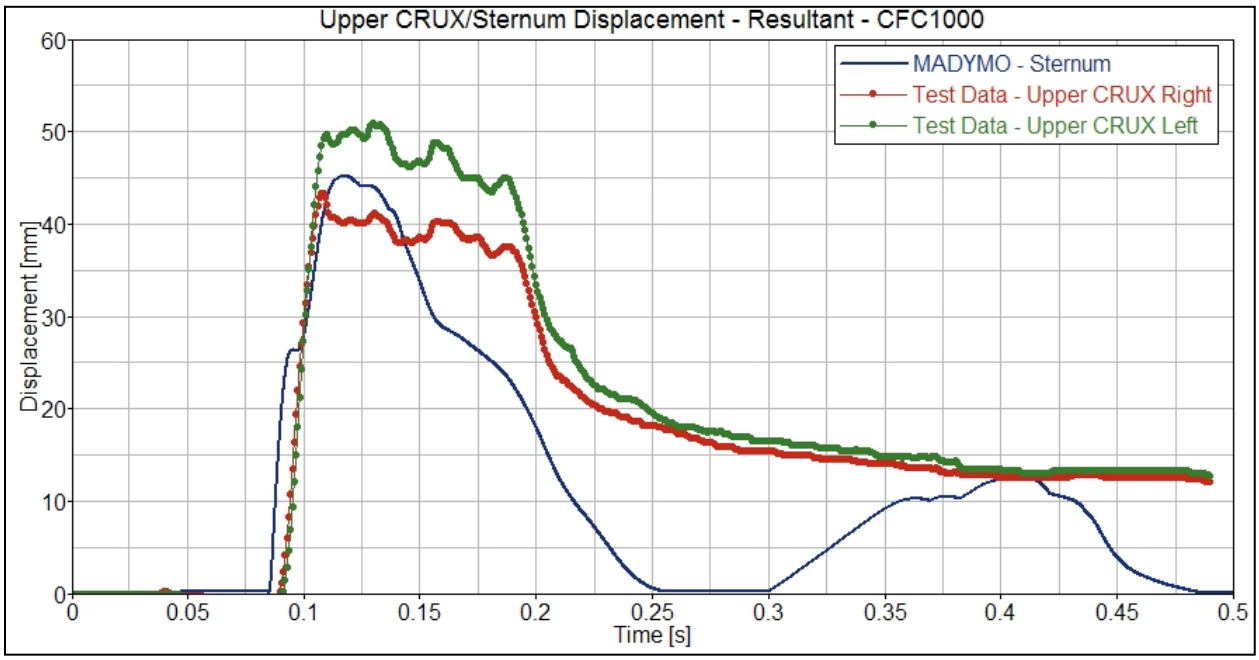

Figure H37. Upper CRUX/Sternum Displacement, Resultant

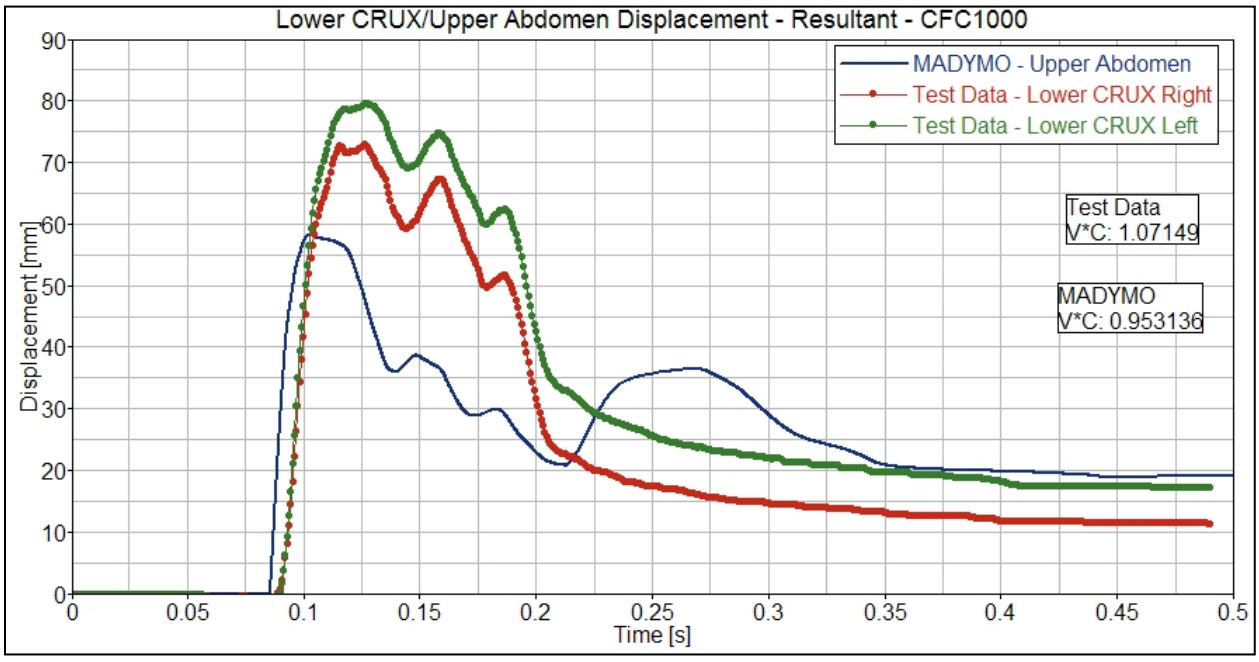

Figure H38. Lower CRUX/Upper Abdomen Displacement, Resultant

Force Time-Histories

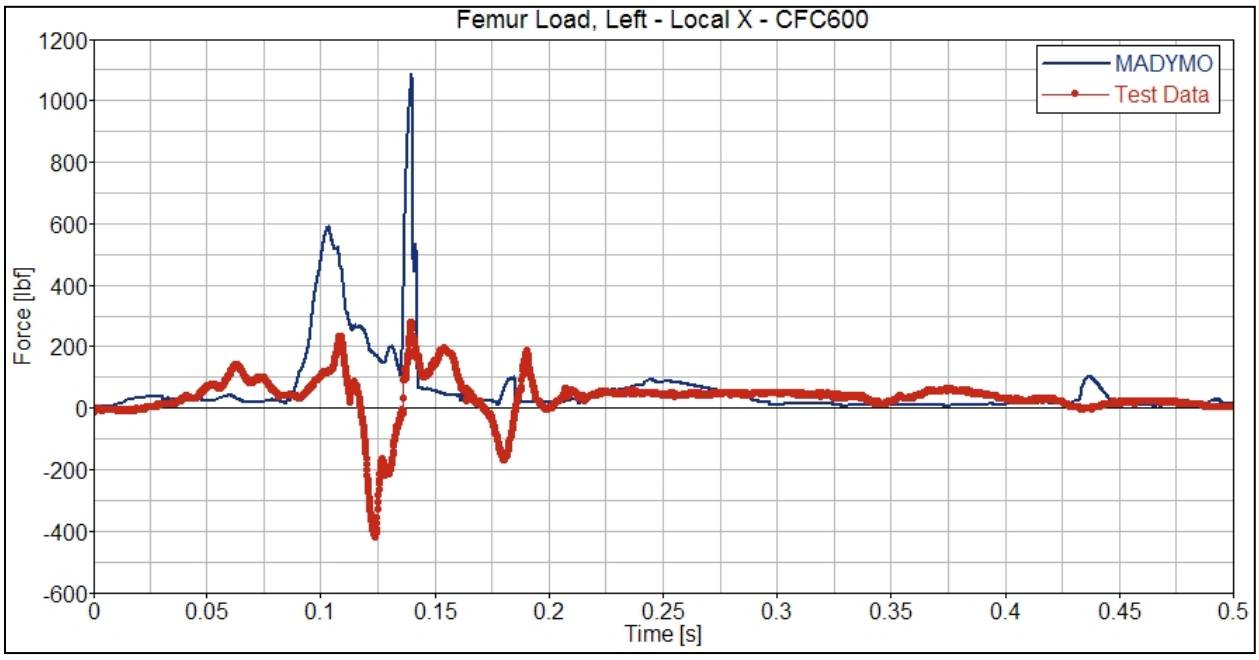

Figure H39. Left Femur Force, Local X

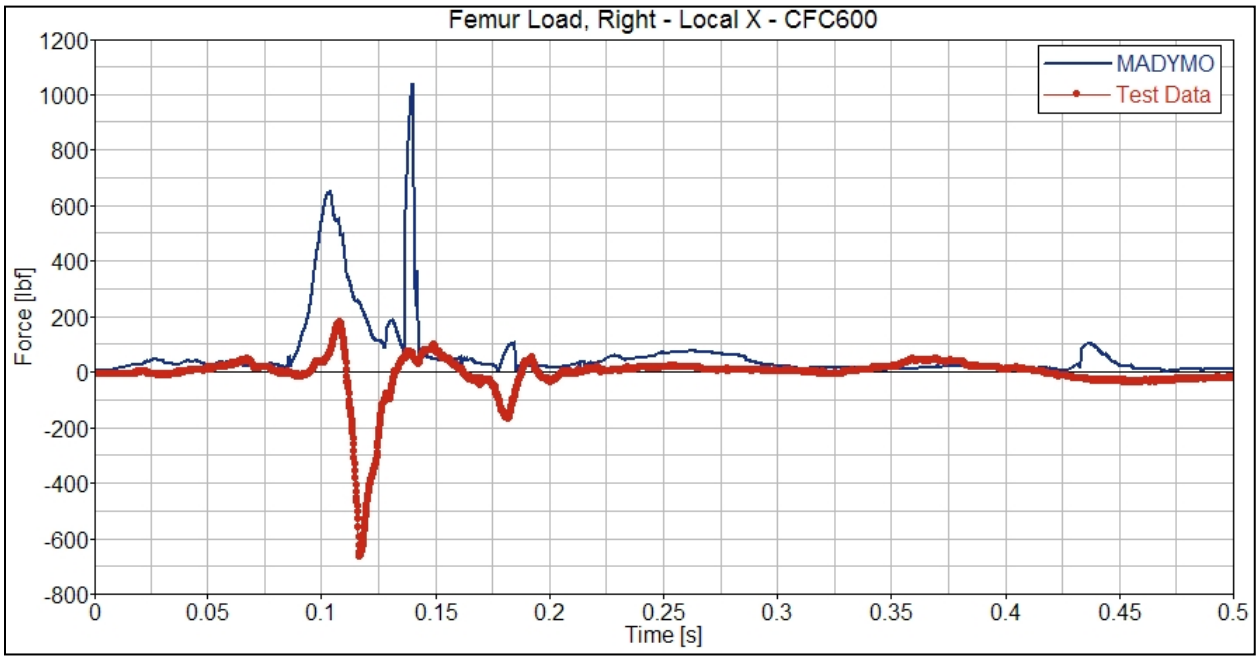

Figure H40. Right Femur Force, Local X

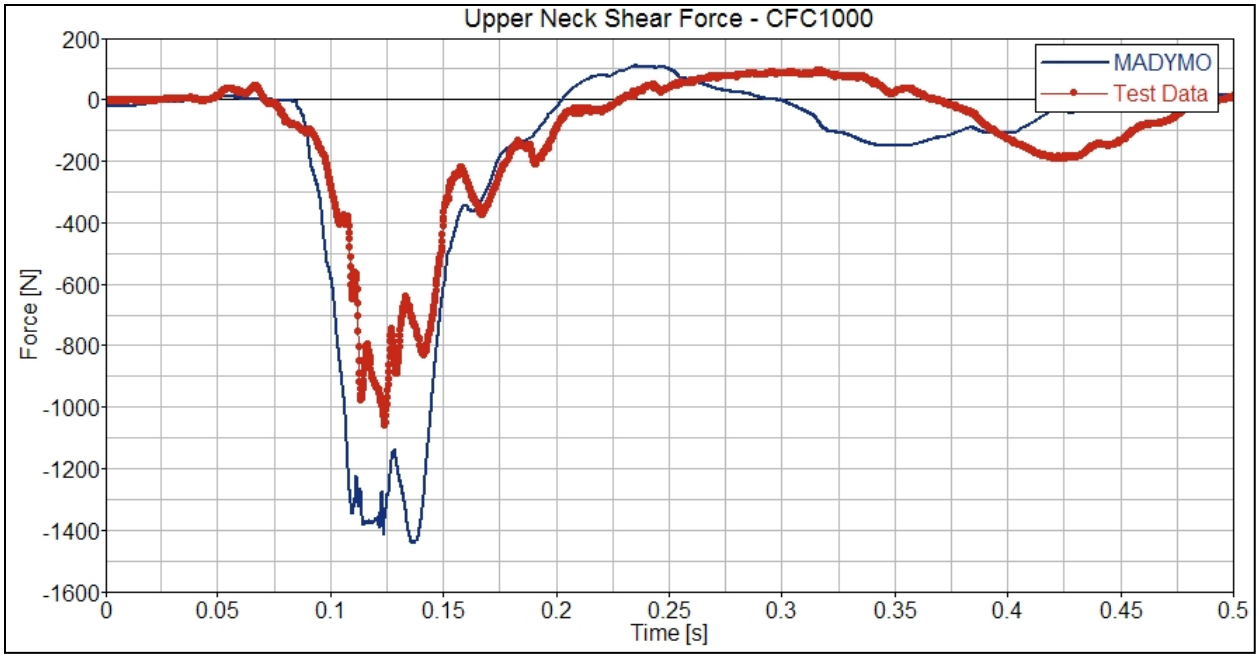

Figure H41. Upper Neck Shear Force, Fx

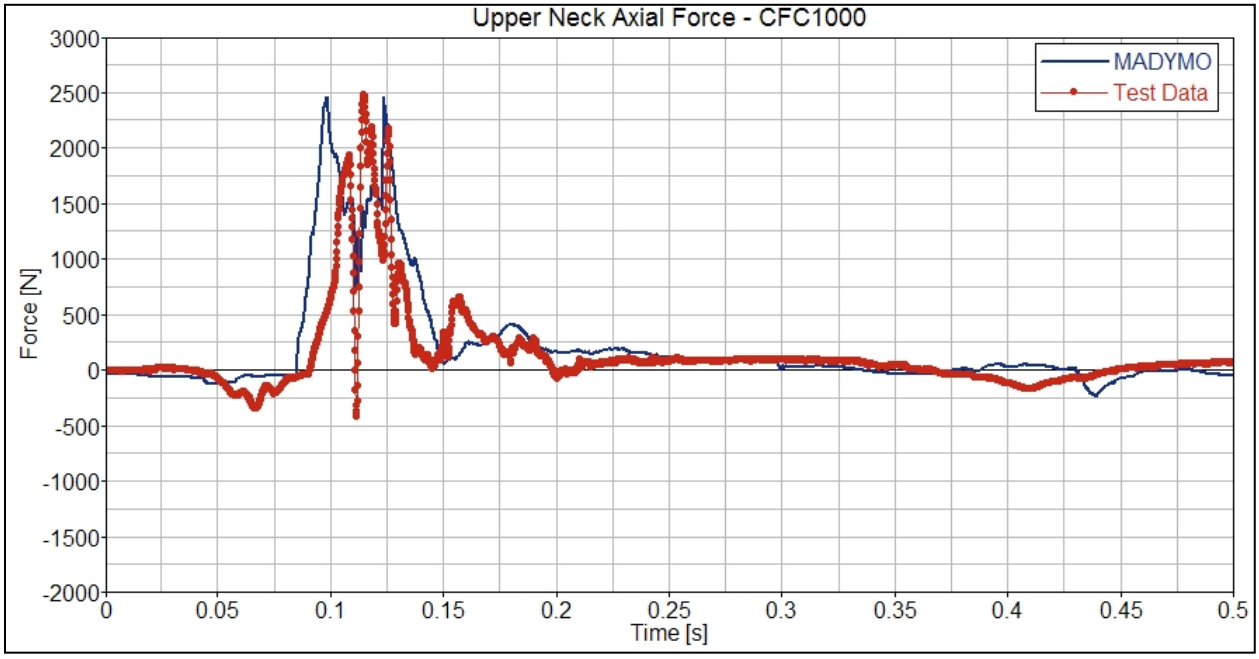

Figure H42. Upper Neck Axial Force, Fz

Moment Time-Histories

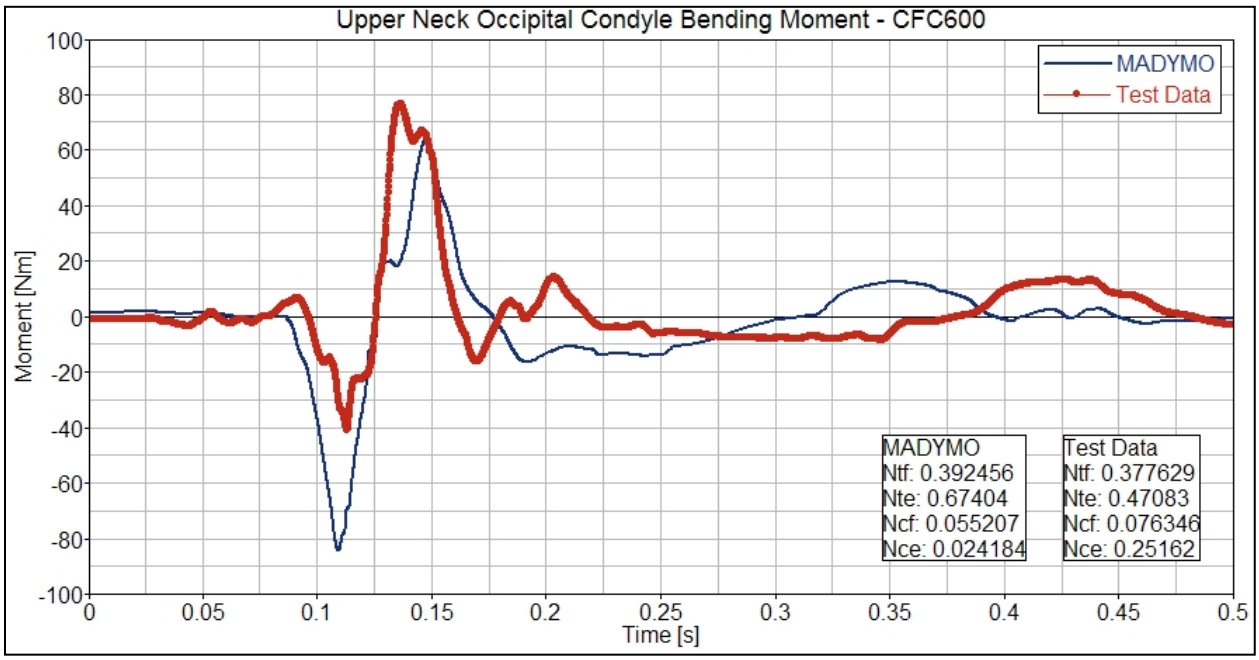

Figure H43. Upper Neck Occipital Condyle Bending Moment, M_y

Kinematics

A series of time-sequence pictures of the ATD kinematics are presented in this section. The pictures are taken from the test video and the MADYMO model output and presented together for comparison.

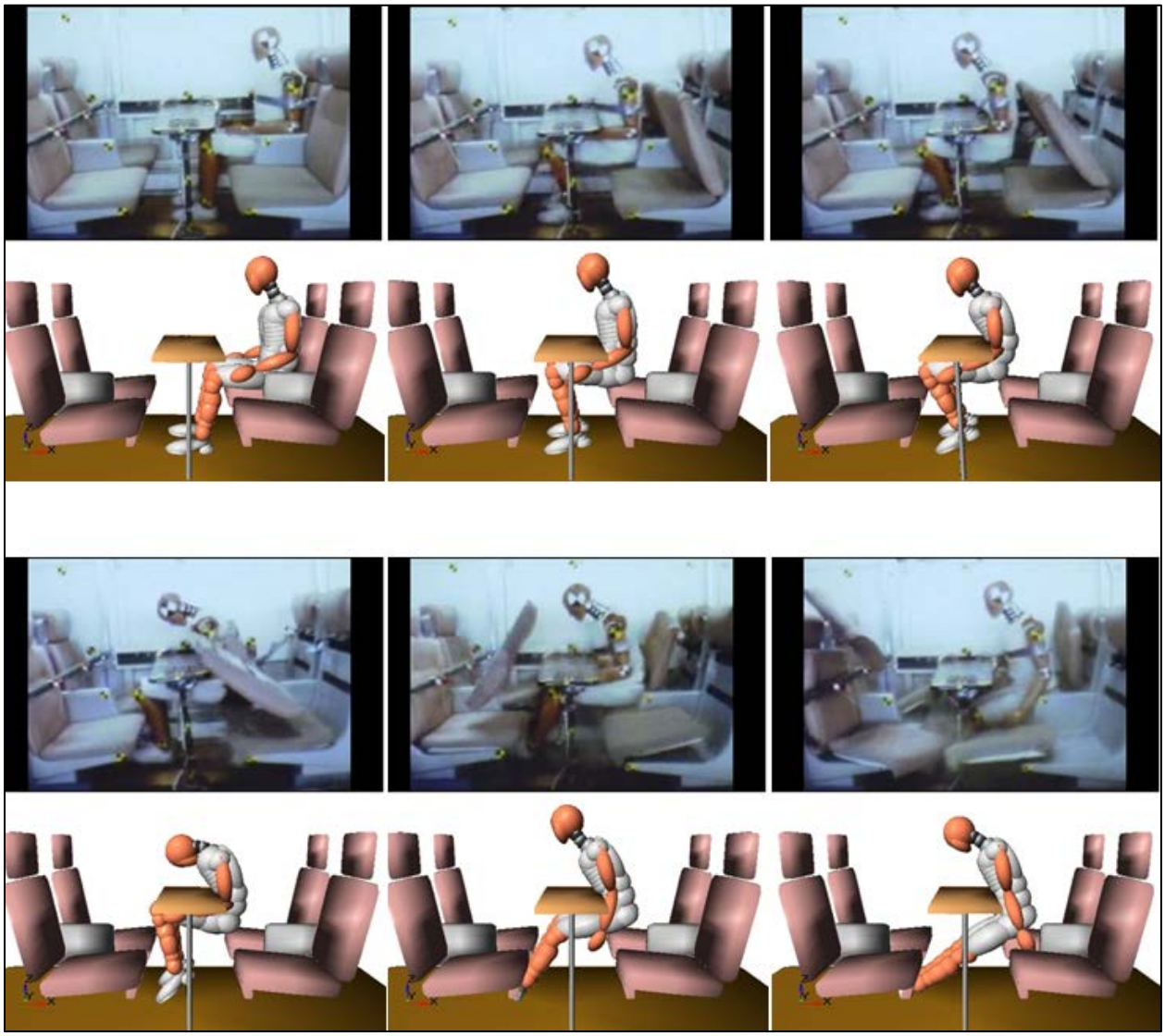

Figure H44. H3RS Test Dummy Kinematics in Table Test, Simulation Results and Test Observations

Table Results

Displacement Time-Histories

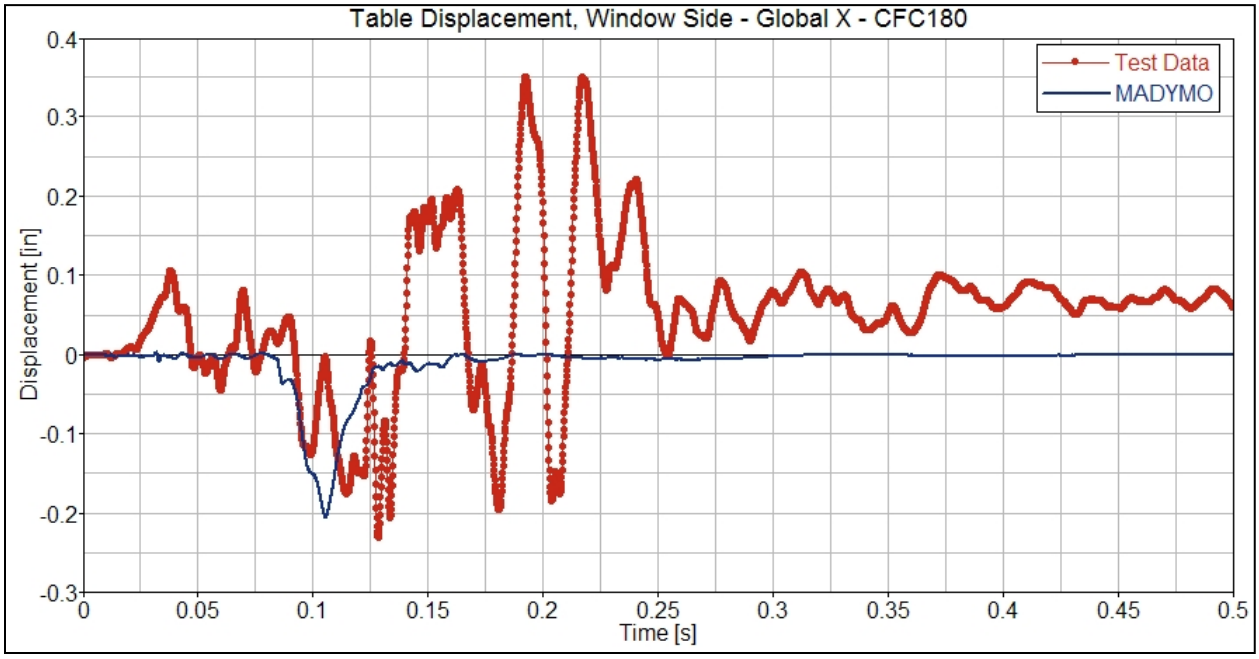

Figure H45. Table Displacement, Window Side, Global X

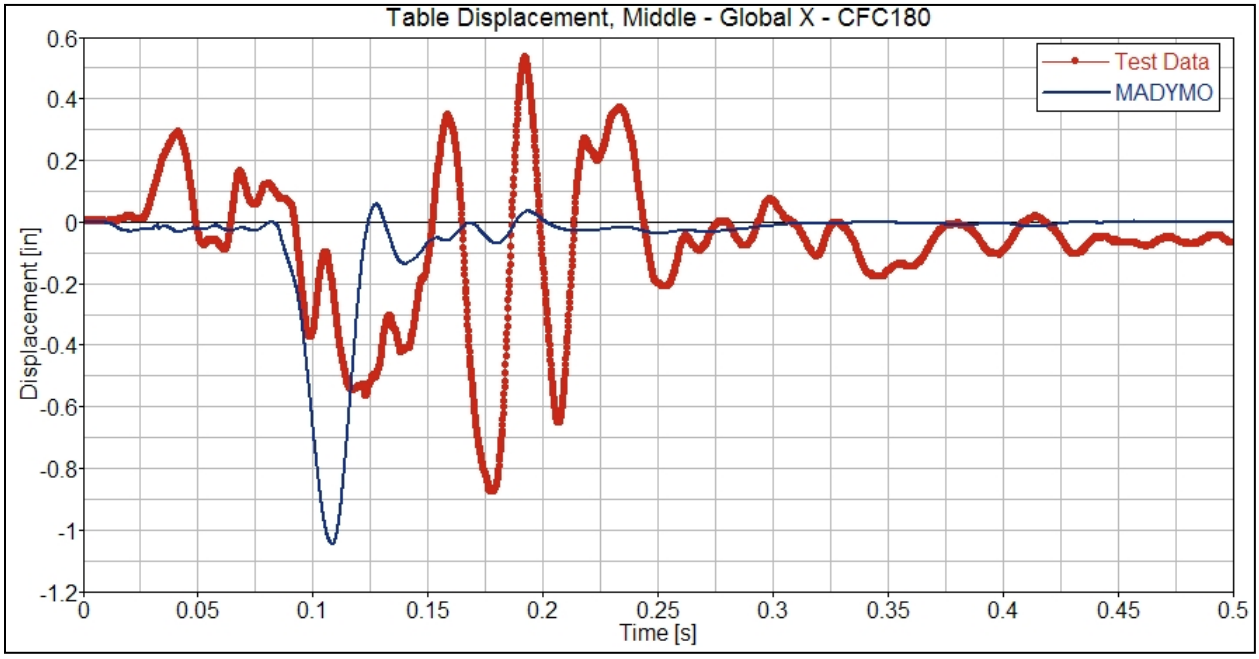

Figure H46. Table Displacement, Middle, Global X

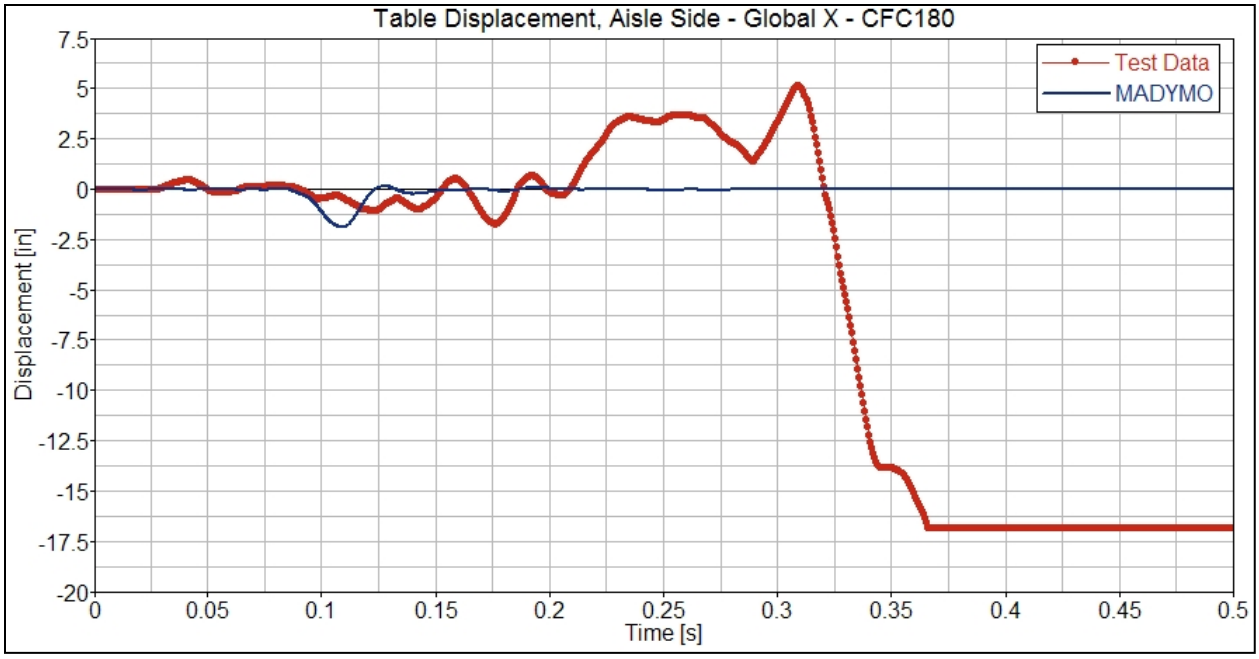

Figure H47. Table Displacement, Aisle Side, Global X

Force Time-Histories

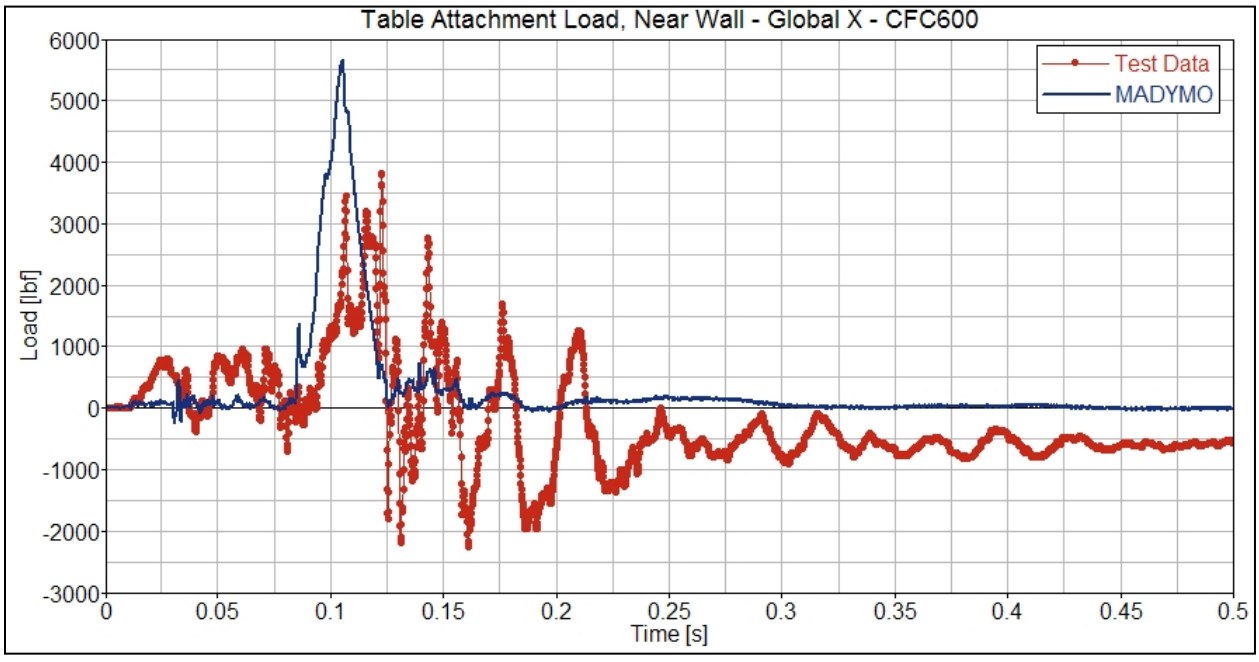

Figure H48. Table Attachment Load, Near Wall, Global X

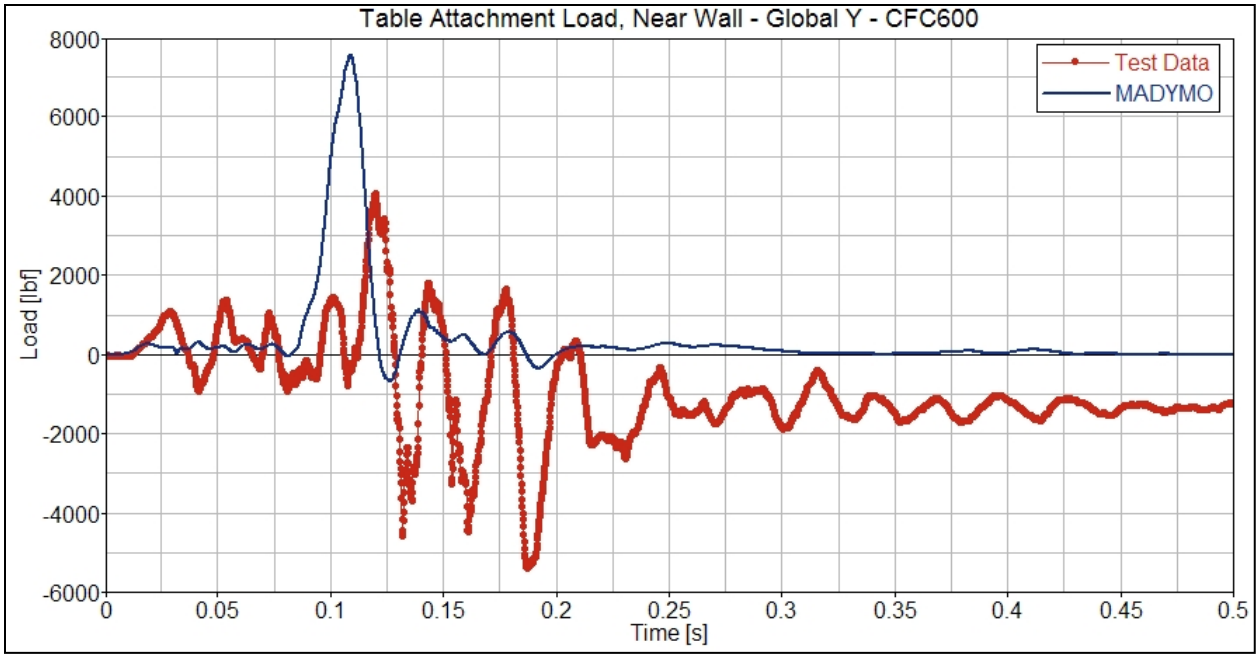

Figure H49. Table Attachment Load, Near Wall, Global Y

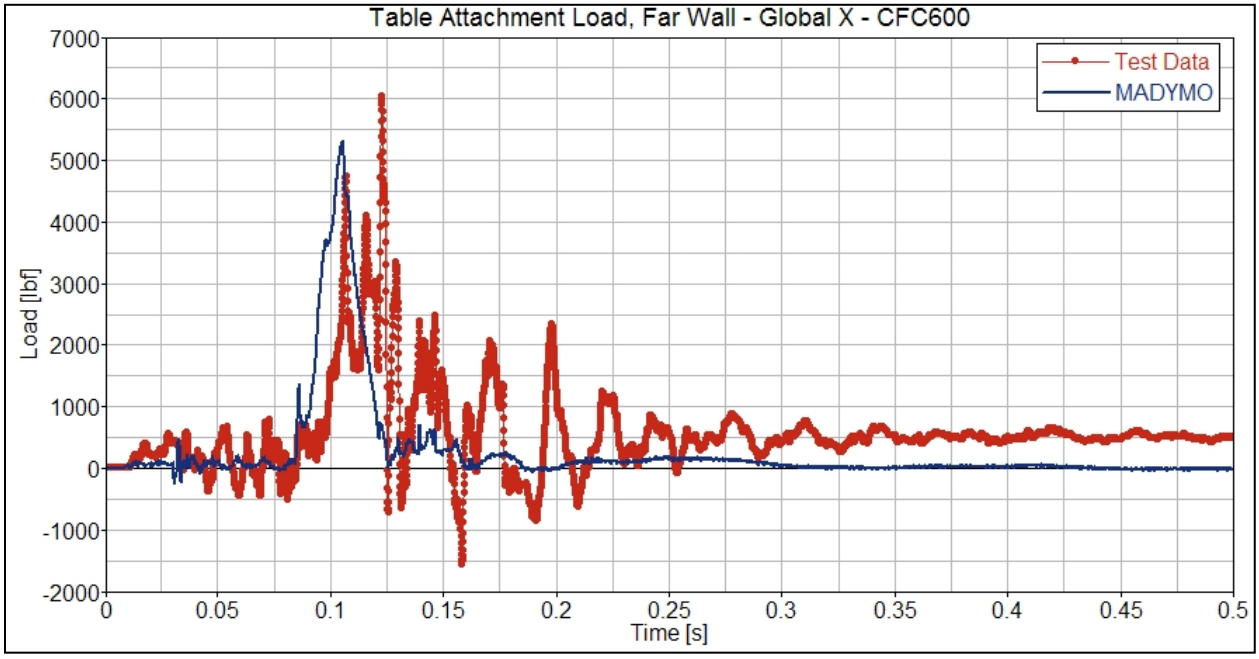

Figure H50. Table Attachment Load, Far Wall, Global X

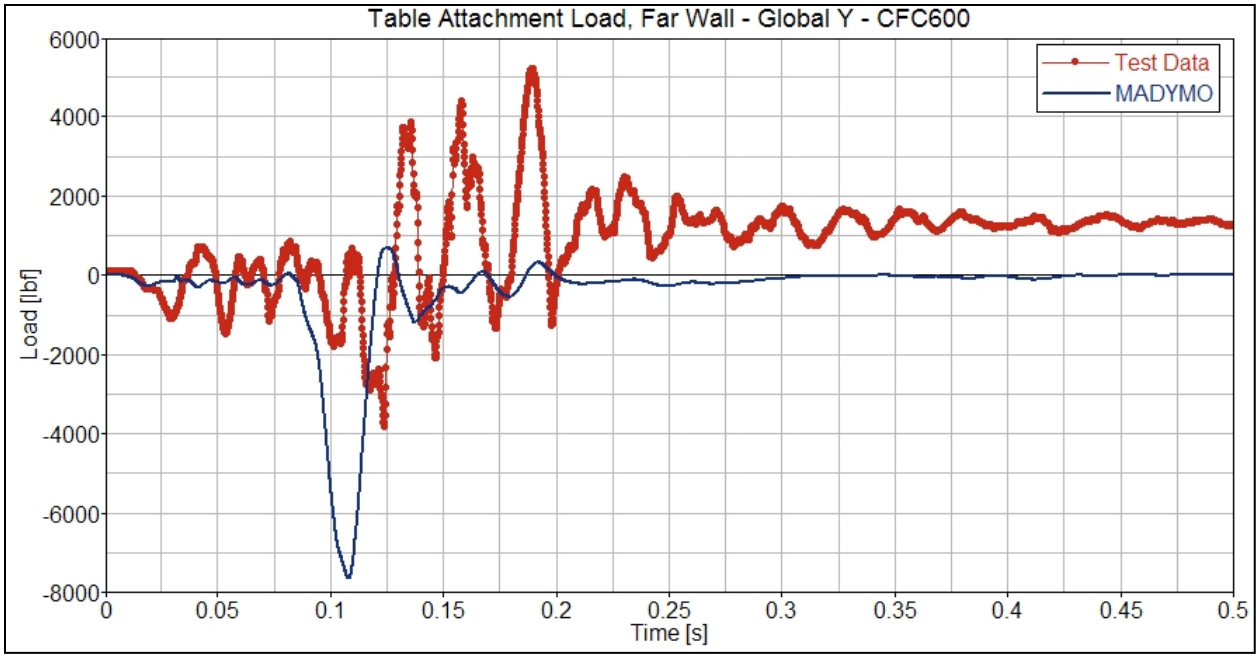

Figure H51. Table Attachment Load, Far Wall, Global Y

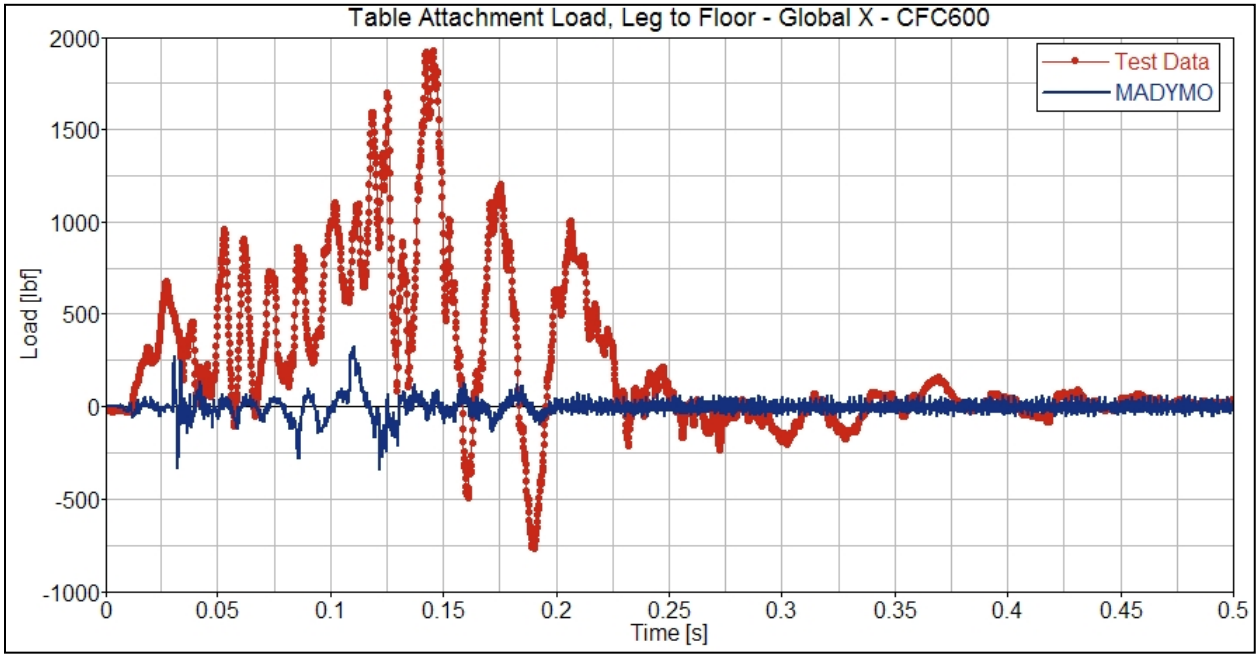

Figure H52. Table Attachment Load, Leg to Floor, Global X

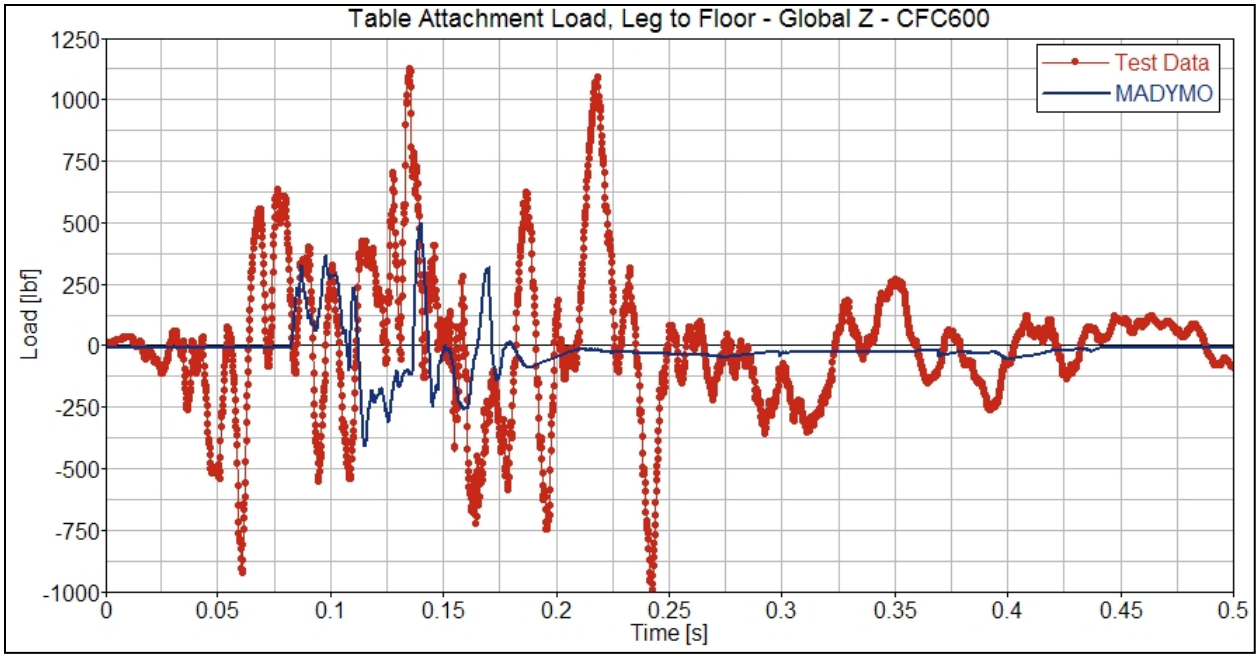

Figure H53. Table Attachment Load, Leg to Floor, Global Z

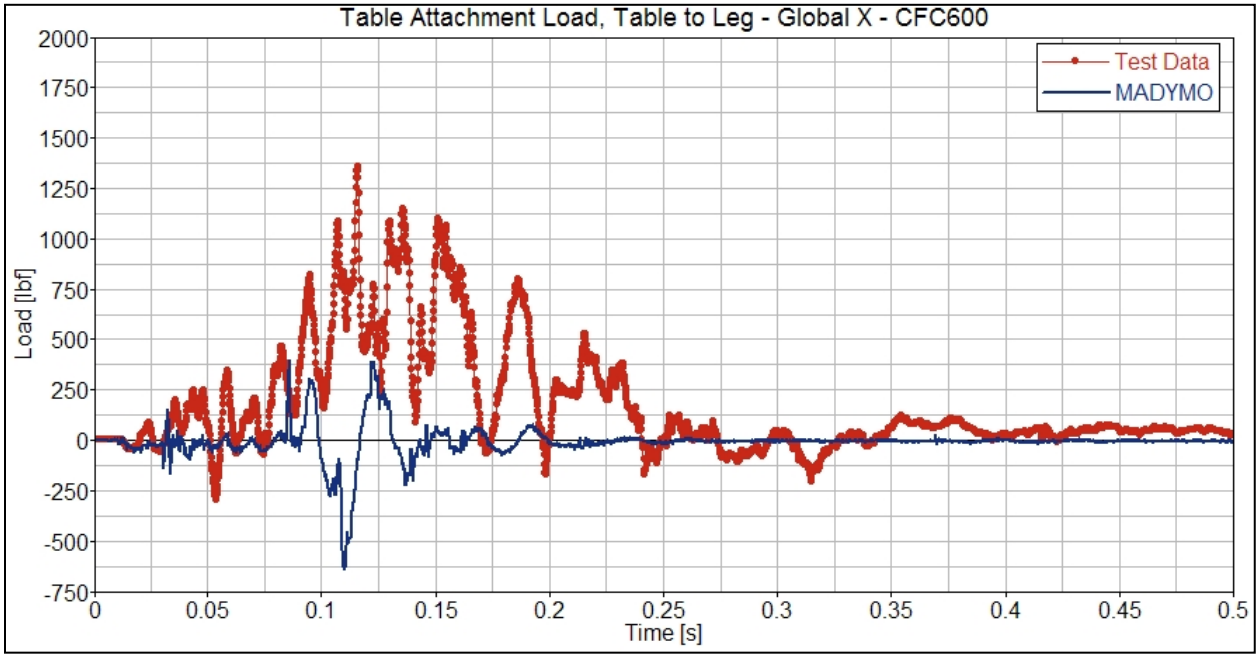

Figure H54. Table Attachment Load, Table to Leg, Global X

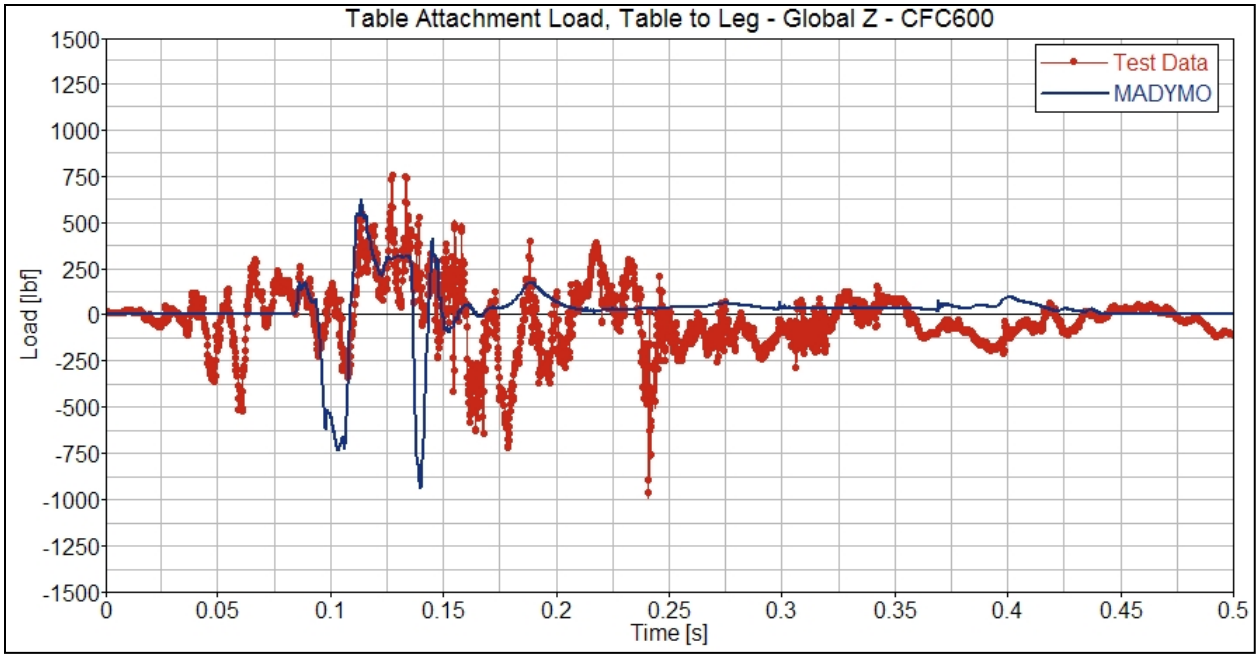

Figure H55. Table Attachment Load, Table to Leg, Global Z

Experiment 1-3: Facing Seats with Workstation Table

Seats with Table, THOR ATD

Dynamics

The following section contains plots of the force, acceleration, and displacement time-histories recorded from the THOR ATD seated in the window seat position of the facing commuter seats with intervening workstation table. The experiment was located near the rear of the lead car. The corresponding time-histories from the ATD in the MADYMO model of Experiment 1-3 are plotted against the test data for direct comparison. The CFC filter frequency (in accordance with SAE J211-1) is indicated on each plot. The HIC injury criteria calculated from the test and model results are located on the head resultant acceleration plots. The chest injury criteria (3 ms clip) are located on the chest resultant acceleration plots. The neck injury criteria (Nij) are located on the neck bending M_y moment plots.

Acceleration Time-Histories

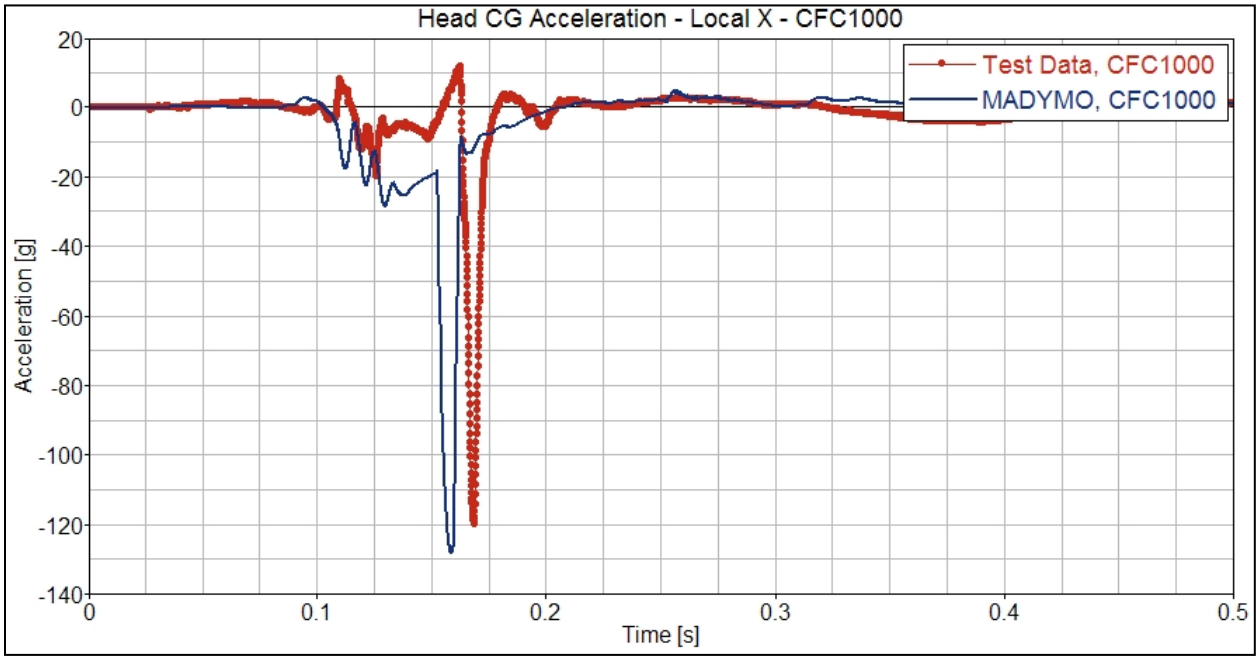

Figure H56. Head CG Acceleration, Local X

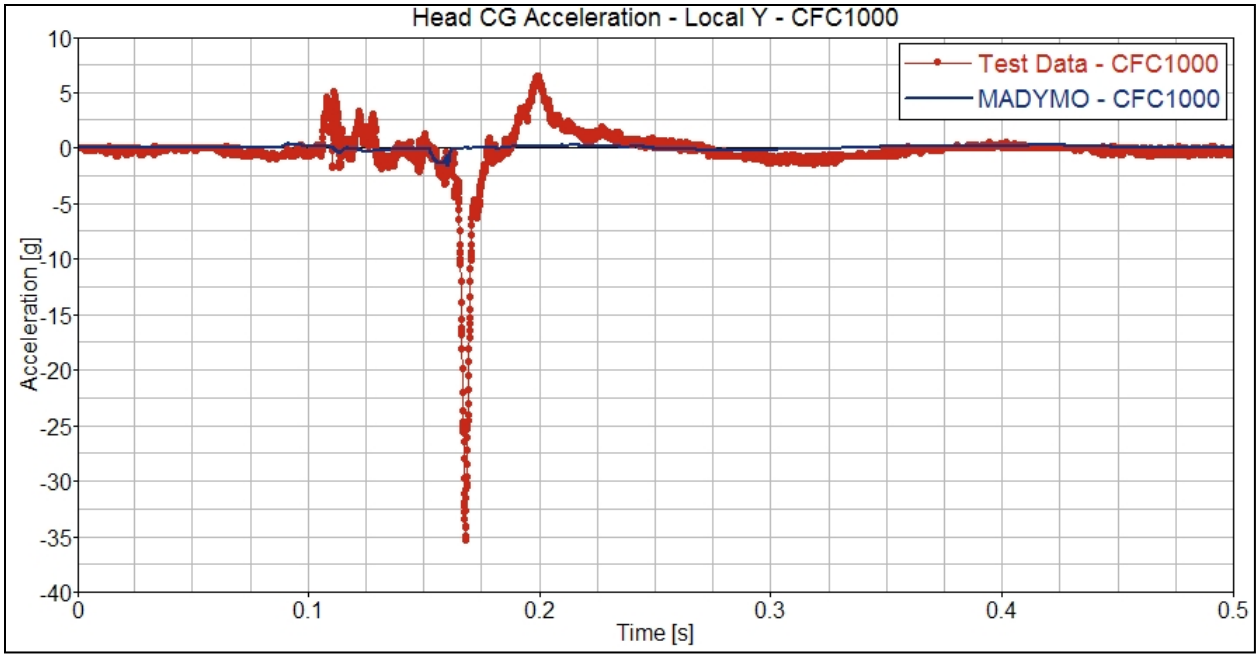

Figure H57. Head CG Acceleration, Local Y

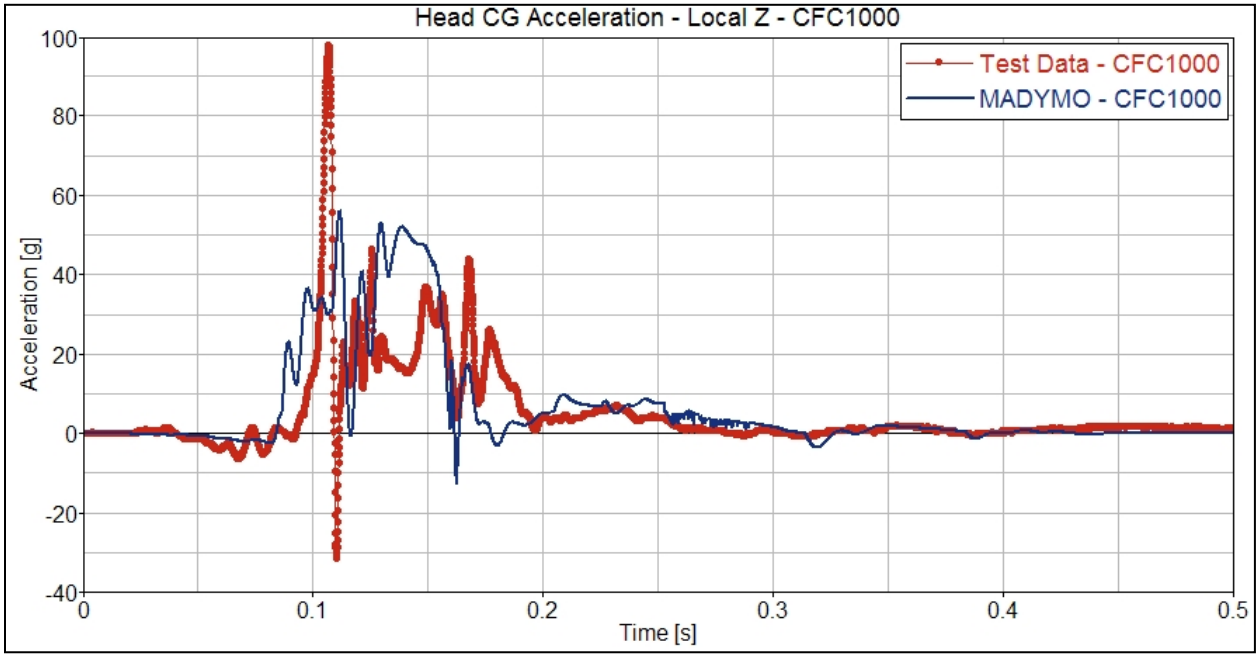

Figure H58. Head CG Acceleration, Local Z

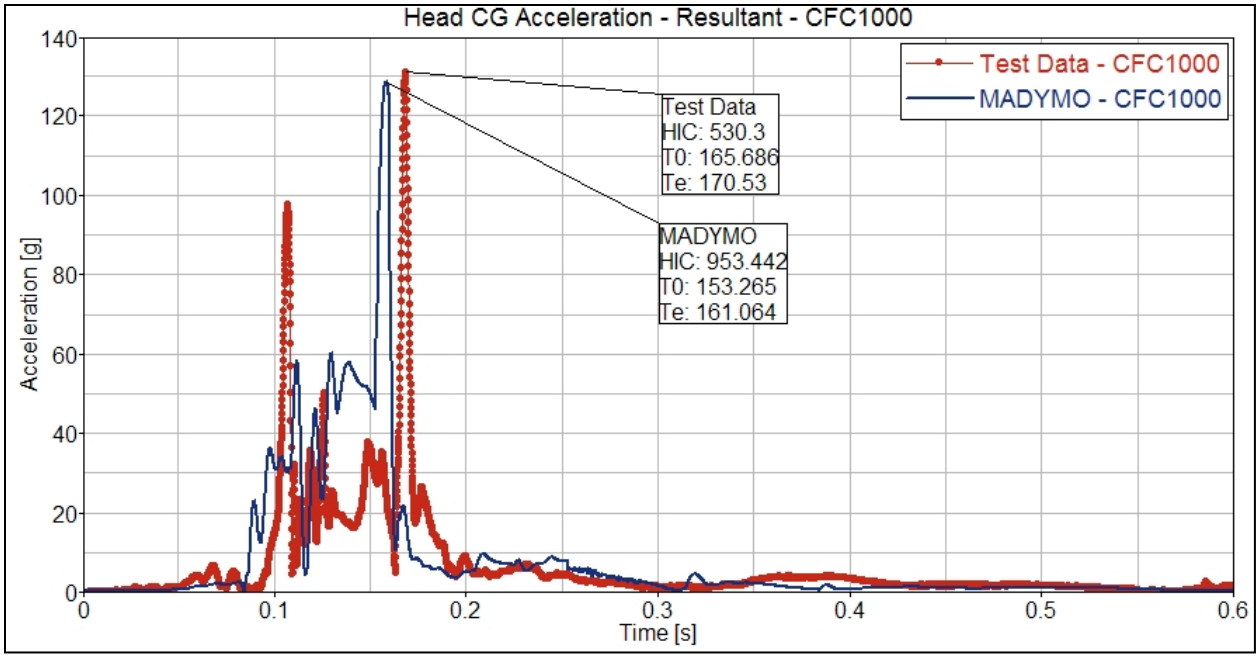

Figure H59. Head CG Acceleration, Resultant

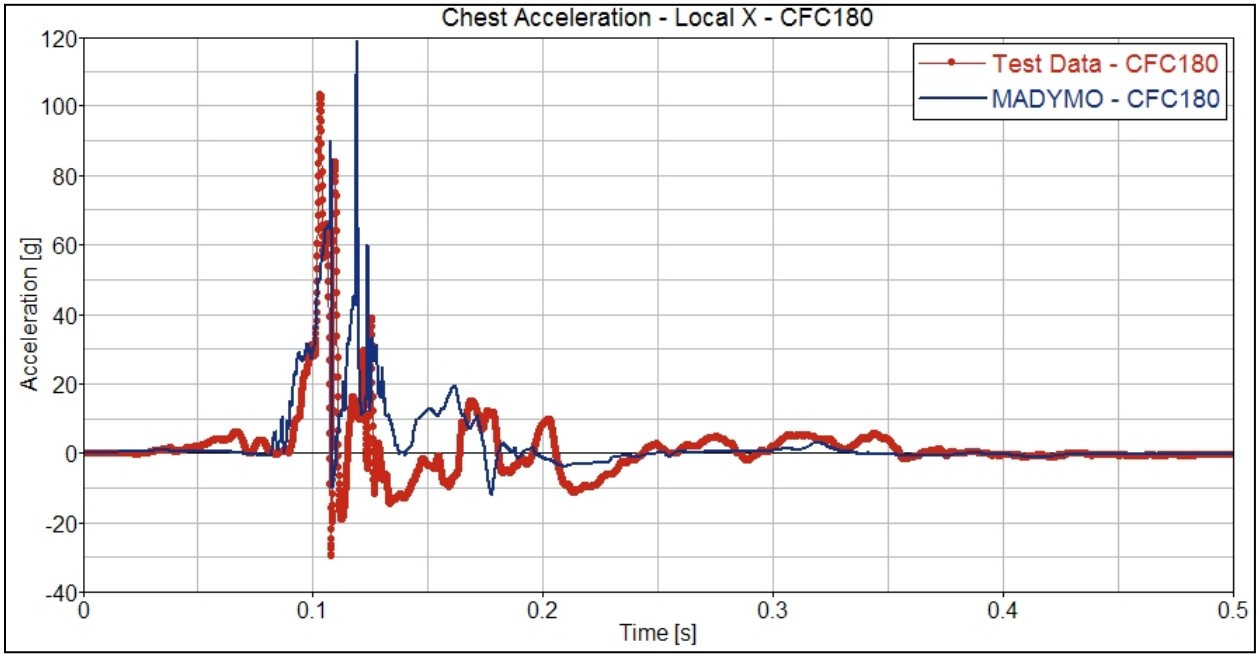

Figure H60. Chest Acceleration, Local X

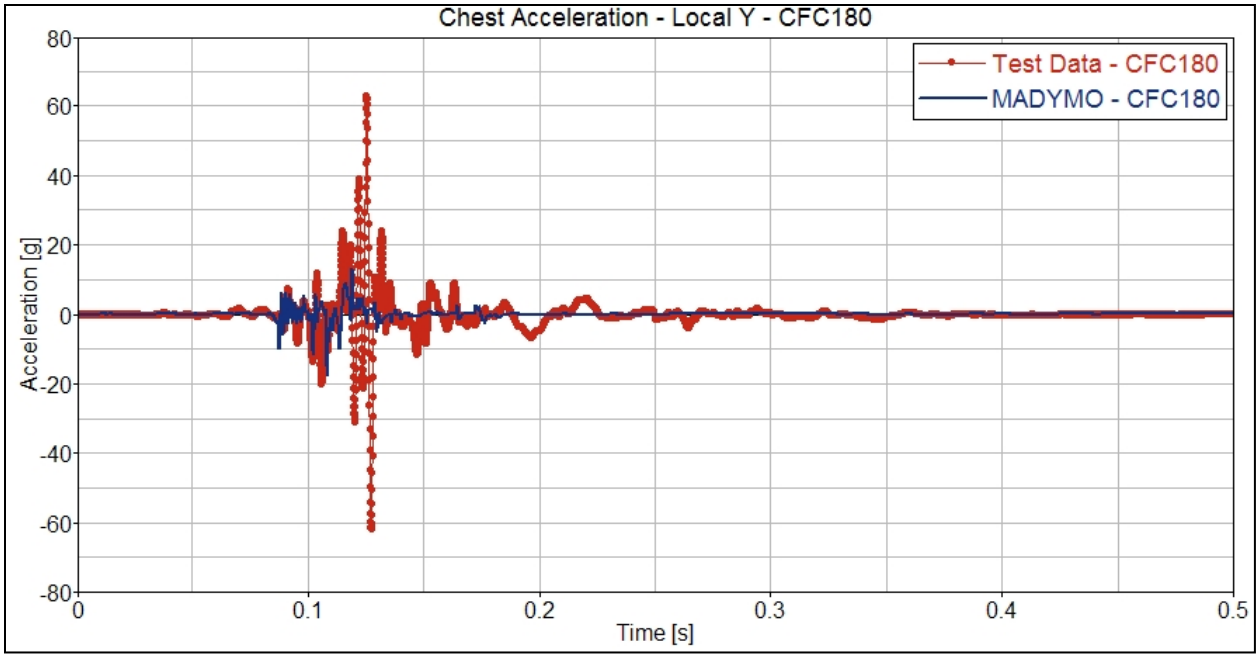

Figure H61. Chest Acceleration, Local Y

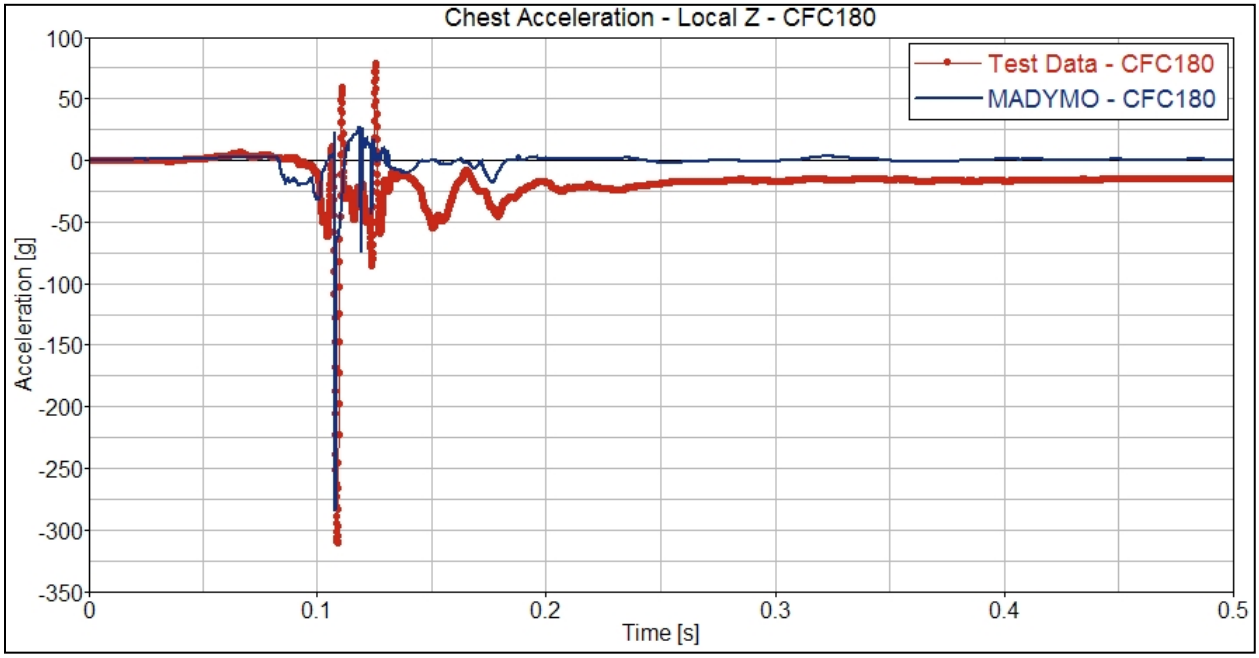

Figure H62. Chest Acceleration, Local Z

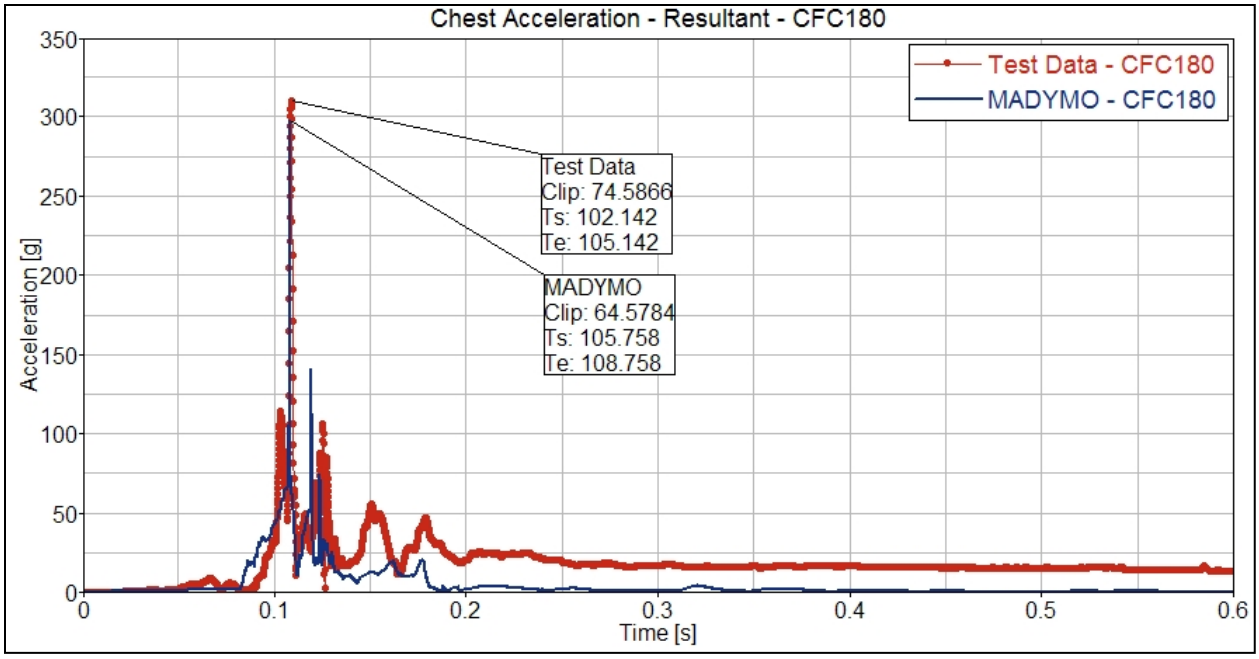

Figure H63. Chest Acceleration, Resultant

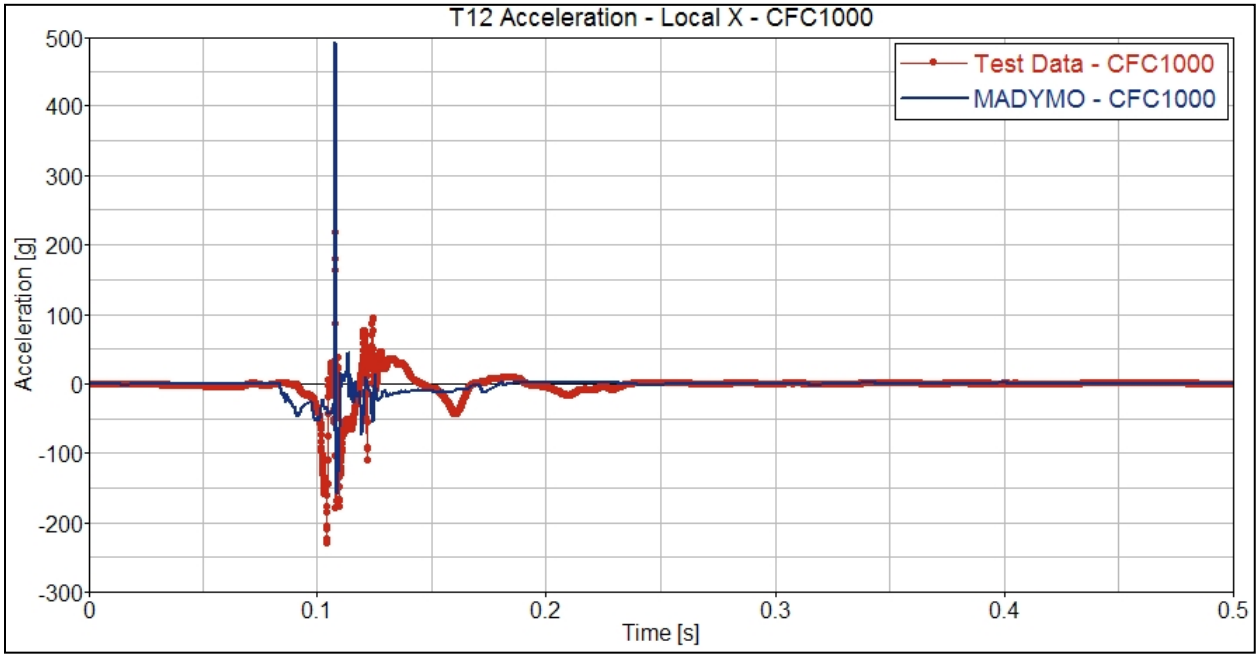

Figure H64. T12 Spine Acceleration, Local X

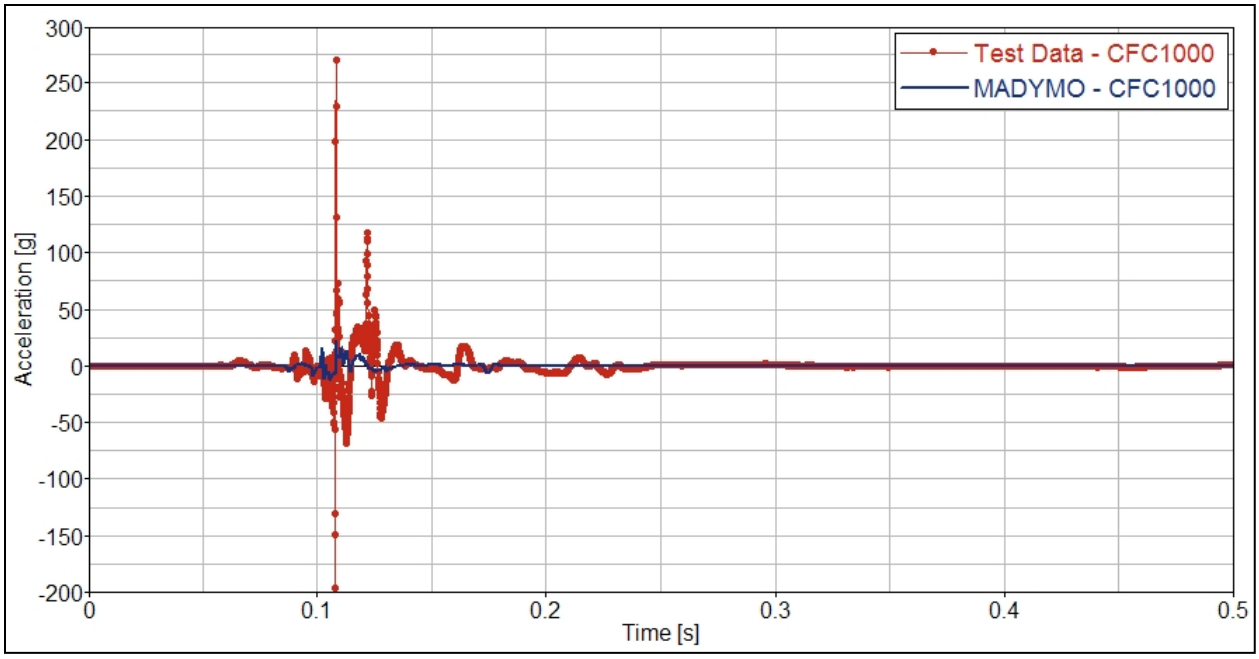

Figure H65. T12 Spine Acceleration, Local Y

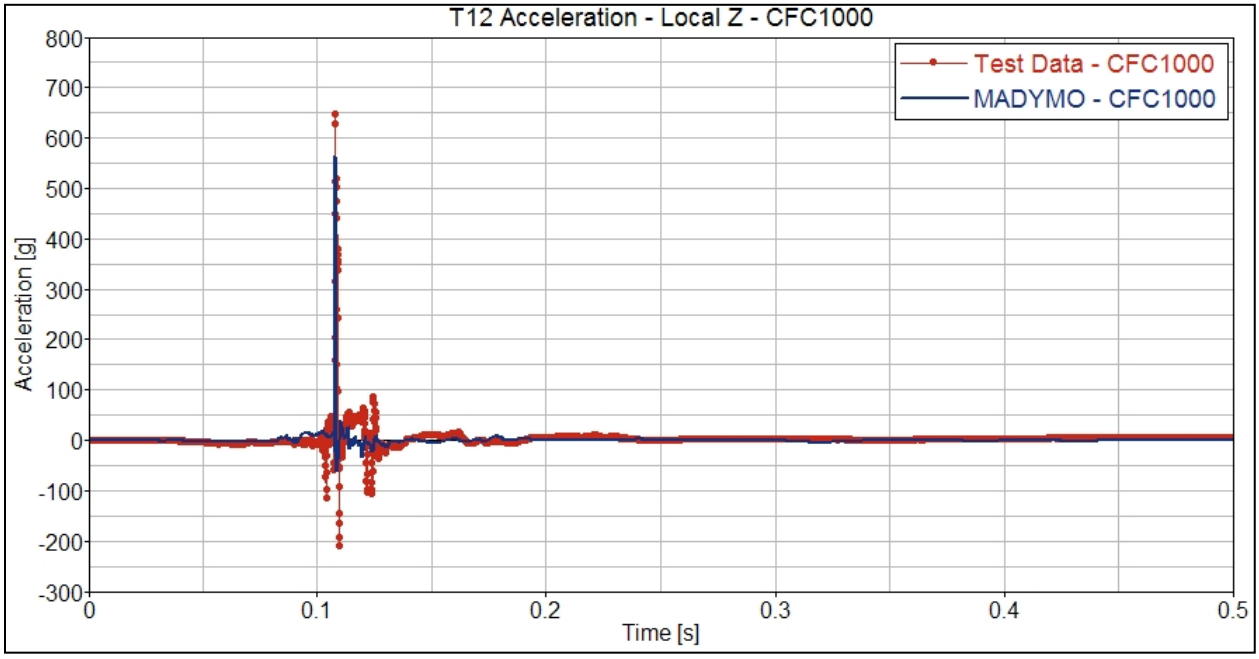

Figure H66. T12 Spine Acceleration, Local Z

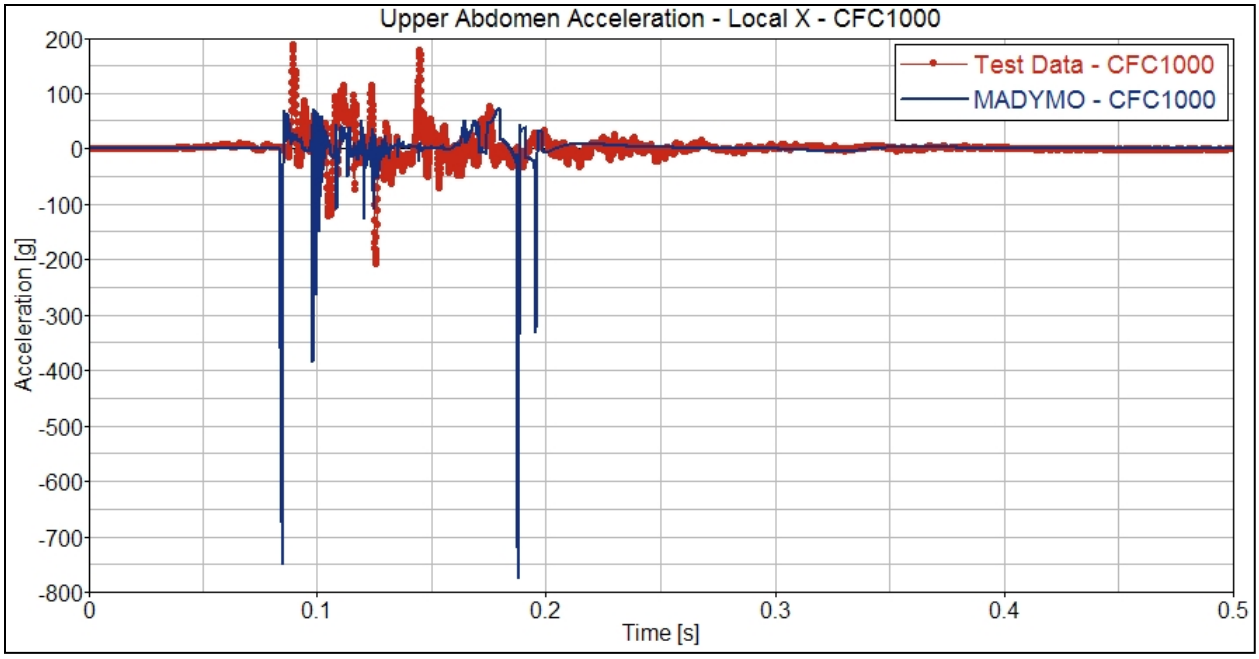

Figure H67. Upper Abdomen Acceleration, Local X

Displacement Time-Histories

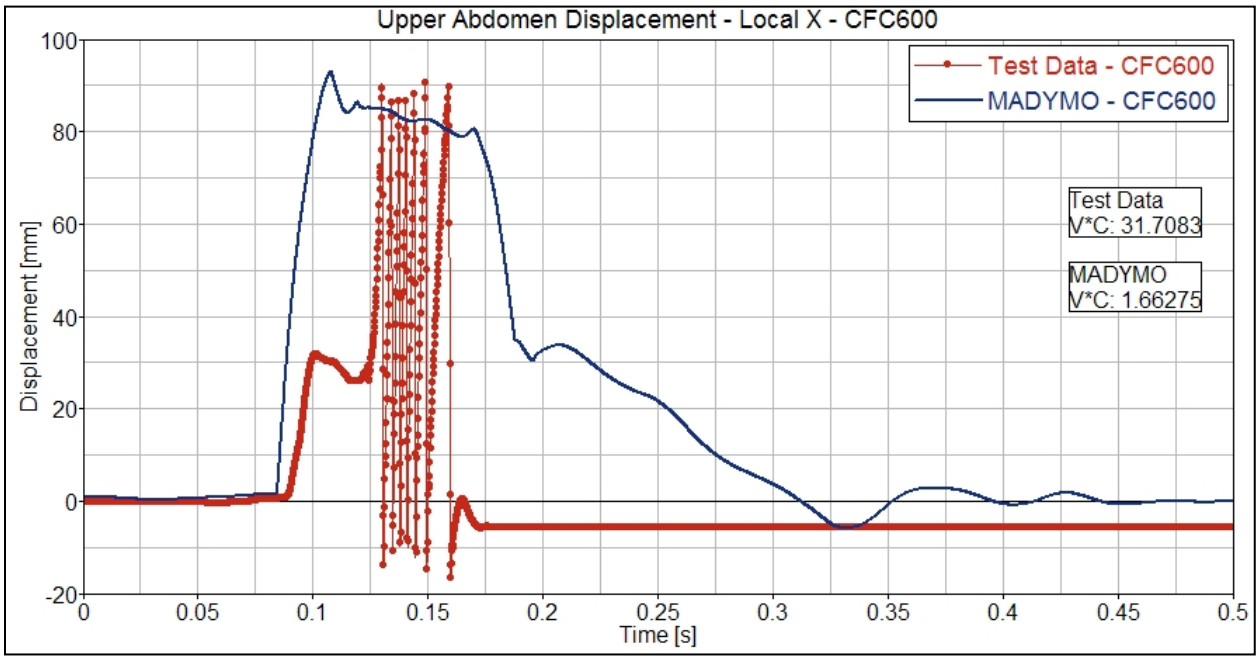

Figure H68. Upper Abdomen Displacement

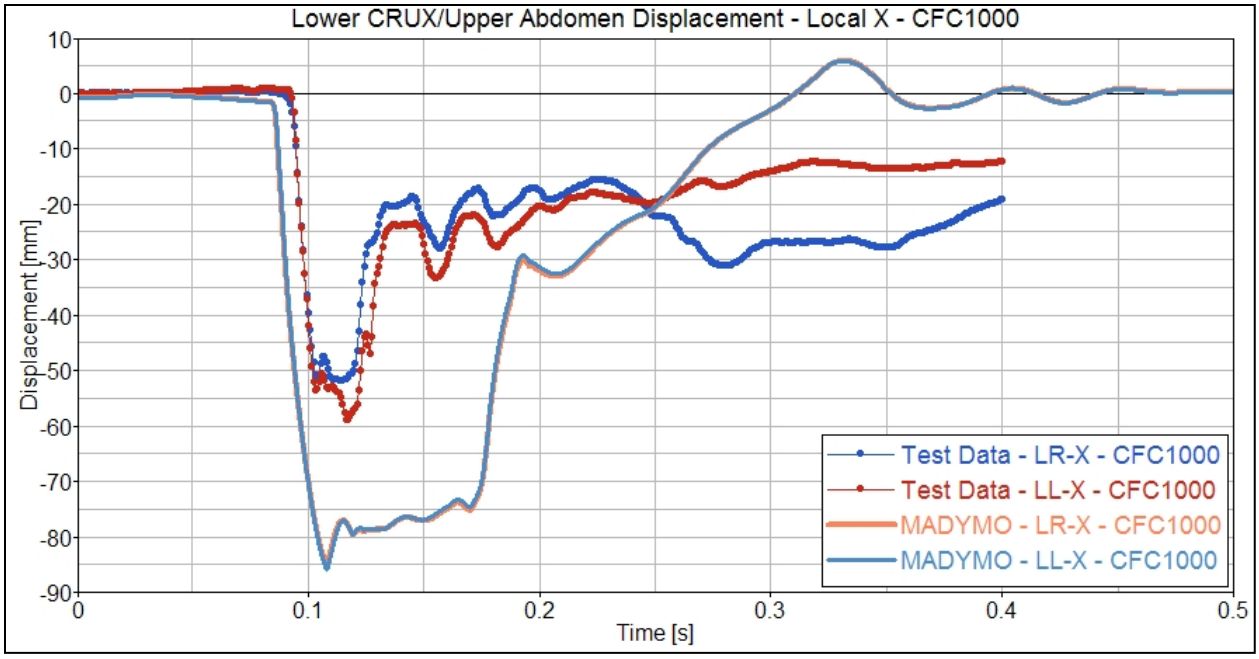

Figure H69. Lower CRUX, Local X

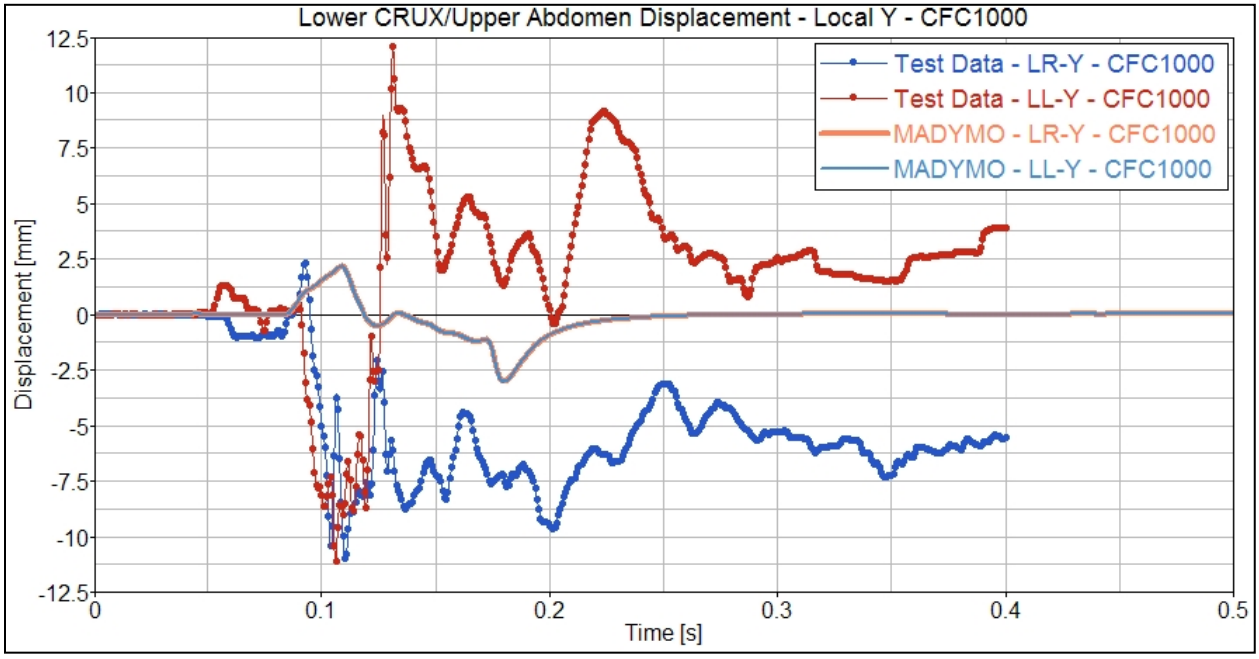

Figure H70. Lower CRUX, Local Y

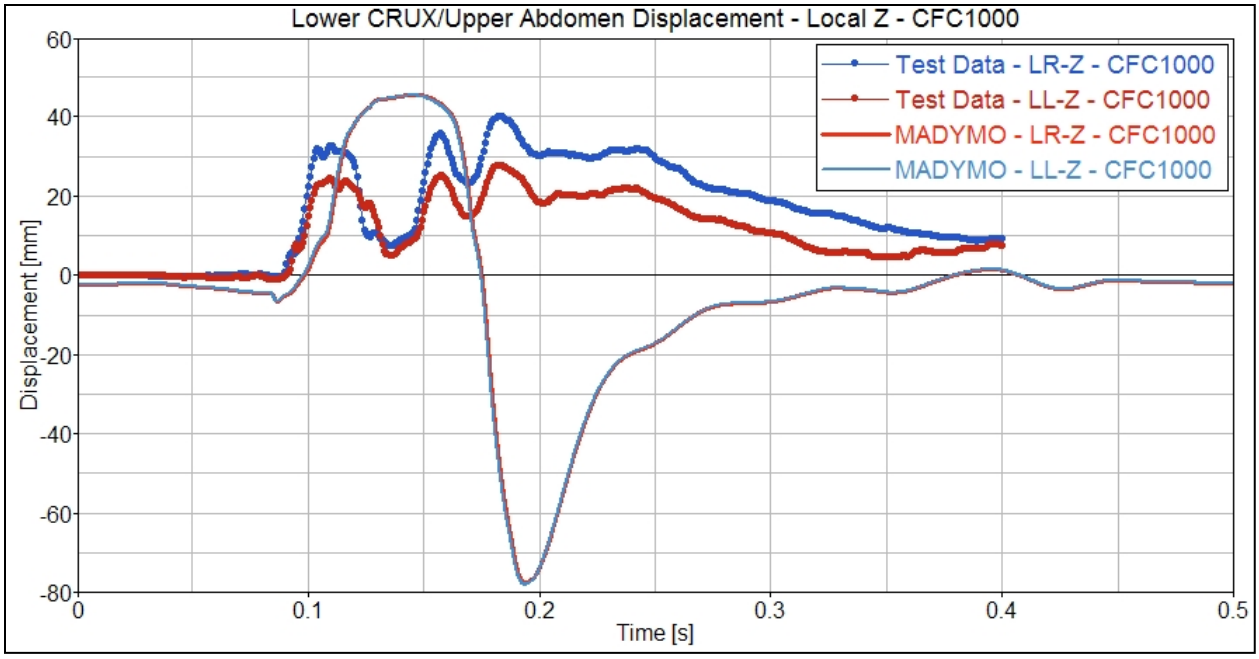

Figure H71. Lower CRUX, Local Z

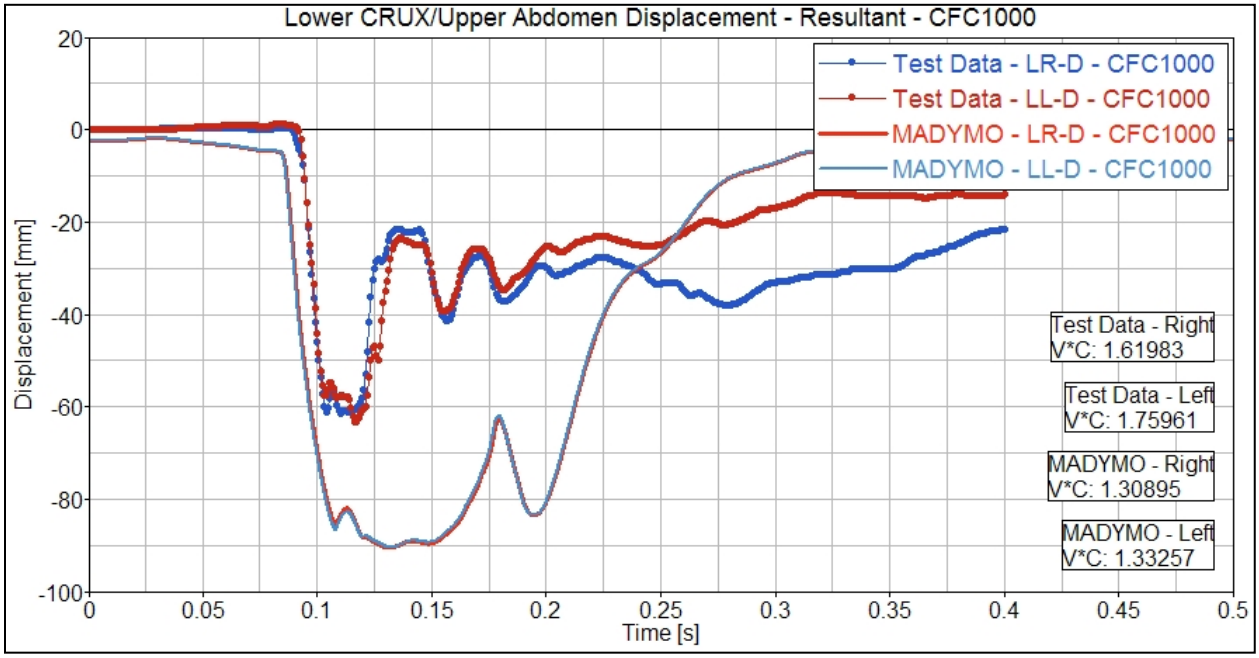

Figure H72. Lower CRUX, Resultant

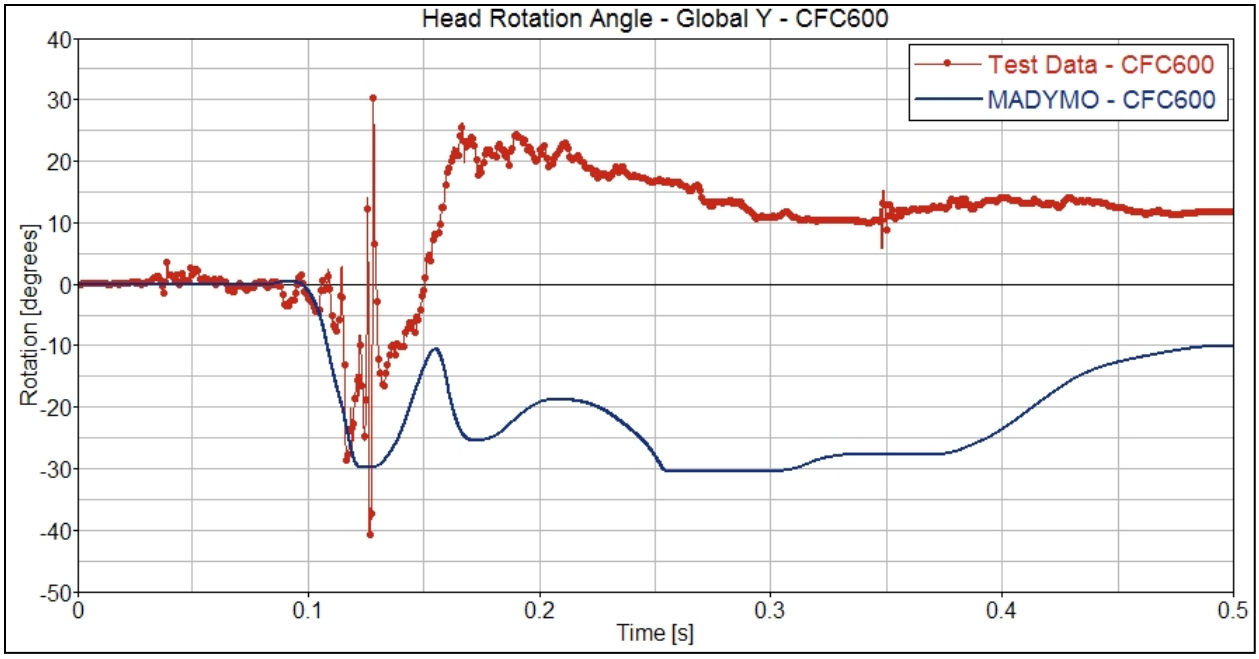

Figure H73. Head Rotation Angle, RY, at OC

Force Time-Histories

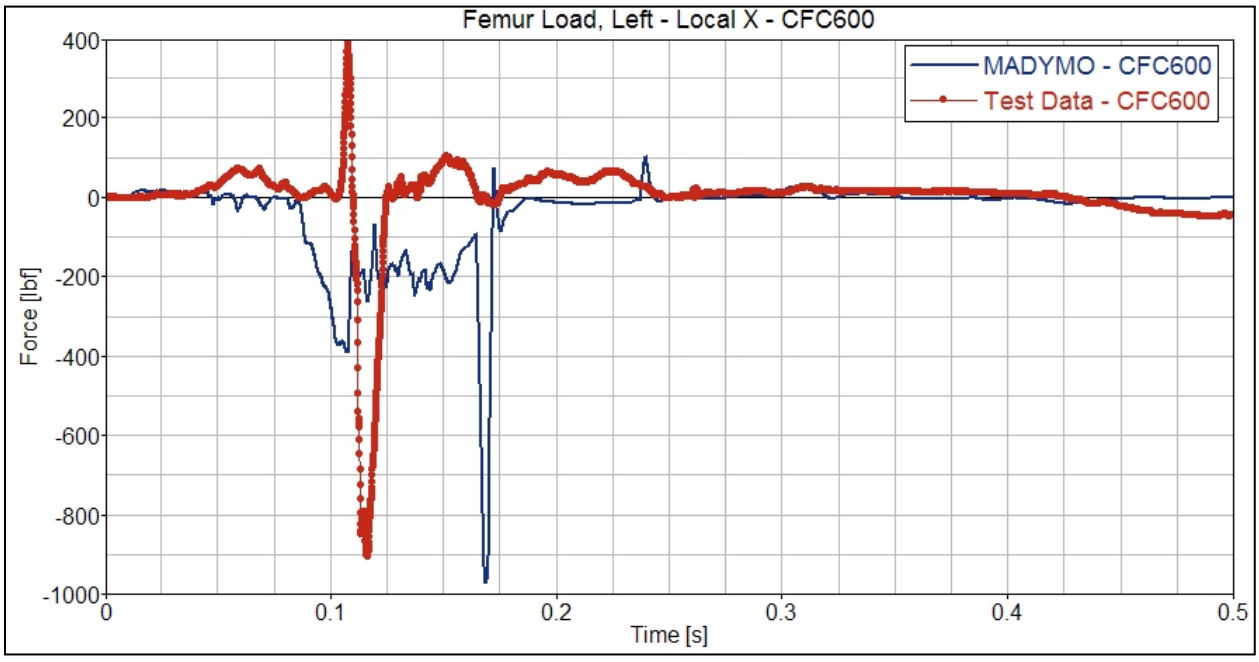

Figure H74. Left Femur Force, Local X

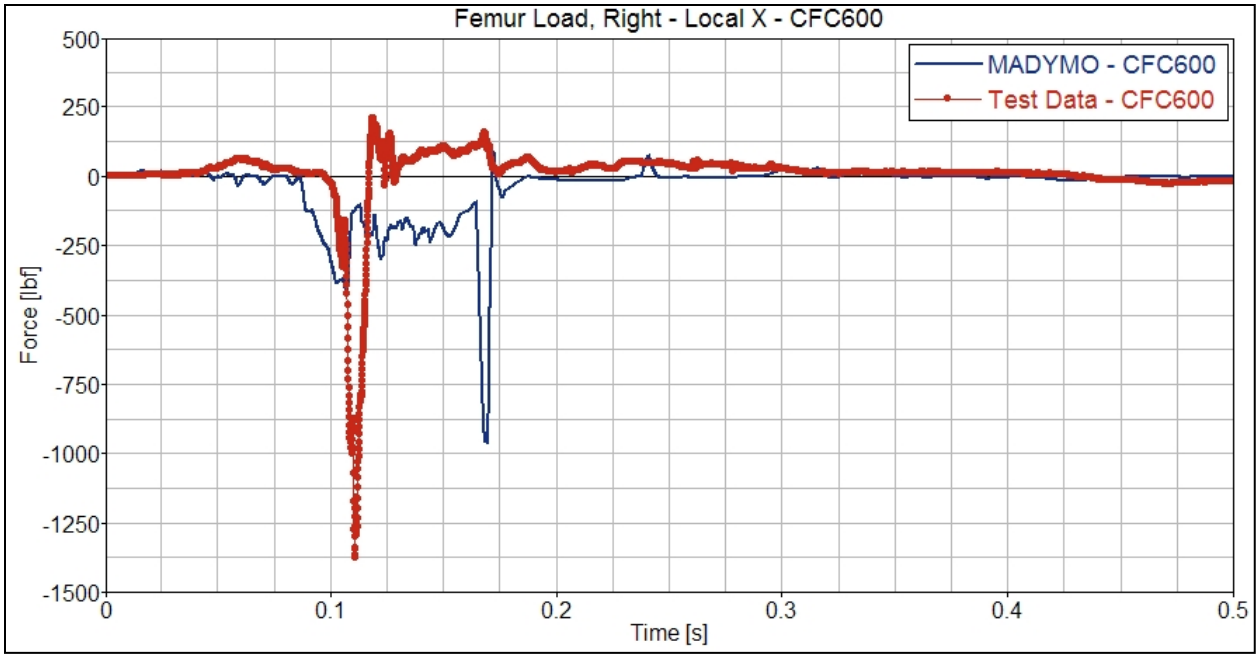

Figure H75. Right Femur Force, Local X

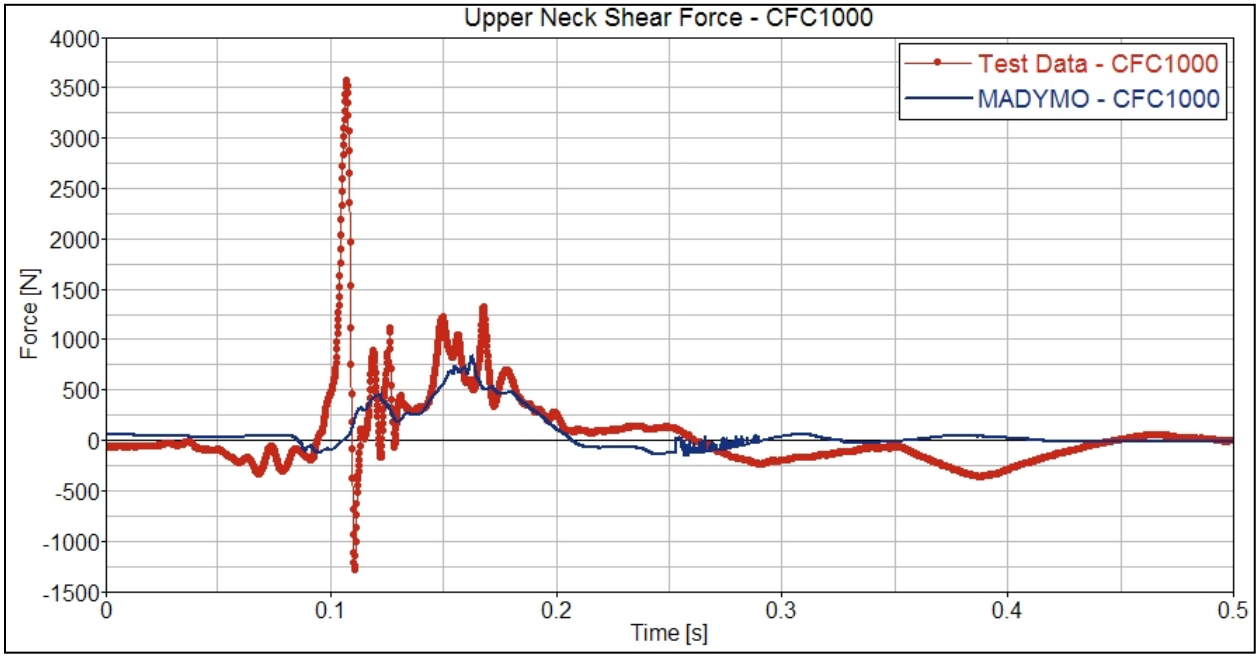

Figure H76. Upper Neck Shear Force, Fx

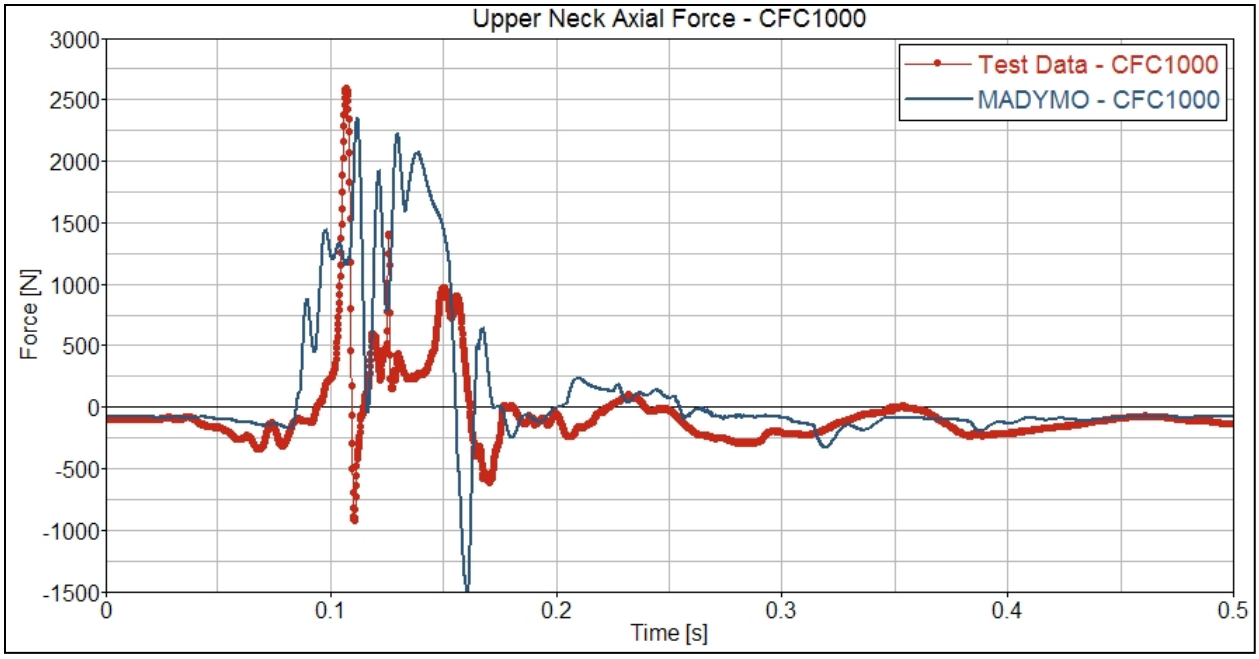

Figure H77. Upper Neck Axial Force, Fz

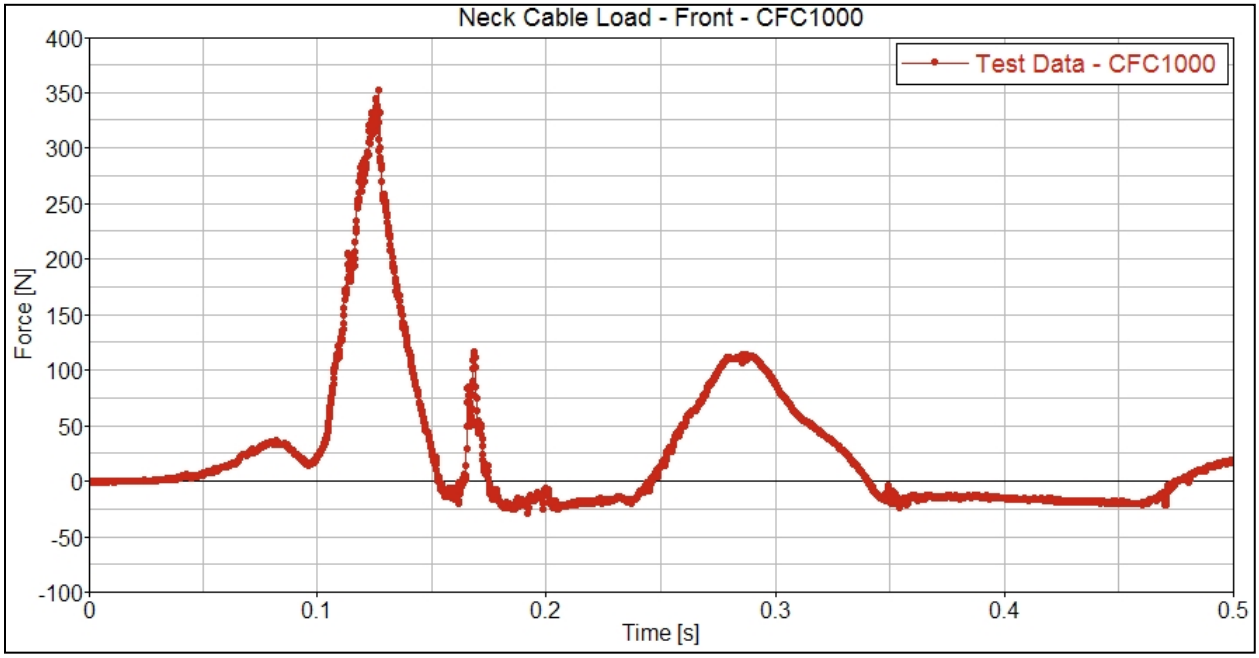

Figure H78. Neck Cable, Front

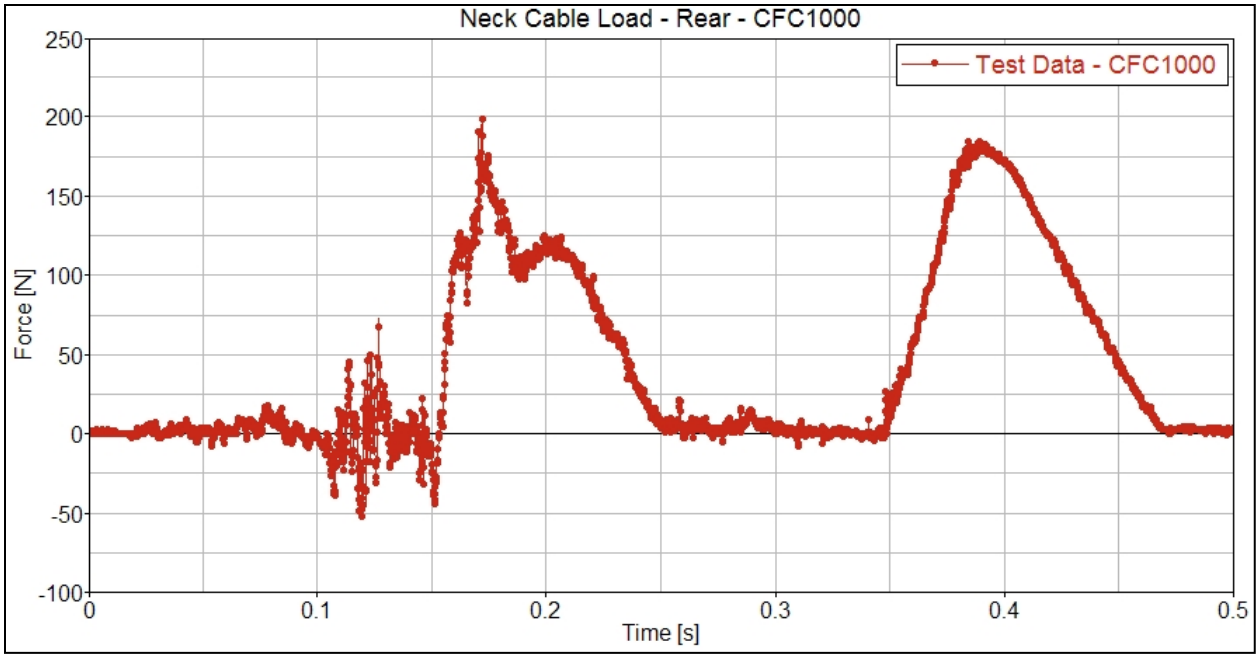

Figure H79. Neck Cable, Rear

Moment Time-Histories

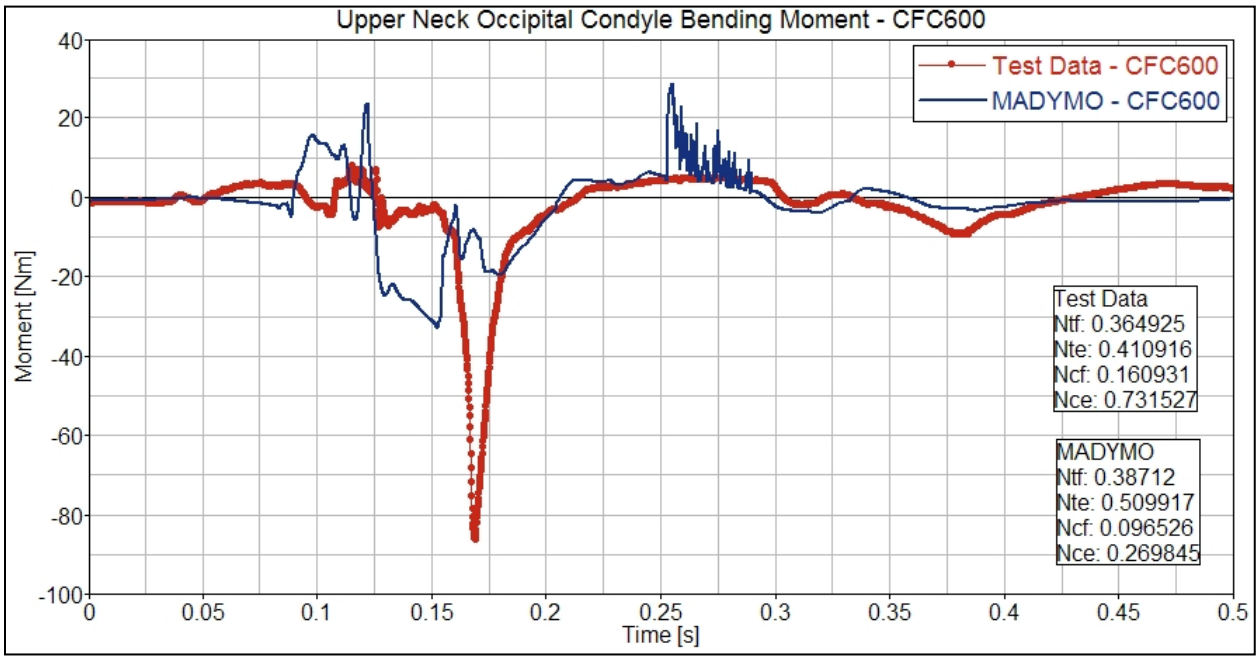

Figure H80. Upper Neck Occipital Condyle Bending Moment, My

Kinematics

A series of time-sequence pictures of the ATD kinematics are presented in this section. The pictures are taken from the test video and the MADYMO model output and presented together for comparison.

Figure H81. THOR Test Dummy Kinematics in Table Test, Simulation Results and Test Observations

Table Results

Displacement Time-Histories

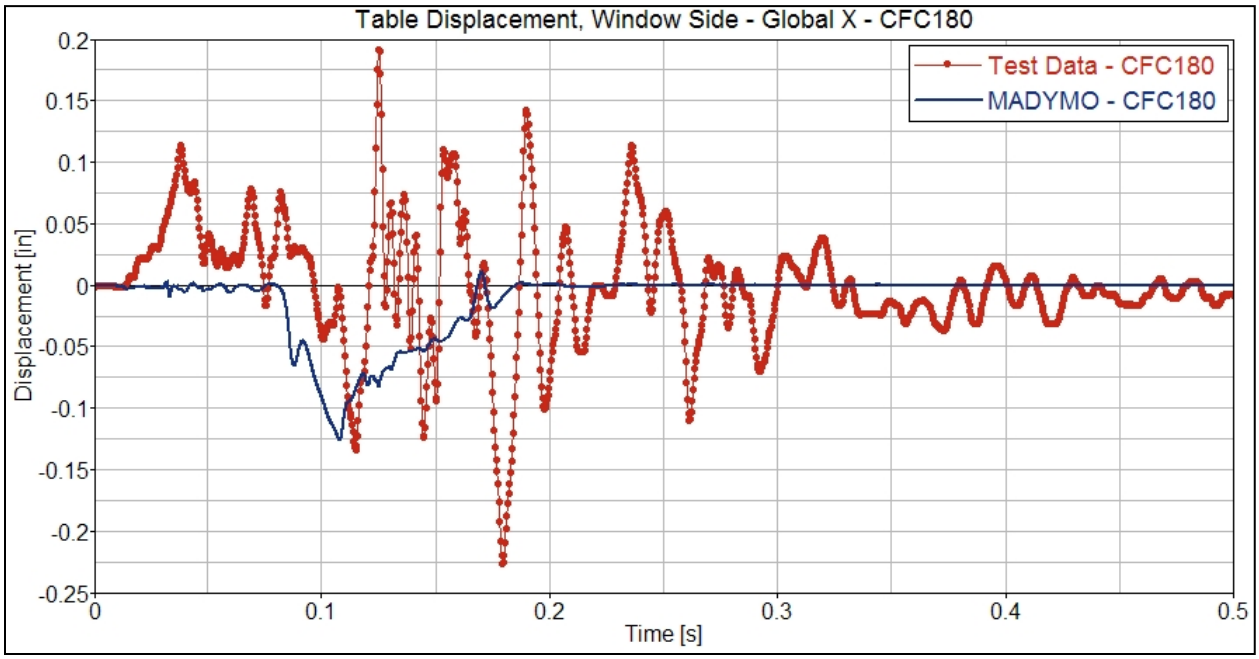

Figure H82. Table Displacement, Window Side, Global X

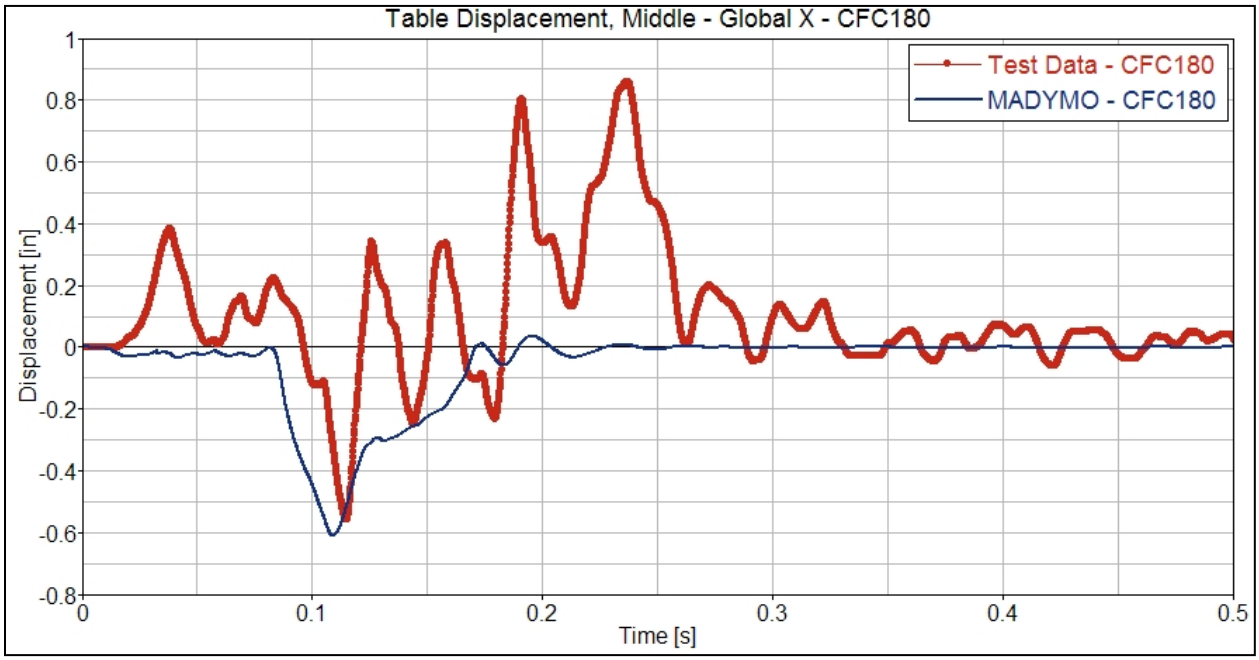

Figure H83. Table Displacement, Middle, Global X

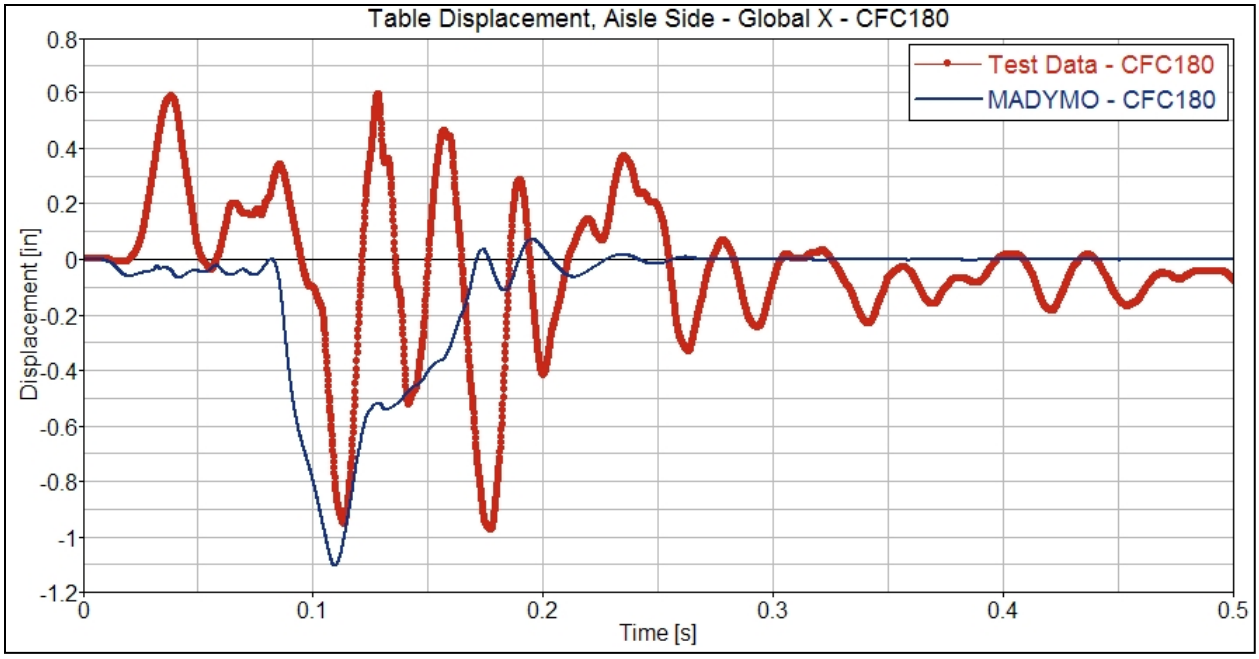

Figure H84. Table Displacement, Aisle Side, Global X

Force Time-Histories

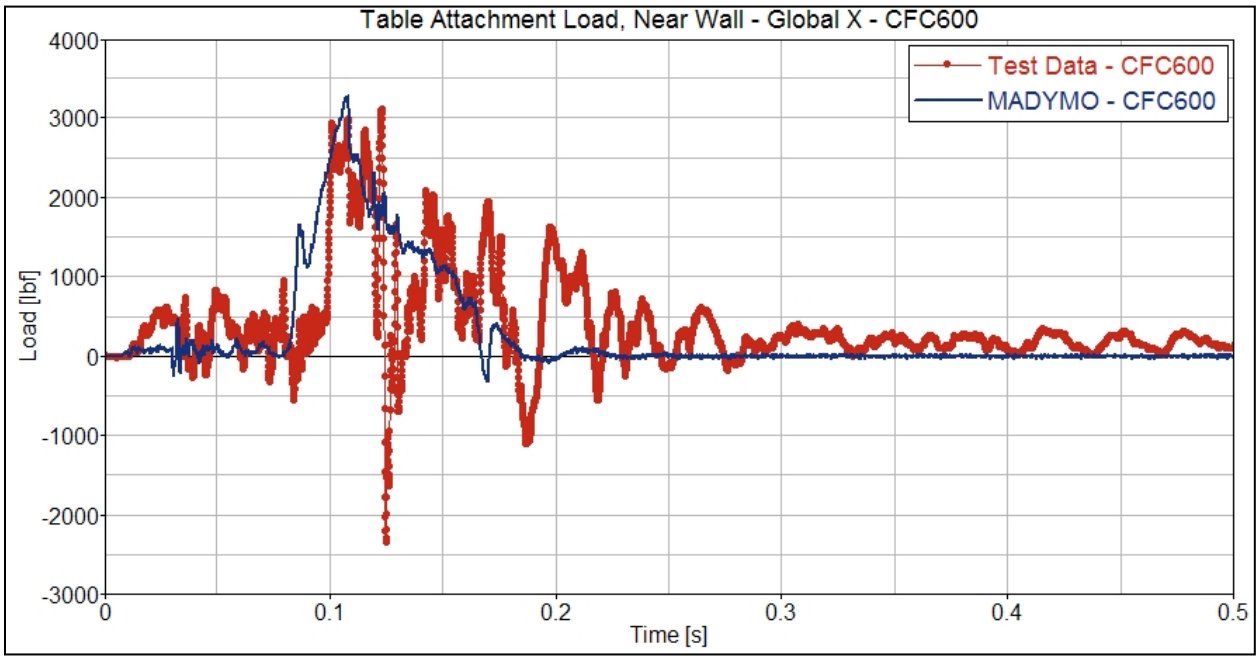

Figure H85. Table Attachment Load, Near Wall, Global X

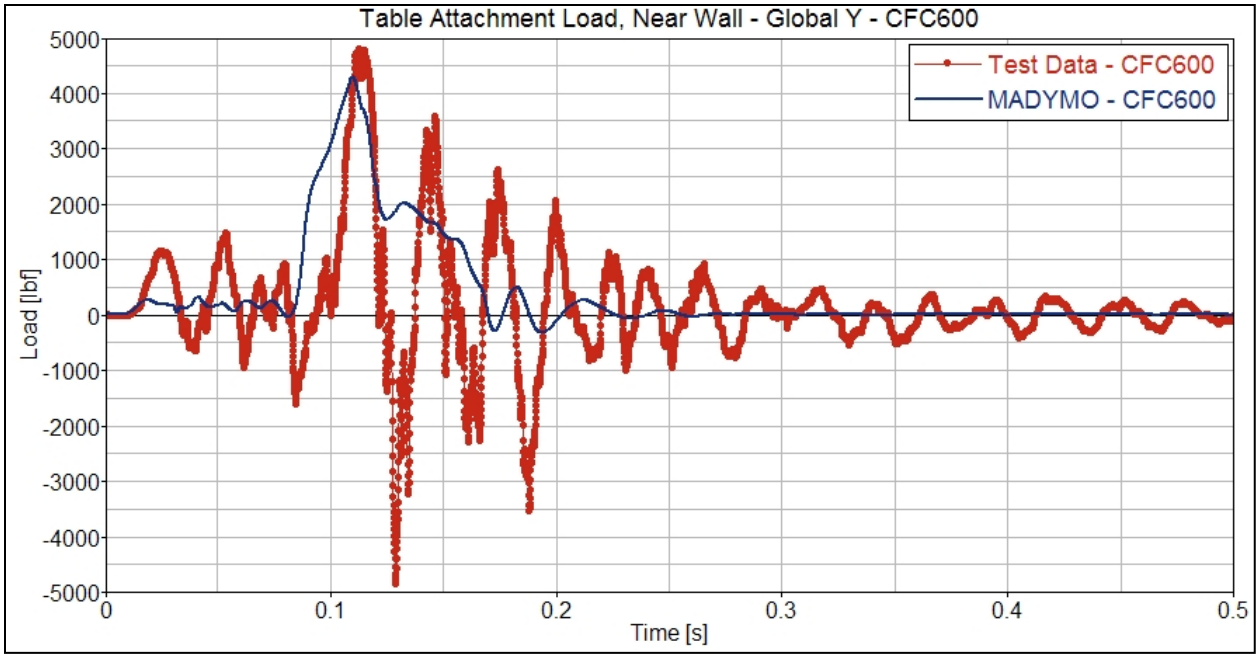

Figure H86. Table Attachment Load, Near Wall, Global Y

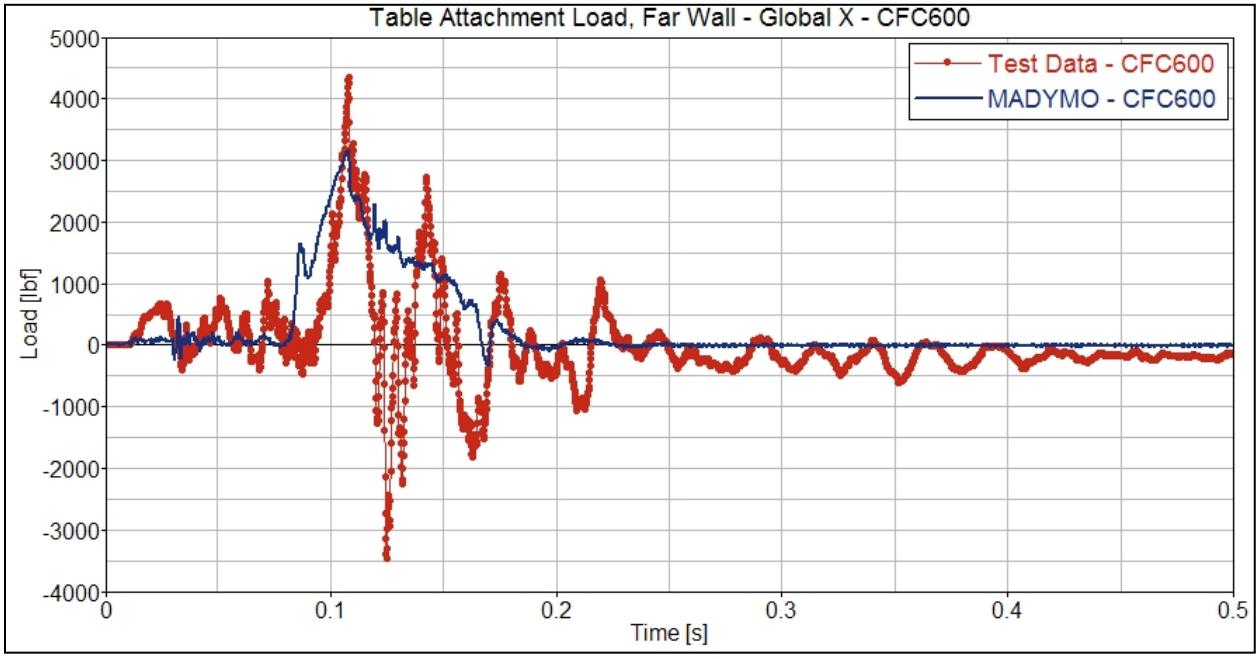

Figure H87. Table Attachment Load, Far Wall, Global X

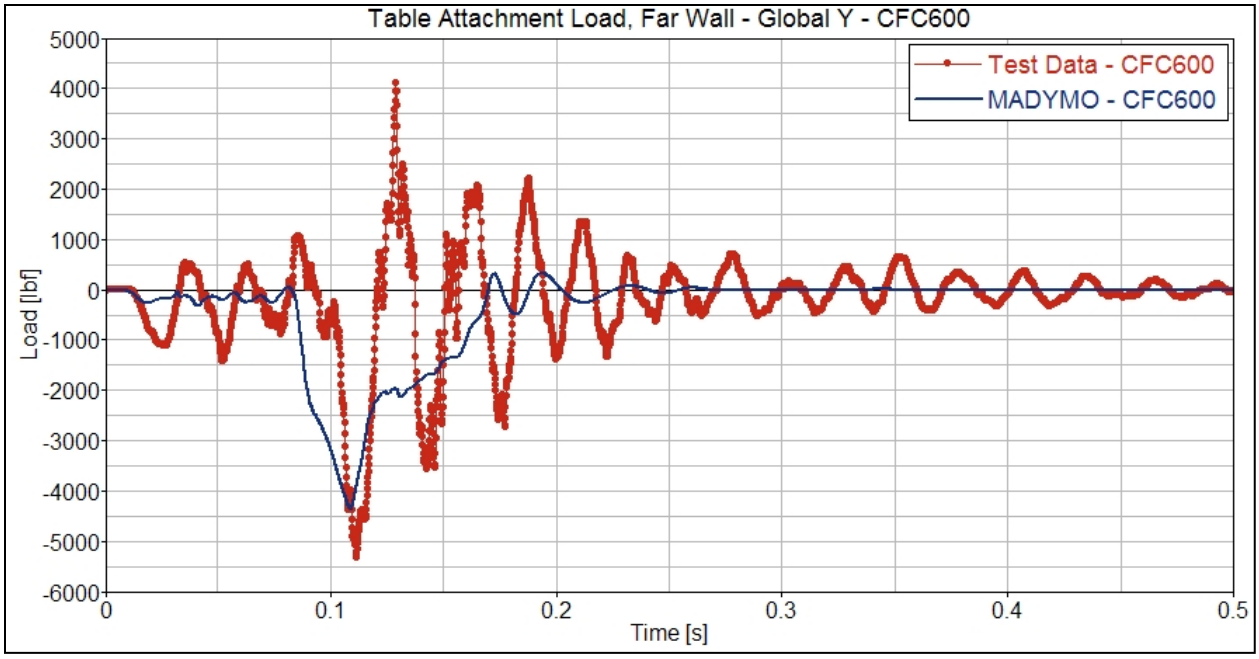

Figure H88. Table Attachment Load, Far Wall, Global Y

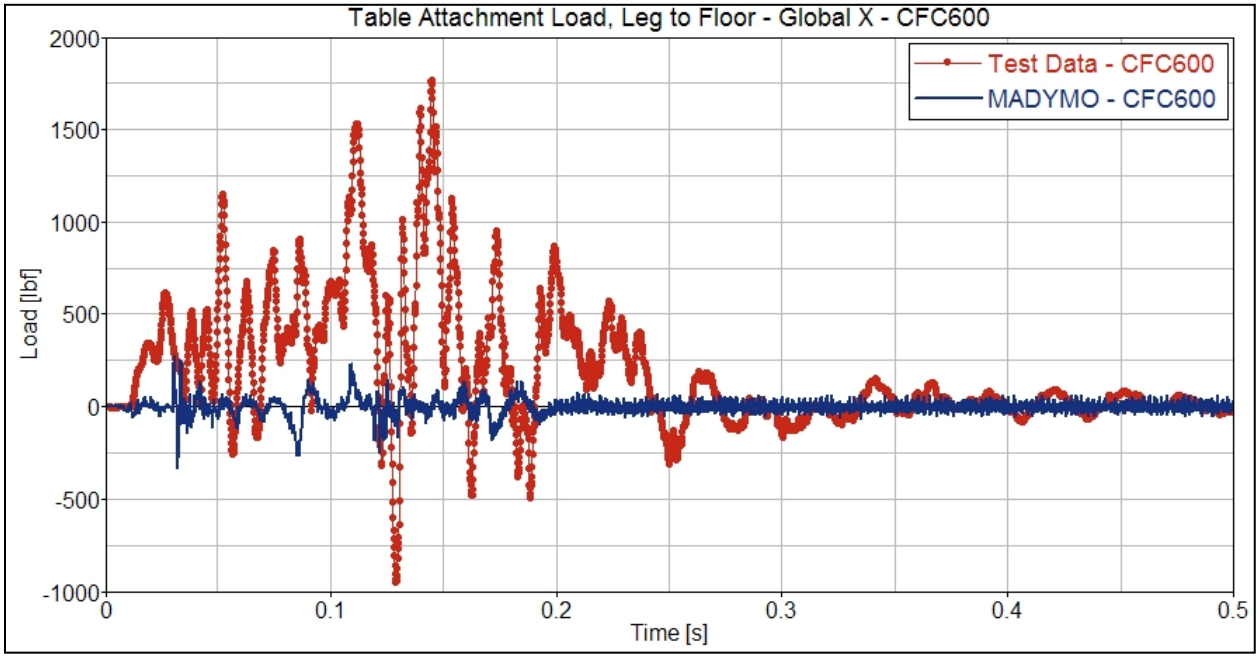

Figure H89. Table Attachment Load, Leg to Floor, Global X

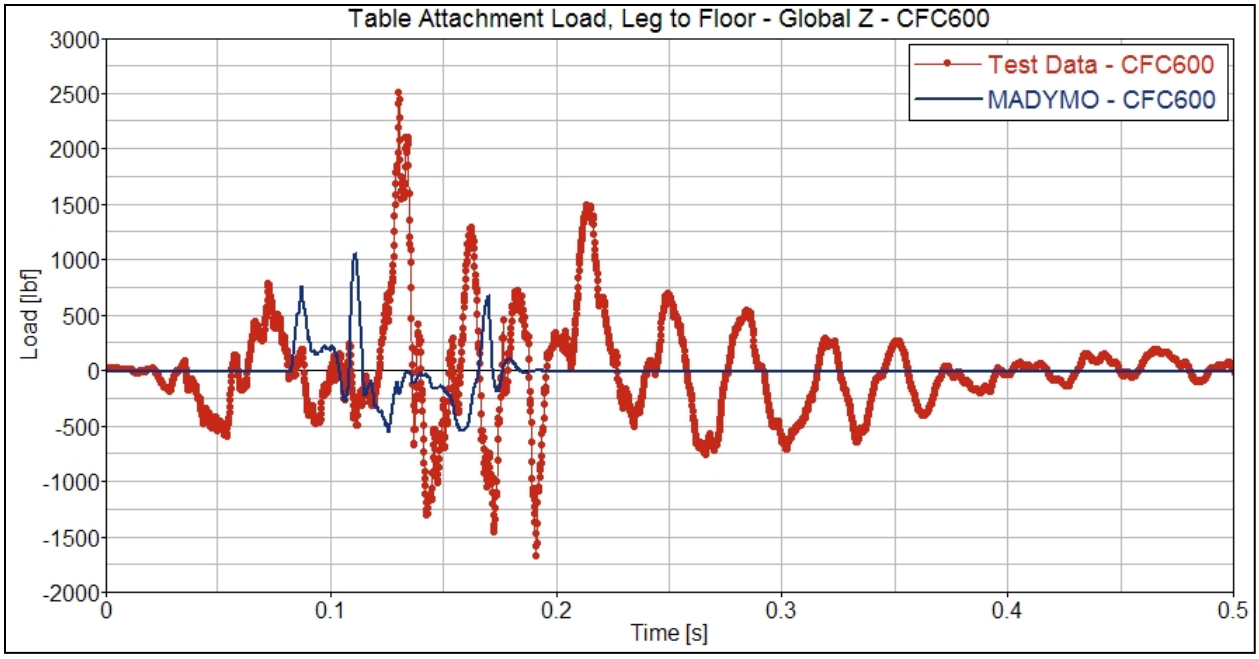

Figure H90. Table Attachment Load, Leg to Floor, Global Z

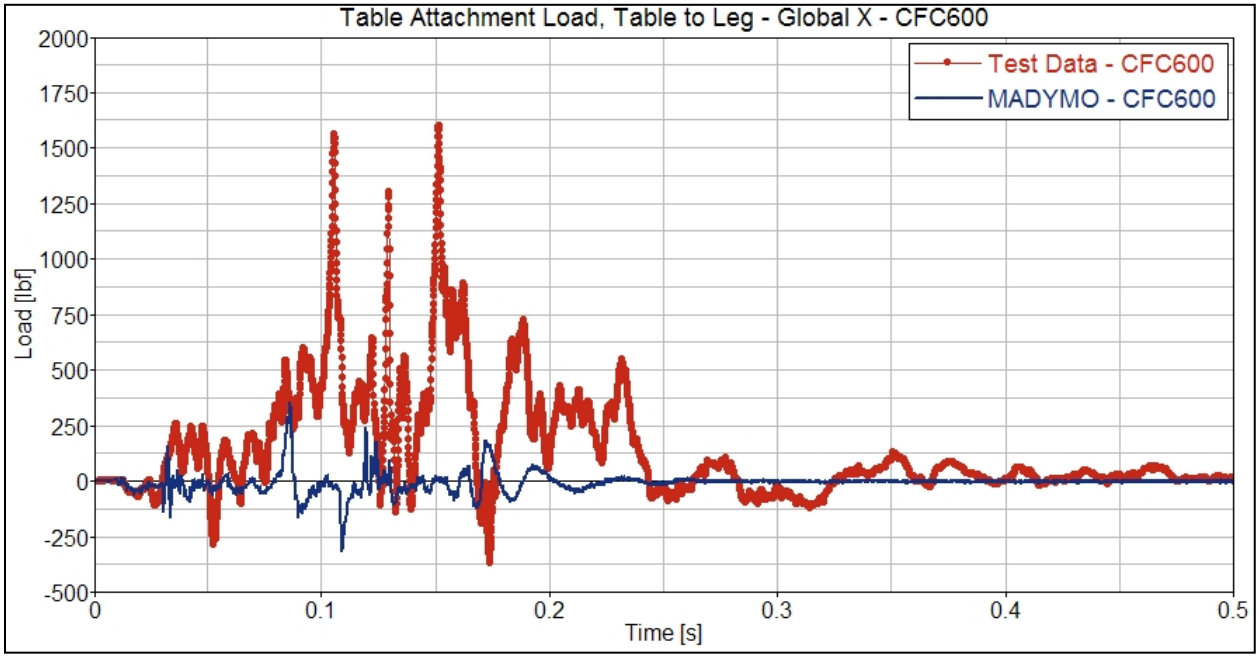

Figure H91. Table Attachment Load, Table to Leg, Global X

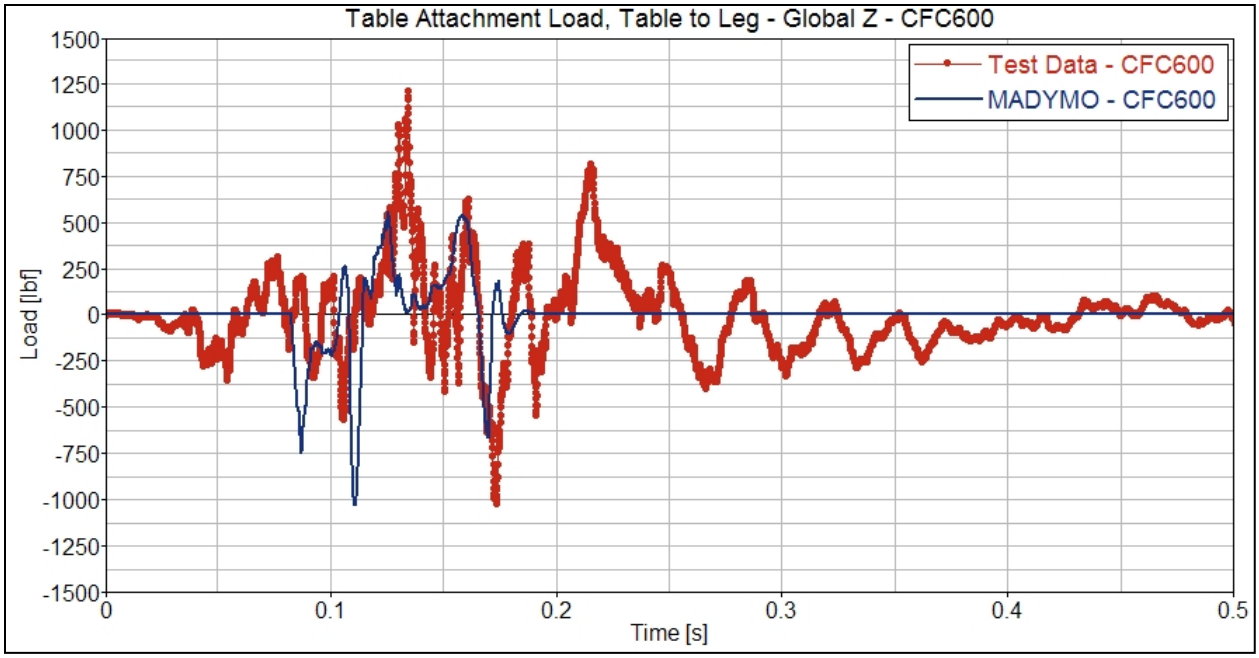

Figure H92. Table Attachment Load, Table to Leg, Global Z

Experiment 2-1: Rear-Facing Commuter Seat

Dynamics

The following section contains plots of the force and acceleration time-histories recorded from the 50th percentile Hybrid III male ATD seated in the center seat position of the rear-facing commuter seat. The experiment was located near the front of the trailing coach car. The corresponding time-histories from the ATD in the MADYMO model of Experiment 2-1 are plotted against the test data for direct comparison. The relevant injury criteria calculated from the test and model results are indicated on each plot. The CFC filter frequency used on both sets of data, in accordance with SAE J211-1, is indicated on each plot.

Acceleration Time-Histories

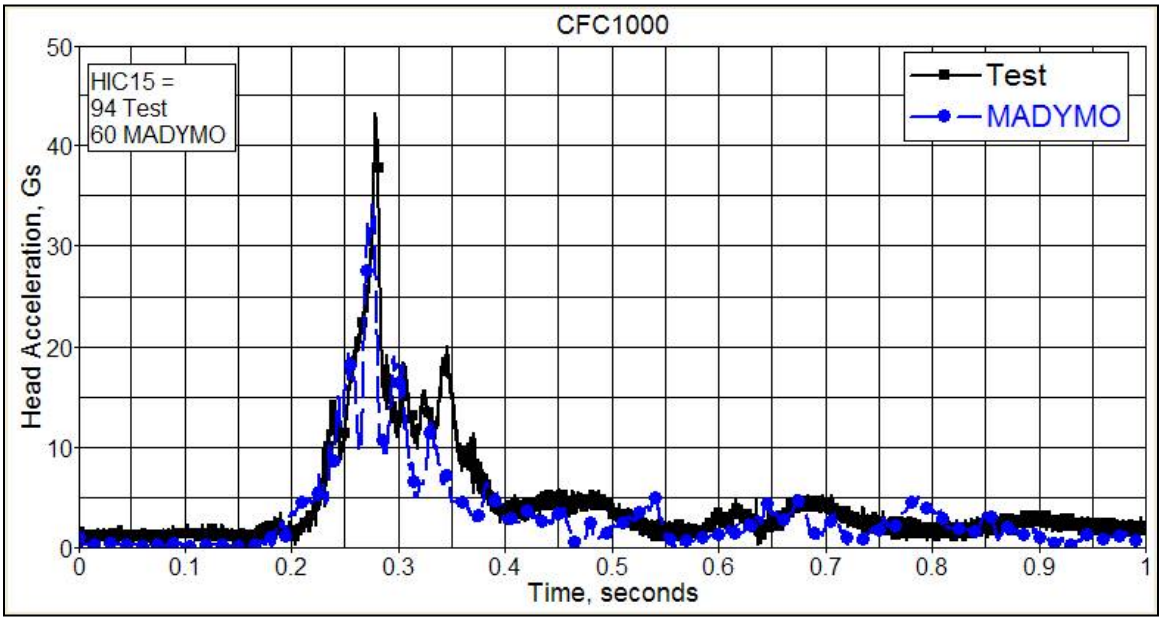

Figure H93. Head Resultant Acceleration

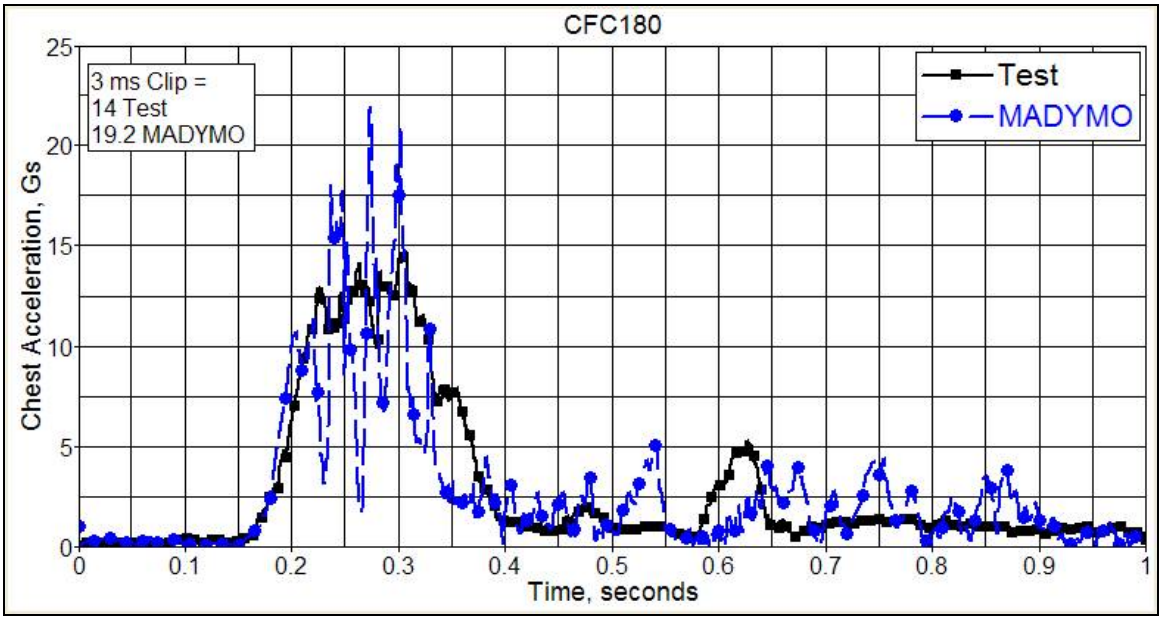

Figure H94. Chest Resultant Acceleration

Force Time-Histories

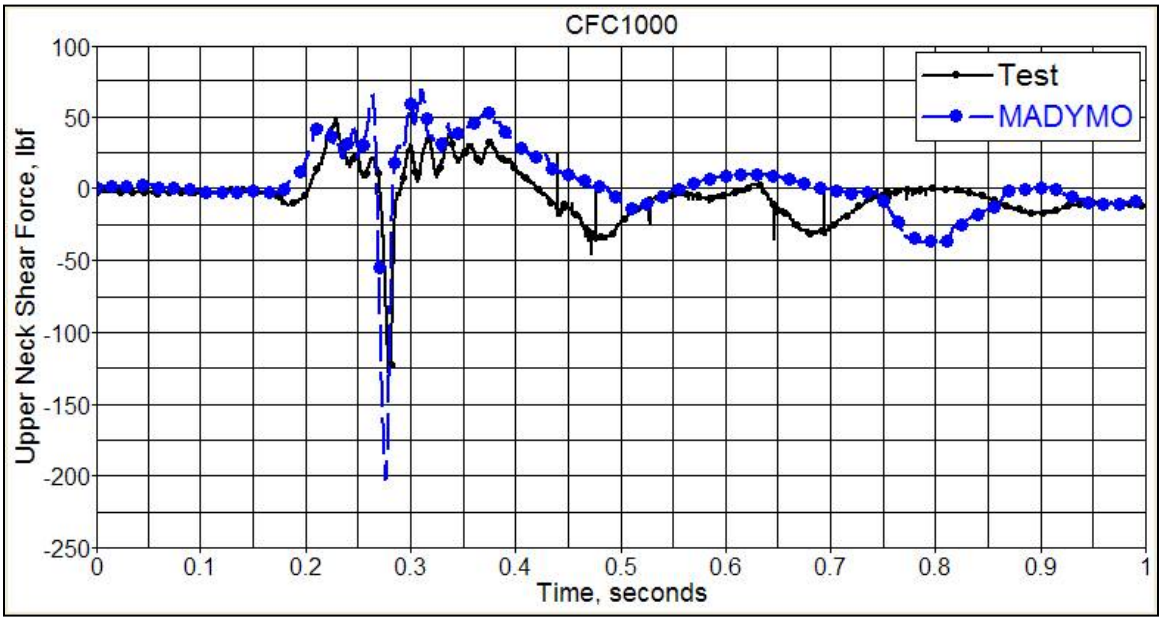

Figure H95. Upper Neck Shear Force, Fx

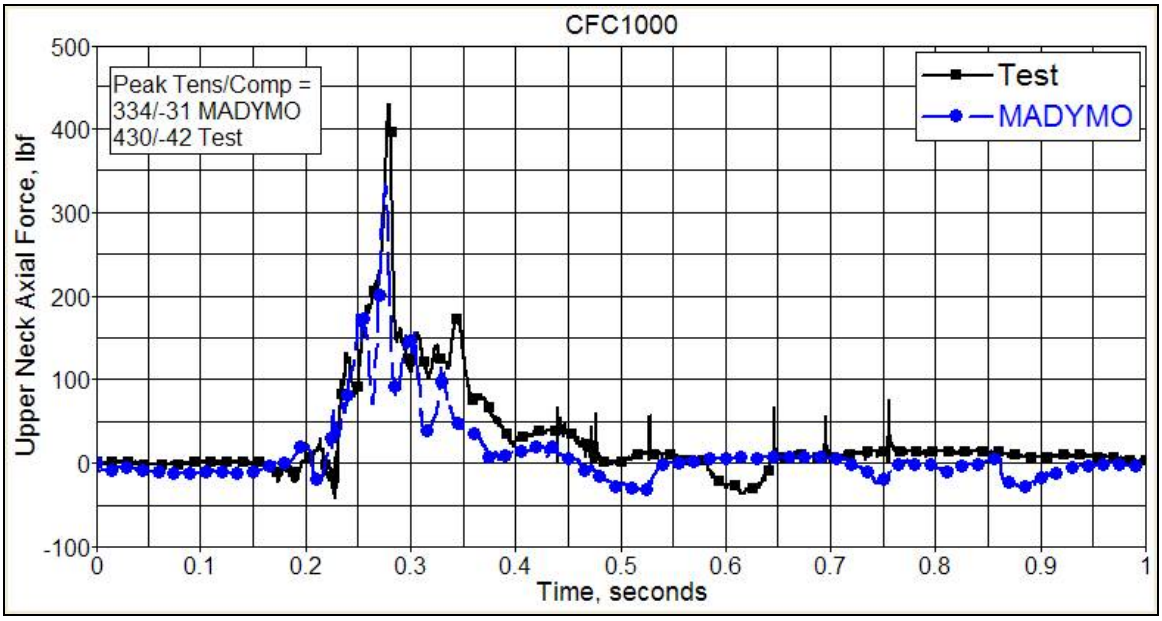

Figure H96. Upper Neck Axial Force, Fz

Moment Time-Histories

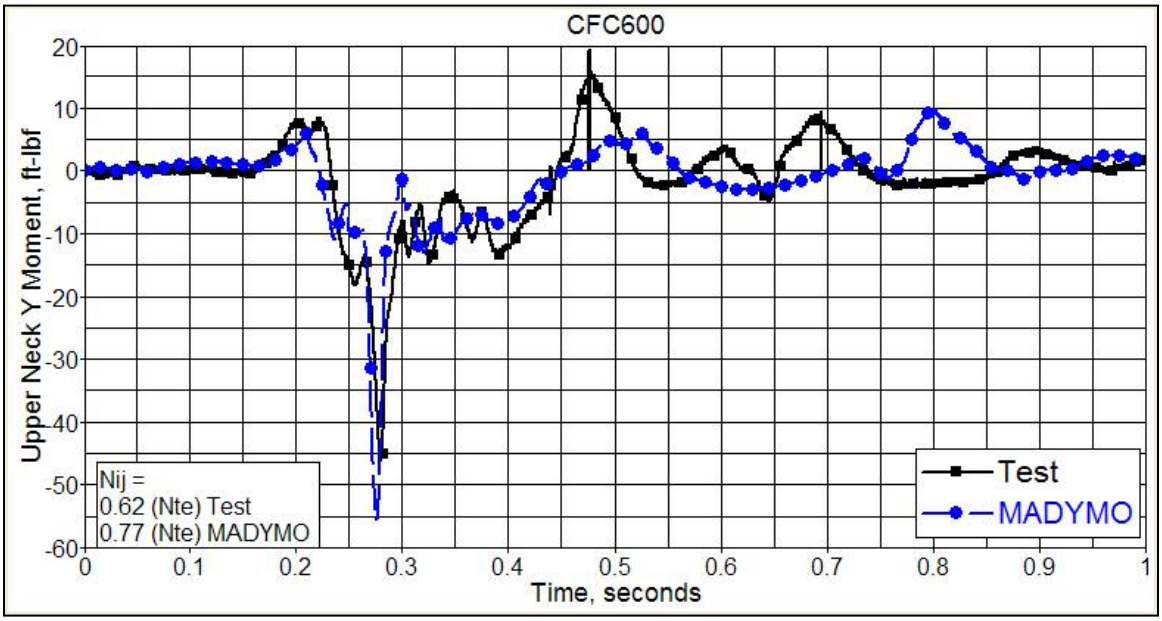

Figure H97. Upper Neck Occipital Condyle Bending Moment, My

Kinematics

A series of time-sequence pictures of the ATD kinematics are presented in this section. The pictures are taken from the test video and the MADYMO model output and presented together for comparison.

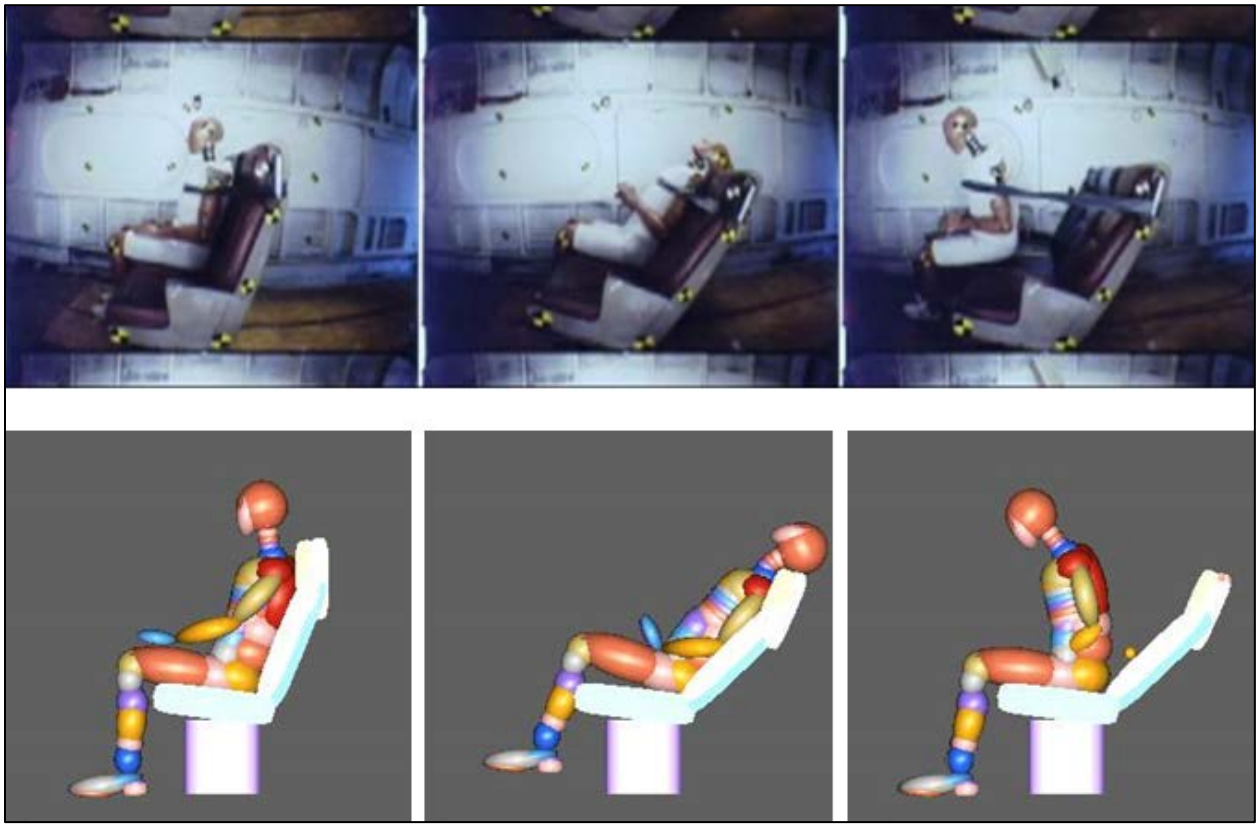

Figure H98. Time Sequence of ATD Kinematics

Experiment 2-2: Forward-Facing Commuter Seat

Dynamics

The following section contains plots of the force and acceleration time-histories recorded from the 50th-percentile Hybrid III male ATD seated in the aisle seat position of the forward-facing commuter seat. The experiment was located at the rear end of the trailing coach car. The corresponding time-histories from the aisle ATD in the MADYMO model of Experiment 2-2 are plotted against the test data for direct comparison. Data were measured from the ATDs in both the aisle and window positions. Since the results are similar, only one set of data is provided. The relevant injury criteria calculated from the test and model results are indicated on each plot. The CFC filter frequency used on both sets of data, in accordance with SAE J211-1, is indicated on each plot.

Acceleration Time-Histories

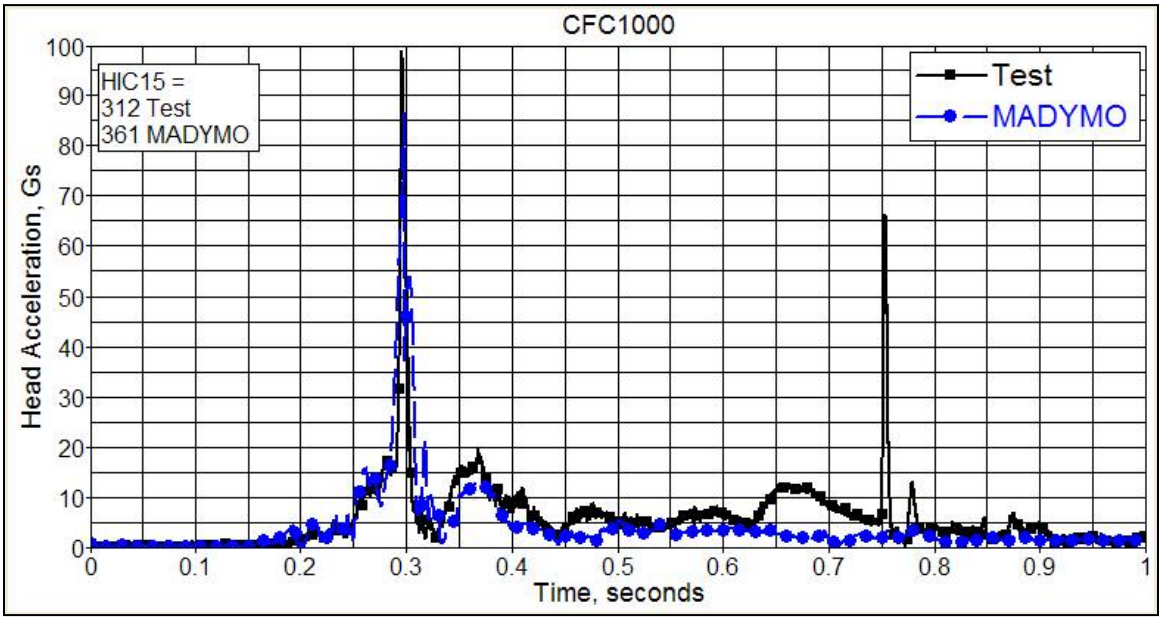

Figure H99. Head Resultant Acceleration

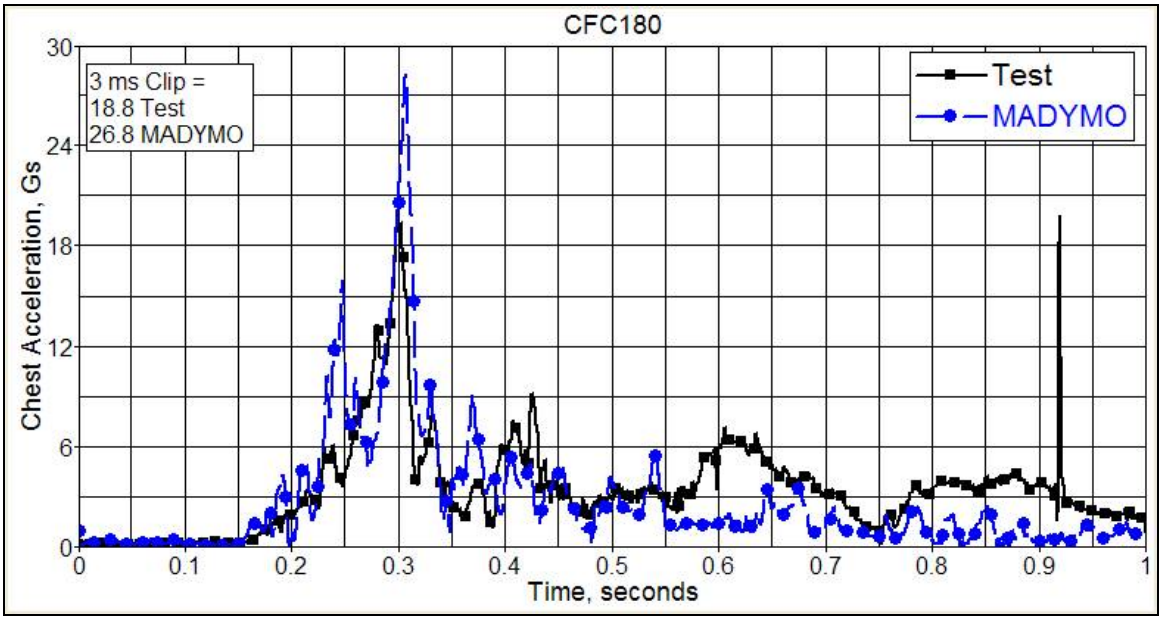

Figure H100. Chest Resultant Acceleration

Force-Time Histories

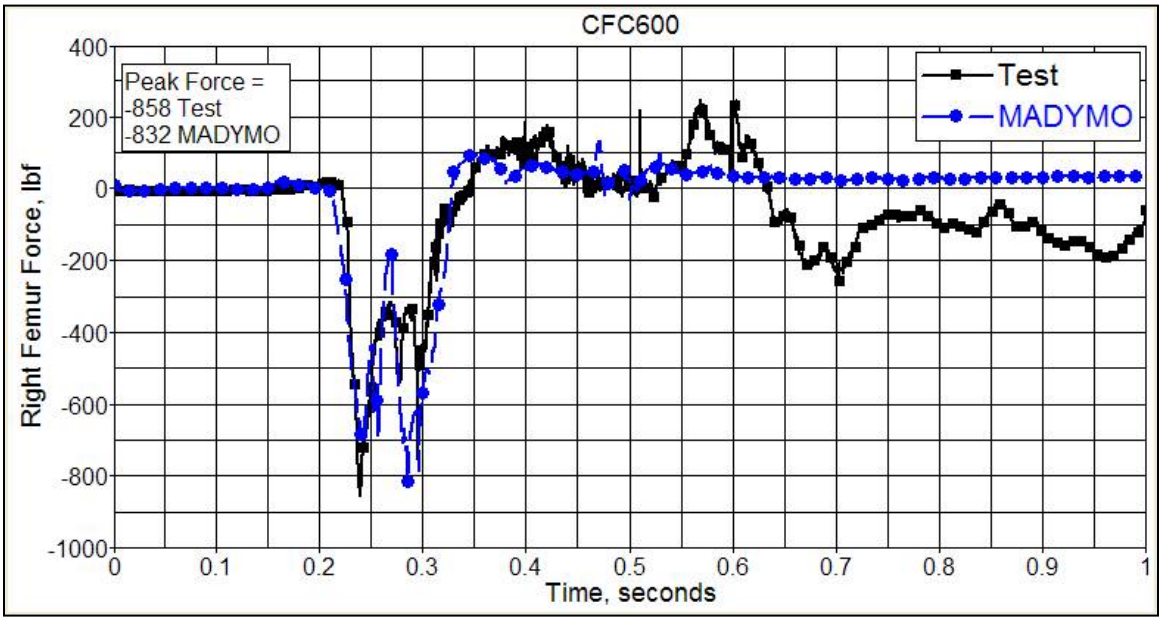

Figure H101. Left Femur Force

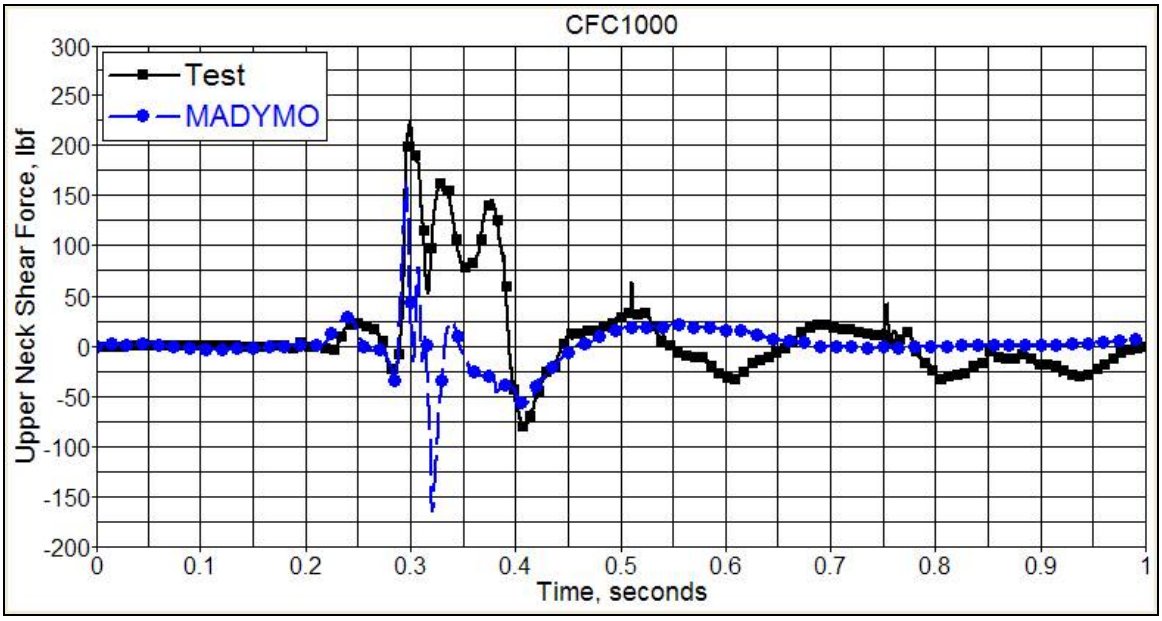

Figure H102. Upper Neck Shear Force, Fx

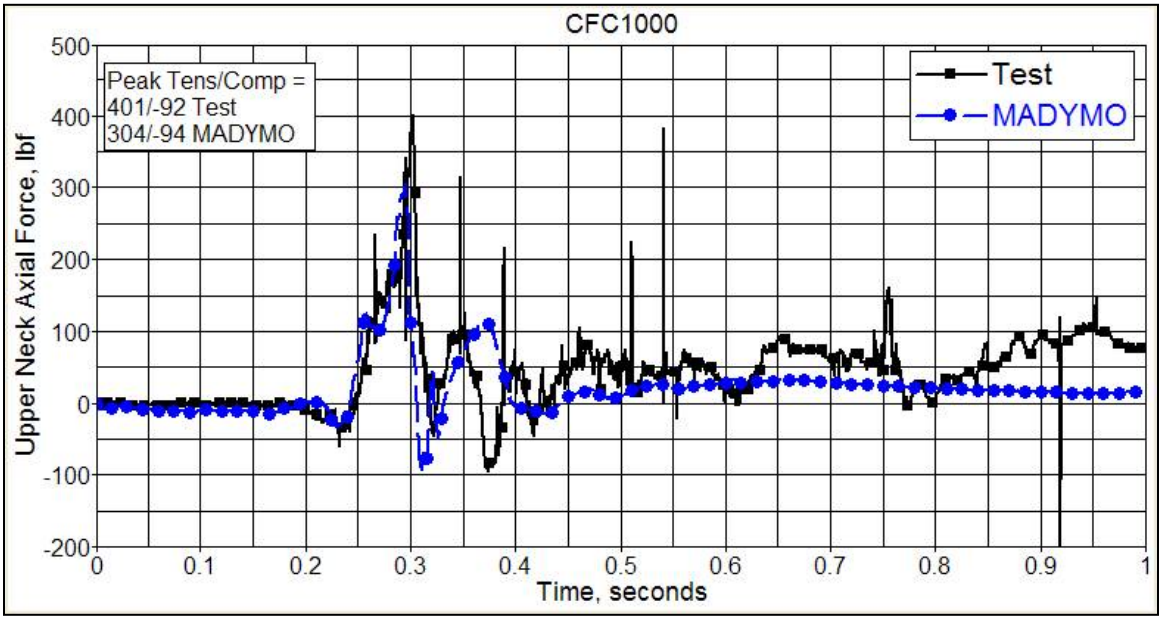

Figure H103. Upper Neck Axial Force, Fz

Moment Time-Histories

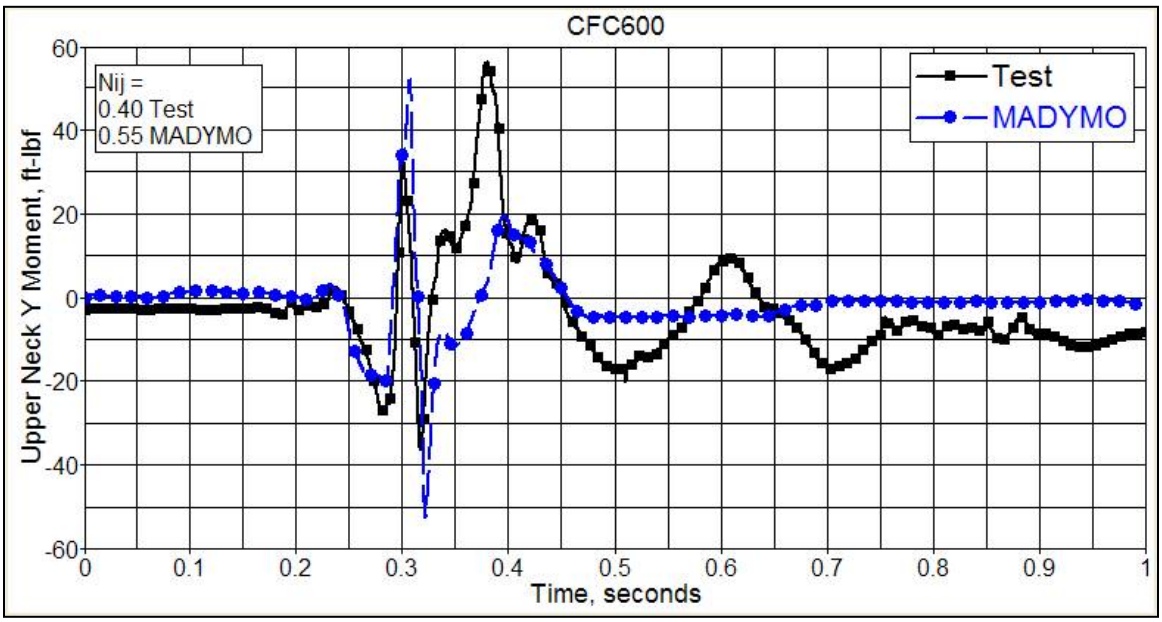

Figure H104. Upper Neck Occipital Condyle Bending Moment, M_y

Kinematics

A series of time-sequence pictures of the ATD kinematics are presented in this section. The pictures shown are taken from an overhead camera view because the side view camera failed during the test. Pictures from the MADYMO model output are presented below the test pictures for comparison.

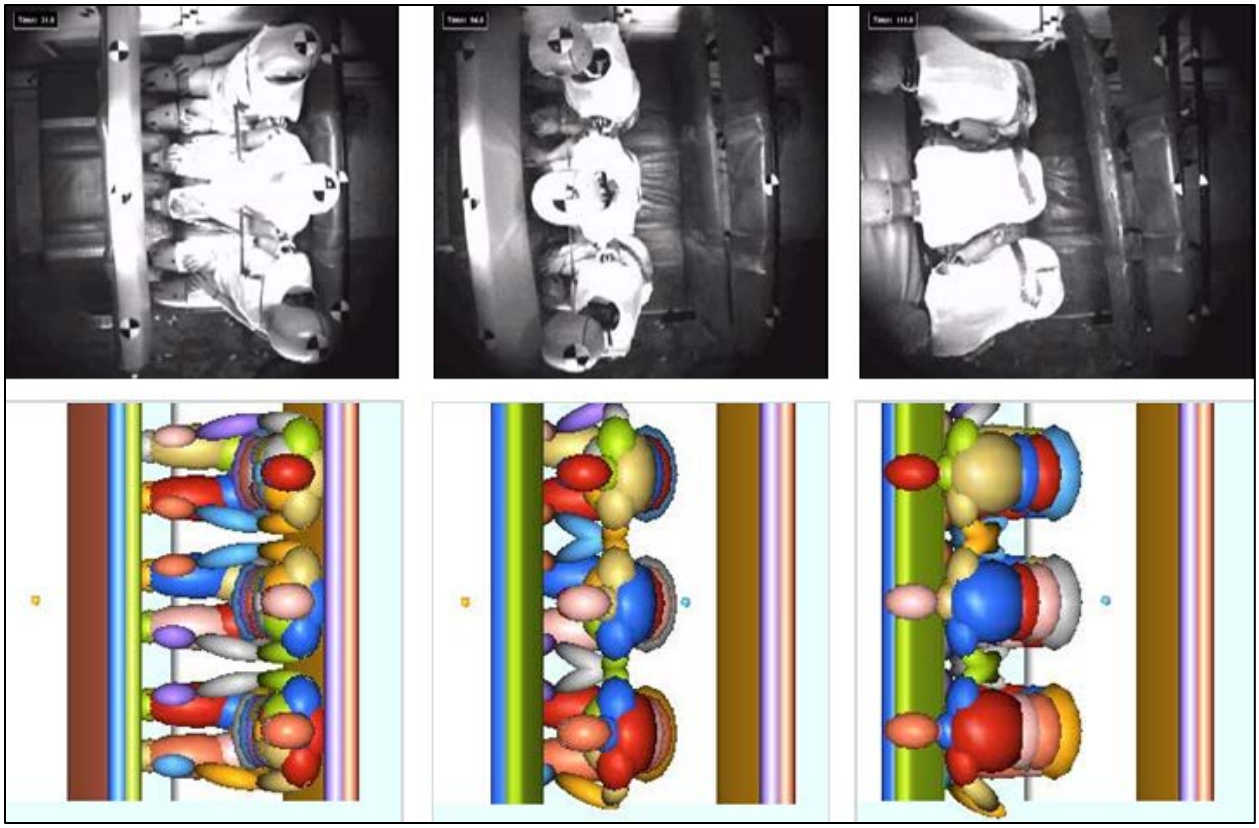

Figure H105. Time-Sequence of ATD Kinematics